# COMPUTER AIDED DESIGN AND CONSTRUCTION OF A MULTI-POINT POSITIONING ACTUATOR SYSTEM

by

**Zhan Wei Shi, B.Sc., M.Eng.**

A thesis submitted in partial fulfilment
of the requirements of the University of Abertay Dundee
for the degree of Doctor of Philosophy

The research programme was carried out
in collaboration with the AT&T Scotland

*April 1997*

**I certify that this thesis is the true and accurate version of the thesis approved by the examiners.**

Signed: [redacted]
**(Director of Studies)**

Date: 22 Sept. 1997

# Declaration

I hereby declare that while registered as a candidate for the degree for which this thesis is presented I have not been a candidate for any other award. I further declare that the work presented in this thesis is original and was carried out by myself at the University of Abertay Dundee, except where due acknowledgement is made.

Signed: 

Date: 19 Sept. 1997

# Acknowledgements

I would like to thank wholeheartedly my supervisor Dr C B Rajanathan and Mr A T Sapeluk for their guidance, advice and encouragement throughout the project. Without their support, this research could not have been implemented.

The full financial support and the provision of the necessary equipment from NCR Scotland is gratefully acknowledged

Thanks also go to the following staffs for the their assistance and advice freely given and gratefully received:

Professor R W Johnson, Professor P F Martin and Dr B Jefferies, who as the Heads of the Department, for their support to the research.

The technical support staffs of the School of Engineering for their assistance in all the engineering aspects from fabrication of actuators, experimental rigs and fabricating PCB boards to the provision of electronic components, etc..

Dr C Main for his help in the measuring of temperature.

Finally, I am greatly indebted to my wife and my child for their patience, understanding and constant supporting during the past three years.

# Abstract

This thesis investigates the development, control, modelling and analysis of single-phase tubular linear induction actuators (TLIA) for the application of multi-point positioning.

A novel TLIA has been successfully developed in the research project. This actuator makes use of the electromagnetic induction principle to produce a force that varies with displacement and can be controlled by the voltage/current applied at its terminals. This enables the position of the actuator to be controlled by a proper external circuitry. Its structure is simpler, compared with traditional TLIA. With the exercise of computer aided design and analysis a monotonously decreasing control characteristic has been obtained. This makes the actuator inherently suitable for stepless positioning under both open loop and closed loop control.

The positioning was realised by changing the terminal voltage applied to the actuator in the actual system. Two forms of power supply units (PSU) have been studied. One is a triac controlled a.c. line phase controller. The other is a single-phase variable-frequency-variable-voltage a.c. converter using PWM technology. Both PSUs' output voltage can be controlled by a DSP board configured as a closed loop control system. Although the PWM PSU is a little more complicated than the triac based one, it offers better performance and more flexibility in control methods.

A second order spring-mass-damper system was used as the fundamental model of the actuator system. The control algorithm consists of a digital controller, a non-linear correction based on the inverse function method and an explicit friction compensation with the Coulomb friction model. With the digital control technique, the restrictions in the characteristics of the actuator have been improved significantly.

To get an in-depth insight of the electromagnetic phenomena happening inside the actuator and to function as a CAD tool, a general-purpose axi-symmetric FEM package

has been developed for the computation of transient electromagnetic field. It can deal with various forms of power supply from standard current excitation to voltage excitation by coupling an external circuit with the electromagnetic field equations. A decomposed magnetic vector potential (DMVP) method, which is based on the indirect coupling of external circuit equations, has been proposed to deal with transient eddy current problems under voltage excitation coupled with external circuit equation. Comparisons between the direct coupling method and the DMVP indirect coupling method have been made. It has shown that the proposed new method can reduce the CPU time and storage considerably. Also a new method to improve the accuracy of Maxwell's stress tensor based force calculation has been proposed along with a fundamental analysis of various sources which cause the error in force computation. The proposed force calculation scheme can achieve two goals: elimination of the path-dependent sensitivity and improvement of the accuracy in the force calculation.

Computation of transient temperature field has been studied as well by FEM. The FEM package for electromagnetic field computation has been further expanded to incorporate the function of transient temperature computation. The coupling between the electromagnetic field and the temperature field was treated in an indirect way. Experimental tests have been carried out on a prototype TLIA to verify the FE simulation. A good agreement between the computed and the tested results has been obtained.

Finally the newly developed TLIA, PSU and DSP-based controller have been put together to form a complete integrated positioning system. Application as a multi-step positioning control system has been successfully achieved.

# List of Symbols

| | |
|---|---|
| $\omega$ | angular frequency of power supply |
| $\sigma$ | electrical conductivity |
| $\Psi$ | magnetic flux linkage |
| $\Omega$ | solution region |
| $\mu$ | magnetic permeability |
| $\rho$ | mass density |
| $\lambda$, $\beta$ | coefficient |
| **A** | magnetic vector potential |
| $\Theta$,$\Im$ | functional or energy function |
| $A_s$ | area of the cross section of a winding |
| **B** | magnetic flux density |
| C,c | constants |
| $C_d$ | damping coefficient |
| $C_s$ | spring constant |
| **E** | electric field strength |
| $\varepsilon$ | error |
| $F$, **F** | force |
| $f$, **f** | force density |
| $\Gamma$ | boundary of a region |
| **H** | magnetic field strength |
| $H(s)$ | transfer function of the plant |
| $\mathbf{H}_c$ | coercive magnetic field strength |
| $h_c$ | heat transfer coefficient |
| $i$, I | current |
| **J** | current density |
| $K$, k | constant |
| $K_p$ | proportional gain |

| | |
|---|---|
| $L$ | Laplace transform |
| $L^{-1}$ | inverse Laplace transform |
| $M$ | mass |
| $\nabla$ | Laplace operator |
| $\nu$ | magnetic reluctivity |
| N | number of turns of the winding |
| $N_i(r,z)$ | shape function |
| $q_e$ | electric charge density |
| $q$ | density of heat source |
| R | electrical resistance or magnetic reluctance |
| S | area |
| s | Laplace transform variable |
| T | sampling time interval |
| $T_\infty$ | ambient fluid temperature |
| $T_s$ | temperature at the surface in contact with the fluid |
| $T$ | temperature |
| $t$ | time |
| $T_d$ | derivative time constant |
| $T_i$ | integral time constant |
| $v$ | voltage |
| $\xi, \zeta$ | auxiliary variable |
| $y$ | displacement |
| z | variable of z-transform |
| $Z$ | impedance or z-transform |
| $Z^{-1}$ | inverse z-transform |

# Table of Contents

# 1 INTRODUCTION

## 1.1 Review of Linear Actuators

The increasing use of control techniques in modern process automation requires a variety of actuators with mechanical output. With regard to the existing actuators, they generally fall into three catalogues: electromechanical actuators, fluid powered actuators and alternative principle actuators (piezo, magneto-strictive, memory metal actuators, etc.). Pneumatic and hydraulic devices can produce very large forces from very small units, and there is no doubt that this type of actuator is supreme for the force/weight criterion. On the other hand, they require a considerable amount of auxiliary equipment that must be kept running even when the actuator is not in action. Usually their dynamic performance can not match those provided by electric devices. In low power applications, electromechanical actuators are extensively used. Those devices that can directly generate linear motion have attracted more study recently because of their unconventional structure and working principle [1~7]. Linear electric actuators belong to the group of linear electric motors (LEM) which have classifications corresponding to their rotary counterparts [8], such as

- d.c. or permanent magnet motors
- a.c. motors (asynchronous induction, synchronous including reluctance and stepping motors)
- Hybrid motors

When linear actuators/motors are used in positioning application, we can also classify them in terms of positioning range which can be roughly divided into four scales, varying

from very small to small, medium and large positioning ranges that roughly correspond to *μm*, *mm*, *cm* and *m* units of scale respectively. The suitable application areas for different forms of linear actuators are largely pre-determined by their working principles. Generally they can be summarised as follows:

- Piezoelectric, magneto-strictive actuators: very small positioning range with very high force/weight ratio
- Electromagnets: small positioning range with medium force/weight ratio
- Linear d.c./step motors: small and medium positioning range with small/medium force/weight ratio
- Linear a.c. motors: medium and large positioning range with medium force/weight ratio

Since our application will cover a small ~ medium range of positioning, the suitable types of actuators seem to be electromagnets or linear d.c./step motors, according to the above general classification.

Electromagnets can provide medium tractive stress up to 20-60N/cm$^2$ rating with high positioning accuracy, if the positioning range is less than 5mm. Due to the saturation of magnetic material that increases magnetic reluctance, extension of the positioning range is limited to 20-25mm, accompanied by a dramatic drop in the power/weigh ratio. Linear d.c./step motors can provide much wider positioning range, but they have the disadvantages of: (i) limited positioning resolution for linear step motors; (ii) higher costs in the electronic/mechanical commutators for linear d.c. motors. Therefore it is interesting to study other possible forms of linear induction devices which may be developed for certain positioning applications in the small/medium positioning ranges

Usual linear induction motors (LIM) are used in long distance delivery or transport, due to their poor positioning accuracy in small and medium range [9~11]. However they possess the advantages such as simple and robust mechanical structure, low cost and little maintenance. Our previous research has revealed that there is high potential that LIMs can be improved by innovative designs for small/medium range applications with high positioning accuracy [7,12]. This provides the basis for this research.

## 1.2 Tubular Linear Induction Actuators

Structurally, the layout of a LIM can be a flat or a tubular form, which can be configured with single-sided or double-sided windings. Their common configurations are shown in Fig. 1.1 and Fig. 1.2.

The obvious advantage for a flat structure is its open secondary structure that enables long distance travelling. On the other hand, the tubular structure has the advantage of compactness that eliminates the end-winding connection and hence the relevant losses which are inevitable in a flat structure. However, owing to the mechanical reason that the secondary core must be exactly in the centre of the primary core, or vice versa, tubular structures are only suitable for applications involving with small and middle range of positioning control systems. This will not pose problems in our research that only involves positioning applications with small/medium stroke. Therefore, the tubular linear induction principle has been chosen as the fundamental form in the development of our positioning actuator.

The operational principle of a TLIA is similar to a rotary induction motor [10,11]. There are several ways to explain the principle, of which the electromagnetic induction theory is used here for its clarity. First of all, there is a primary winding which generates a main electromagnetic field travelling along the direction of mechanical movement. This travelling electromagnetic field induces an electric potential and eddy current in the secondary. The induced eddy current interacts with the main magnetic field and generates an electromagnetic force between the primary and the secondary. The principle is also illustrated in Fig. 1.3

The traditional method to generate a travelling electromagnetic field is by using multiple-phase windings located at different mechanical positions. The multi-phase windings should be energised with a.c. current with different phase angle for each winding. Other configurations, such as a shaded-pole structure and split-phase structure, etc., have an electric mechanism to produce the equivalent effects of multiple-phase windings. Those induction machines have a common characteristic similar to that shown in Fig. 1.4(a).

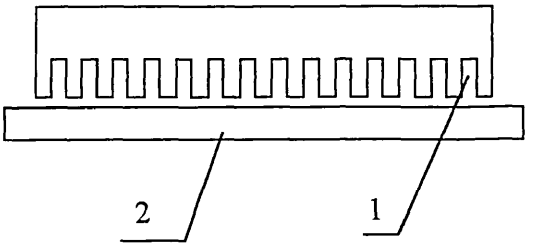


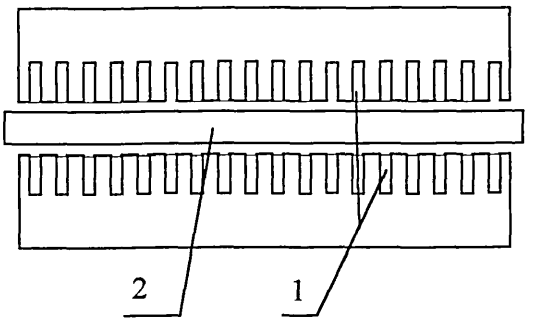


1 — primary, 2 — secondary

Fig. 1.1(a) Flat single-sided LIM

Fig. 1.1(b) Flat double-sided LIM

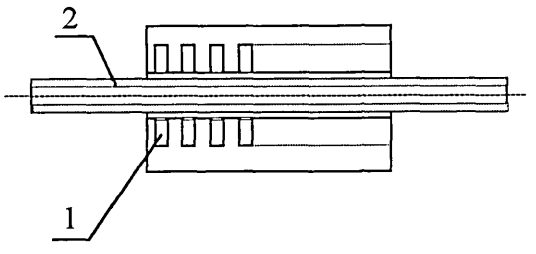


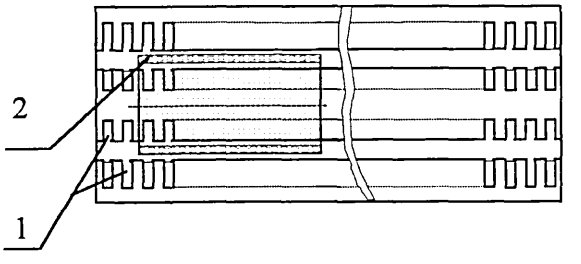


1 — primary, 2 — secondary

Fig. 1.2 (a) Tubular single-sided LIM

Fig. 1.2(b) Tubular double-sided LIM

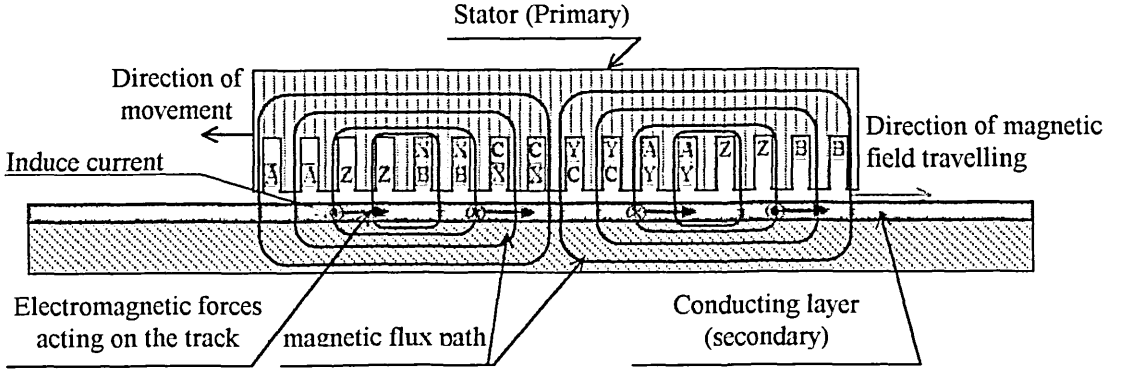


Fig. 1.3 A double-layer three phase winding of a single-sided LIM with short-stator

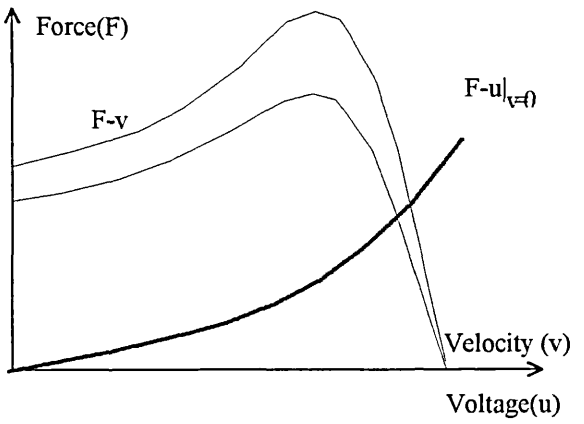


Fig. 1.4(a) General characteristics of LIM

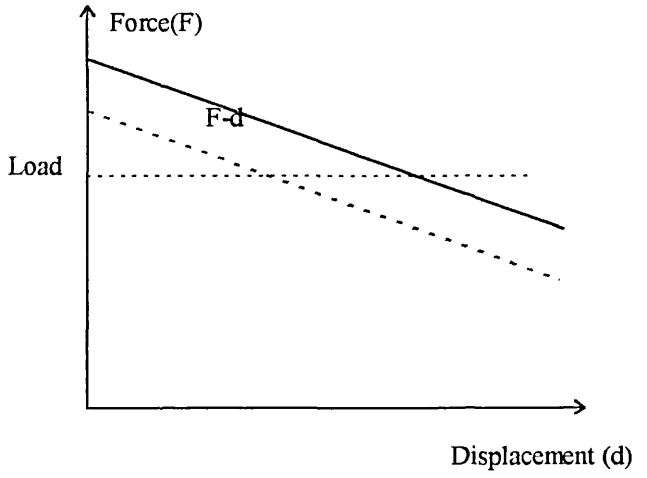


Fig. 1.4(b) Desired characteristics for positioning application

The characteristic of Fig. 1.4(a) is suitable for traction purpose. For a positioning purpose, a monotonously decreasing characteristic like Fig 1.4(b) is desirable. It means that, instead of the traditional configuration of a LIM, new structures for those TLIAs used for short stroke positioning applications should be sought after.

## 1.3 Development of a Single Phase TLIA for Positioning System

LIMs/TLIAs usually have a similar winding configuration and power supply as their rotary counterparts. The common way to make use of a single-phase power supply is to build an auxiliary winding along with the primary winding to assist the generation of a travelling electromagnetic field. Is it possible to remove the auxiliary windings as to simplify the structure? We have observed some phenomena that weights can be lifted by a single a.c. coil even without any auxiliary winding/coil, such as the 'jumping ring' and 'a.c. magnetic levitation' shown in Fig. 1.5.

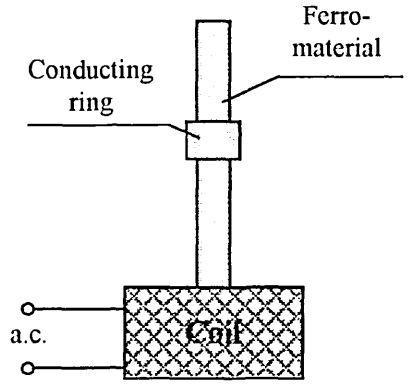


Fig. 1.5(a) jumping ring

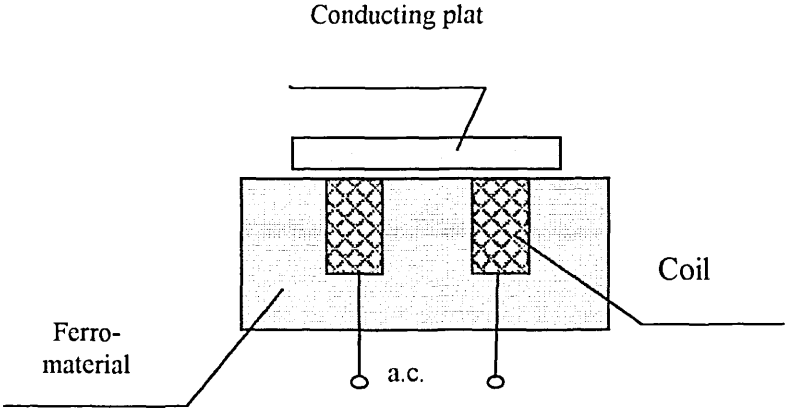


Fig. 1.5(b) a.c. magnetic levitation

Although the ring or the plate, made of conducting material, can be considered as an equivalent auxiliary winding which helps generation of travelling field, it is better to put this into another category in which the asymmetric magnetic structure is the main motivation behind the phenomena. This is a bit similar to reluctance motors, but not the same. Apparently, if the structure is symmetric, such as those shown in Fig. 1.6, we could not expect a net average force to be generated on the secondary - the conducting ring. Electromagnetic forces are actually generated on the secondary, but they are cancelled by the symmetry of the structure.

So we come to the idea to develop a novel single phase TLIA by making use of the asymmetry in structures. Previous research has been carried out on two actuators: XI core TLIA and the TLIA-0 that are shown in Fig. 1.7 and 1.8 respectively. The research has revealed that these two actuators are only suitable for fast traction applications. We need to modify the design to accommodate the requirement for multi-steps positioning.

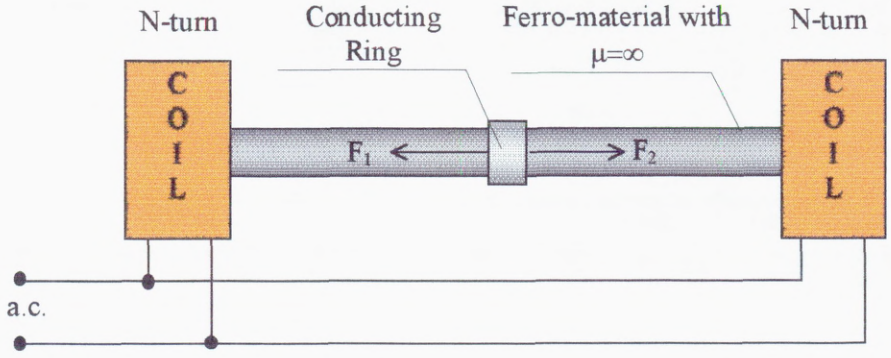


($F=F_1-F_2=0$, if two coils are identical and $\mu=\infty$)

Figure 1.6 An symmetric electromagnetic structure generates zero net forces

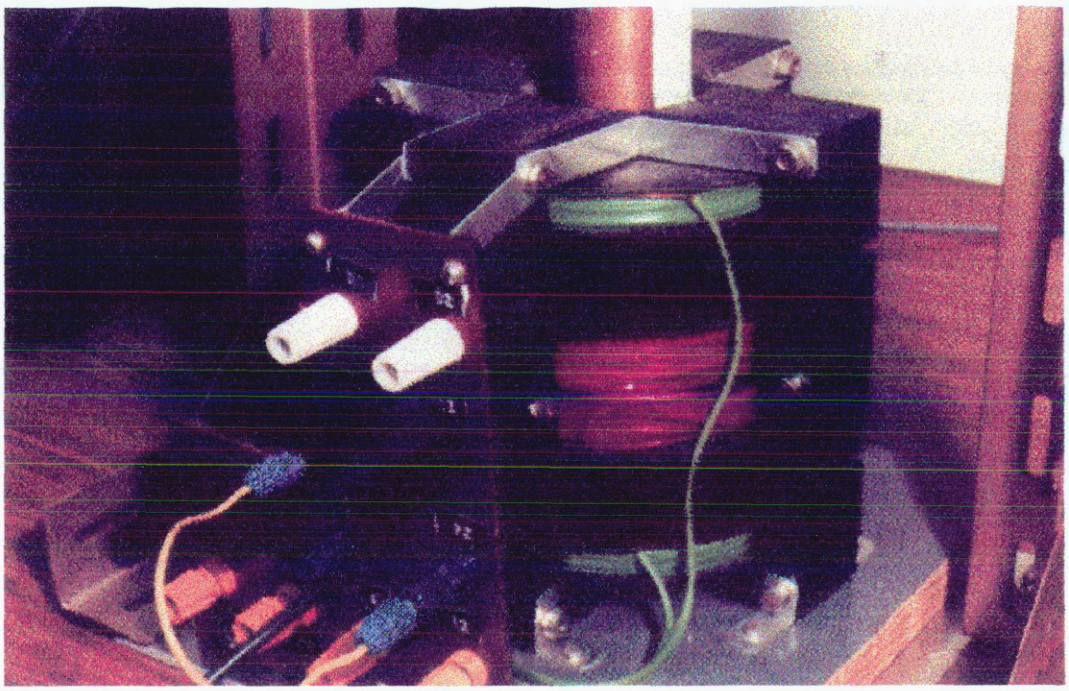

Fig. 1.7 The XI-core TLIA

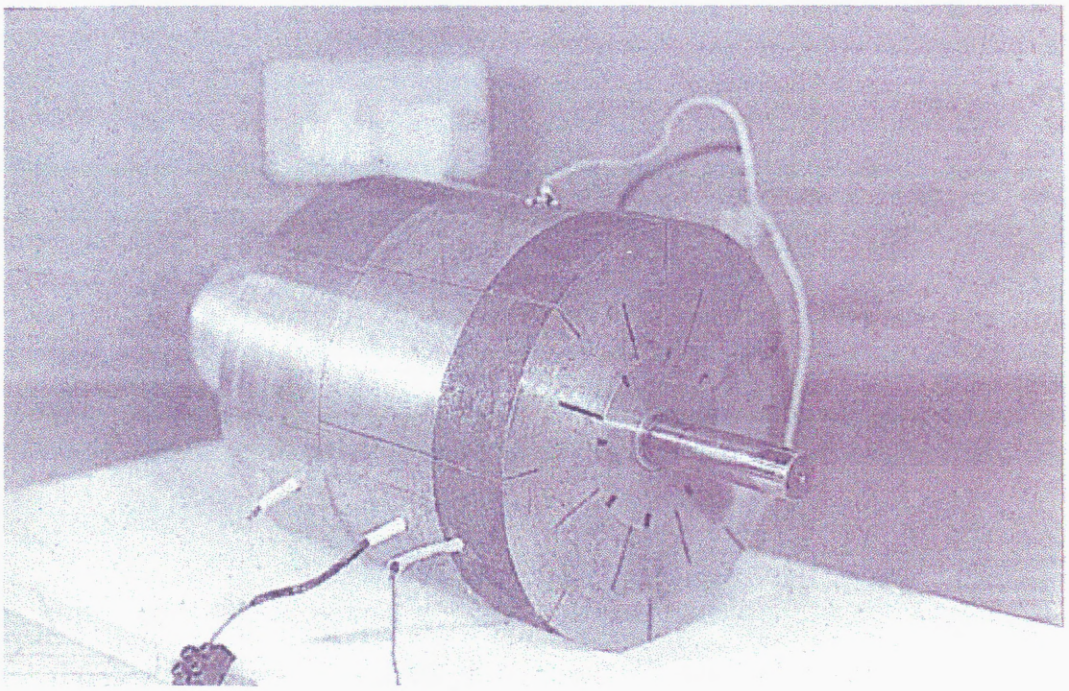

Fig. 1.8 The TLIA-0

## 1.4 About the Project

This research project is financially funded by AT&T GIS Scotland. It requires to develop a single-phase TLIA and its associated multi-step positioning control system. At the actuator side, its emphasis is to achieve a small size TLIA with a proper control characteristic. That means different structure configurations should be investigated to assess their performance, capability and characteristics for positioning applications. Computer aided analysis by FEM is used for the design of actuators. On the other hand, control methods and electronic devices, including power supply units and digital control hardware, should be studied and developed along with the development of actuators. Intensive theoretical studies on the actuator, electronic drive and control method should be carried out in order to fulfil the target of the project. To verify the theory and the technology adopted, a practical system should be built up. Therefore this is an exercise in research and development of system engineering.

## 1.5 Major Aspects of the Research

This research covers extensive investigation of the TLIA positioning system from theoretical and experimental studies to practical engineering realisation. Details can be summarised as follows:

(1) Computer aided design of new TLIAs. The CAD would be based on the electromagnetic field computation in time harmonic form by FEM. The criterion of the design was concentrated on the geometric structure configuration to obtain good characteristics for positioning application, which involved many related topics such as the dynamics, size, stroke, thrust, linearity of control characteristics, etc. Also, since the CAD tool can only process a given structure among the possible configurations of potential TLIAs, the operating theory of TLIAs should be intensively studied to achieve improvement of the design, and to avoid fruitless trails.

(2) Experimental investigation of different TLIAs. Experiments should be designed to investigate the characteristics of the TLIA developed. Characteristics obtained from the experiment would be used for the design of PSUs and the design of control

algorithms. They would also serve as an effective verification to the proposed methods. Experiments will also reveal problems that have not been considered, but should be fully considered in the design.

(3) Development of CAD tools. There were four tasks here:

- Development of the time-harmonic FE package for the computation of electromagnetic field.
- Development of software to simulate transient electromagnetic field by FEM, which should take account of more real operation conditions such as voltage-driven, switch-mode power supply.
- Investigation of the accuracy problem in force calculation, particularly in the Maxwell's stress tensor (MST) based method implemented by FEM.
- Development of software to simulate transient temperature field by FEM. This will complete the analysis tools for design, given the importance of temperature rise in all electric machines.

(4) Design and fabrication of a triac PSU with digital control interface. This was the first PSU to be build for its simplicity and low-cost. For a TLIA with back-to-back configuration, a single-input control method will be used to reduce the requirement to the control hardware and software.

(5) Design and fabrication of a PWM-controlled PSU with digital control interface. Since the triac PSU has some inherent limitation for accurate positioning, a more sophisticated power supply device based on PWM switch-mode technology was needed. For the research purpose, it was designed to be a variable voltage inverter with an adjustable output frequency. Many engineering problems, such as switching power loss, electromagnetic interference, protection, etc., were to be tackled. In addition to single-input control model, this PSU should be able to work in two-input control mode to allow more flexibility of control configurations. Since a DSP was to be used to implement control algorithm, both the triac PSU and the PWM PSU should be designed with control interface compatible with the A/D and D/A converters on the DSP board.

(6) Development of a digital control algorithm and the associated program coding. Based on the experimental results of the control characteristics, a digital controller was to be designed to implement a closed loop control of positioning. These

involved study of digital control theory, microprocessor hardware and A/D & D/A configuration. Assembly language was required to implement the real-time digital control algorithm on a DSP.

(7) Realisation of a closed loop positioning control by using DSP control technology for the system comprising of the TLIAs and PSU developed in this project. Finally the whole positioning system should be integrated on an experiment rig to conduct real positioning application. Demonstration should be given to the company to prove the successful fulfilment of the project.

## 1.6 Outline of the Thesis

For such a complete engineering project there was obviously much engineering work involved in addition to theoretical studies. However, this thesis is planned to explain mainly the theoretical and experimental studies involved in the whole project. They are divided into nine chapters that are arranged as:

Chapter 1 is an introduction about tubular linear actuators and the background of the research project. After a brief review about linear actuators, focus is put on the single phase TLIAs and their prospects in positioning applications. By the end, the theoretical and technical achievements are outlined.

In Chapter 2, the main objective is to design a novel TLIA that is suitable for positioning application. The analysing method used to aid the design is based on the computation of time-harmonic electromagnetic field by FEM. Firstly several conceptual designs have been studied by the FEM analysis. They were then manufactured and experimented. Comparisons among these prototype actuators were made. A back-to-back TLIA with descending control characteristics was selected for the realisation of closed loop positioning control.

In order to investigate the electromagnetic field happening in actuators driven by switch-mode power supply, a simulation software based on FEM method has been developed in Chapter 3, which indirectly couples external circuit equations with the Maxwell's electromagnetic field equation. Due to the very small time-steps that are required in

simulating the transient electromagnetic field driven by switch-mode power supply, a new eddy current model based on the decomposed magnetic vector potential (DMVP) method has been proposed to accelerate the computation. Comparisons with other methods have been carried out. It has shown that a considerable CPU time can be saved under certain conditions.

The calculation of thrust force through FEM computation looks simple, but it still suffers from the fact that the force accuracy is dependent on the integral path, the mesh size and distribution, the shape function, etc. Although the MST method is universal, its error is more susceptible to mesh discretization and integral path. In Chapter 4 starting with the investigation of various sources of errors through a fundamental theoretical study, a new method is proposed to improve the accuracy of force calculation and also to eliminate the path-dependency. Then several numerical experiments were carried out to show the effectiveness of the proposed method.

Chapter 5 discusses the computation of transient temperature field. We know that temperature rise plays a very important role in the safe operation of electrical devices. For our current design, there is not forced ventilation measures to cool the actuator. Because the existence of eddy current induced in the plunger of the actuator is necessary to produce a thrust force, the temperature rise mainly caused by the eddy current loss will becomes a critical issue which determines the actuator's thermal capability. The FEM simulation software developed for electromagnetic field computation has been expanded to incorporate the function of the computation of transient temperature field. The experiment on an actual actuator was carried as well to verify the computed results. The critical time for continuous safe operation can then be determined with the aid of the computation of the distributed temperature field.

From Chapter 6, we move on to the design and development of PSUs and realisation of positioning control. In Chapter 6, a triac controlled PSU was designed to match the specifications derived from the TLIAs' tests. Both design and analysis have been presented. The actual circuit has been fabricated and tested to drive TLIAs successfully.

To obtain higher performance and more flexible control of TLIAs, a PWM single-phase inverter has been developed in Chapter 7. Similar to the previous chapter, both design and analysis have been presented. Some issues particular to high-frequency/high-voltage switching, such as switching losses and electromagnetic interference, are discussed as well. The inverter has also been physically fabricated and tested. This proves the successes of the design.

Chapter 8 is on the digital control of positioning by using DSP. At first, the theory of digital controller design is studied with the model of a general second order linear plant. Non-linear correction and dry friction compensation are discussed thereafter. Then some technical key factors on hardware and software implementation on a DSP are stressed to get the control algorithm work on the actual hardware, simply because we will start from a general-purposed DSP board instead of specialised one. Finally we demonstrate the positioning application with our TLIA, PSU and DSP controller. We will come to see that good results have been achieved as system engineering.

Finally we come to the conclusions to the whole project in chapter 9. Achievement has been summarised there briefly in addition to the conclusion at the end of each previous chapter. For the purpose to help further research, it holds a special section to discuss topics on how to improve the TLIA positioning system. It also looks forward to the future development of the proposed methods.

# 2 COMPUTER AIDED DESIGN OF SINGLE-PHASE TLIA

## 2.1 Introduction

Traditionally electromagnetic devices have been designed by combining empirical rules based on experimental evidences with simplified mathematical models [13]. Most of these models consist of magnetic equivalent circuits postulated on the basis of experience and intuition. From the design engineer's viewpoint, they are relatively easy to apply. However, they are usually restricted to a narrow class of devices because the various correction factors are empirically introduced. With the increase of specifications and the structural complexity, the traditional design rules are no longer adequate and suffer the inability to accommodate new situations that are frequently encountered in the development of new products. Only numerical analysis is capable of dealing with both the geometric complexity and various material properties. Therefore, design by analysis, instead of by rules, means at the very least computer aided analysis and increasingly has come to mean full-fledged computer aided design [14,15].

CAD has grown to occupy an important role since 1960s. Design by analysis, based on reasonably detailed solution of the underlying electromagnetic field problems, becomes a normal practice nowadays [16]. Most CAD software packages, commonly known as turnkey systems, are created by integrating major components that could include geometric modelling, design analysis, engineering drafting and data management, etc., where numerical analysis usually plays the kernel role of the whole CAD package. Instead of buying an expensive turnkey CAD system, a FE software from previous research has been adopted as the frame work for further improvement involved in the development of the CAD analysis tool for the design of TLIAs. Although the original

software has a limited capability in both analysis and data management, it still has enough potential to be improved to meet the requirements of the project. In addition to developing new methods to enrich the software, which will be discussed in the next two chapters, efforts have been made on such work as reorganising storage management of the solver, enlarging nodes/meshes' limits, accelerating solution, auto-mesh generating, error checking, etc.

In optimising old designs or developing new products by CAD tools, one of the principal responsibilities for design engineers is to synthesise the product based on certain concepts the designers have regarding their nature. The synthesis usually involves selection from a number of options, some of which may perform better than the others or may be easier to manufacture and maintain. A designer thus tries to optimise the design even before it is created. In the CAD of electromagnetic devices, there are three major categories of design methodologies:

- Traditional designer-guided optimal (DGO) method with the aid of numerical analysis of electromagnetic field [17]. Modifying material property and geometry is made by the designers' interventions according to the previous results from numerical analysis and their knowledge.
- Optimised Geometry (OG) Method [18]. It aims at obtaining an optimised geometric shape and dimensions of specific features by starting from a pre-determined structure and materials base under certain constraints. Its effectiveness depends on the optimising algorithm.
- Optimised Material Distribution (OMD) Method [19]. It attempts to synthesise a device by starting from a specified region with very simple material combinations or even an empty space.

The current state is that the DGO method has been accepted for wide range of application, the OG method has found some applications in certain areas, and the OMD method is just at the initial stage of research.

The design and optimising of TLIAs' development are more or less qualitative in nature, due to lack of experience in both manufacturing and operation. Its geometric shape and

performance specification are wide open to be determined, which should be much dependent on applications. As with all qualitative analysis, it is extremely difficult in most cases to obtain mathematical equations - the objective function in optimisation theory through which the quantitative optimisation could be arrived at. So, in this chapter no attempt is made to develop optimisation techniques for design synthesis. The DGO method is employed with the numerical computation of time-harmonic eddy current field to exercise the CAD.

## 2.2 Development of Design Analysis Tools

The analysis tools for design purposes are mainly FEM packages that carriy out the computation of the electromagnetic field. The quasi-static/time-harmonic eddy current model will be applied at the conceptual design stage [20~26]. Once a preferable design has been arrived at, more accurate transient simulation could be carried out by the method developed in chapter 3. The design tools, including the FEM solver, pre-processor and post-processor, are based on the original ones that were developed in the previous research. The major work that has been done relevant to this project was on accelerating the solution, improving the pre-processor to ease the use of FEM, and improving the force calculation accuracy in the post-processor.

### 2.2.1 FEM for Time-harmonic Eddy Current Field Problems

If the excitation current density is denoted as $J_s$ and the displacement current is neglected, the Maxwell's equation in time-harmonic form can be expressed as:

$$\nabla \times \nu \nabla \times \mathbf{A} + j\omega\sigma\mathbf{A} = \mathbf{J}_s \tag{2.1}$$

with the following definition and constitution relationship

$$\mathbf{B} = \nabla \times \mathbf{A}$$

$$\mathbf{H} = \nu\mathbf{B}$$

$$\mathbf{E} = -\frac{\partial \mathbf{A}}{\partial t}$$

Equation (2.1) has the following corresponding variational functional

$$\Im = \frac{1}{2}\int_R [\nu\nabla \times \mathbf{A} \cdot \nabla \times \mathbf{A} + j\omega\sigma\mathbf{A} \cdot \mathbf{A} - \mathbf{A} \cdot \mathbf{J}_s]dv - \oint_\Gamma \mathbf{A} \times \nu\nabla \times \mathbf{A} \cdot d\mathbf{s} \tag{2.2}$$

As we know, the problem to solve (2.1) can be converted to an equivalent problem to minimise (2.2) with certain gauge that ensures the uniqueness of the solution, i.e.,

$$\min_{A \in R} \Im(\mathbf{A})\Big|_{\nabla \cdot \mathbf{A}=0} \Rightarrow \frac{\partial \Im(\mathbf{A})}{\partial \mathbf{A}}\Big|_{\nabla \cdot \mathbf{A}=0} = 0 \tag{2.3}$$

When a FEM is used, the whole solution region $R$ is divided into $m$ sub-regions $R_e$ within which an interpolation function is applied:

$$\mathbf{A}^e = \sum_{k=1}^{n} N_k^e \mathbf{A}_k^e \quad \{R_e \in R, e=1,2,...m\} \tag{2.4}$$

where '$_n$' is the number of nodes which consist of element '$e$'. Solution of the discrete potential **A** is obtained by solving the following linear simultaneous algebraic equation obtained by putting (2.4) and (2.2) into (2.3):

$$[\mathbf{K}][\mathbf{A}]=[\mathbf{b}] \tag{2.5}$$

Equation (2.5) is usually a large-sparse linear matrix equation. There are many algorithms available to solve such type of equations. The original program developed many years ago uses the Gauss Elimination (GE) method, which works very slowly for FE application. To achieve fast solution, we have adopted the complex form of the Incomplete Choleski Conjugate Gradient (ICCG) method by taking the advantages of symmetry and sparseness of the [**K**] [27]. Unlike the traditional ICCG method that uses the same size of fixed storage for the factorized matrix as that for [K], the ICCG method we employed has adopted following techniques:

- Scalar-controlled incomplete factorisation that allows balancing the size of the factorized matrix and iteration numbers, which directly affect the total storage and CPU. Details will be discussed in section 3.2.5

- Only none-zero elemental contributions recorded, including those in both the stiffness matrix and the incomplete factorized matrix.
- Dynamic storage management which adjusts the memory arrangement according to the size of the factorized matrix. Therefore it makes use of computer's memory more efficiently and brings more flexibility in accommodating discretisation with various nodes/meshes.

Our experience has shown that the ICCG method with the above techniques arrives at a speed of 1~2 order faster than the GE method for a moderate node number. With the increase of node number, the ICCG method works more efficiently.

### 2.2.2 Pre-processor and Post-processor

The tedious task in using FEM is the data preparation. So a pre-processor is introduced to prepare all necessary physical data to be assembled. Improvements to the pre-/post-processor have been carried out without changing the three-piece structure of the original design tool. In addition to improving graphical interface, removing bugs and expanding nodes/meshes' limits, efforts have also been put on auto-mesh generation and data management in the pre-processor. The auto-mesh generation comes in two forms: one is to generate a mesh from an input file describing quadrilateral regions; the other is to refine mesh from a coarse mesh. The pre-processor generates two data files for the solver. One contains geometric and material information in binary format. The other contains controlling information in ASCII format. Separating the controlling data from geometric and material data enables user to change all controls (such as material properties, excitation conditions, frequencies, tolerance, etc.) in a simple and much smaller file instead of returning to elemental level. So, with one geometric data, many combinations of different material properties, excitation conditions and/or operating conditions can be studied with quick preparation of control data file.

Post-processing is used to convert the mathematical solution into engineering results. A post-processor is a major part of any design system since it allows relevant data to be extracted from the solution and presented in a way that has meaning to users. The major

improvement to the original postprocessor was on the force calculation. Two methods have been used to calculate the electromagnetic force. One is the Lorentz method that is only suitable to compute electromagnetic force on non-ferromagnetic materials. Another is the Maxwell's stress method, which is universal and can be described as

$$\mathbf{F} = \int_s [\mu H_n H_t \cdot \mathbf{t} + 0.5\mu(H_n^2 - H_t^2) \cdot \mathbf{n}] ds \tag{2.6}$$

If the integral region does not contain any ferromagnetic materials, Lorentz formula is easy to implement and provides higher accuracy than the Maxwell's one. Otherwise, (2.6) should be used no matter whether any massive current exists inside the ferromagnetic materials or not. Although (2.6) can be used as a general method to calculate electromagnetic force, its accuracy is sensitive to the accuracy of **B** and **H** whose errors are unavoidable in FE computation. The improved force calculation method, based on the Maxwell's stress tensor method which will be discussed in Chapter 4 in detail, has been developed and incorporated into the post-processor.

Because of the axially symmetric structure of the tubular actuator, an axi-symmetric form of FEM will suffice for the design analysis. In this case, a 2D pre-processing and post-processing will be actually involved.

For the FE thermal analysis, it has many similarities to the FE electromagnetic analysis, particularly in program structure, assembly and solution of matrix equation. Therefore, they are integrated with electromagnetic analysis in one package in which the preprocessor, the solver and the postprocessor are shared, and the same data files are used. The only difference is laid on that different subroutines for computing elemental stiffness will be called by the assembly subroutine. Because of the sharing of most source code and data structure between the FE thermal analysis and the FE electromagnetic analysis, the coding task is significantly reduced.

## 2.3 Study of the TLIA-1

The development of the actuator has started from the investigation of the first actuator, TLIA-1, which was designed in previous research work for traction application. The actual actuator and its topology are shown in Fig. 2.1 and Fig. 2.2 respectively. It consists of five fundamental parts with specific technical requirements, which can be summarised as:

- The stator/yoke, which should be made of ferromagnetic material with high magnetic permeability and low electric conductivity, such as laminated silicon steel or ferrite.
- The mandrel, which has the same requirement and could be built with the same material as the stator.
- The plunger, which should be made of materials with high electric conductivity such as copper or aluminium.
- The bearing, which should have small friction force and should be placed at proper position with least influence from the main electromagnetic field if it is made of steel.
- The coil and its supporting frame, which has the similar requirement to ordinary coils used in a.c. motors/transformers.

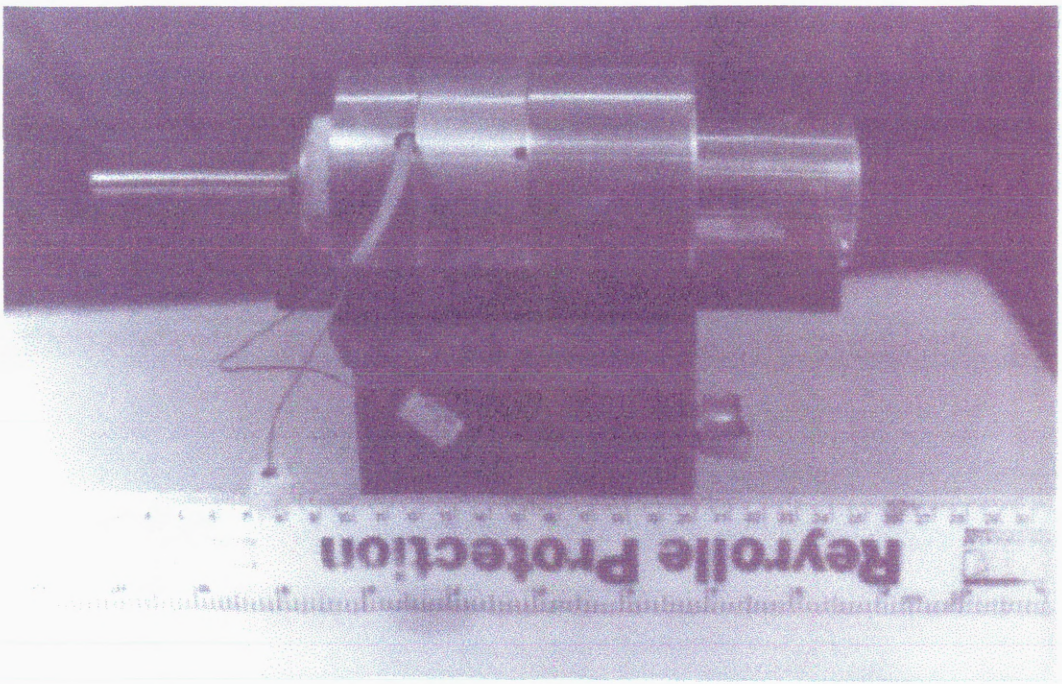


Fig. 2.1 Photograph of the actual TLIA-1

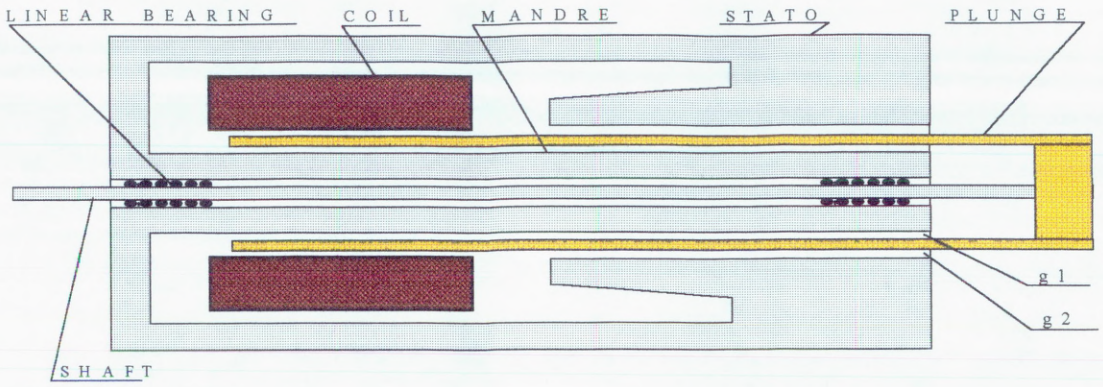


Fig. 2.2 Illustration of the structural configuration of TLIA-1

Along with those parts mentioned above, two air gaps (g1, g2) and a shaft are necessary to let the plunger move freely, thus deliver force and displacement to the workpiece.

The first look at the structure of the TLIA-1 will give an impression that it looks a bit similar to a solenoid electromagnet. Actually its operating principle, as explained in the following section, is different from either solenoid electromagnets or conventional LIMs.

### 2.3.1 Operational Principle

As we know, solenoid electromagnets generate a magnetic attractive or repulsive force between magnetic poles and moving piece. And conventional LIMs generate a hauling force between the main moving magnetic field and the secondary magnetic field that is induced by the main magnetic field. They both can be easily explained as the interactive force between magnetic poles. However, it is difficult to give an intuitive meaning if the TLIA-1 is explained in the same way. Here the mechanism of the force generated in the TLIA-1 is elucidated by the Lorentz law.

According to the Lorentz law, electromagnetic force density can be calculated by

$$\mathbf{f} = \mathbf{J} \times \mathbf{B} + q_e \cdot \mathbf{E} \tag{2.7}$$

where the electric charge $q_e$ is zero for TLIAs. As shown in Fig. 2.3, the magnetic field can be classified into three types, $\mathbf{B}_m$, $\mathbf{B}_{l1}$ and $\mathbf{B}_{l2}$. They are called as main magnetic field, primary leaked magnetic field and secondary leaked magnetic field respectively. Defined in the similar way as in the analysis of electric machines, here $\mathbf{B}_m$ is the magnetic field coupling both the winding and the plunger; $\mathbf{B}_{l1}$ is the magnetic field generated by and coupled with the winding only; and $\mathbf{B}_{l2}$ is the magnetic field generated by and coupled with the plunger only. It is the $\mathbf{B}_m$ that induces, in the plunger, an eddy current $\mathbf{I}_e$ that also makes its reactive contribution to $\mathbf{B}_m$ as the excitation current $\mathbf{I}$ does. In idealised conditions where conductivities of the yoke and the mandrel are neglected and the plunger's conductivity is very high, the phase angle of $\mathbf{I}_e$ will be nearly $180^0$ lag of the $\mathbf{I}$ according to the Faraday law. Applying the Lorentz law or the right-hand rule, we will find that two opposite forces ($\mathbf{F}_-$, $\mathbf{F}_+$) might exist on the plunger and their directions do not change with the direction of the excitation current, as shown in Fig. 2.3. The reason why $\mathbf{F}_-$ exists is that not all of $\mathbf{B}$ will follow the desired path of yoke-plunger-mandrel-yoke (YPMY) encompassing the coil. From electromagnetic point of view, this is obviously an asymmetric structure in axial direction. It is the asymmetry that ensures $\mathbf{F}_+$ will not be fully counteracted by $\mathbf{F}_-$, and therefore generates the net $\mathbf{F}$ on the plunger. We can predict that $\mathbf{F}_-$ will be smaller than $\mathbf{F}_+$ even at the worst condition because the asymmetric structure can still guide the majority magnetic flux to follow the desirable path YPMY. Beyond a certain point, the $\mathbf{F}_-$ will disappear. Therefore we can predict that the force-displacement characteristics will initially increase to some extent and then decrease, as shown in Fig. 2.4.

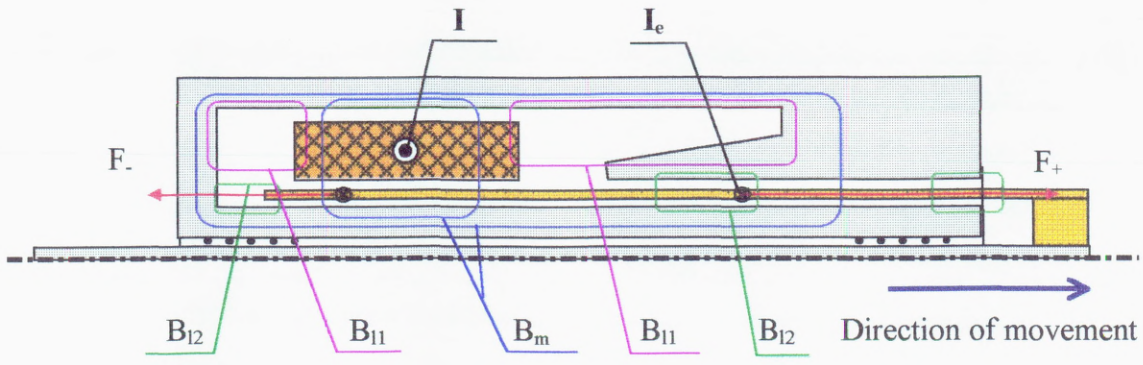


Fig. 2.3 Illustration of the operational principle of the TLIA-1

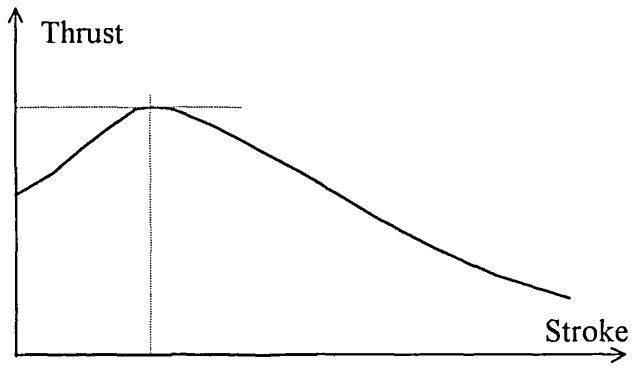


Fig. 2.4 predicted thrust-stroke characteristics of the TLIA-1

### 2.3.2 Measurement of the Characteristics

Further investigations on the TLIA-1 have related to experimental tests. Two experiments, the blocked state and the spring-loaded state, have been carried out to investigate its static characteristics. Measurements were made with the following instrumentation:

- A 2kg load cell, used to measure the standstill force
- Digital voltmeters and ammeters, used to measure the voltage and current
- A ruler, used to measure displacement manually

As illustrated in Fig. 2.5, the whole system was placed on an experimental rig that was adjustable to enable the plunger placed on a horizontal level so as to eliminate the force coming from the plunger's mass. There are two sliders on the rig, which were mounted with the actuator and the load cell respectively. For the blocked state measurement, the load cell was placed on the way of the plunger's movement. In this way, the load cell receives pushing force and serves as a stopper in the mean time. Changing of displacements was made by adjusting manually the distance between the two sliders through two screws. For the spring-loaded state measurement, the load cell was placed at the same side of the spring, off the way of the plunger's movement, with their connecting joint located on the same axis of the spring-plunger. The load cell receives pulling force in this configuration. Both of experimental configurations were designed

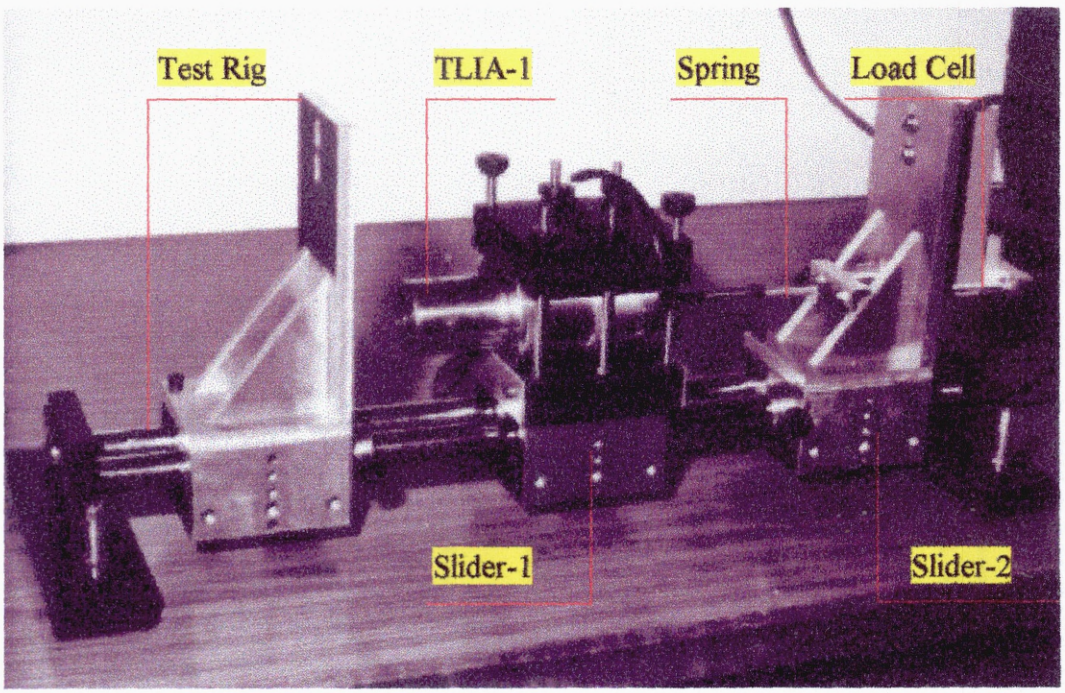


Fig. 2.5 The TLIA-1 on the test rig with spring load

to ensure that the electromagnetic force generated on the plunger is delivered to the load cell directly.

The control characteristics in blocked state are illustrated in Fig. 2.6 ~ Fig. 2.9. It has been found that:

- At a fixed displacement, the relationship between forces and excitation currents shows non-linearity
- In the whole range of the stroke, the voltage versus current curve is nearly linear at a fixed displacement, as shown in Fig. 2.7. It means that the actuator works in the linear part of the ferromagnetic material's property, which implies that the design can be optimised further. This also implies that the force is proportional to the square of voltage as a result.
- If the current is maintained constant, the variation of voltage with displacement increases monotonously, as shown in Fig. 2.8

- A hump exists in the force versus displacement curves shown in Fig. 2.9, which is coincident with our prediction. The increasing part of the curve means that the actuator will be unstable under open loop control with a constant load. So only the decreasing part of the curves is useful for open-loop positioning control.

The characteristics under spring loads are shown in Fig. 2.10 to Fig. 2.13. A special phenomenon found was that the plunger would not move until the voltage and current reached some critical value. At the critical point, the plunger leaps forward and stops at the equilibrium position and current decreases in the mean time. With the voltage increasing further, the current keeps decreasing a little further, and then reverses to increase with the voltage. This can also be seen in the Fig. 2.10. The voltage versus force curves are more close to a square relationship, starting forwards from the first balanced position after the initial leap, as shown in Fig. 2.11. However the force versus current curves, as shown in Fig. 2.12, appear a bit complex. After the initial forward leap, force increases with increasing voltage while current reduces in a reverse way to some extent and then turns back to increase, as shown in Fig. 13. This was the combined result of a non-linear force driving a linear (not constant) load.

Difficulties have been encountered in repeating experiments to reproduce characteristics exactly. It can be mainly ascribed to two reasons. One comes from the heating that changes material properties. The actuator's temperature rises fast to an insulation crisis in 30 minutes at 2 amperes of continuous excitation. The other arises from mechanical assembly and manufacturing imperfection. The mechanical problem could be reduced to its minimum, the heating from stator and mandrel can also be reduced by using lamination or high frequency ferromagnetic material. However the heating in the plunger can not be reduced because the actuator works on the excitation current and eddy current in it.

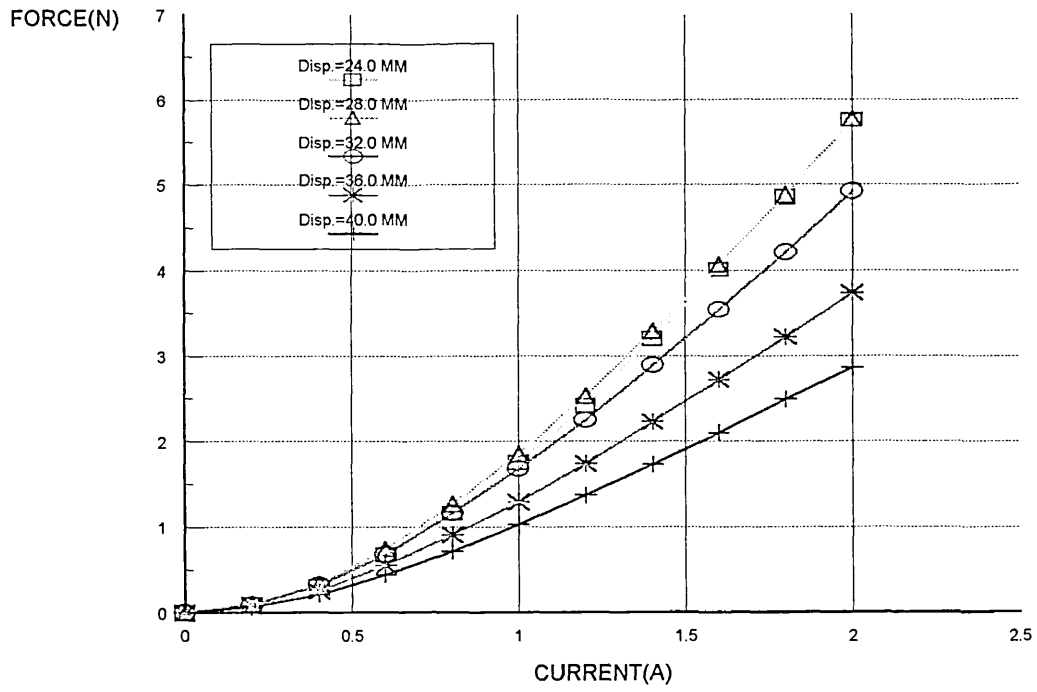


Fig. 2.6 Force versus current at different displacement under blocked-state

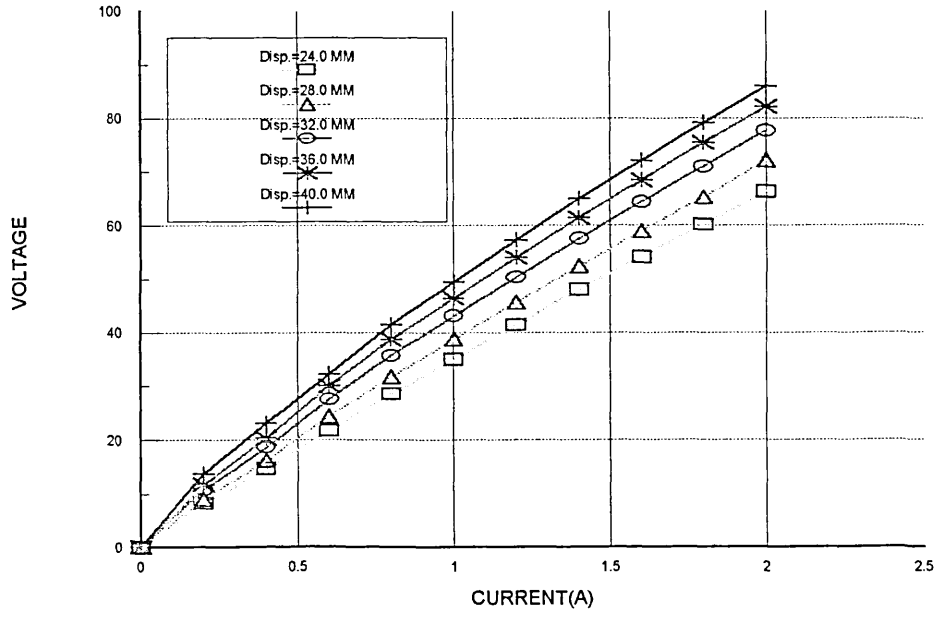


Fig. 2.7 Voltage versus current at different displacement under blocked-state

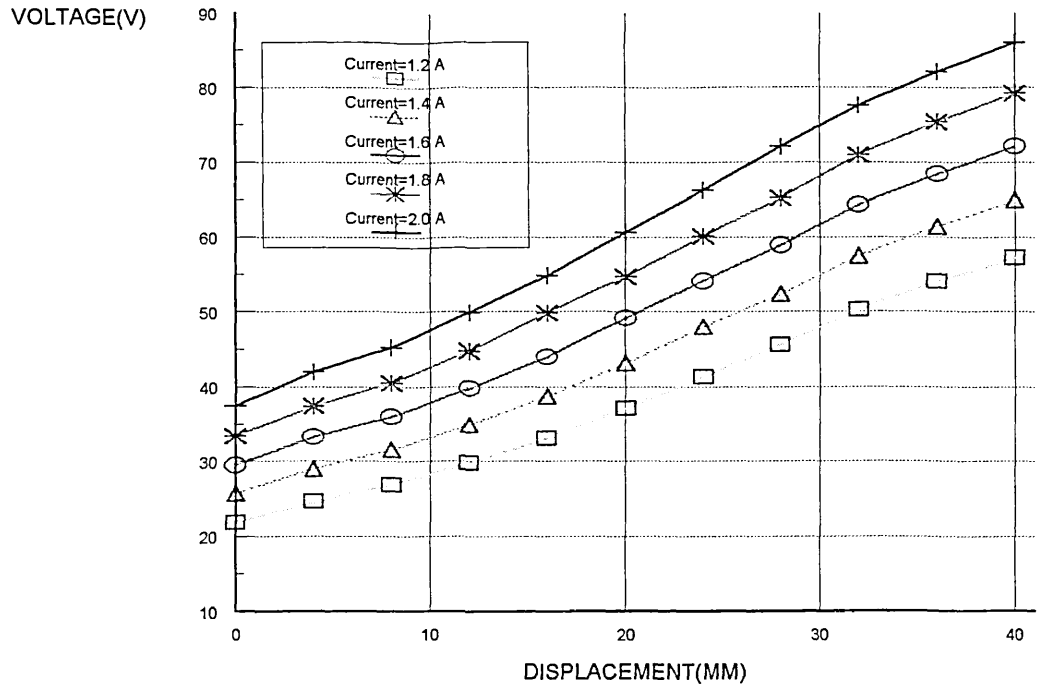


Fig. 2.8 Voltage versus current at different displacement under blocked-state

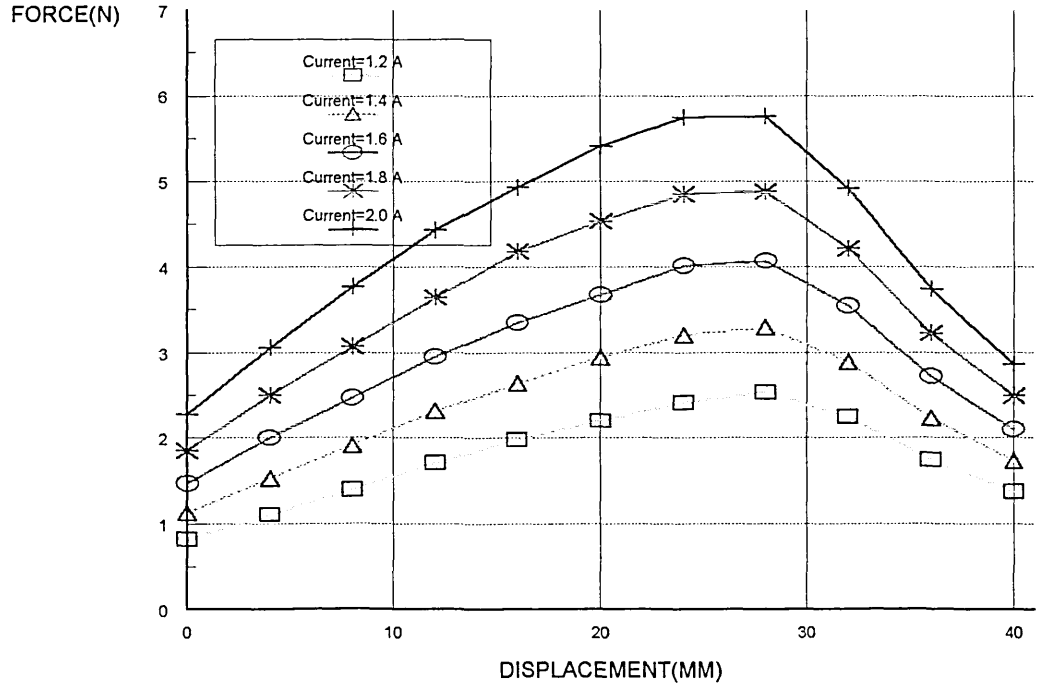


Fig. 2.9 Force versus displacement at different current under blocked-state

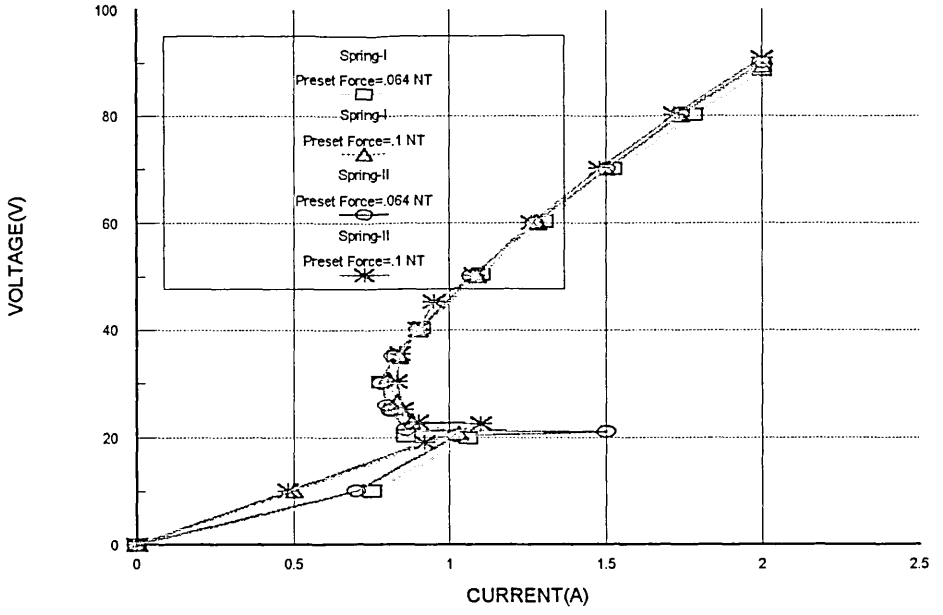


Fig. 2.10 Voltage versus current under two spring-loads

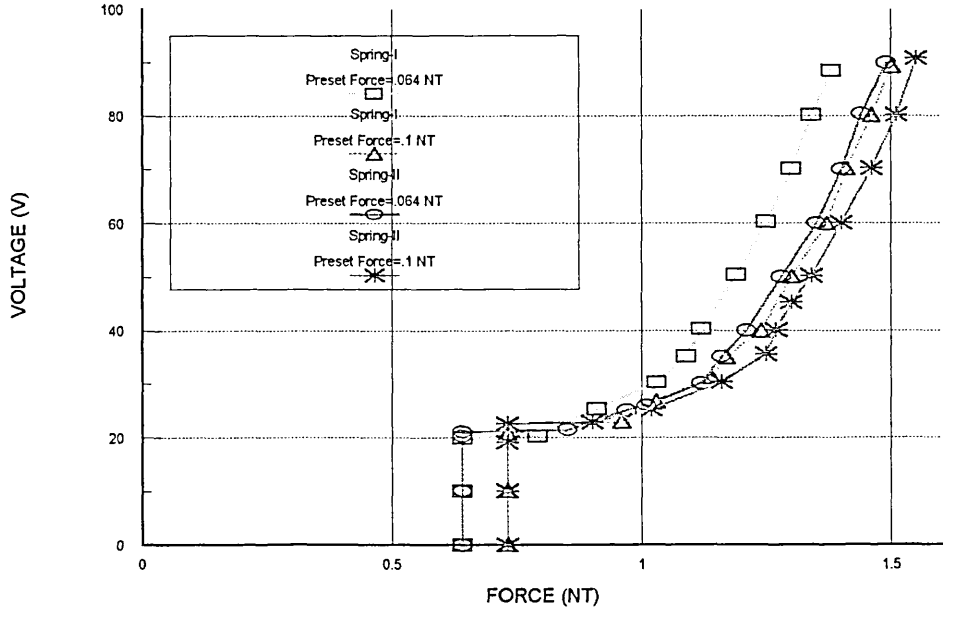


Fig. 2.11 Voltage versus Force under two spring-loads

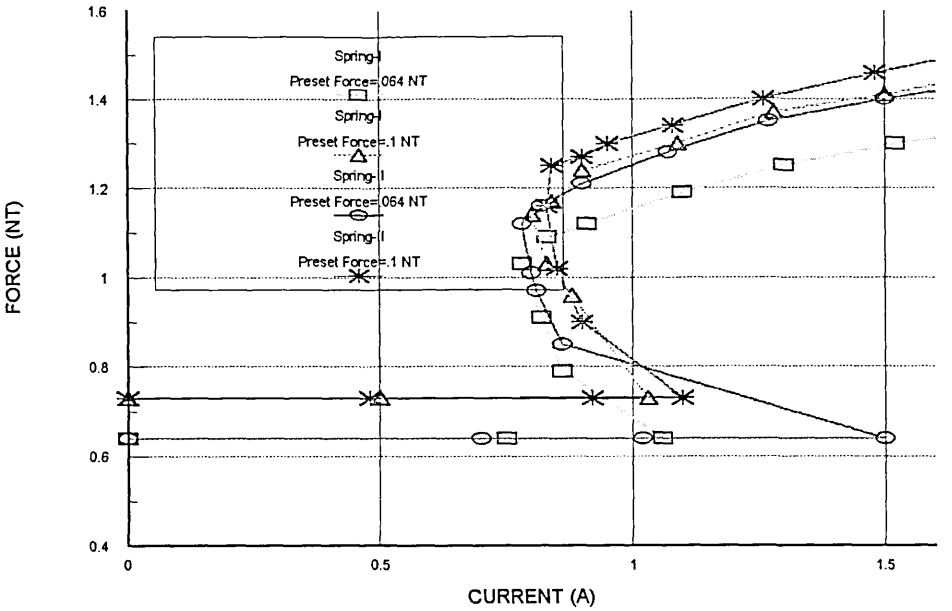


Fig. 2.12 Current versus Force under two spring-loads

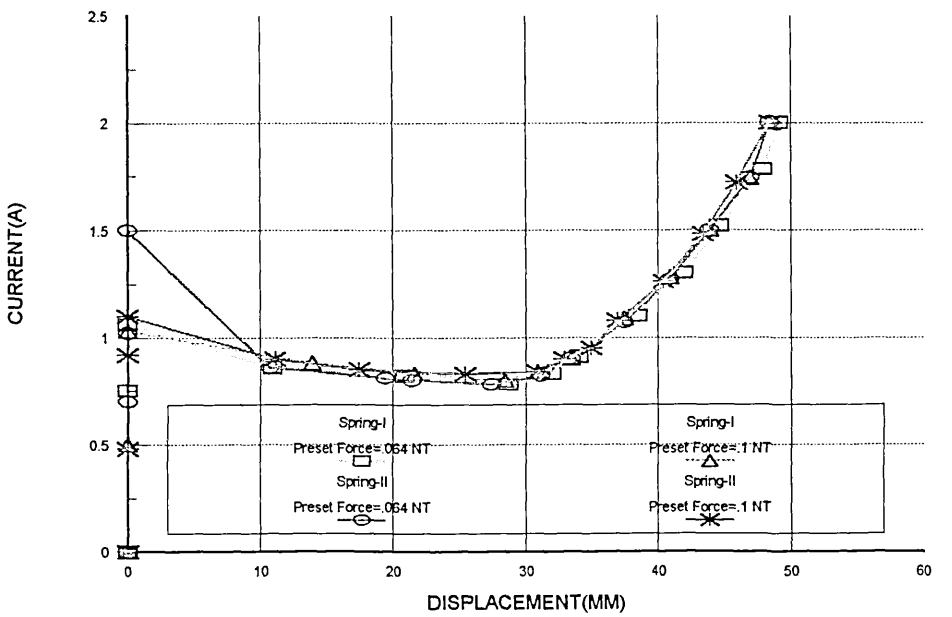


Fig. 2.13 Current versus Displacement under two spring-loads

## 2.4 Conceptual Design with the Aid of Computer Analysis

The conceptual design is the most creative design stage in which majority of the system engineering problems should be synthetically solved or pre-determined. The favourable design configurations, which determine their intrinsic futures and suitability for a certain application, should be drawn out at this stage. The main problems to be tackled in the development of the actuator could be summarised as:

(i) Replace force restraining spring by a mechanism which can generate variable force controlled electrically or electronically

(ii) Enlarge the range of useful stroke

(iii) Obtain higher force

(iv) Improve the linearity of force-displacement characteristics

(v) Reduce the geometric size

It was realised that, if the new TLIA possesses a monotonously descending thrust-stroke characteristic, it can be easily controlled electrically. Therefore the TLIA itself is an electrical spring. In this case task (i) could be easily fulfilled in an integrated configuration by employing two TLIAs assembled in back-to-back structure. After synthesising the requirements mentioned above, several draft designs shown in Fig. 2.14 to Fig. 2.17 have been proposed based on our accumulated knowledge and experience. These draft designs have been analysed by employing the computer aided analysis tool discussed in section 2.2. Their typical flux distributions are illustrated through Fig. 2.18 to Fig. 2.21. Because the most difficult tasks are the (ii), (iii) and (iv), the concentration was put on the study of thrust-stroke characteristics. The computer analysed results are shown in Fig. 2.22. Because the diameters of the mandrels and plungers for different designs are different, it is difficult to draw a conclusion on which design provides highest thrust before we establish the criteria of judgement. The criteria could be set up as the peak thrust divided by the total weight, the weight of plunger, the input power, or their combinations, etc. We think the suitable definition of the criteria is more application dependent factor than a universal definition. Instead of establishing the criteria without identifying practical application we come to qualitative comparison. The results are summarised in the Table.2.1. The simulated results show that no significant difference of

the peak thrust among the CD-2, CD-3 and CD-4 for the similar geometric dimensions. However the CD-1 has much lower peak-thrust than the others. To ease the comparison of the linearity, the characteristics of Fig.2.22 are scaled to unit relative to their peak thrust.

Table 2.1 Comparison of Different Designs

| | Peak Force | Force Dropping | Force Linearity | Mechanical Dynamics | Effective Stroke |
|---|---|---|---|---|---|
| CD-1 | much lower | N.S.C.[+] | N.S.C. | much worse | shorter |
| CD-2 | N.S.C. | faster | worse | better | shorter |
| CD-3 | N.S.C. | faster | worse | better | shorter |
| CD-4 | N.S.C. | slower | better | better | longer |

[+] N.S.C. stands for no-significant-change.

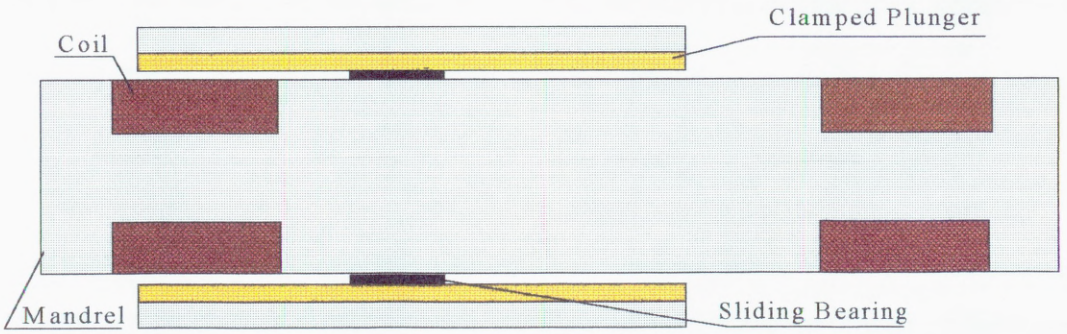


Fig. 2.14 Structural configuration of the Conceptual Design-1 (CD-1)

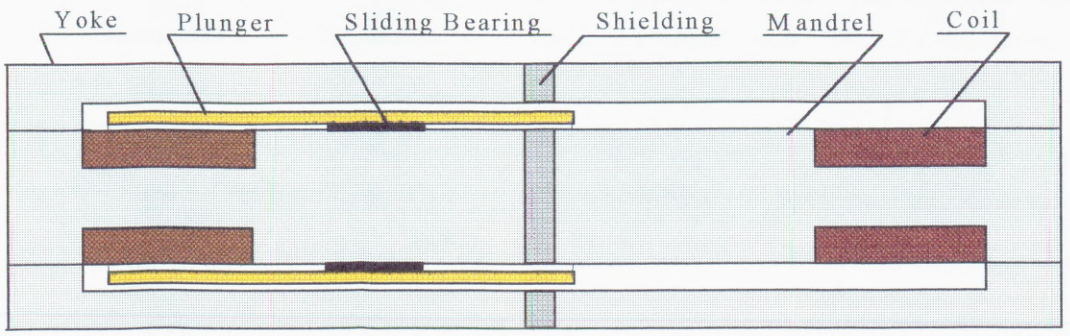


Fig. 2.15 Structural configuration of the Conceptual Design-2 (CD-2)

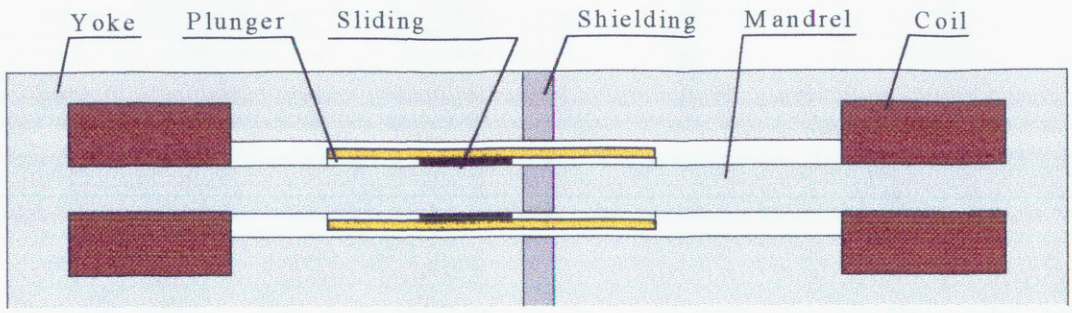


Fig. 2.16 Structural configuration of the Conceptual Design-3 (CD-3)

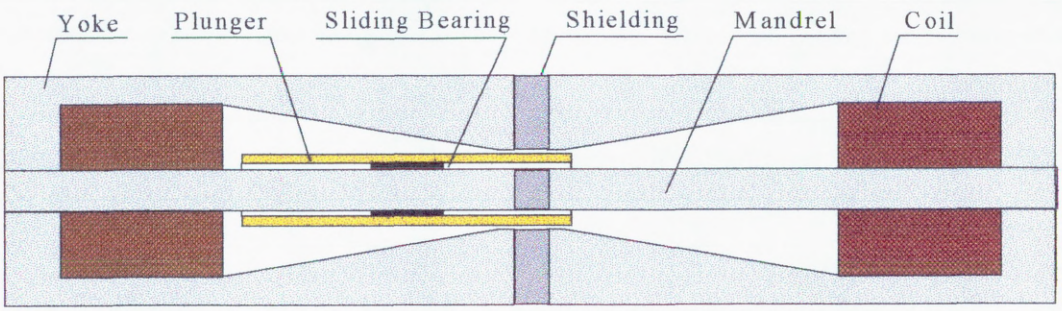


Fig. 2.17 Structural configuration of the Conceptual Design-4 (CD-4)

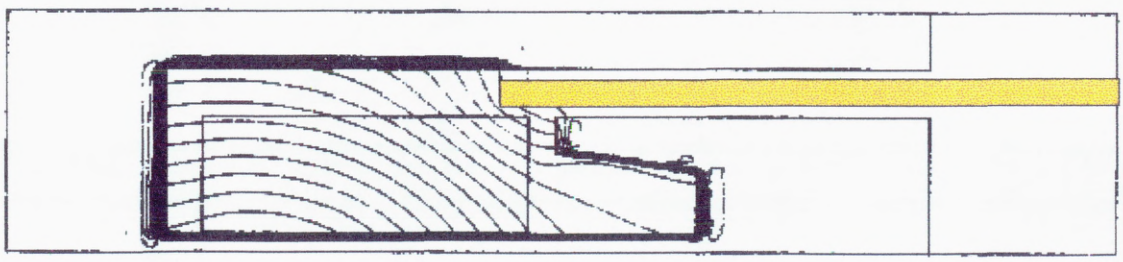

Fig. 2.18(a) Typical field distribution of the TLIA-1 (real part)

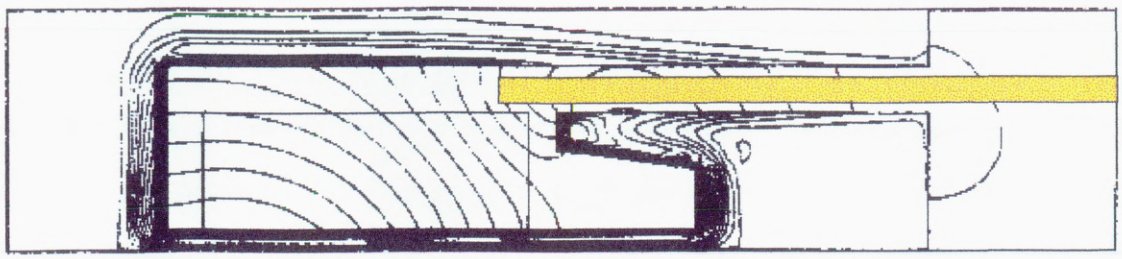

Fig. 2.18(b) Typical field distribution of the TLIA-1 (imaginary part)

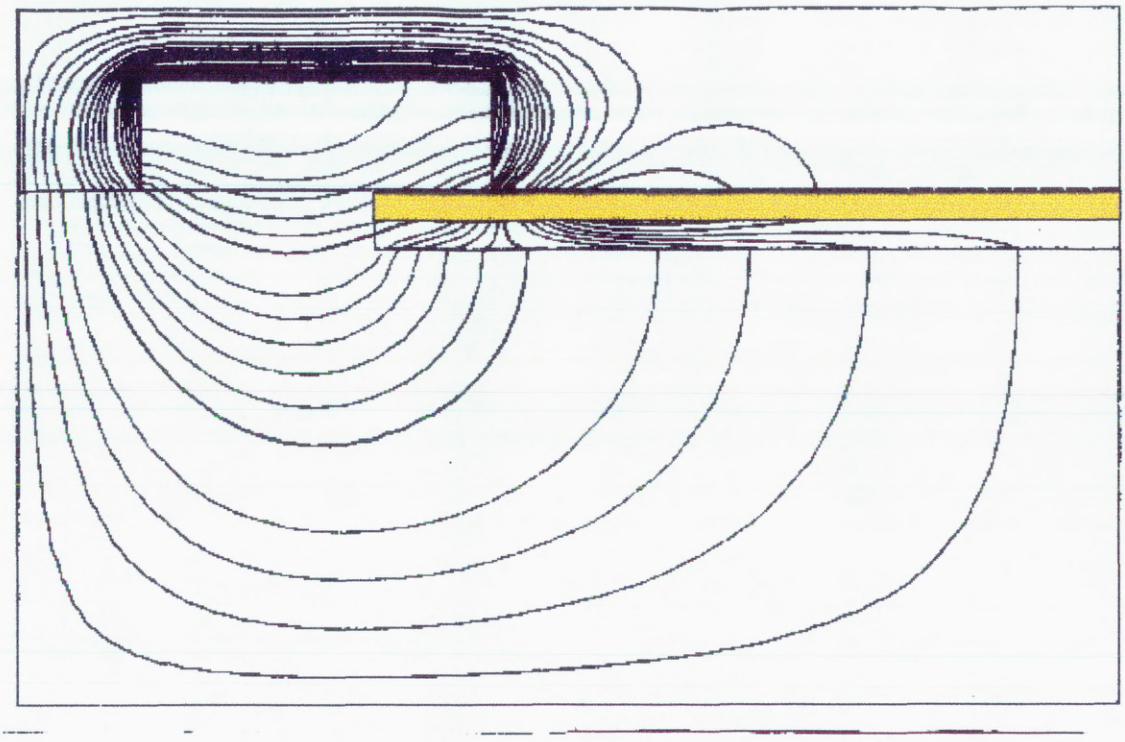

Fig. 2.19(a) Typical field distribution of the CD-1 (real part)

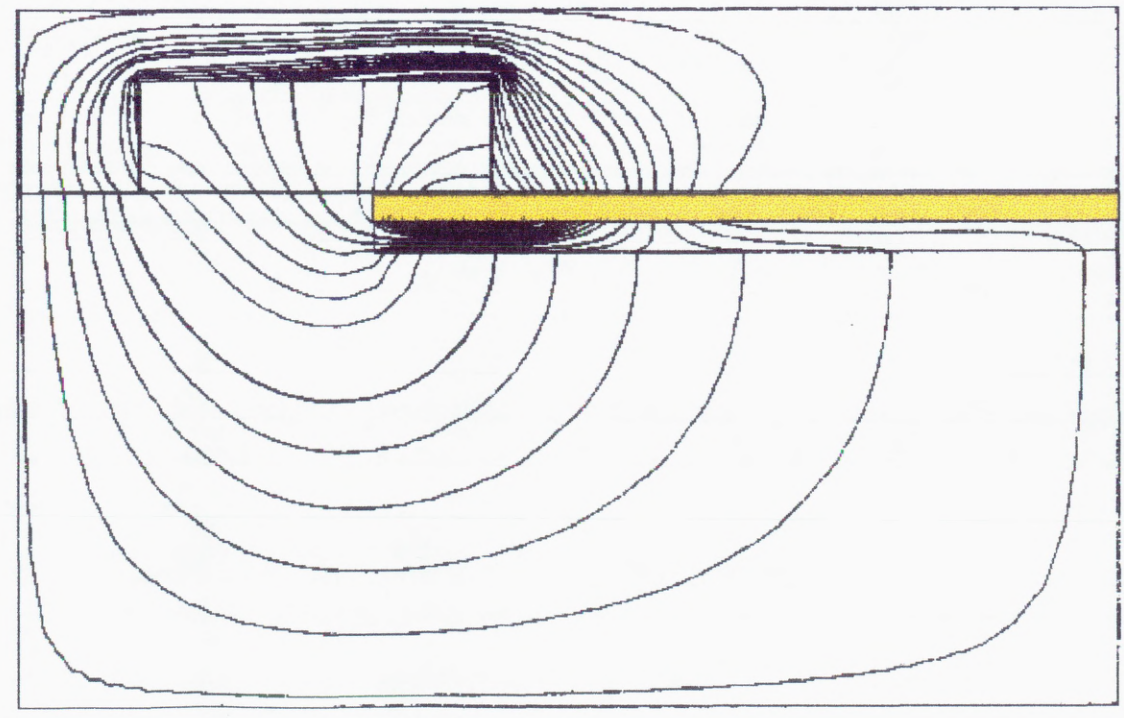

Fig. 2.19(b) Typical field distribution of the CD-1 (imaginary part)

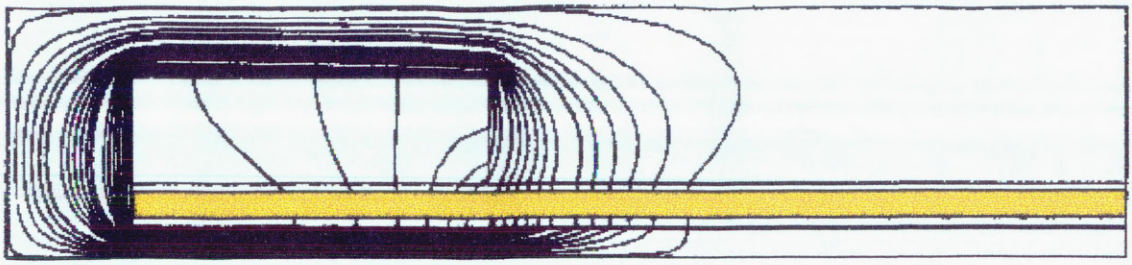

Fig. 2.20(a) The distribution of the real part of the field of CD-2 at displacement of 0mm

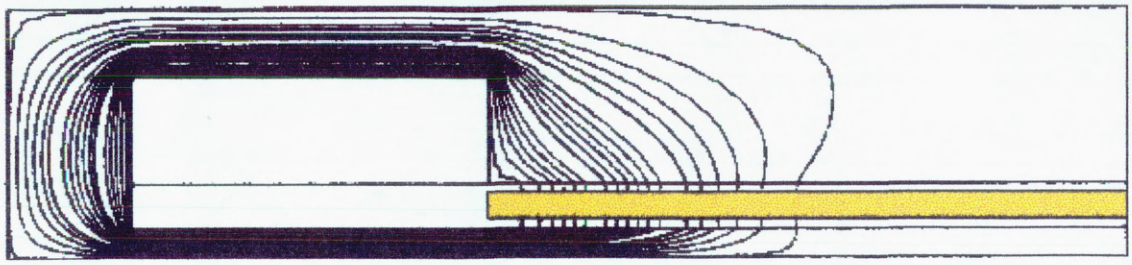

Fig. 2.20(b) The distribution of the real part of the field of CD-2
at displacement of 35mm

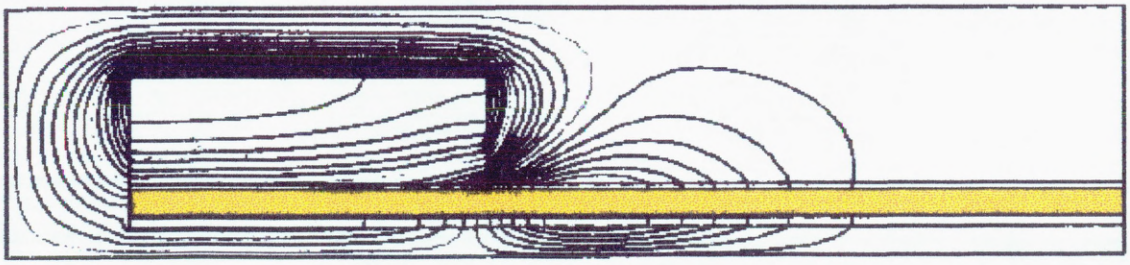

Fig. 2.20(c) The distribution of the imaginary part of the field of CD-2
at displacement of 0mm

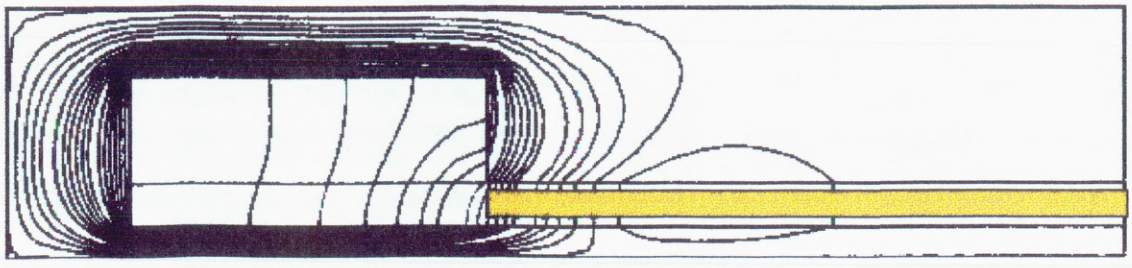

Fig. 2.20(d) The distribution of the imaginary part of the field of CD-2
at displacement of 35mm

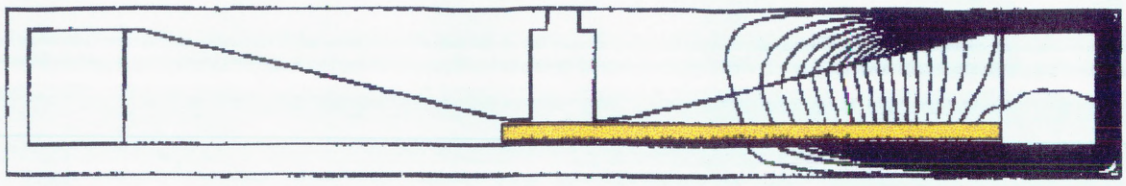

Fig. 2.21(a) The distribution of the real part of the field of CD-4 at displacement of 15mm

Fig. 2.21(b) The distribution of the real part of the field of CD-4 at displacement of 30mm

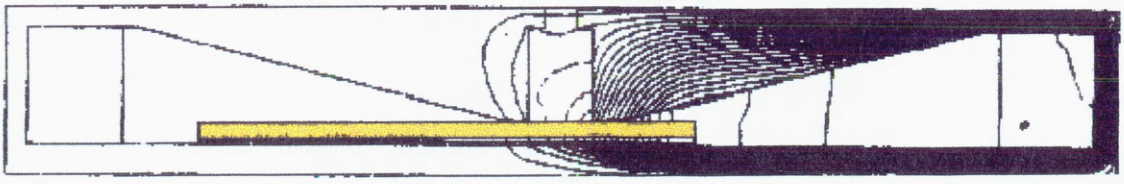

Fig. 2.21(c) The distribution of the real part of the field of CD-4 at displacement of 45mm

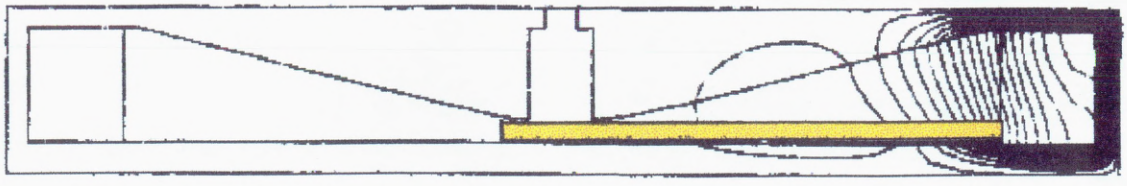

Fig. 2.21(d) The distribution of the imaginary part of the field of CD-4 at displacement of 15mm

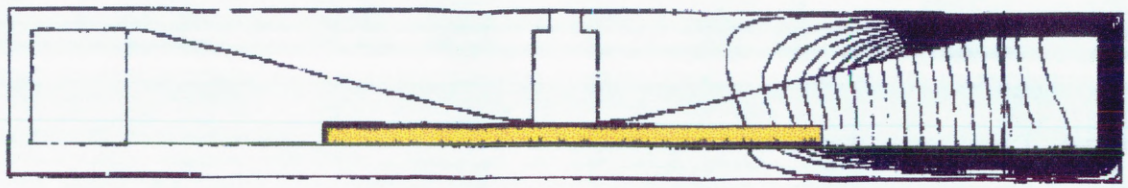

Fig. 2.21(e) The distribution of the imaginary part of the field of CD-4 at displacement of 30mm

Fig. 2.21(f) The distribution of the imaginary part of the field of CD-4 at displacement of 45mm

From the Fig. 2.22 one can observe that the CD-1 and CD-2 have humps in their thrust-stroke curves, and CD-3 and CD-4 have monotonously descending curves. It has been explained that the ascendant part of the characteristics is caused by the $\mathbf{F}_{..}$ From the electromagnetic point of view, it is because the plunger has experienced two opposite magnetic flux distribution, as illustrated by Fig.2.23. This happens when the plunger covers the coil to some distance as shown in Fig. 2.3. The peak thrust position should be where the plunger's working end locates at the neutral position of the magnetic field. The physical axial position corresponding to the magnetic neutral line should be somewhere within the range covered by the coil.

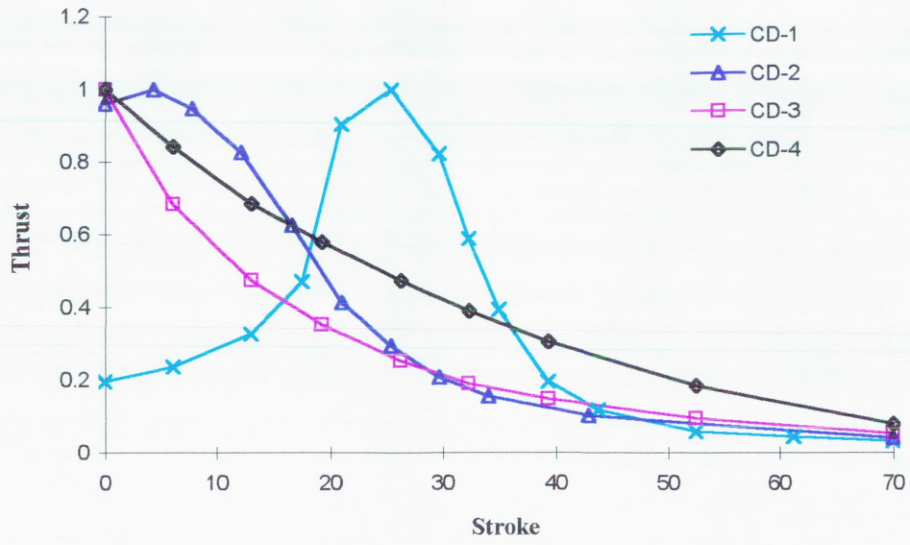


Fig. 2.22 The computed thrust-stroke characteristics for the four conceptual designs

Outside the range covered by the coil the magnetic field will be unidirectional. The **F** disappears and the thrust-stroke characteristics will be monotonous. This is shown by the CD-3 and CD-4 structure. The main difference between CD-3 and CD-4 is that a sloping yoke is used in CD-4 instead a flat-shaped yoke used in CD-3. For CD-3 and CD-4, it is easy to understand that the main magnetic flux $\mathbf{B}_m$ coupling the plunger will decrease when the displacement increases. When $\mathbf{B}_m$ decreases the eddy current induced by the $\mathbf{B}_m$ will decrease as well. This causes the thrust force drops dramatically. To increase the thrust in the middle range position, one of the remedies is to increase the $\mathbf{B}_m$. This ideal realised in design is reflected by the introduction of the slope-shape yoke. With the introduction of large air-gap created by the slope, more $\mathbf{B}_m$ can be obtained than the flat-shape yoke. The simulated results also prove that CD-4 has a larger thrust than CD-3. Ultimately the yoke and/or mandrel can be made of U-shape as shown in Fig.2.24. It is worthy to investigate the U-shape yoke/mandrel structure in the future study.

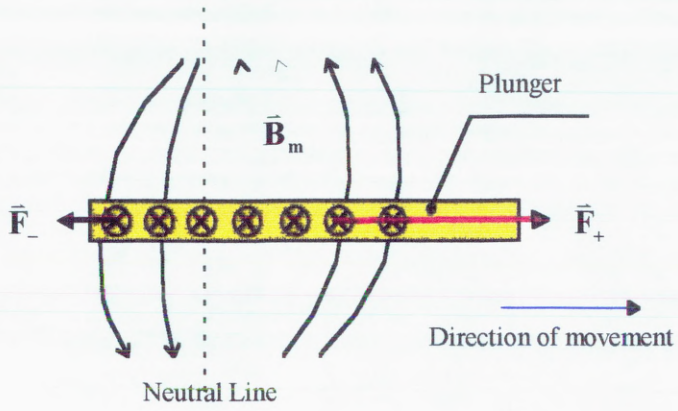


Fig. 2.23 Illustration of magnetic effects on the thrust

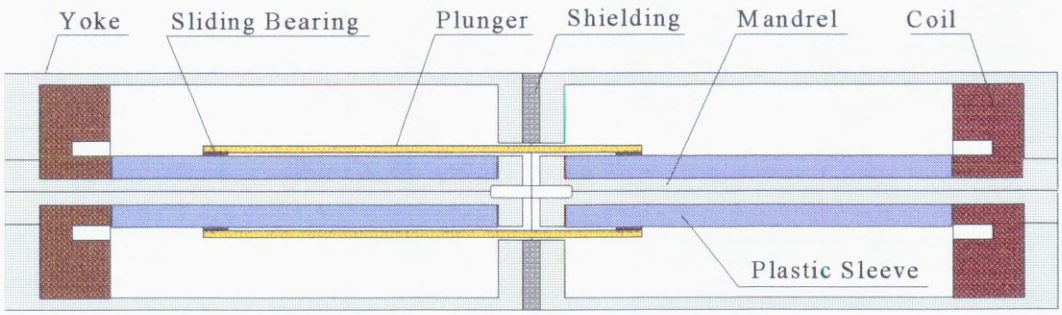


Fig. 2.24 Outline of the proposed U-shape yoke/mandrel structure

## 2.5 Fabrication and Test

Following the above analysis, we come to the conclusion that CD-4 has an overall better performance and hence been chosen for further study. It has been manufactured by the departmental workshop. The photograph shown in Fig. 2.25 is the actuator TLIA-2 with

the CD-4 structure. For the purpose of verifying the simulated results and backing up the design theory, two additional actuators with different configurations have been fabricated as well. The one coded as the TLIA-3 has the CD-2 structure. Its assembly is shown in Fig.2.26. The other one coded as the TLIA-4 with the configuration shown in Fig.2.27, is the inverse structure of TLIA-3 with a stepping mandrel instead of a flat one. The reason to use stepping mandrel instead of sloping one is to let the actuator easier to be machined. Experiments have been carried out on the three actuators under constant voltage excitation condition. The static thrust-stroke characteristics obtained by experimental measurement are shown through Fig.2.28 to Fig. 2.30. Firstly comparing the Fig.2.28 and Fig. 2.29 with the CD-3 curve and CD-2 curve in Fig.2.22 respectively, we can find that the computer simulated thrust-stroke characteristics match well with the experimental results. Secondly comparing the Fig.29 and Fig.2.30, we can observe that the thrust has been significantly improved for the TLIA-4 due to the only change of mandrel's shape.

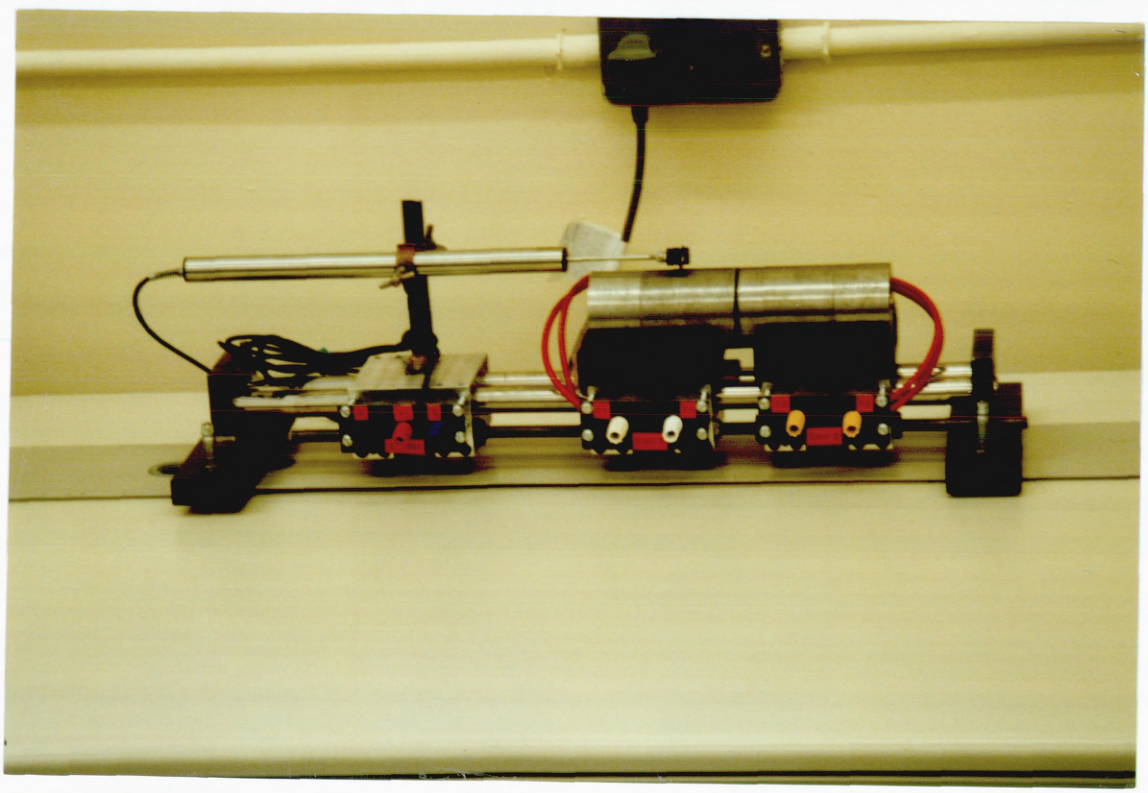

Fig.2.25 TLIA-2 on the test rig

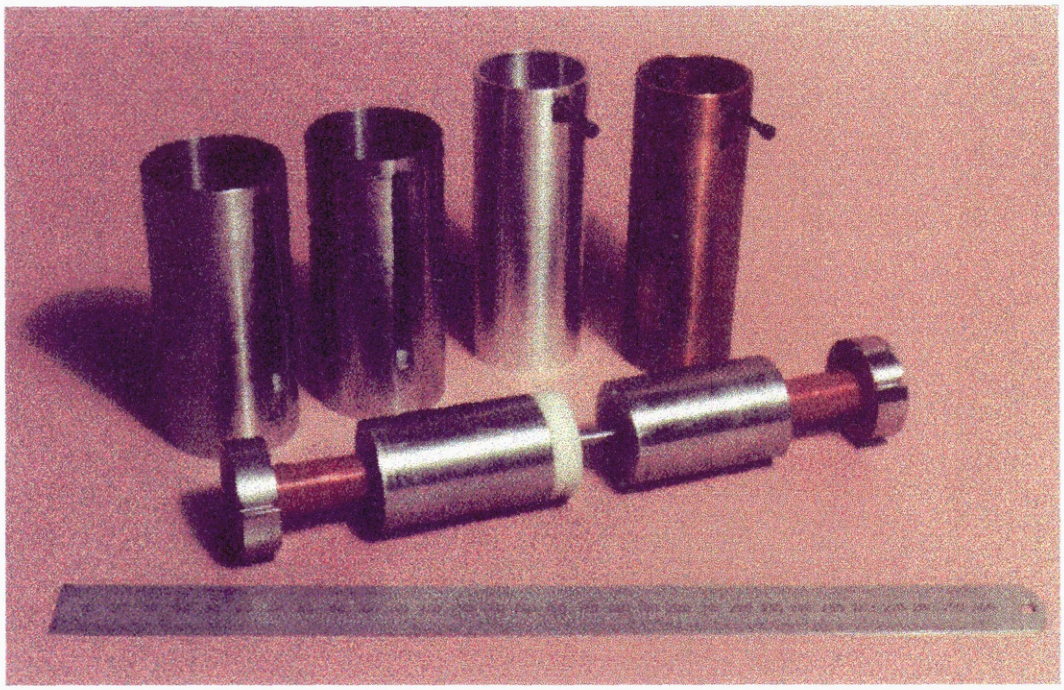

Fig.2.26 The assembly of TLIA-3

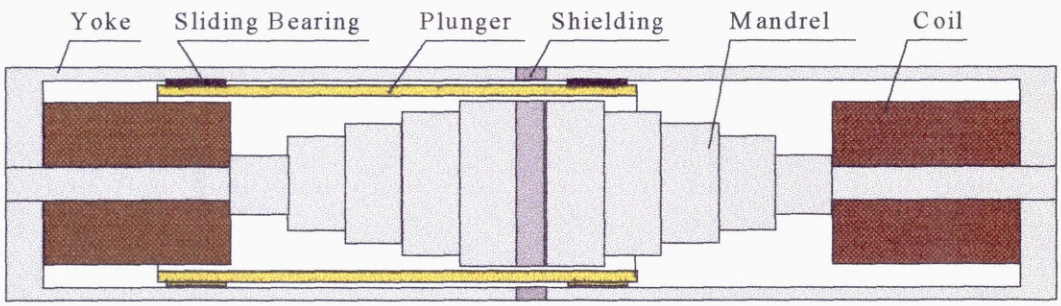


Fig. 2.27 Structural configuration of the TLIA-4

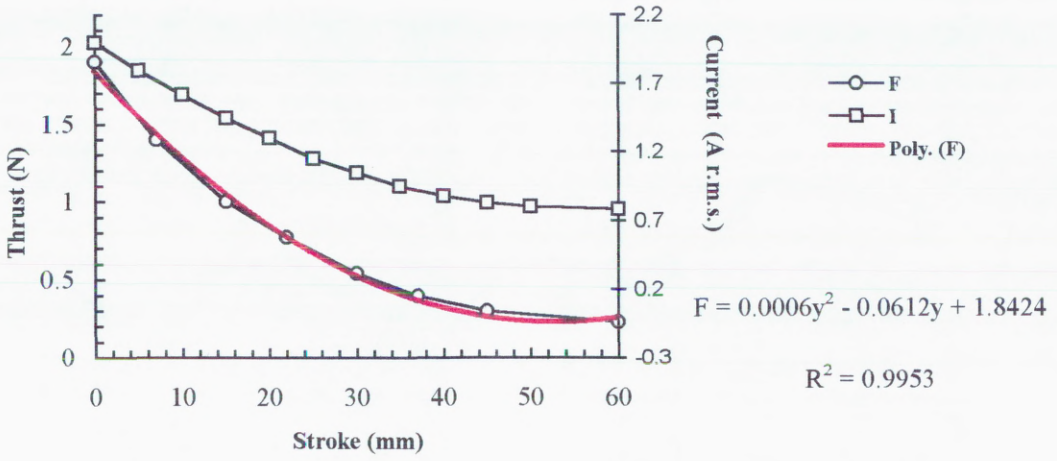


Fig 2.28 Tested thrust-stroke characteristics and the excitation current for the TLIA-2(CD-4 type) under constant voltage of 38V(r.m.s.)

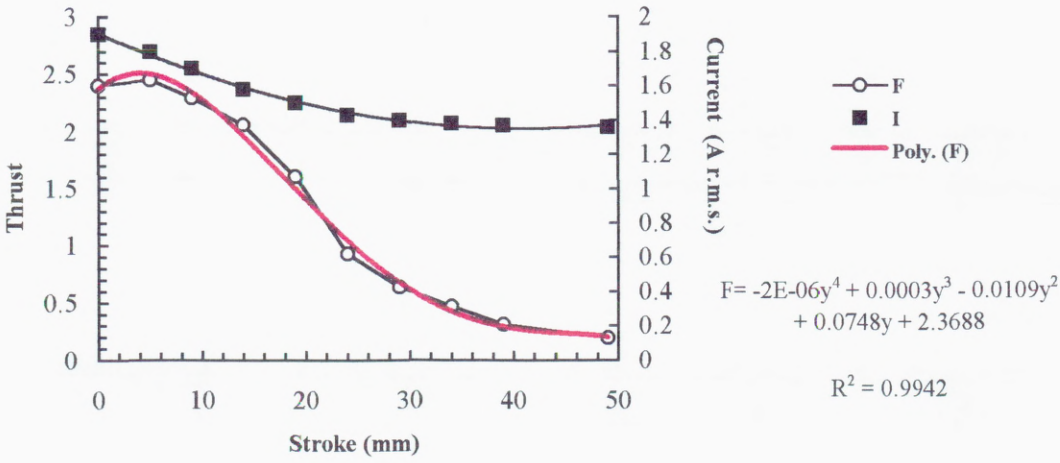


Fig 2.29 Tested thrust-stroke characteristics and the excitation current for the TLIA-3 (CD-2 type) under constant voltage of 40V(r.m.s.)
(Peak thrust occurs at 5mm or 34mm relative to TLIA-4 with 80mm stroke)

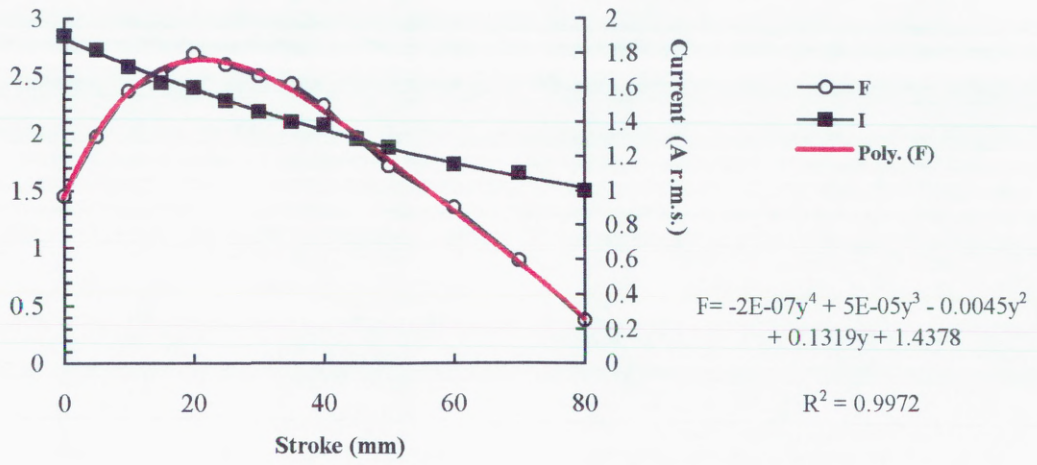


Fig 2.30 Tested thrust-stroke characteristics and the excitation current for the TLIA-4 (CD-2 type) under constant voltage of 59V(r.m.s.) (Peak thrust occurs at 22mm)

From both the computer analysis and experiments, we have acquired more knowledge about how to improve the design of this type of actuator. They can summarised as

- Introducing the stepping or sloping yoke/mandrel, which equivalently increases the air-gap between the yoke and mandrel, will improve the thrust, particularly in the middle range of stroke
- The relative position of the coil determines the basic shape of the thrust-stroke characteristics, i.e. whether it has a thrust hump or not.
- Temperature rising will be an important factor that determines the continuous operation period that the actuator can withstand.

## 2.6 Conclusions

A computer aided design tools based on time-harmonic eddy current model by using FEM has been developed. Started from investigating the TLIA-1 and based on our understanding of the TLIAs' operational principle, four conceptual designs have been

identified for further investigation by the CAD tools. These conceptual designs employ a back-to-back structure to obtain the retaining force, which enable us to remove the spring required in positioning application. The computer simulated results unveil that the thrust-stroke characteristics can be considerably improved by altering the structural configuration. The conclusion has been arrived at that the CD-4 configuration is the best one among the four. Therefore TLIA-2 has been fabricated as the preferable actuator for positioning application. To further verify our knowledge about the operational principle and the CAD tools, other two actuators of different configurations, TLIA-3 and TLIA-4, have been also fabricated for test purpose. Experiments have been carried out on the TLIA-2, TLIA-3 and TLIA-4. The experimental results agree well with the computer simulated ones. The successful application of the computer aided design tools developed here also gives us the confidence to use it in the future development work, such as optimisation of design, control of thrust-stroke characteristics, etc. The results coming from both the computation and experiment also enable us to draw some rules to guide the design of this type of actuators. Finally another prospective actuator using U-shape yoke/mandrel structure has been spotted out with a potential to obtain higher thrust. It could be considered for further investigation.

# 3 SIMULATION OF THE TRANSIENT ELECTROMAGNETIC FIELD

## 3.1 Introduction

With the ever increasing application of numerical computation to aid practical design in industry, requirements on the capability and accuracy of computer aided design tools have been put to a new high level. This is reflected in some recent development in computational electromagnetic fields to simulate precisely the actual operation of electromagnetic devices under different operation conditions [28~34]. They can be briefly categorised into three groups

(i) Incorporating mechanical movement into transient simulation.

(ii) Coupling other physical phenomena, such as temperature, stress, electronic drives, etc.

(iii) Modelling of highly none-linear material property such as hysteresis.

Although we have seen several papers that incorporate hysteresis model into FEM [35,36], the majority activities in the modelling of hysteresis stay in the stage of constructing mathematical models of magnetic materials. It seems that much more work in establishing mathematical models of materials needs to be done before modelling magnetic hysteresis can lead to significant impact on FEM application in practical electromagnetic design.

The major problem associated with coupling mechanical movement in FE formulation is that it requires much more computation time, which rises from the redistribution of meshes and the asymmetry in the stiffness matrix when the contribution of velocity term is not negligible. No significant progress in mathematical treatment has been found to

reduce considerably the extra solution time required in the simulation of mechanical movement. It is considered that parallel computation is very suitable for those problems, particularly for large-scale complicated ones.

Apart from taking account of mechanical movement, which can also be considered as a moving-boundary coupling, non-moving-boundary coupling is another active area. In this chapter we will investigate coupling external driving circuits with the focus on switch-mode drives. Coupling with temperature will be left to the next chapter.

Compared with the FEM derived from standard Maxwell's equations described in terms of current excitation, all the above-dedicated simulation imposes much more requirement to the computer power. Although the today's computer power increases at a very high speed, it still far more sufficient to carry out complicated 3D simulations at the price and time that is suitable for the purpose of routine design. Searching for better models and fast algorithms that can reduce the requirements to computer resources is still a favourable solution to the problem rising from limitations of computer hardware. In this chapter, a new eddy current model is developed for simulating transient eddy current field coupled with external excitation circuit under voltage excitation.

Traditionally, electromagnetic devices and their controlling circuits have been studied separately at first, and then coupled together in a weak form in which parts of their static or dynamic parameters are used. This type of analysis will lead to significant errors when the combined system is non-linear. Consequently, it is necessary to use a strong coupling method, which solves the electromagnetic field equation and external circuit equation simultaneously [31,37~39]. In the simultaneous solution of these coupled equations, two strategies are often adopted. They are the direct coupling methods and the indirect coupling methods. Unlike coupling mechanical movement which could result in an asymmetric stiffness matrix [2], coupling external circuits by either method may preserve the original symmetry of the stiffness matrix for many simple driving circuits if the original one is symmetric. In this case, it enables use to use fast algorithms to solve large sparse symmetric matrix equation instead of using much less efficient algorithm to solve

asymmetric matrix equations.

The direct coupling again can be carried out in two ways. One is to consider excitation currents as new variables to be solved together with field potential variables [39]. This results in a higher order of asymmetric matrix equation [35,40]. The other is to put the constraints of the circuit equations implicitly into the field equations. This results in a same order, but less sparse matrix equation. Both approaches require modifying the global stiffness matrix arising from the discretised field equations and increase the non-zero elements and bandwidths. Although the direct coupling method needs only one computation to satisfy both field and circuit equations at each time step or non-linear iterative step, the total storage demanded and the CPU time incurred could be significantly larger than the indirect coupling method if the discretised nodes in the winding area are a moderate fraction of the total number of nodes [17,39].

The indirect coupling method is an iterative procedure based on a current-searching scheme. It preserves the original global stiffness matrix by separating circuit equations from field equations. If the original global stiffness matrix is symmetric and sparse, as are most cases in FEM, this could bring a significant advantage. The drawback is the necessity to introduce iterations between the solution of field equations and circuit equations. However, those iterations can be confined to be carried out only on the circuit equations in linear cases by separating magnetic vector potential into two components. In the indirect method, the standard procedure executes nested iterations, for example, current searching nests non-linear search iteration that nests conjugate gradient searching. The total iterations will be $N_i N_n N_t$, where $N_i$, $N_n$ and $N_t$ stand for iteration numbers in the above three searches respectively. Since the convergence of all searching methods is related to initial conditions, another way to accelerate the convergence is by improving the initial estimations of starting vector. Better initial estimation can be obtained by proper extrapolation methods for transient simulations.

Since our TLIAs are driven by a PSU under switch-mode that is favoured in power electronic driving circuits, owing to its lesser power consumption incurred in the power

semiconductors working under this mode, our study will be focused on this mode of operation. It means that the high frequency components in both voltage and current will be rich, especially in pulse width modulated (PWM) mode. Therefore the number of discrete time steps should be much more than those under continuous mode. For example, a typical PWM a.c. driving circuit could work at a switching frequency above tens of times higher than its base frequency, and a PWM dc driving circuit could work at about 100kHz. The fact of very high harmonic frequency in driving circuits and the relatively low electric/mechanical time constant of the device demands very fine and much more time steps in the integration to cover the electric/mechanic transient period. This particular character could be treated in a special way to accelerate the numerical simulation process.

There is much literature available on the coupling of field and circuit equations [31,37~41]. However few of them particularly concentrated on practical power electronic circuits working in the switch mode. Bearing in mind of the advantage of indirect coupling method and the special feature in modelling electromagnetic devices driven by switch-model power supply, we propose to decompose the conventional magnetic vector potential into two components to accelerate the solution. Although the method is initially derived from discretised form in linear condition, it can be extended to compute the non-linear cases.

For the decomposed magnetic vector potential (DMVP) method, non-linearity in material property could be treated by three methods which are the time-domain elemental piece-wise linearisation (TEPL) method, the modified Newton-Raphson (MNR) method or the combination method. The combined method switches between the TEPL method and the MNR method according to the instantaneous saturation level. The balance between the simulation speed and the computation accuracy is achieved by the judicious choice of non-linearity treatment methods.

## 3.2 Eddy Current Model Coupling External Circuit

### 3.2.1 Standard Transient Eddy Current Model

At low frequencies where displacement current can be neglected, the Maxwell's electromagnetic equations can be expressed as

$$\nabla \times \mathbf{H} = \mathbf{J} = \mathbf{J}_s + \mathbf{J}_e \tag{3.1}$$

where $\mathbf{J}=\mathbf{J}_s+\mathbf{J}_e$ represents the total current, $\mathbf{J}_e$ denotes for eddy current density inside a massive material and $\mathbf{J}_s$ denotes all the rest current density which is generated by the source voltage.

What is considered here is that the electromagnetic field is generated directly by a voltage source instead of current source, which is the dominant operating condition for vast majority of electromagnetic devices. Under this condition, **J** can be considered to be affected by three types of voltages: the voltage supply $V_s$, the electric potential $e_m$ induced by flux linkage and the electric potential $e_e$ induced by eddy current reaction. The voltage $e_m$ and $e_e$ are governed by the electromagnetic induction equation:

$$\nabla \times (e_e + e_m) = -\frac{\partial \mathbf{B}}{\partial t} \tag{3.2}$$

This classification will give the meaning that $\mathbf{J}_s$ is generated by $V_s$ and $(e_m+e_e)$, and $\mathbf{J}_e$ is generated by $e_e$.

Most of FE electromagnetic field computation is carried out with some auxiliary potentials, such as the magnetic scalar potential $\Omega$, magnetic vector potential $A$, electric vector potential $T$, and electric scalar potential $\Phi$, due to the fact that they lead to easier treatment of boundary conditions than using **B**, **H** or $I$ [20,42,43]. Although there could be several methods using different potential and/or their combinations to solve the same problem, it appears that magnetic vector potential (MVP) method is the most widely used one that is generally suitable for all conditions. Therefore the MVP method is

chosen in our study. In term of the MVP's definition

$$\mathbf{B} = \nabla \times \mathbf{A} \tag{3.3}$$

We can derive the expression $\mathbf{J}_e$ as

$$\mathbf{J}_e = \sigma e_e = -\sigma(\frac{\partial \mathbf{A}}{\partial t} + \nabla \Phi) \tag{3.4}$$

The definition of (3.3) implies that **A** could be superimposed by another gradient scalar field to produce the same **B**, such as the $\Phi$ in (3.4). This is so-called uniqueness problem. There are some papers discussing the uniqueness problems [44]. For transient eddy current problems, the uniqueness of MVP can be achieved by employing the Gauss gauge. This will lead to a constant $\Phi$ that can be set to zero. In this case (3.1) can be rewritten as

$$\nabla \times \nu \nabla \times \mathbf{A} + \sigma \frac{\partial \mathbf{A}}{\partial t} = \mathbf{J}_s \tag{3.5}$$

We use variation functional to derive FEM formulation. The functional for (3.5) is

$$\Theta = \frac{1}{2}\int_R [\nu \nabla \times \mathbf{A} \cdot \nabla \times \mathbf{A} + \nu(\nabla \cdot \mathbf{A})^2 + \mathbf{A} \cdot \frac{\partial \mathbf{A}}{\partial t} - \mathbf{A} \cdot \mathbf{J}_s] dv - \oint_\Gamma (\mathbf{A} \times \nu \nabla \times \mathbf{A}) ds \tag{3.6}$$

Following the standard FE routine (subdividing the whole solution region into a number of sub-regions/elements, interpolating potential by using values at the vertices of elements, elemental analysing and assembling), one can obtain an algebraic matrix equation that can be expressed as

$$[\mathbf{K}][\mathbf{A}] + [\mathbf{E}][\frac{\partial \mathbf{A}}{\partial t}] = [\mathbf{C}][\mathbf{J}_s] \tag{3.7}$$

If the excitation current $\mathbf{J}_s$ is known, (3.7) can be solved in a straightforward manner. When devices are voltage-driven. The excitation current could not be obtained before the electromagnetic field is calculated. The interaction between electromagnetic field and the associated circuitry needs to be coupled together to obtain the solution.

### 3.2.2 Coupling of External Circuit

From the driving circuit point of view, an electromagnetic device is usually considered as a circuit element described by an equivalent circuit model with a certain relationship. A general equation that is valid for most electromagnetic devices to describe the relationship between terminal voltage and terminal current can be stated as follows

$$V_s(t) = R_{eq}(t) \cdot i(t) + e_{bmf}(t) \tag{3.8}$$

where the back electromotive force $e_{bmf}$ is the sum of $e_m$ and $e_e$. Resistance $R_{eq}$ should be considered as an equivalent one. Coupling the electromagnetic equation (3.5) with a voltage source is to substitute (3.4) and (3.8) into (3.5). When eddy current in windings is neglected, $\mathbf{J}_s$ can be easily calculated from excitation current. The coupling relationship will be

$$\begin{aligned} e_{bmf} &= -\frac{\partial \Psi}{\partial t} \\ &= \sum_{m=1}^{c} K_m \nabla \times \frac{\partial \mathbf{A}}{\partial t} \end{aligned} \tag{3.9a}$$

$$j_s(t) = \frac{N}{S} i(t) \tag{3.9b}$$

where N, S and $\Psi$ are the number of turns, cross-section area and flux linkage of the winding carrying current *i(t)* respectively. So, (3.7) and (3.8) can be solved simultaneously through the coupling relationship (3.9). Putting the three equations together, the direct coupling method will lead to the equation

$$\begin{aligned} [\mathbf{K}_{st}][\mathbf{A}] + [\mathbf{E}_c][\frac{\partial \mathbf{A}}{\partial t}] &= [\mathbf{C}](V_s(t) - \sum_{m=1}^{c} K_m \nabla \times \frac{\partial \mathbf{A}}{\partial t}) R_{eq}^{-1} \\ &= ([\mathbf{C}]V_s - [\mathbf{C}][\mathbf{K}'_m][\frac{\partial \mathbf{A}}{\partial t}]) R_{eq}^{-1} \end{aligned} \tag{3.10}$$

FE analysis tells us that the matrix $[\mathbf{K}_{st}]$ and $[\mathbf{E}_c]$ are sparse. When circuit equation is coupled, its first influence is that it changes the sparseness of the stiffness matrix. The

degree of the influence on the sparseness is determined by the node numbers coupled in the $e_{bmf}$ calculation that is reflected as the summing term in the RHS of (3.10). The above discussion is just based on single circuit equation to be coupled. When several circuit equations are involved, the sparse property will be much worse. It is also apparent that the direct coupling term in the R.H.S. of (3.10) may affect the symmetry and positive-definiteness of the stiffness matrix. However, these two properties are very favourable to obtain a fast solution to a linear sparse matrix equation. The eventual influence will depend on the external circuits involved and the method of establishing the circuit equations.

Due to those disadvantages in direct coupling we prefer to separate the FE equation from the external circuit equations by introducing an iterative search algorithm to find the excitation current which can satisfy both the field and circuit equations. This is the indirect coupling method. The disadvantage caused by the extra iterative searching of excitation current could be compensated by its advantages in the following aspects:

(i) The original property of stiffness matrix is retained.

(ii) Easy to incorporate complicated circuit equations.

(iii) Calculation of circuit equation takes very small friction of the time required for the solution of field equation.

(iv) Transient current can be well predicted by extrapolation method, and therefore the iteration numbers can be significantly reduced, due to the inductive property of the devices.

(v) At each iteration, solution time for the field equation is reduced in comparison with the direct coupling method.

It is difficult to draw a unanimous conclusion on which coupling method will give faster solution in terms of the total time required. It is very dependent upon both the electromagnetic structure and the complexity of the external circuit. However the (ii) is obviously attractive from practical engineering point of view. An electromagnetic device usually has a very limited number of independent excitation currents or excitation windings. This means that the searching of currents involves few variables. Consequently

the convergence can be easily obtained.

### 3.2.3 Time-Stepping Method to Treat Transient Terms

Equation (3.10) appears as a parabolic partial differential equation. There are several methods available to treat the time differential terms, but each has its preferred application areas. One of the most frequently used methods in the computational electromagnetic field is the finite difference type of algorithm that can be generally expressed as

$$\frac{\mathbf{A}(t+\Delta t)-\mathbf{A}(t)}{\Delta t}=\lambda\frac{\partial \mathbf{A}}{\partial t}\bigg|_{t+\Delta t}+(1-\lambda)\frac{\partial \mathbf{A}}{\partial t}\bigg|_{t} \qquad 0\leq\lambda\leq1 \qquad (3.11)$$

When $\lambda$ is set to 0, 0.5 or 1, (3.11) will take the form of Forward Euler Difference (FED) algorithm, Crank-Nichoslon (CN) algorithm and Backward Euler Difference (BED) algorithm respectively [45,46]. Among the three algorithms the BED formulation is the most stable one. The other two formulations will suffer convergence problem more or less, particularly the FED formulation. The BED formulation is therefore adopted in this study. In this case discretised form of (3.5) is

$$\nabla\times\nu\nabla\times\mathbf{A}^{n}-\sigma\frac{\mathbf{A}^{n}}{\Delta t^{n}}=\frac{N}{S}i(t^{n})-\frac{\sigma}{\Delta t^{n}}\mathbf{A}^{n-1} \qquad (3.12)$$

Since many time-steps will be involved in the simulation of transient process as mentioned before, we will not solve (3.12) at this stage. Instead, we separate it into two equations which solve two new magnetic vector potentials decomposed from **A**.

### 3.2.4 The Decomposed Magnetic Vector Potential Method

Tacking the time-stepping eddy current formulation (3.12) and knowing the advantage of the indirect coupling method, we are able to formulate the DMVP method. The left hand side of (3.12) indicates that the actual potential **A** can be considered as the total effect from two independent sources: the instant excitation current and the previous excitation

history reflected as $\mathbf{A}^{n-1}$. Since the assumption implied by the BED method in that the $\mathbf{A}^{n-1}$ is constant during the current time interval, the only factor influencing $\mathbf{A}^n$ is the current *i(t)*. This gives us the intuition that some computation could be saved if superposition method can be applied.

3.2.4.1 Decomposing MVP in Linear Cases

The ideal cases to apply a superposition method are the linear ones. The linearity concerns two aspects: the governing equation and the materials. First of all, all the mathematical operations we have encountered so far are linear. Therefore, when we discuss linearity or non-linearity we are confined to referring to material properties. Considering cases for which material properties are linear or can be linearised by a certain method, we define two new magnetic vector potentials based on the discretised integration form of (3.12). Their definitions are

$$\mathbf{A} = \mathbf{A}_i + \mathbf{A}_e \tag{3.13}$$

$$\nabla \times \nu \nabla \times \mathbf{A}_i^n - \sigma \frac{\mathbf{A}_i^n}{\Delta t^n} = \frac{N \cdot i(t^n)}{S} \tag{3.14}$$

$$\nabla \times \nu \nabla \times \mathbf{A}_e^n - \sigma \frac{\mathbf{A}_e^n}{\Delta t^n} = -\frac{\sigma}{\Delta t^n} \mathbf{A}^{n-1} \tag{3.15}$$

The physical meaning is that $\mathbf{A}_i^n$ is the contribution from current $i(t_n)$ and $\mathbf{A}_e^n$ is the contribution from historical $\mathbf{A}^{n-1}$. $\mathbf{A}_i^n$ and $\mathbf{A}_e^n$ are uncoupled within the interval of current integration step. However, their combined effect is passed to the next integration step. Because (3.14) and (3.15) have the same differential operator, they will possess the same stiffness matrices that can be expresses as:

$$[\mathbf{K}_{st}(\Delta t^n)][\mathbf{A}_i^n] = [\mathbf{C}] i(t^n) \tag{3.16}$$

$$[\mathbf{K}_{st}(\Delta t^n)][\mathbf{A}_e^n] = [\mathbf{E}_c][\mathbf{A}_i^{n-1} + \mathbf{A}_e^{n-1}] \tag{3.17}$$

3.2.4.2 Search and Extrapolation Method

The TLIAs under the investigation use single-phase a.c. power supply. It means that only one terminal voltage and one terminal current are involved in the circuit equation. A second-order discretised Newton algorithm, expressed in (3.18), is employed here to search the excitation current.

$$i(x_{k+1}) = i_k + \frac{i_k - i_{k-1}}{u_k - u_{k-1}}(u_{k+1} - u_k) \tag{3.18}$$

For multiple excitation cases, (3.18) should be expanded to multi-degree formulation. Because of the inductive nature of electromagnetic devices, the current wave-form is much smoother than the voltage wave-form. There is no particular problem to get a fast convergence. This also means other search methods, which may be found in optimisation theory, can be easily applied here.

In order to accelerate the current searching, an extrapolation will be carried out before commencing each searching iteration in order to produce a good initial estimation of the excitation current. A second-order Lagrange algorithm, expressed as (3.19), is used for the extrapolation.

$$\begin{aligned} f_{t+1} = & \frac{(t_{t+1} - t_{t-1})(t_{t+1} - t_t)}{(t_{t-2} - t_{t-1})(t_{t-2} - t_t)} f_{t-2} + \frac{(t_{t+1} - t_{t-2})(t_{t+1} - t_t)}{(t_{t-1} - t_{t-2})(t_{t-1} - t_t)} f_{t-1} \\ & + \frac{(t_{t+1} - t_{t-1})(t_{t+1} - t_{t-2})}{(t_t - t_{t-1})(t_t - t_{t-2})} f_t \end{aligned} \tag{3.19}$$

When an iterative algorithm is used to solve the final linear algebraic equations, (3.19) can also be used for the extrapolation of potentials of $\mathbf{A}_e^n$ and $\mathbf{A}_i$ to get a better starting vector. Extrapolation of $\mathbf{A}_e^{n+1}$ could be carried out once at the beginning of each time-step. Superposition of $\mathbf{A}_i^{n+1}$ could be carried out for each current-searching iteration.

For a summery, the time-stepping simulation then can be carried out in the following way:

(i) Solve (3.16) for each independent current variable (total of $k$). When factorisation method (such as LU,ICCCG) is used to solve the algebraic matrix equation with constant time step, this requires factorisation of the stiffness matrix once only and backward substitutions $k$ times for the whole span of transient integration.

(ii) Solve (3.17) once to obtain $A_e^{(n)}$

(iii) Carry out time-stepping integration by:

(a) Extrapolating potential by using (3.19)

(b) Iterative search excitation current:

(b.1) Extrapolate current by using (3.19)

(b.2) Superimpose $\mathbf{A}_i$, at each iteration

(b.3) Calculate the excitation current by (3.8)

(b.4) Compare the currents obtained from (b.3) and the estimated one at (b.1). If the searching has reached its stop criteria, go to (ii) for next time-step.

(b.5) Otherwise, search next current by (3.18) and return to (b.2)

### 3.2.4.3 Treatment of Non-linearity by TEPL Method

Non-linear material properties could be treated as an elemental piece-wise linear property in transient simulation if the current change in two consecutive steps is small enough. In this case, the material properties, such as magnetic permeability and/or conductivity, are updated elementally according to the local field density computed from the previous time step. Then the properties remain unchanged within the next integration step. Because this treatment of non-linearity results in elementally linearized properties for each integration step, the DMVP is still effective. The difference in the implementation is to combine step (a) into step (b.1). Compared with purely linear cases, it just requires one more backward substitution for each time step to compute $A_e^n$, but at lower matrix order than direct coupling. For many engineering applications, this type of approximation to transient none-linear problems can provide sufficient accuracy with appropriate time steps. The other advantage of TEPL method is that it has no convergence problems at all. This will be very attractive in dealing with sophisticated material properties such as hysteresis and highly saturated grain-oriented steel.

3.2.4.4 Full Non-linear Treatment

In addition to the TEPL method that enables us to use the DMVP method, we can also extend the DMVP method to a relatively true none-linear method. From the loading method point of view, non-linearity could be treated in two ways. One is to apply full excitation suddenly in one step. A robust, hence relatively complicated, iterative searching method may be required. Another is to apply an excitation in several loading steps, which is called artificial annealing. With the artificial annealing, non-linear iteration converges quickly in each annealing step. Since the simulation of transient problems by using discrete time integration technique usually takes place from zero state, time-stepping integration brings the equivalent effect of artificial annealing to non-linear property. Therefore searching of the excitation current should converge quickly as well. Since we have the artificial annealing effect hidden in the time-stepping integration, the remaining task is to find a simpler searching algorithm that can explore the potential advantages of the DVPM. We have found that the modified Newton-Raphson method is particularly suitable for this purpose.

When Newton-Raphson algorithm is used to treat the non-linear, (3.16) and (3.17) are implemented in the following forms respectively

$$[\mathbf{J}_p^q][\mathbf{A}_{i,m+1}^n - \mathbf{A}_{i,m}^n] = [\mathbf{C}]i_{m+1}(t^n) - [\mathbf{K}_{st,m}][\mathbf{A}_{i,m}^n] \tag{3.20}$$

$$[\mathbf{J}_p^q][\mathbf{A}_{e,m+1}^n - \mathbf{A}_{e,m}^n] = [\mathbf{E}_{c,m}][\mathbf{A}^{n-1}] - [\mathbf{K}_{st,m}][\mathbf{A}_{e,m}^n] \tag{3.21}$$

where the subscript '$_m$' and superscript "$^n$" denote iterative index and time-stepping index respectively. The modified Newton-Raphson method is implemented in the way that the Jacobian $[\mathbf{J}_p^q]$ is updated at an interval of '$p$' iterations or '$q$' time steps. The simplest way is to set a constant $[\mathbf{J}_0]$ that is calculated at the zero-state condition. Because the modified Newton-Raphson method uses constant Jacobian, the DMVP method can be applied straightforward. When $[\mathbf{J}_p^q]$ is set to a constant $[\mathbf{J}_0]$, the solution procedure for linear cases can be adopted. When $[\mathbf{J}_p^q]$ is updated, the similar solution procedure for the

TEPL method can be adopted.

Compared with standard MVP method which implements Newton-Raphson non-linear iteration as

$$[\mathbf{J}_p^q][\mathbf{A}_{m+1}^n - \mathbf{A}_m^n] = [\mathbf{C}]i_{m+1}(t^n) + [\mathbf{E}_{c,m}^n][\mathbf{A}^{n-1}] - [\mathbf{K}_{st,m}][\mathbf{A}_m^n] \tag{3.22}$$

the DMVP method will involve one more backward substitution if factorisation method is used to solve the linear matrix equation. This is the only drawback to use DMVP implement full non-linear treatment. Even if the time for backward substitution is usually a fraction of that for factorisation, the story does not stop here.

For single-phase devices, their magnetic saturation level changes in proportion to the excitation current. It means that magnetic saturation, which is the main causes of the non-linearity of electromagnetic devices, will change between linear and non-linear status. During low saturation period, we can apply the TEPL method. During high saturation period we can apply Newton-Raphson type (NR-type) method expressed in (3.20) and (3.21). The switching between the TEPL/DMVP method and the NR-type method should be determined by a certain criterion. We propose to use the time differential of average magnetic reluctivity, i.e.,

$$\beta = \left|\frac{d\tilde{\nu}}{dt}\right| = \left|\frac{\partial\tilde{\nu}}{\partial B}\frac{\partial B}{\partial t}\right| \approx \left|E_{bmf}\frac{\partial\tilde{\nu}}{\partial B}\right|$$

where $E_{bmf}$ reflects the change rate of magnetic flux density which is similar to back electromotive force. Therefore $E_{bmf}$ can be considered proportional to the voltage applied at the terminal. When $\beta$ is small the TEPL/DMVP method could be used effectively. Otherwise the NR-type method should be used instead. Figure 3.1 shows the $\partial\tilde{\nu}/\partial B$ curve of a typical grain oriented steel lamination. For a given critical value of $\beta$, the border between the two methods, distinguished by P1 and P2 in Fig. 3.2, can be determined by the average reluctivity. Alternatively P1 and P2 can also be determined by giving critical excitation currents for a given device. This is a much easier way to implement, but needs preliminary knowledge of the correspondence between current and

saturation level. It is obvious that the standard method (3.22) could not provide $\mathbf{A}_e$ and $\mathbf{A}_i$ to interface TEPL implemented in DMVP formulation.

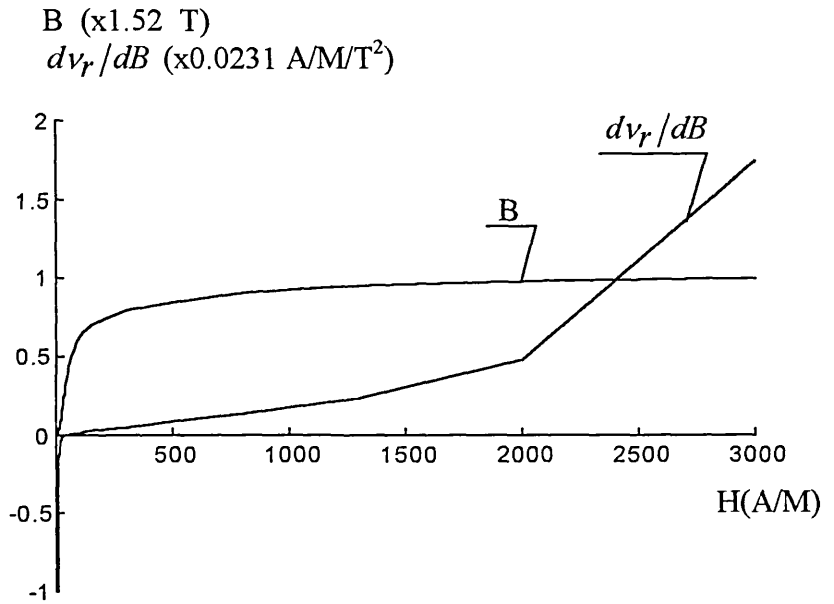


Fig.3.1 The B-H curve and $dv_r/dB$ curve of a typical lamination

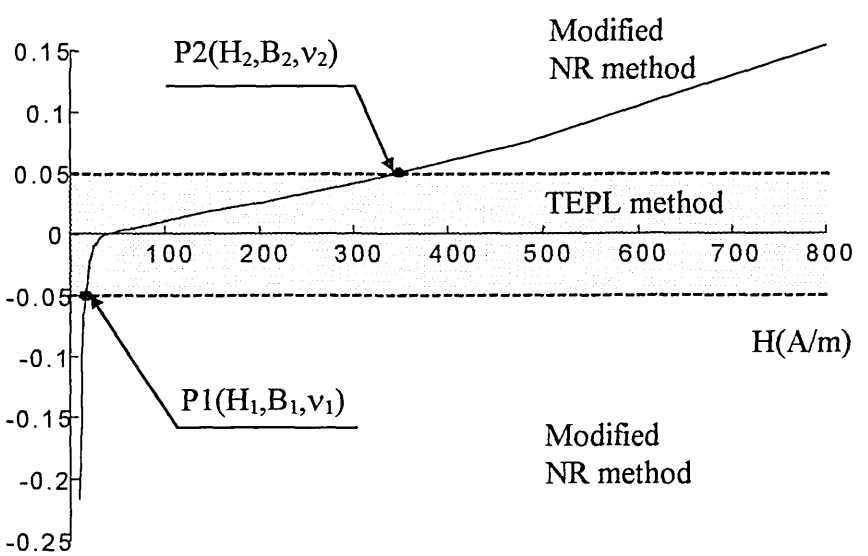


Fig.3.2 The areas for TEPL method and Modified NR method with the setting of $|d\tilde{v}_r/dB|$=0.05

### 3.2.5 The Solver

All the advantages of DMVP method are rooted in the fact that the method has very fast solution for transient linear problems. For non-linear problem, they should be linearised to take the advantages of the methods. In addition to the advantages generated by the method itself, it also enables the possibility to save huge redundant computation incurred in the solution of the final matrix equations by using factorisation-based algorithm to solve the linear algebraic matrix equation. The algorithm used in our study is a scalar-controlled Incomplete Conjugate Gradient method (ICCG). The scalar controlled ICCG uses a scalar variable as the criteria to determine whether a new factorised element should contribute to the incompletely factorised matrix or not. The criteria we used can be expressed as

$$\eta = \left| \frac{\tilde{a}_{ij}^2}{\bar{a}_{ii}\bar{a}_{jj}} \right| \tag{3.23}$$

where the $\tilde{a}_{ij}^2$ is the element to be factorised, $\bar{a}_{kk}$ $(k=i,j)$ is the diagonal element.

Apparently the criterion reflects a certain degree of the influence of the would-be newly factorized contribution to the solution. When $\eta$ is small, we can reasonably suppose the would-be contribution has small influence to the solution, and hence it can be discarded from the factorised matrix. By controlling the scalar $\eta$ (0-1), we can control the size of the incomplete factorized matrix and also the speed. Once the stiffness matrix is factorised, the factorised matrix can be reused until the stiffness matrix is changed.

Unlike fully-factorised direct solution algorithms, the ICCG algorithm is a semi-iterative one whose convergence is affected by the initial condition. In time-step integral solution where the excitation current is a continuous function of time (so as the magnetic vector potentials) a good initial estimation of the potential can be obtained by proper extrapolation such as (3.19). The effectiveness of using extrapolated potential as starting vector will be influenced by other factors such as the interval of time stepping, voltage

change rate, the degree of non-linearity and eddy current, etc.. The smaller the time steps and/or the voltage change rate, the more efficient the extrapolation. The initial searching vector of the Conjugate Gradient (CG) method starting from a non-zero vector $[\mathbf{A}_0^n]$ could be expressed as

$$[\mathbf{p}_0^n] = -[\mathbf{g}_o^n] = ([\mathbf{L}]^{-1}[\mathbf{M}][\mathbf{L}]^{-T})([\mathbf{L}]^T[\mathbf{A}_0^n]) - [\mathbf{L}]^{-1}[\mathbf{r}] \tag{3.24}$$

where [**M**] is the stiffness matrix or Jacobian matrix, [**L**] is the lower triangle matrix incompletely factorised from [**M**], [**r**] is the right hand side of the linear matrix equation, $[\mathbf{p}_0^n]$ is the initial searching direction for the CG iteration and $[\mathbf{g}_0^n]$ is the initial gradient direction.

### 3.2.6 Potential Application of the DMVP in Parallel Computing

Parallel computation represents one of the current research directions to solve extremely complicated problems with huge discretisation. One of the major problems in parallel computation is to find a proper model/algorithm that enables data to be processed in parallel. Looking at the DMVP model, one can realise that at each time step

(i) $\mathbf{A}_i$ and $\mathbf{A}_e$ are uncoupled

(ii) Independent current sources are uncoupled from each other

All the uncouplings can be processed at the same time. It means that the DMVP model is superior to any other models known at the present in terms of parallel computation. Unfortunately we have not been able to test it in parallel computation, but the advantages are obvious.

## 3.3 Comparisons of Different Methods

### 3.3.1 Comparison between the ICM and the DCM

To make comparison between the ICM and the DCM, two discretisation schemes for the same problem have been studied. The details of discretisation are listed in Table I. For

the DCM the voltage was treated as a direct excitation source while the circuit equation was merged into the FE field equations. For the ICM, the DMVP method was employed and the excitation current was treated as an independent variable governed by (3.8). The storage requirement and CPU time for both cases are presented in Table II. The CPU time in Table II is based on a single solution of linear matrix equation that involves incomplete factorisation once and CG backward substitution twice.

From Table II we can observe that the storage requirement of ICM is much less than that of DCM, as is the CPU time. The ratio of $N_w/N_t$ is introduced here to serve as the indicator to measure storage and CPU time. For the DCM, the bigger the $N_w/N_t$, the larger the storage and CPU time for the same discretised node number. When $N_w/N_t$ is very small, there is no significant difference between these two methods. The total CPU saving is directly linked with the total number of integrations. The whole transient process will usually last several cycles, which requires several hundreds or thousands of integral time steps, depending on the frequency and waveform of the excitation voltage. For linear cases the ICM will take the CPU time of about $(T_2+N_n*T_3)\,|_{ICM}$, where the $T_2$, $T_3$ are defined in Table II and $N_n$ are the total number of integral time steps in the whole transient simulation. The DCM will, however, take the CPU time of about $(T_2+ N_n*T_3/2)\,|_{DCM}$. Because $T_3\,|_{DCM}$ is much more than twice of $T_3\,|_{ICM}$, the CPU time is therefore saved significantly.

For non-linear cases with the TEPL method, a conclusion similar to linear cases can be obtained. However, for the full non-linear computation or the combined method presented in section 3.2.4.4, there is no clear conclusion to determine which method is superior because of factors such as level of non-linearity or saturation, length of time steps, balancing strategy between CPU time and storage, etc.

TABLE I. DETAILS OF DISCRETISATION

| | Total Elements | Total Nodes($N_t$) | Nodes in Winding Area ($N_w$) | $N_w/N_t$ |
|---|---|---|---|---|
| Scheme A | 3128 | 1654 | 192 | 0.116 |
| Scheme B | 7594 | 3927 | 523 | 0.133 |

TABLE II

COMPARISON BETWEEN DIRECT AND INDIRECT COUPLING METHODS

| | Scheme B & ICM | Scheme A & ICM | Scheme B & DCM | Scheme A & DCM |
|---|---|---|---|---|
| Storage (32-bit) | 15447 | 6417 | 148918 | 23683 |
| Iterations | 80 | 46 | 56 | 40 |
| $T_1$(second) | 2.29 | 0.78 | 12.22 | 2.52 |
| $T_2$(second) | 0.27 | 0.09 | 76.99 | 3.56 |
| $T_3$(second) | 9.37 | 2.36 | 46.29 | 5.56 |

Storage: Number of total non-zero elements in the matrix [**L**]

$T_1$: CPU time in the assembling

$T_2$: CPU time in the Incomplete Choleski factorisation

$T_3$: CPU time in the Conjugate Gradient iterations from zero initial condition of $A_0^n$.

* The computation was carried out on a DEC Alpha 3000/400 workstation.

### 3.3.2 Error Comparison for Non-linear Cases

Now we come to investigate the accuracy problems associated the proposed schemes based on DMVP method. The step response of the TLIA has been studied in this issue. An equal length of integral time step has been used with the setting of $\Delta t=2.5\text{x}10^{-5}$ second. Four methods (the full NR method, the full TEPL method, the combined method and the linear method with $\mu_r$=6000) have been investigated. Figure 3.3 shows the current response obtained by employing the full NR method which serves as the reference to assess the accuracy of other three method. The error relative to the full NR method is also shown in the same figure. We therefore can observe that

(i) The smallest error is the *eer1(i)* from the combined method with a proper setting of $P_1$ and $P_2$ level

(ii) There is very small difference among three methods when *i* is small. This is the direct result caused by the existence of air gap and non-ferromagnetic material in the path of the main flux which reduces the non linearity level at a low current

(iii) Larger error for *err-3*, corresponding to pure linear DMVP method, occurs at both ends of low and high current. But the error at low current end is not severe.

(iv) Larger error for *eer-2* occurs after $P_2$.

(v) With the increase of the maximum current, the maximum values of err-1 and err-2 have limited bounds while that from err-3 trends unlimited.

So, for the combined method the $P_1$ point can be set at $i$=0 without loss of accuracy. The setting of $P_2$ should be determined by the non-linear saturation level which can be calculated according to the method proposed in section 3.2.4.4. For single-phase a.c. devices, its saturation level changes with the excitation current. That means its saturation level changes periodically. Therefore we can effectively apply the combined method to simulate a device working at a highly saturated level.

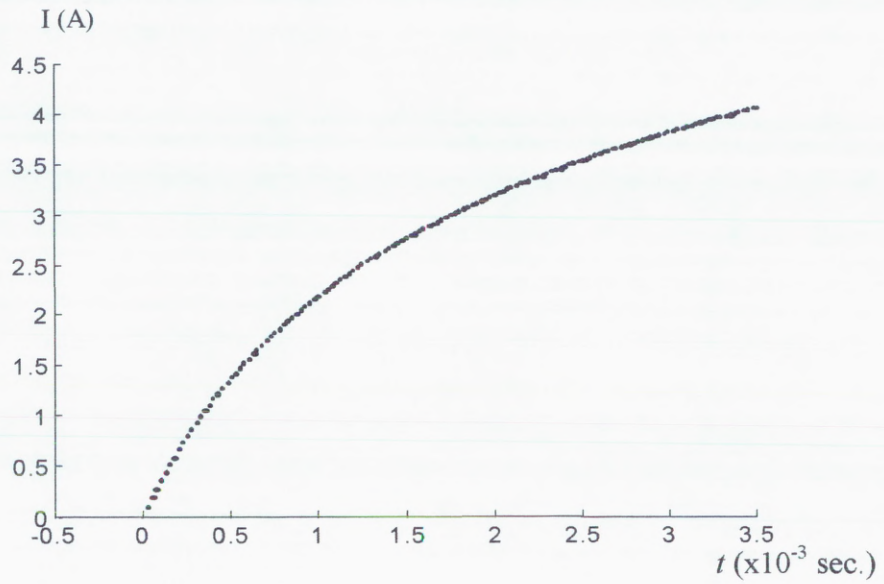


Fig.3.3(a) The step response of the TLIA in non-linear condition

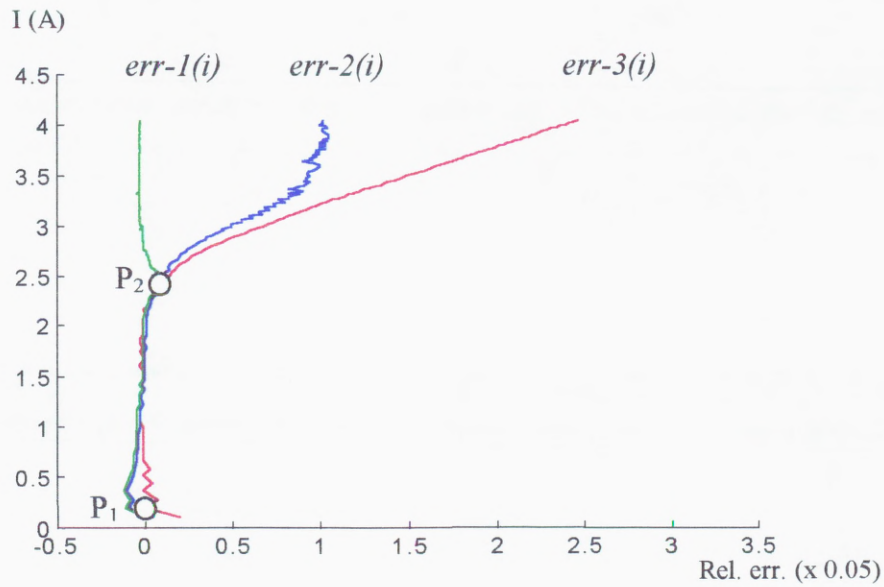


Fig.3.3(b) Comparison of relative errors from three methods

*i(i):* excitation current computed by the full NR method

err-1*(i):* the error from the combined method, relative to *i(t)*, with border settings at $i(P_1)=0.1$ *(A)* and $i(P_2)=2.5$ *(A)*

eer-2*(i):*the error from the full TEPL method, relative to *i(t)*

eer-3*(i):*the error from the full linear method, relative to *i(t)*

## 3.4 Application to the TLIA

The proposed method is applied to simulate the TLIA-1 operating under different voltage waveforms with different external driving circuits. Due to the symmetric structure of the TLIA, an axi-symmetric finite element form has been adopted. The resultant matrix equation is solved by the scalar-controllable ICCG method. The finite element model was created with 3927 nodes and 7594 elements.

### 3.4.1 Sinusoidal Excitation

The first operating condition simulated has employed a sinusoidal voltage source without any control circuits involved. The measured winding resistance was used as the $R_{eq}$ of in (3.8). Three cases have been investigated for different switch-on phase angle $\phi_0$. They have the following settings:

(i) $\phi_0=0^0$, $V_m=50$ V

(ii) $\phi_0=90^0$, $V_m=50$ V

(iii) $\phi_0=314^0$, $V_m=50$ V

The first two used software to generate a pure sinusoidal. The third one used both actual testing wave-form and software generated wave-form with the same voltage and phase. The reason for using the actual wave-form was to compare with tested results. The other reason was that the actual wave-form was distorted by the transformer. A time step of $0.2\text{x}10^{-3}$(s) was used in the BED time-stepping. The simulated current responses are illustrated in Fig. 3.4. The results have shown that

- There exists a transient process during the first several cycle after switch on
- The current response lags the voltage

These results coincide with our knowledge relating to the response of induction machines.

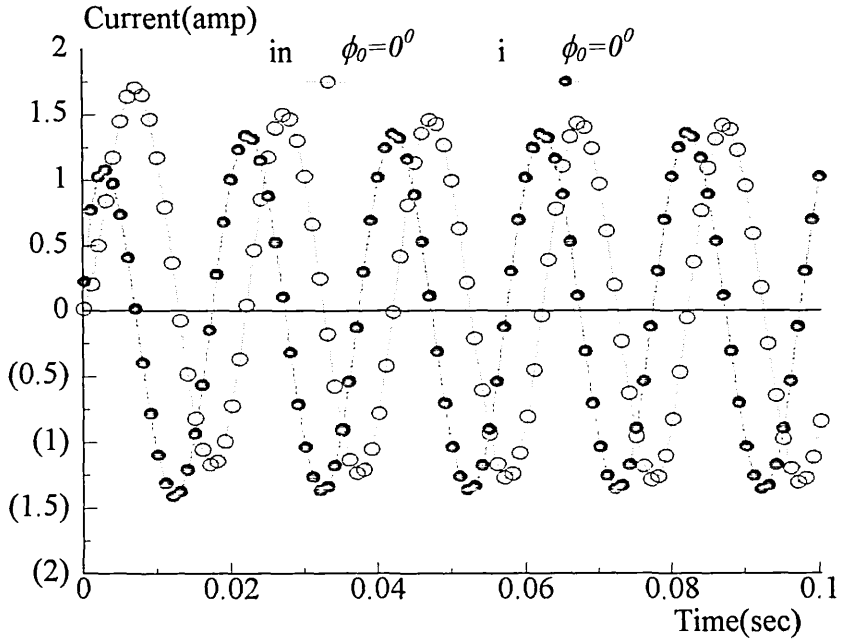


Fig. 3.4(a) The current responses of cases (i) and (ii) with software generated wave-form

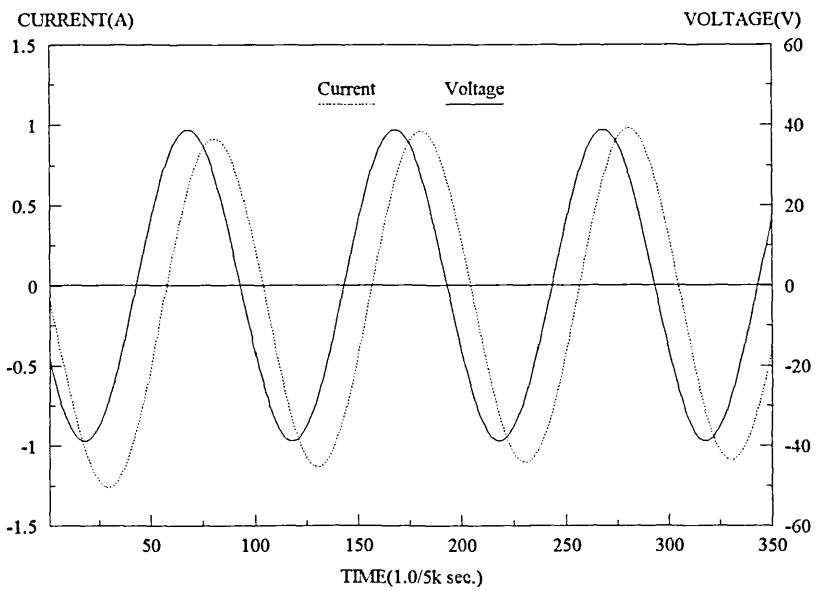


Fig.3.4(b) The current response of cases (iii) with software generated wave-form

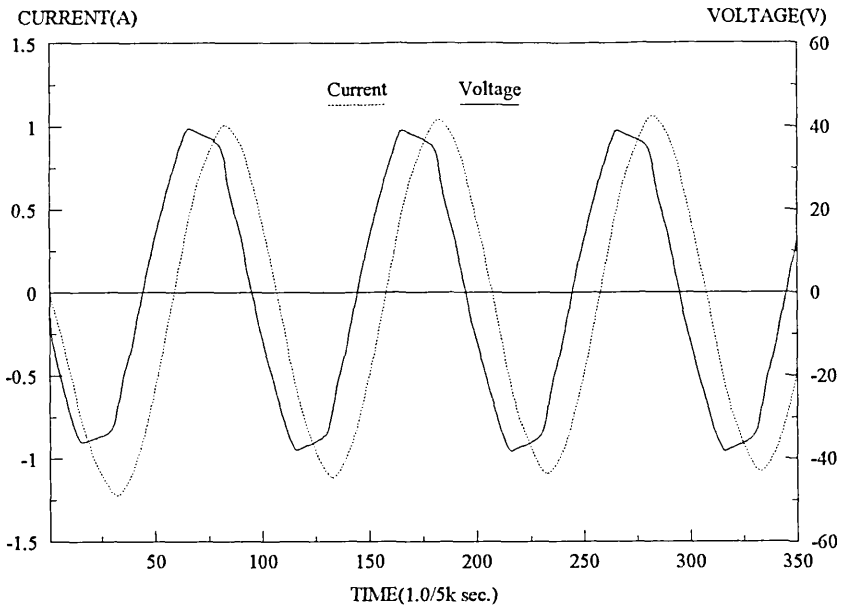


Fig. 3.4(c) The current response of cases (iii) by using the measured voltage

### 3.4.2 Excitation from Switch-mode Power Supply

The second attempt was to simulate the TLIA working with switch-mode power supply. At present the actuator is designed to be driven by two circuits: a triac controlled a.c. line controller and a PWM inverter.

(i) *Triac controller:* As shown in Fig. 3.5, part of sinusoidal voltage is suppled to an actuator under the control of a triac.

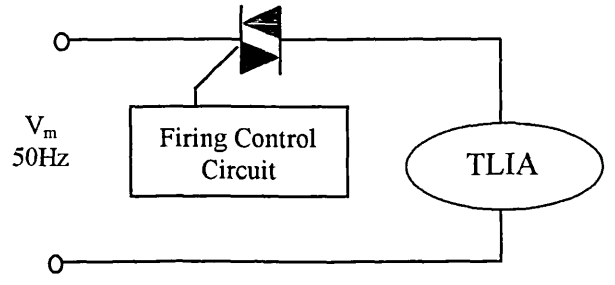


Fig. 3.5 TLIA under the triac control

The following relationships are used for (3.8)

- $u(t)=V_m Sin(2\pi ft+\phi_{tr})-V_{th}$
- $R_{eq}(t)=r$ when the triac is in conducting mode
- $R_{eq}(t)=10^7 r$ when the triac is in inhibited mode

where $V_m$ is the voltage amplitude, $\phi_{tr}$ is the firing phase angle, $V_{th}$ is the voltage drop through the triac in conduction and $r$ is the winding resistance.

Special attention should be paid to $R_{eq}(t)$ when load is inductive, because the triac will be inhibited from conducting only after the current crosses the zero level and before the next triggering pulse arrives. For a fixed time step that is difficult to predict the exact time when the current reaches zero. This is the critical point at which triac will be inhibited. An interpolation or a variable step length is required to calculated the BMF at the time the triac switches from conducting to inhibiting state. We treat this problem by the use of a delayed switch technique which sets the triac to inhibiting state after the current crosses the zero level. When the time step is small, the delayed switching works very well because of the very small time delay of switching of practical components. A large resistance of $10^7 r$ is used to express the triac in the inhibiting mode. As for the voltage drop $V_{th}$, although it is current dependent, its magnitude relative to $V_m$ is small. A constant value of 1.0 volt of $V_{th}$ in conducting mode was used in our computations.

*(ii) PWM controlled DC to AC converter*: A fully controlled bridge with IGBTs and flywheel diodes, as shown in Fig. 3.6, was designed to drive the actuator.

It is assumed that the inductance of the inverter's output filter and the PWM frequency are properly chosen to maintain a continuous current flow between two consecutive PWM pulses. The following two relationships are used in (3.8).

- $u(t)= sign(sin(2\pi ft+\phi_{tr}))(V_{dc}- 2V_{sat})$, when the IGBTs are switched on
- $u(t)= -sign(Sin(2\pi ft+\phi_{tr}))2V_{cl}$, when the IGBTs are switched off

- $R_{eq}(t)$=r

where $V_{sat}$ is the saturated voltage drop on a IGBT, $V_{cl}$ is the voltage clamped by the flywheel diodes.

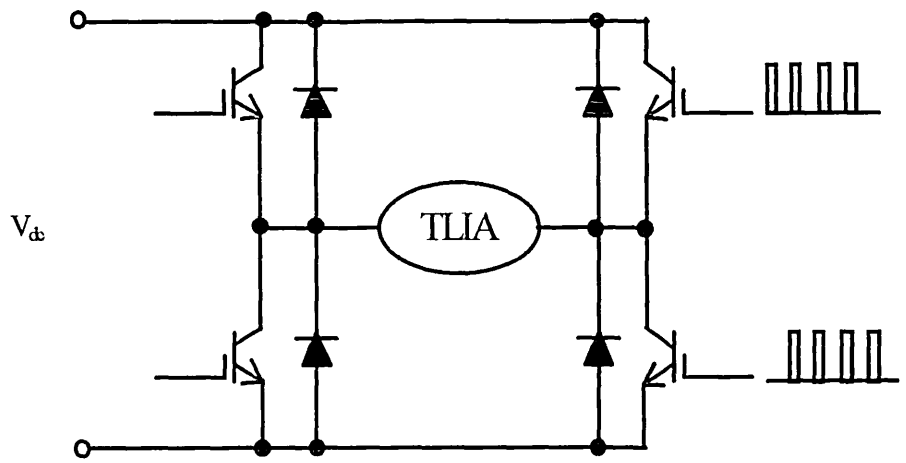


Fig. 3.6. Full bridge PWM controlled TLIA

For more accurate modelling of power semiconductors, classical expressions involving exponential forms can be adopted. However this will lead to complexities in the treatment of the non-linearity in circuits' components. For simplicity we treat this non-linearity as a two switching states with a fixed voltage drop.

Three forms of triac-controlled power supply and one PWM-controlled power supply have been simulated with an equal length of integral time step at $\Delta t=2.5x10^{-5}$ second for a power supply with 50Hz base frequency. The BMF combined with the supplied voltage and the current simulated are shown in Fig. 3.7 ~ Fig. 3.9. Figure 3.7 and 3.8 were simulated in non-linear condition by a TEPL method. Figure 3.9 was simulated by a linear DMVP method just to demonstrate different responses from different power supply.

Finally the transient response of TLIA-1 driven by the PWM circuitry shown in Fig. 3.6 was simulated by the TEPL method as well. The base frequency and the PWM switch frequency were set at 100Hz and 1.5kHz respectively. The duty cycle of the PWM pulse was 0.3 and the switch-on phase angle was $74^0$. A $2.5x10^{-5}$ fixed time step was used, which gives 8 integral steps within the duty period and 19 integral steps in the off-duty period. The responses are given in Fig. 3.10.

In the above simulations whereas TEPL method was used, the saturation level was determined by the instantaneous current value with the setting of $i(P_1)$=0 and $i(P_2)$=2.5 ampere. This setting was based on the study of step response of the actuator. In this case TEPL method based on the DMVP method is sufficient due to the fact that maximum current has not gone beyond the $P_2$ point.

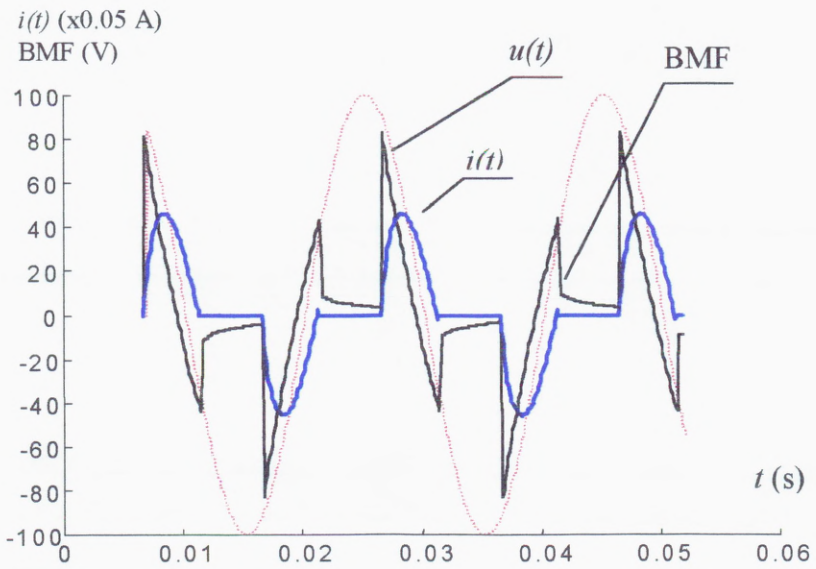


Fig. 3.7 The simulated responses of TLIA-1 under triac controlled sinusoidal voltage supply with the setting: $\phi_0$=0 and $\phi_{tr}$=$120^0$

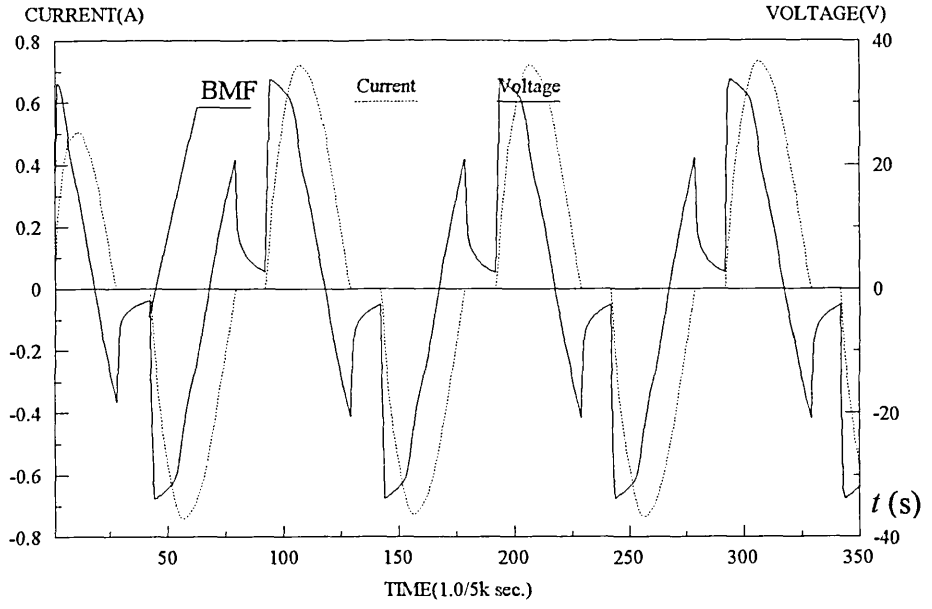


Fig. 3.8 The simulated responses of TLIA-1 under triac controlled sinusoidal voltage supply with the setting: $\phi_0$=115.2$^0$ and $\phi_{tr}$=90$^0$

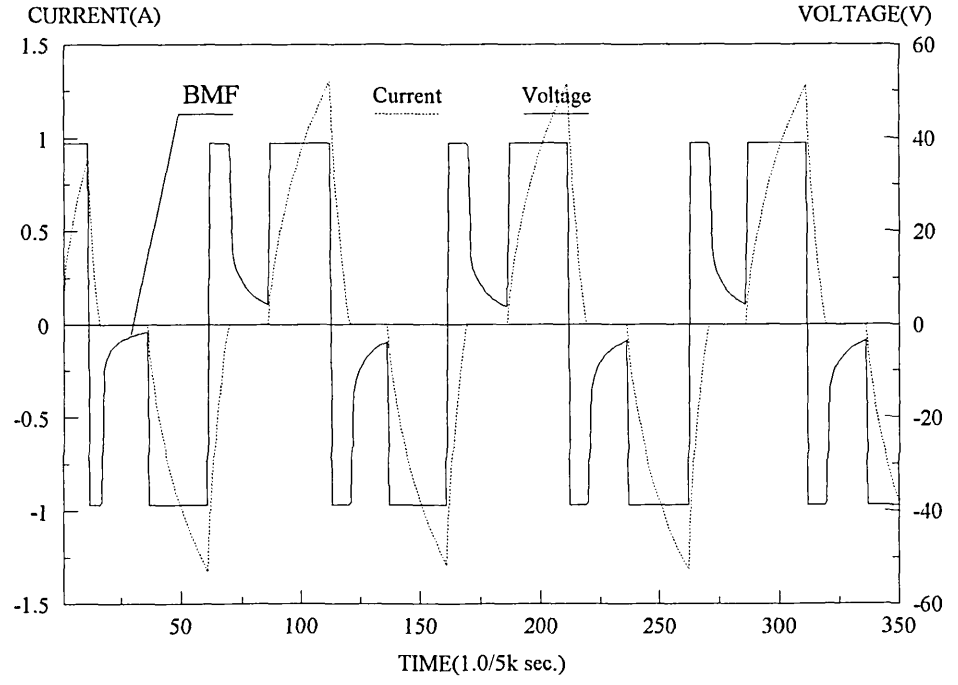


Fig. 3.9 The simulated responses form a actuator with an ideal square wave excitation at $\phi_0$=90$^0$ and $\phi_{tr}$=135$^0$

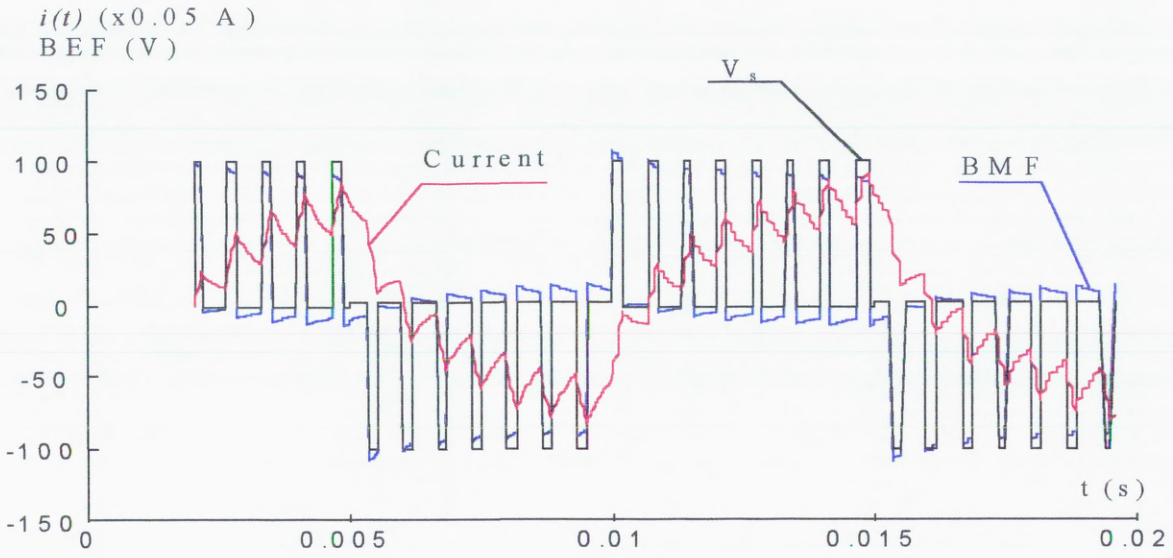


Fig. 3.10 The response of BEF and current of the TLIA under PWM driving

### 3.5 Experimental Investigation

Experimental work was carried out on the TLIA-1 with triac controller. The control circuit designed and constructed uses a 0-5($V_{dc}$) to control the firing phase of the triac. A precision linear potentiometer was used to detect the position of the plunger and to generate a feedback voltage reflecting the position. A TMS320C26 DSP processor served as the central real time controller. The responses of the system were recorded by a digital data acquisition (DAQ) board mounted in a PC. This configuration is illustrated in Fig.3.11.

In the experiment, the supply voltage for the triac circuit was obtained from the 240V mains through a transformer. It was observed that due to the magnetic saturation inside the transformer the output waveform was distorted. To enable more accurate comparison, the real voltage waveform was recorded into a file that was used as the input voltage for the FE simulation.

The experimental work was carried out under standstill conditions, the same condition as the simulation. In this case the closed loop feedback was disabled and the firing phase-delay angle was controlled by a d.c. voltage generated from a D/A converter on the DSP board. Two types of voltage waveforms, the full a.c. one and the triac-control controlled one, were investigated with different switch-on phase and firing phase angles. The transient voltages and currents recorded by DAQ are shown in Fig.3.12 and Fig.3.13.

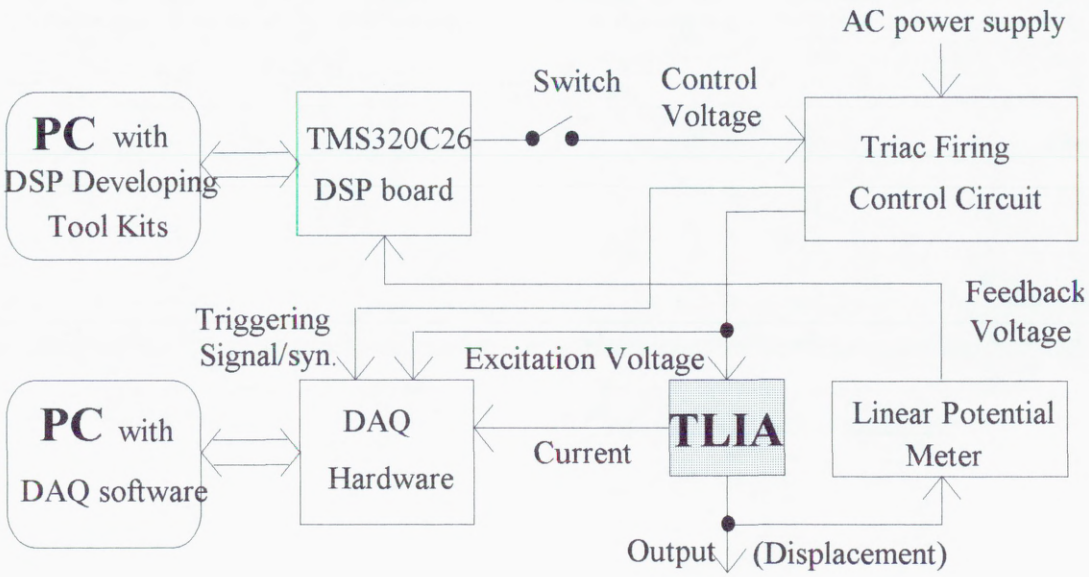


Fig. 3.11 Diagram of test configuration for triac controller

Comparing Fig. 3.12 and Fig. 3.13 with Fig. 3.4(c) and Fig. 3.8 respectively, we will find that the simulated results are very closed to the tested results. The close-up comparison will reveal that the higher relative error happens at low current value. This could be attribute to:

- Ferromagnetic material has higher non-linearity in low flux density.
- Material property used in the simulation is not exactly the same used in the TLIA. The yoke and mandrel of the TLIA are made of common steel whose type was uncertain. Also the magnetic hysteresis has been neglected.
- Mathematically, the same absolute error will give higher relative error in low value than in high value.

According to our understanding, the simulation can be further improved if material properties are modelled more accurately along with proper settings of $i(P_1)$ & $i(P_2)$ level and the interval of time stepping.

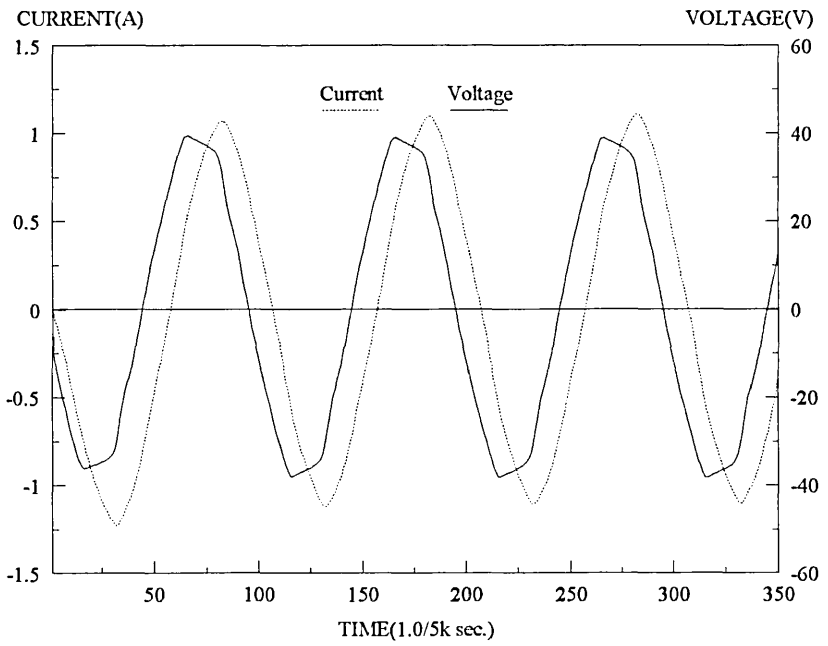


Fig. 3.12 The tested wavesforms of current and terminal voltage at $\phi_0$=314$^0$ without triac control

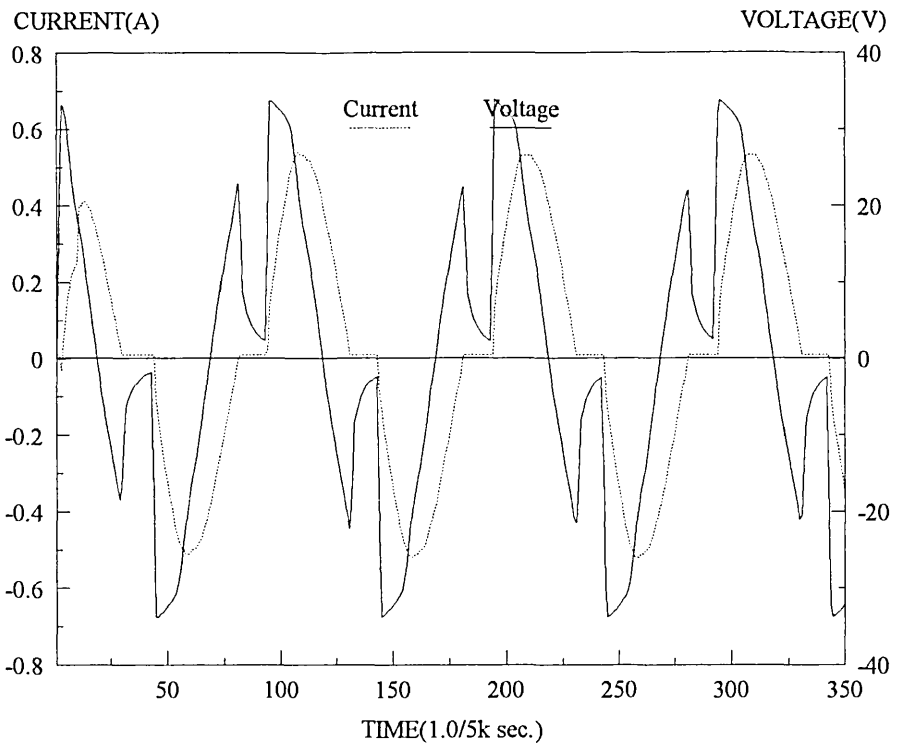


Fig.3.13 The tested wave forms of current and terminal voltage under triac controlled sinusoidal excitation at $\phi_0$=115.2$^0$ and $\phi_{tr}$=90$^0$

## 3.6 Conclusions

A DMVP method indirectly coupling external circuits has been proposed and studied in this chapter. This method was initially derived from the time-stepping BED form in linear cases. It was then extended to non-linear cases under which other two sub-methods the TEPL method and the combined method have been developed as well. The main advantages that the proposed methods can claim could be summarised as

- Particularly suitable to switch-mode operation in which very fine time-step and huge discrete integration are involved.
- Fast solution to eddy current problems under voltage driven conditions and requiring coupling external circuit equations
- Flexibility to deal with complicated external drive circuit equations

- High potential for parallel computation

Its major problems could be the accuracy and speed in highly non-linear cases, which could be the topic of future research.

Two numerical experiments have been carried out to verify the effectiveness of the proposed method. One is on the CPU comparison between DCM and ICM. The other is on the error's comparison among four methods. Those comparisons provide a sound foundation to implement the proposed method confidently. This method has been applied to simulate the actual TLIA under different forms of excitations to demonstrate its capability. Finally some of the simulated responses have been compared with the response recorded in the designed experiments by using DAQ technique. A good agreement between the tested and simulated results has been obtained. It will be interesting as a further research topic to look into its application in parallel computation and in modelling hysteresis.

# 4 CALCULATION OF ELECTRO-MAGNETIC FORCE

## 4.1 Introduction

The TLIAs are electromechanical devices to produce force. This is the major reason for their existence. Consequently, the evaluation and computation of mechanical forces produced by these devices becomes the major concern in their design and analysis. Therefore the accurate determination of forces becomes extremely important for evaluating a design and predicting the performance.

In computer aided analysis of electromagnetic devices, the force calculation is usually carried out in the post-processing stage of FE analysis package, if no dynamic mechanical movement is involved in the analysis. Since the force calculation by FEM will inevitably involve errors, efforts have also been directed to the investigation of force calculation in parallel with the development of the CAD tools.

There are several methods that can be used to compute the electromagnetic forces [47~53]. No matter which method is used, the results should be very close for the same design. In the practical application of FEM, the various methods may give answers with considerable difference, due to the approximation property of numerical methods [47,52]. Usually, FEM employs auxiliary potentials as a media to assist the numerical computation of electromagnetic fields in low and medium frequency range. Using direct field variables (**B**, **H** or **I**) will bring more difficulties in the determination of boundary conditions for numerical analysis. This entails more accuracy problems in force computation than in the computation of field quantities and the auxiliary potentials. From

the numerical point of view, accuracy problems associated with force calculation could be caused by elemental discretisation (ED), elemental interpolation (EI) and integral path (IP) [49].

Computation of forces in electromagnetic devices is usually carried out by three methods: Maxwell's stress tensor based method (MSTBM), virtual work principle (VWP) and Lorenz force formula (LFF). In addition to the standard Maxwell's stress method several subclass methods can be derived from the MSTBM, such as the equivalent current method and the equivalent magnetic charge method. The LFF is implemented only over the current-carrying regions and thus may involve little calculation. Its advantage is also its disadvantage: it can not be employed to calculate forces on magnetic objects. Therefore the LFF is of limited use. The MSTBM and VWP are the first choice in most applications, due to their universal suitability. The MSTBM is particularly attractive when local force on ferromagnetic materials is required. However, the MSTBM suffers accuracy problems in numerical computation as reported by many researchers.

To improve the accuracy of force calculation, several remedies have been found to tackle the problem from different angles, which can be summarised as:

(i) Improvement of the computation accuracy of auxiliary potential by using higher order element [47], or element refinement technique [48].
(ii) Improvement of the calculation accuracy of the field quantities by using dual potential method [49].
(iii) Improvement of the accuracy of the field quantities by employing error cancellation techniques, such as the mean-difference potential (MDP) method [50] and discretised current sheet (DCS) method [51].
(iv) Implementation of force integration along appropriate path [52], plus correction of field quantities by using extrapolation or weighted factor techniques [53].

The first two groups of methods can, without doubt, improve the accuracy of potential and thus the accuracy of forces, but more computer resource in terms of CPU time and storage will be required. The MDP method is suitable in virtual work principle (VWP)

and also requires solutions of the FE equation twice. Although it is claimed that DCS method has the accuracy of analytical methods and path-independence, it may suffer slow convergence problem in non-linear cases. As for the last group, the main task of correcting the field still remains a problem. Except the DCS method and the VWP method, all the other methods are more sensitive to the integral path. Despite the abundance of practical results and computational techniques to improve the accuracy of force calculation, rigorous analysis and definitive conclusion are still lacking.

In this chapter the MSTBM is investigated against its sensitivities in FE application. A method is proposed to improve the accuracy in volume force calculation. Comparisons will be given to demonstrate the effectiveness of the proposed method.

## 4.2 The MSTBM

According to the standard Maxwell's stress method, the total force acting on a closed surface '*s*' encompassing a volume can be obtained by the integration of

$$\vec{F} = \oiint_s \vec{\vec{\mathbf{T}}} \cdot d\vec{s} \tag{4.1}$$

where $\vec{\vec{\mathbf{T}}}$ is the Maxwell's stress tensor with terms given by,

$$\vec{\vec{\mathbf{T}}}\Big|_{x,y,z} = \begin{bmatrix} B_x H_x - BH/2 & B_x H_y & B_x H_z \\ B_y H_x & B_y H_y - BH/2 & B_y H_z \\ B_z H_x & B_z H_y & B_z H_z - BH/2 \end{bmatrix} \tag{4.2}$$

Because the $\vec{\vec{\mathbf{T}}}\Big|_{x,y,z}$ is a symmetric tensor, it can be transformed to the local axis [$\vec{n}$, $\vec{t}_1$, $\vec{t}_2$] with $\vec{n}$ directed in parallel with $\vec{\mathbf{B}}$. In this case, $\vec{\vec{T}}$ is a diagonal tensor that has the form of

$$\vec{\vec{\mathbf{T}}}\Big|_{n,t1,t2} = \begin{bmatrix} BH/2 & 0 & 0 \\ 0 & -BH/2 & 0 \\ 0 & 0 & -BH/2 \end{bmatrix} \tag{4.3}$$

The local surface force density can be derived from the (4.3), which gives

$$f_n = \frac{dF_n}{dS} = \frac{1}{2\mu}(B_n^2 - B_t^2) \tag{4.4a}$$

$$f_t = \frac{dF_t}{dS} = \frac{1}{\mu} B_n B_t \tag{4.4b}$$

### 4.3 Analysis of Error Sources in Force Calculation

From either (4.2) or (4.4), it can be seen that the accuracy of $\vec{F}$ is directly linked with the accuracy of $\boldsymbol{B}$ and $\boldsymbol{H}$ instead of any auxiliary potential. Given that $\boldsymbol{B}$ and $\boldsymbol{H}$ are calculated from auxiliary potential, we can attribute errors in the calculated force to three sources. They are

(i) Errors caused by inaccurate solution (IS) of the large simultaneous equations
(ii) Errors introduced in potential approximation (PA) in the interpolation.
(iii) Errors introduced from field approximation (FA) by the differentiation of the potential

The IS-error is caused by the truncation error stemming from the computer hardware, the algorithm, and the associated error spreading inside algorithms. The only effective means to reduce this error is to choose sufficient length of digital number. It is realised that truncation error will spread into the final solution. The practical experience tells us that the IS-error could be neglected when proper length of digital number is used.

The PA-error cannot be avoided except in some simple cases involving homogeneous field distributions. To reduce the PA-error, higher order element and mesh refinements are the commonly used techniques.

The FA-error discussed here is defined as the error rising from the mathematical implementation of numerical differentiation to the interpolated potential. It is different from the PA-error although PA-error will be passed to the FA-error. Since the interpolation is an approximation to the actual distribution, the error reflected in field

quantities (**B**, **H**) could come from both the PA-error and the FA-error. So, even if exact potentials are obtained, error will still exist in the field calculation from potential interpolation.

### 4.4 Path-dependency of Force Calculation

It is observed that different integral path will give different force value in FE analysis. Equivalently the error in force calculation is path-dependent. For simplicity, a triangular element is used here to investigate the mechanism behind this phenomenon.

When hysteresis is neglected, Maxwell's stress method implies that the integration of (4.1) must be zero if the force integration is carried inside a single source-free material. We can separate the integration into two terms defined as

$$\begin{aligned} \vec{F}^e &= \oiint_{s^e} \vec{\mathbf{T}} \cdot d\vec{s} \\ &= \oiint_{s^i} \vec{\mathbf{T}} \cdot d\vec{s} + \oiint_{s^b} \vec{\mathbf{T}} \cdot d\vec{s} \\ &= \vec{F}_i + \vec{F}_b \\ &= 0 \end{aligned} \tag{4.5}$$

where $s^e = s^i + s^b$. We choose $s^i$ as part of $s^e$ plus one elemental edge and $s^b$ as two elemental edges, as shown in Fig. 4.1. Accordingly the first and second integral terms are denoted by $\vec{F}_i$ and $\vec{F}_b$ which are defined as interior error and boundary errors respectively. For permanent magnets, the remnant magnetic flux density or coercive force is naturally caused by magnetic hysteresis, therefore (4.5) can not be applied directly. However (4.5) will be applicable if a proper treatment (such as the equivalent magnetic charge method or the equivalent current sheet method) is given.

As is well known that FEM can strictly satisfy only one of the two interface conditions imposed by the Maxwell's electromagnetic theory, which are

$$B_{n1} = B_{n2} \tag{4.6}$$

$$H_{t2} - H_{t1} = J_s \tag{4.7}$$

where $J_s$ is the current sheet density on the interface. For instance, when the magnetic vector potential method is used, only (4.6) is strictly satisfied; and when the magnetic scalar potential method is used, only (4.7) is strictly satisfied. Therefore the $\vec{F}_b$ would not be zero even if $\mu_1 = \mu_2$ and $J_s = 0$.

As for the term $\vec{F}_i$, its path-dependency is dependent upon the interpolation or the shape function of the potential. Mathematical rule tells us that the sufficient condition of integral path-independence of (4.1) is

$$div\vec{\vec{T}} = 0 \tag{4.8}$$

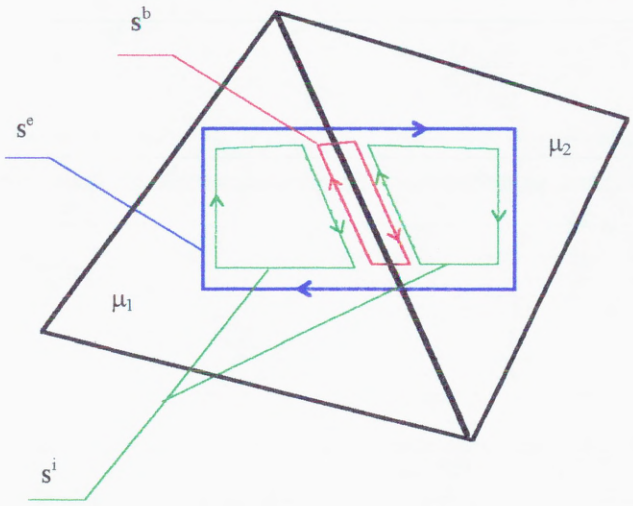


Fig. 4.1 Illustration of integral path

For the first order Lagrangian elements, (4.8) can be satisfied, however, with the loss of accuracy of field (**B**, **H**) distribution. This rough field distribution consequently brings larger error in $\vec{F}_b$. Higher order elements allow field changes more smoothly within elements and on borders, but the relationship of (4.8) is usually not satisfied - at least we are not aware of any reported work that uses higher order shape function which takes account of the constraint (4.8). The fact that either $\vec{F}_i$ or $\vec{F}_b$ is not zero is the cause of the path-dependency in force calculation.

## 4.5 Analysis of the Field Calculation Error

As mentioned before, the FA-error is another source causing error in addition to the PA error. Usually, we will think the differentiating operation in **B&H** will enlarge the error in auxiliary potential. This is largely based on our intuition. Because of the complicated nature of the errors caused by both the potential interpolation and the discretised differentiation, this intuition may be true, subjected to some conditions that will be discussed later. From our literature survey, it seems that few researchers have studied the relationships of error spreading among the mathematical implementations of force calculation [47-56].

Here we will tackle the problem from some basic mathematical operation involved in FE analysis. Assuming that a solution has been obtained in terms of the potential **A**, we calculate a FD form of differentiation inside an element along the direction *'q'* as,

$$\left.\frac{\partial A_c}{\partial q}\right|_{q0=\frac{q1+q2}{2}} \cong \frac{(A^*_{c,q2} - A^*_{c,q1}) + (\varepsilon_{q2} - \varepsilon_{q1})}{\Delta q} \tag{4.9}$$

where the superscript '*' denotes the exact value, $\varepsilon$ denotes the error in the potential component $A_c$, $q_1$ and $q_2$ are the two nodes defining the direction $q$. This is a basic discretised form to calculate differentiation which is required to obtain **B&H** from **A**.

Equation (4.9) can be also considered as a mathematical model of a differential amplifier in electronics. As we know, a differential amplifier will reject common-mode (CM) error ($\varepsilon_{q1}*\varepsilon_{q2}>0$) and amplify the differential-mode (DM) error ($\varepsilon_{q1}*\varepsilon_{q2}<0$). So if the error in the potential is of common-mode, the error in **A** will be partly cancelled in (4.9) under the assumption of continuous **A**. The assumption is generally acceptable if we do not take any idealised models which use equivalent current sheet to replace massive current distribution. Particularly the differentiation will be better calculated at the middle point $q_0$, due to the fact that central difference form has one order higher of truncation errors than non-central ones. The $\dot{A}_c|_{q0}$ can also serve as a good approximation of the average value of $\dot{A}^*_c|_{q1\sim q2}$ due to the natural continuity of potential A*. Our observation shows

that vast majority of elements have CM errors in potential at the vertex of each element, at least for the examples we have studied. Here what we can provide as evidence are the examples in section 4.6. The strictly mathematical proof of universal or conditional applicability is another challenging topic in any future work.

For elements that have DM errors on elemental vertex, the absolute value of potential's error will be much smaller than those of other elements with CM errors, due to the basic continuity assumption of potential and the natural continuity of the field if no current sheet is involved. Therefore it is reasonable to consider that the differentiation at the midpoint $q_0$ will be more accurate than the potential itself. We call such points as Relatively Optimal Gauss Sampling Points (ROGSP). So, we can postulate that

- On average the fields **B** and **H** at ROGSP are closer to the exact values than at other points.
- The differential mode errors play a less important role in the calculation of **B** and **H** than the common mode errors

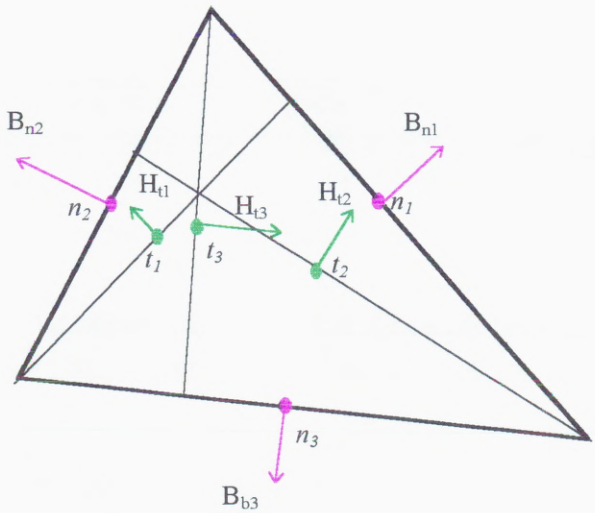


Fig. 4.2 ROGSP for $B_n$ and $H_t$ for a triangular element

For the 2D triangular elements using magnetic vector potential, $B_n$ is best approximated at the midpoints on each element edge and the relevant $H_t$ is best approximated at midpoints of their altitude. Referring to Fig. 4.2, points $n_1$, $n_2$, and $n_3$ hold the best average $B_n$ values and points $t_1$, $t_2$ and $t_3$ hold the best average $H_t$ values. It is obvious that the ROGSPs for $B_n$ and $H_t$ are not located at the same point, so it is not possible to choose an integral path with ROGSPs for both $B_n$ and $H_t$ in the same location, which is vital to reduce the error in the integration of Maxwell's stress.

Because the vast majority of elements have CM error, we can design a scheme to take advantage of this in force computation.

### 4.6 The Proposed Method

Since the ROGSPs of $B_n$ are located at the midpoints of the element edges for MVP, we propose the following scheme to carry out the stress integration:

- Chose an arbitrary integration path
- Calculate the $B_n$ on the ROGSP of each edges
- Calculate the corrected $H_t$ at the same ROGSPs as $B_n$
- Calculate $\vec{F}_T$, $\vec{F}_i$, $\vec{F}_b$ and $\vec{F}$ according to the following formula

$$\begin{aligned}\vec{F} &= \vec{F}_T - \vec{F}_i - \vec{F}_b \\ &= \sum_{l=1}^{E^T} \vec{F}_T^{\,l} - \left(\sum_{m=1}^{E^i} \vec{F}_i^{\,m} + \sum_{n=1}^{S^b} \vec{F}_b^{\,n}\right)\end{aligned} \tag{4.10}$$

where

$E^T$: All the elements completely encompassed inside the integral loop plus parts of elements that are partially encompassed in the integral loop

$E^i$: Elements having non-zero $\vec{F}_i$ and those elements that are cut by the integral path

$S^b$: The border joining two elements with same material, except those elemental borders that is part of the integral path

$\vec{F}_T^{\,l}$: Integration of Maxwell's stress along the entire border of element $l$ in $E^T$

$\vec{F}_i^m$: Integration of Maxwell's stress along all the border of element $m$ in $E^i$

$\vec{F}_b^n$: Integration of Maxwell's stress along the border $n$ in $S^b$

Equation (4.10) comes out as the results of the study of section 4.5 where we found that the non-zero $\vec{F}_i$ and $\vec{F}_b$ is the cause of path-dependency. So we can eliminate them by deducting them from the total force. The above scheme is for an arbitrary integral path. If the integral path is chosen along elemental border, $\vec{F}_i$ can be avoided, which makes the calculation simpler.

Under the assumption of using MVP, which mean that $B_n$ is continuous on the edge and that $B_n$ at the ROGSPs can be calculated straight forward, the remaining task is to find a good approximation of $H_t$ at the same locations of ROGSPs of $B_n$. For any element, there are four possible positions of the elemental edges that should be considered in correcting $H_t$. They are

(i) Edge on the boundary of the whole region to be solved
(ii) Edge belongs to element with massive current inside
(iii) Edge joining two elements with the same material
(iv) Edge joining two elements with magnetic material and non-magnetic material respectively

Case (i) can be treated by the direct boundary condition constraints used in solving the potentials. Cases (ii) and (iii) imply that the potential is continuous. To get a continuous $H_t$ on the element edge, we propose to use higher order secondary interpolation involving all the vertices of the two elements joined at the edge. As shown in Fig. 4.3, the secondary interpolation could be a quadratic function consisting of the potentials at nodes 1,2,3 and 4 for the edge $L_{12}$. With this interpolation it is possible to construct local meshes to have the ROGSP of $H_t$ located at the same position of the ROGSP of $B_n$, which requires

- Line $L_{34}$ goes through the middle point M of $L_{12}$,
- $L_{3M}$ equals $L_{4M}$

This turns out that the adjacent triangle forms a parallelogram. Even if the above conditions are not satisfied, a better $H_t$ on $L_{12}$ can still be expected with the higher order secondary interpolation.

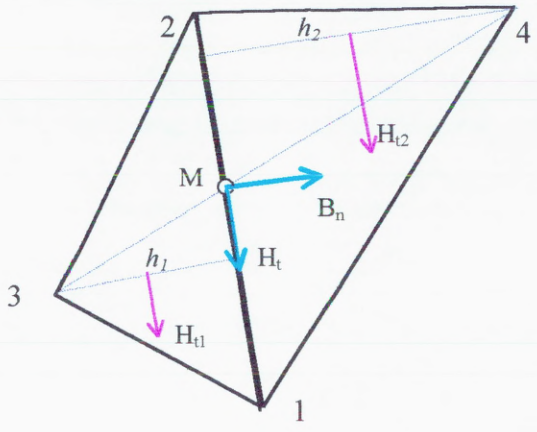


Fig. 4.3 Calculating $H_t$ on $L_{12}$ by using high order interpolation using all the vertices 1 to 4

For case (iv), the magnetic permeability changes abruptly at the joining border and $H_t$ may also change dramatically after entering/leaving magnetic material. The higher order secondary interpolation method does not work effectively. In this case we propose to use an equivalent magnetic circuit to correct the $H_t$ . As shown in Fig. 4.4, the corrected $H_t$ will be

$$H_t = H_{t1} + \frac{H_{t2} - H_{t1}}{R_2 - R_1} R_1 \tag{4.11}$$

with the magnetic reluctance $R$ is approximated by

$$R = \frac{2h}{\mu L}$$

where '$h$' is the altitude on the border and '$L$' is the length of the border.

By now we have only used MVP in triangular element to explain the scheme. For magnetic scalar potential method, the scheme needs just swapping $H_t$ and $B_n$. It can be easily extended to other elements and to three-dimensional cases. The proposed scheme improves the accuracy from low level or fundamental principle. Other high level methods belonging to (i) of section 4.1 can still be applied in conjunction the proposed method to get better results.

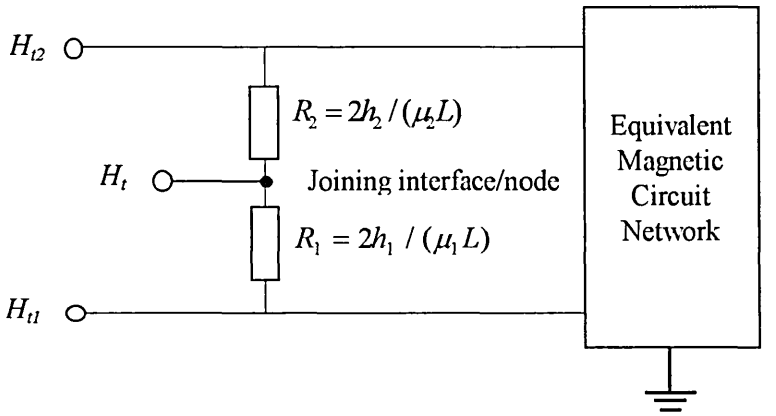


Fig. 4.4 Equivalent Magnetic Circuit for Correcting $H_t$

## 4.7 Computational Experiment

To verify the effectiveness of the proposed method, three examples are investigated. Two of them have analytical solutions, so comparisons can be made directly. And the third one is a relatively complex structure to provide further demonstration without loss of generality. The numerical approximation uses 2D FEM with magnetic vector potential and triangular elements.

The first example is a massive conductor in a slot as shown in Fig. 4.5. Two current carrying conductors with rectangular cross section are placed in the slot so that different combinations of excitation can be examined. This problem has an analytical solution with

the following boundary conditions:

$$B_n\big|_{s1,s2,s3} = 0$$

$$A\big|_{s4} = 0$$

Appendix C gives the analytical solution of potential $A_z$. For this problem, the accuracy in the force calculated by FEM and its sensitivity to integral path were studied. The following factors were investigated

(i) Excitations: two excitations, the same and the opposite directions of currents in the two conductors.

(ii) Mesh size: three levels of discretisations with ratios of node/element at 2177/4168, 517/1048 and 225/392

(iii) Integral loop: two arbitrary integral loops as shown in Fig. 4.5

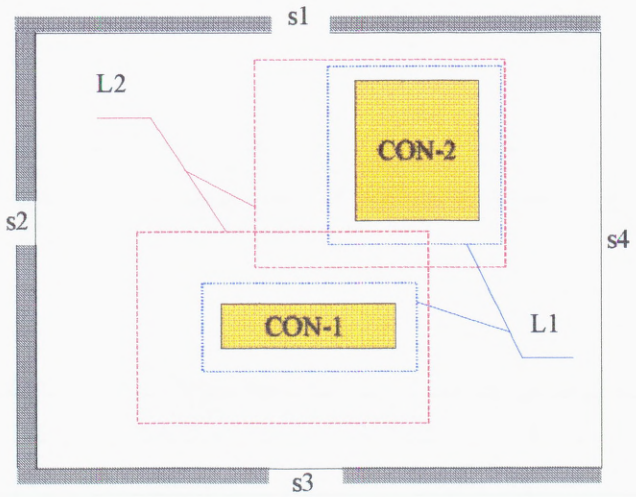


Fig. 4.5 Configuration of the first example

The comparison of force calculation is given in Table-4.1. The results show that the proposed method provides better and more stable accuracy than the standard Maxwell's stress method, and is independent of integral path. In very rough mesh discretisation as in the case of Mesh-C, good accuracy can still be retained.

The contours of local relative errors of potential have been shown in Fig. 4.6 and Fig. 4.7 respectively for two excitation conditions. The relative error is defined as

$$relative\_error = \frac{exact\_value - FEM\_value}{abs(exact\_value)}$$

It can be seen that the positive error contours and negative error contours seldom cross each other. This suggests that the potential errors on elemental vertices are CM errors for the majority of elements. Therefore the errors that appeared in the potential will partially counteract in the differentiation of field solution (**B**, **H**).

The second example concerns an air-iron interface with limited magnetic permeability as shown in Fig. 4.8. Two cases with relative magnetic permeability values of 1000 and 50 have been investigated. The analytical solution is

$$A_z\big|_{x>0} = -\frac{\mu_1 i}{4\pi}\left\{\ln[(x-x_0)^2+y^2]+\frac{\mu_2-\mu_1}{\mu_2+\mu_1}\ln[(x+x_0)^2+y^2]\right\}$$

$$A_z\big|_{x<0} = -\frac{\mu_1\mu_2 i}{2\pi(\mu_2+\mu_1)}\ln[(x-x_0)^2+y^2]$$

Because this is an open boundary problem, the boundary conditions required in FE analysis were imposed by using the analytical results. Therefore the boundary errors are eliminated completely. The error caused in the FE solution stemmed only from the discretisation and interpolation. The comparisons between different methods are given out in Table-4.2. Again better force accuracy and integral path-independence were obtained. The contour of relative error is given in Fig. 4.9, which also supports our previous analysis that arrives at a conclusion that elemental potential errors are mostly of the common-mode type.

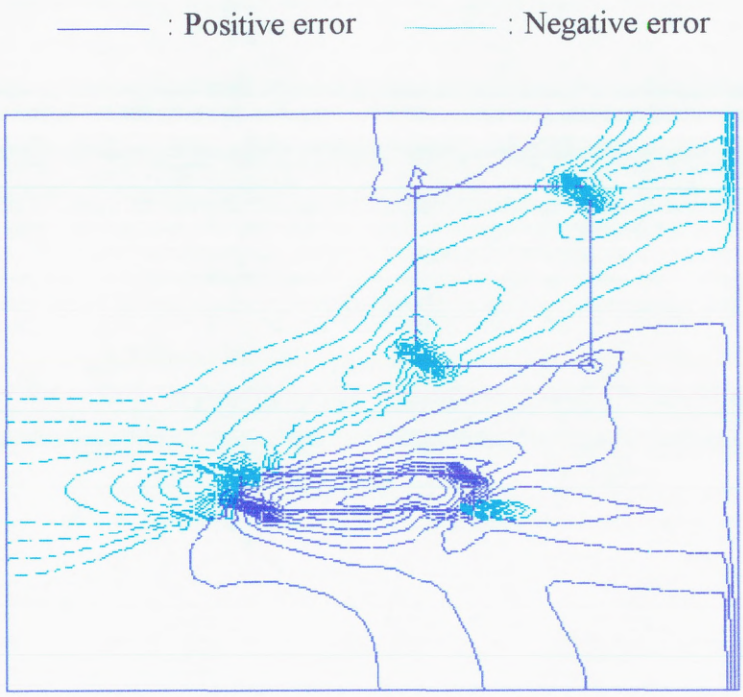


Fig. 4.6 Contour plot of relative errors for Case-I with $J_a=J_b=1.0x10^7$ A/m$^2$

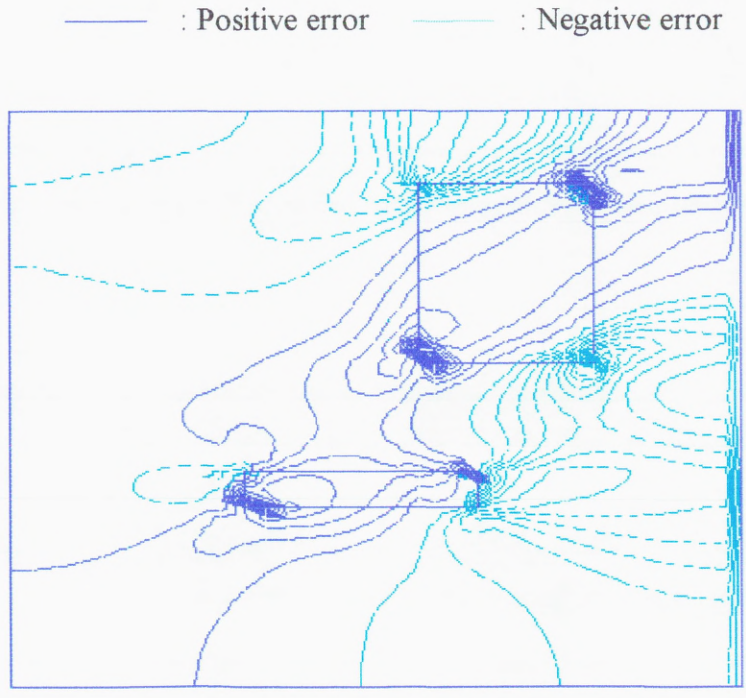


Fig. 4.7 Contour plot of relative errors for Case-II with $J_a=-J_b=1.0x10^7$ A/m$^2$

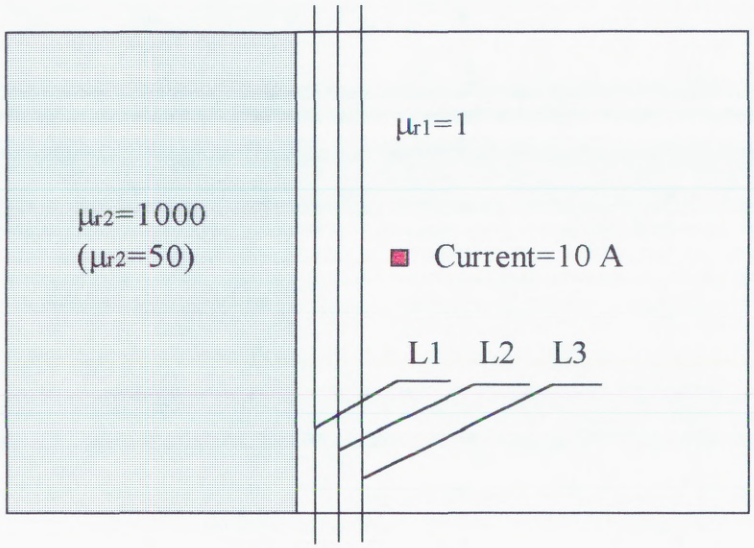


Fig. 4.8 Configuration of Example-2

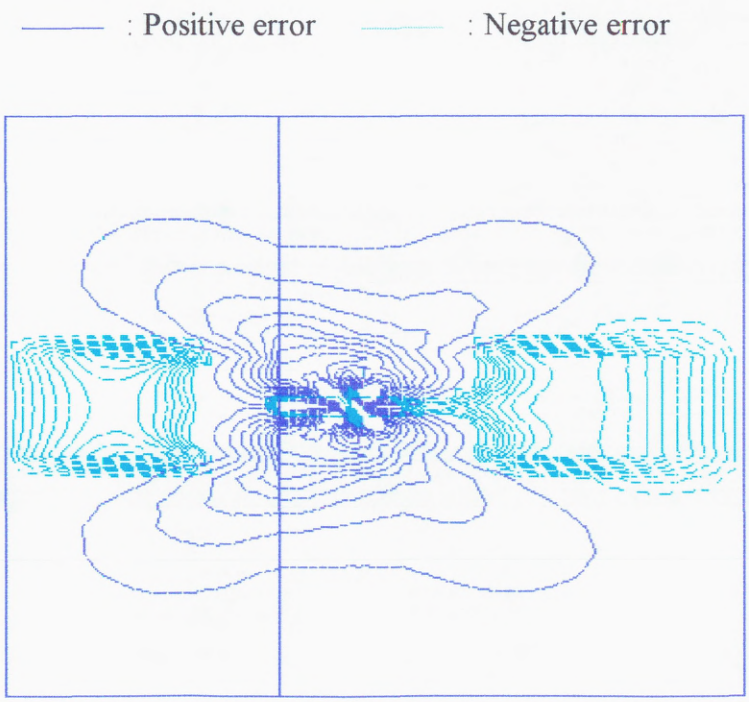


Fig. 4.9 Contour plot of relative error for Example-2

Table-4.1a: Force comparison for Case-I with the excitation current density of $J_{con-1}=J_{con-2}=1.0x10^7$ A/m$^2$

| | Loop | Mesh | Force (N) Conductor-1 | | Force (N) Conductor-2 | |
|---|---|---|---|---|---|---|
| | | | Standard Maxwell | Proposed Method | Standard Maxwell | Proposed Method |
| $F_x$ | L1 | A | -1.2954 | -1.3601 | -10.830 | -11.005 |
| | | B | -1.5017 | -1.3547 | -10.947 | -10.939 |
| | | C | -1.4797 | -1.3650 | -11.097 | -10.959 |
| | L2 | A | -1.3926 | -1.3601 | -10.900 | -11.005 |
| | | B | -1.3226 | -1.3547 | -11.584 | -10.939 |
| | | C | -1.4241 | -1.3650 | -10.883 | -10.959 |
| $F_y$ | L1 | A | 0.91837 | 0.94860 | 0.88284 | 0.9790 |
| | | B | 1.0328 | 0.94541 | 0.95232 | 0.9485 |
| | | C | 1.0313 | 0.95512 | 0.96325 | 0.9932 |
| | L2 | A | 0.97358 | 0.94860 | 0.93678 | 0.9790 |
| | | B | 0.92618 | 0.94541 | 1.10669 | 0.9485 |
| | | C | 0.98712 | 0.94542 | 1.07649 | 0.9932 |
| Exact $F_x^*$ | | | -1.3619469 | | -11.005910 | |
| Exact $F_y^*$ | | | 0.949808417 | | 0.974973973 | |

Mesh-A: 2177 nodes, 4168 elements

Mesh-B: 517 nodes, 1048 elements

Mesh-C: 225 nodes, 392 elements

Table-4.1b: Force comparison for Case-II with the excitation current density of $J_{con-1}=-J_{con-2}=1.0x10^7$ A/m$^2$

| | Loop | Mesh | Force (N) Conductor-1 | | Force (N) Conductor-2 | |
|---|---|---|---|---|---|---|
| | | | Standard Maxwell | Our Method | Standard Maxwell | Our Method |
| $F_x$ | L1 | A | -1.1724 | -1.2093 | 2.8790 | 2.8805 |
| | | B | -1.1589 | -1.2099 | 2.6092 | 2.8381 |
| | | C | -1.1935 | -1.2124 | 3.0712 | 2.8953 |
| | L2 | A | -1.1821 | -1.2093 | 2.8432 | 2.8805 |
| | | B | -1.1521 | -1.2099 | 2.7802 | 2.8381 |
| | | C | -1.1731 | -1.2124 | 2.9220 | 2.8953 |
| $F_y$ | L1 | A | 0.25639 | 0.26017 | -5.9541 | -5.9094 |
| | | B | 0.21611 | 0.25758 | -5.7798 | -5.8493 |
| | | C | 0.24264 | 0.24879 | -6.0810 | -5.8464 |
| | L2 | A | 0.23825 | 0.26017 | -5.9265 | -5.9094 |
| | | B | 0.19121 | 0.25758 | -5.8632 | -5.8493 |
| | | C | 0.22666 | 0.24879 | -6.1039 | -5.8464 |
| Exact $F_x$ | | | -1.2094520578 | | 2.8789663465 | |
| Exact $F_y$ | | | 0.26092882321 | | -5.9119005850 | |

Mesh-A: 2177 nodes, 4168 elements

Mesh-B: 517 nodes, 1048 elements

Mesh-C: 225 nodes, 392 elements

Table-4.2: Comparison of force calculation for Example-2

| | | $F_X$ (N x$10^{-3}$) | | |
|---|---|---|---|---|
| Case | Loop | Standard Maxwell | Proposed Method | Analytical |
| A | L1 | -1.9726 | -2.0146 | 2.01458 |
| | L2 | -2.0167 | -2.0146 | |
| | L3 | -2.8158 | -2.0146 | |
| B | L1 | -1.8880 | -1.9595 | -1.90333 |
| | L2 | -1.9370 | -1.9595 | |
| | L3 | -2.1926 | -1.9595 | |

Case-A: $\mu_r$=1000

Case-B: $\mu_r$=50

Discretisation: 1472 nodes and 2790 elements

The error contour plots of Fig. 4.6 and Fig. 4.7 also reveal that the maximum error points and maximum error gradient occur at the corners of the conductor. And Fig. 4.9 reveals that those points will occur at the interface between ferromagnetic material and air in addition to the corners of the conductor. So, in addition to choosing the integral path far from the iron as recommended by some authors, we should add that the integral path should be far away from current source as well when implementing the standard Maxwell's stress integration.

Finally a more practical problem of an attractive levitation magnet, shown in Fig. 4.10, has been studied. Three discretisation schemes and two integral paths have been investigated. Because of the lack of exact solution, the most accurate value was considered as that obtained from the integration through the centre line in the air gap under fine mesh discretisation. The results are compared in Table-4.3, which again validates the effectiveness of the proposed method.

Table-4.3 Forces obtained by different methods for Example-3

| Loop | Dir. | Mesh | Force (N) | | | |
|---|---|---|---|---|---|---|
| | | | Standard Maxwell | Method-2 | Method-3 | Proposed Method |
| L1 | $F_x$ | A | 27.146 | 36.961 | 25.604 | 26.637 |
| | | B | 24.442 | 37.092 | 24.761 | 25.479 |
| | | C | 22.871 | 38.023 | 23.174 | 23.535 |
| | $F_y$ | A | -123.64 | -131.79 | -121.94 | -123.37 |
| | | B | -121.55 | -131.22 | -115.63 | -120.47 |
| | | C | -120.80 | -126.62 | -111.42 | -114.71 |
| L2 | $F_x$ | A | 28.707 | same as L1 | | |
| | | B | 29.962 | | | |
| | | C | 23.954 | | | |
| | $F_y$ | A | -124.21 | | | |
| | | B | -123.66 | | | |
| | | C | -113.33 | | | |
| Compared force $F_x^*$ | | | | 26.9135 | | |
| Compared force $F_y^*$ | | | | -123.690 | | |

Case-A: 8594 nodes, 16818 elements

Case-B: 2008 nodes, 3838 elements

Case-C: 550 nodes, 1008 elements

Method-2: Integration of Maxwell's stress on the air-iron boundary with standard method to calculate $B_n$ and $H_t$

Method-3: Integration of Maxwell's stress on the air-iron boundary with the (4.11) to calculate $B_n$ and $H_t$

Compared force: Case-A calculated by the standard Maxwell's stress method with an integral path that goes through the centre line of air gap.

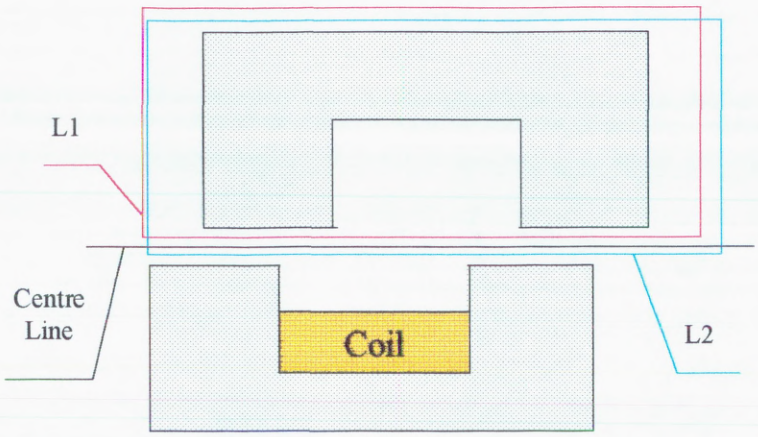


Fig. 4.10 Configuration of Example-3

## 4.8 Conclusions

Based on the fundamental analysis of the error sources of numerical force calculation an interesting phenomenon has been found that most of the elements have common mode errors. This was solidly proven by two examples with comparison between analytical and FEM results. This discovery has led to two intermediate influences to implement force calculation: better local field quantities (B,H) can be obtained at ROGSPs and errors are more concentrated near the source. The second influence backs the experience of other researchers to choose the integral path away from sources that include the excitation source and iron-air interface.

This fundamental study and the discovery of the dominance of elemental CM errors have led to the birth of the proposed method to improve the accuracy of force calculations of MSTBM. The method transforms the standard integration into a summation of forces acting on edges of elements contained in the integral region. The method requires the magnetic field strength or the magnetic flux density to be corrected at the ROGSPs by higher order secondary interpolation of potential or equivalent magnetic circuit, depending on the type of auxiliary potential used. Improvement in force accuracy and path-independence of integration have been achieved with the proposed method. This method can be immediately combined with other high-level measures, which improve potential accuracy, to further improve the force accuracy.

# 5 SIMULATION OF TRANSIENT TEMPERATURE FIELD

## 5.1 Introduction

The fundamental thermal problem in the design of electromagnetic devices is to avoid overheating. Overheat of windings will break down their electrical insulation. Overheated spots in mechanical structure will cause structural damage and/or degradation of material property. So not only the electromagnetic field should be known in the design but also the temperature field. Although heat sources could be in several forms, only the electromagnetic losses in low frequency domain are of interest here. It accounts for eddy current loss, winding resistance loss and magnetic hysteresis loss.

The temperature rise in our positioning TLIAs becomes more severe due to the following three main factors:

- Large inevitable eddy current losses in the plunger
- Poor ventilation facilities
- Temperature dependence of properties of materials

In addition to the possible thermal overheating of windings, side effects caused by overheating will bring extra burden in positioning control. When forced ventilation becomes unavoidable the whole system will become more complex than their rotary counterpart. In this case, some of the inherent advantages of linear induction actuators, such as robustness and simplicity, suddenly disappear. Therefore a precise temperature calculation plays a vital role in the design of a positioning TLIA whose temperature rise could be the main factor limiting its operating duration under continuous excitation.

The traditional non-numerical analytical methods can only predict the average temperature in particular components of electromagnetic devices with simple structures [57]. Practical devices usually have complicated structures whose empirical parameters required by analytical method will not be available or accurate enough at the development stage of a product. Even if the TLIA we developed has a simple structure, it is still too difficult to use analytical method for its temperature analysis. Modern development in the FEM overcomes these problems and enables the accurate computation of the entire temperature distribution within electromagnetic devices with complicated structure. Therefore, we turn to the FEM again to compute the transient temperature field in the TLIA.

Generally speaking, the physical properties of materials such as electric conductivity, magnetic permeability, etc., are temperature dependant. Therefore temperature field equation and electromagnetic field equation should be coupled together when the temperature range will significantly affect material properties.

Coupling temperature with electromagnetic field could be implemented in a strong way or a loose way, determined by the maximum temperature and the temperature dependence of material properties [58,59]. In the strong coupling method, temperature field and electromagnetic field are solved in one simultaneous equation. In the loose coupling method, the temperature field and the electromagnetic field are solved separately by two simultaneous equations that are formed without taking account of their transient interaction.

If the temperature rise is very high and involve significant change of material properties such as the Curie transition that happens in induction heating, strong coupling will provide better solutions. For electromagnetic devices working in the low frequency range, their electrical transient time constants are one or two orders lower than their thermal time constants. The maximum temperature will usually not exceed beyond their Curie point after which material properties change dramatically. In these cases, the thermal equation and the electromagnetic equation can be solved efficiently by the loose coupling method. Therefore the loose coupling method is suitable and will be used for

our TLIAs.

As for the computation of losses, the simpler time-harmonic form of Maxwell's equations could provide an adequate accuracy for the purpose of temperature computation for those electromagnetic devices with constant loads. In positioning applications, however, the time-harmonic form is not good enough, due to the fact that the position may change in unpredictable patterns and that the total settling time required will be different from position to position. So, a time-dependent form of the Maxwell's equation will be more appropriate in these cases. The method studied in chapter 3 to simulate transient electromagnetic field is employed here to compute the distribution of electromagnetic losses. The electric losses in the winding area are calculated by redistributing the total resistive winding losses into the whole winding area. The eddy current losses in the winding area are neglected. The magnetic hysteresis losses are calculated by empirical formula according to the magnetic field density. The standard Backward Euler's Difference method is used to treat the time derivative term in the thermal equation.

## 5.2 Finite Element Analysis of Transient Heat Transfer Equation

### 5.2.1 The Heat Transfer Equation

In the computation of the temperature field in the actuator, we will only concentrate on the process by which the energy transport takes place. This is the so-called heat transfer problem that differs from the thermodynamics that deals with the relation between heat and other forms of energy. The heat transfers are generally classified into three basic modes of mechanism: conduction, radiation and convection. Of these mechanisms, conduction and radiation can be considered as pure propagating process without mass transport of energy. Convection, on the other hand, is a mixture of conduction and mass transport of energy. Since most heat transfer occurrences involve more than one mode, it will be necessary to take into account of all significant modes involved. Because the actuators work in low temperature range, we will neglect the radiation effect and consider convection and conduction modes only.

The diffusion equation, describing the temperature field associated with the heat conduction and velocity, is governed by the energy conservation equation:

$$\nabla \cdot (k\nabla T) - \rho c(\frac{\partial T}{\partial t} + \vec{v} \cdot \nabla T) = -q \qquad \text{in } \Omega, \text{ t>0} \tag{5.1}$$

together with the following possible boundary conditions and initial condition, without considering radiation effects and velocity:

- Dirichlet boundary condition: $T|_{\Gamma_1} = f(\mathbf{x}, t)$ for $\mathbf{x}$ on $\Gamma_1$, t>0 (5.2a)
- Neumann boundary condition: $k\frac{\partial T}{\partial n}\Big|_{\Gamma_2} = q_n(\mathbf{x}, t)$ for $\mathbf{x}$ on $\Gamma_2$, t>0 (5.2b)
- Convection boundary condition: $\frac{\partial T}{\partial n}\Big|_{\Gamma_3} = h_c(\mathbf{x}, t)(T - T_\infty)$ for $\mathbf{x}$ on $\Gamma_3$, t>0 (5.2c)
- Initial condition: $\begin{cases} T = T_0(\mathbf{x}) \\ q_n = q_{n0}(\mathbf{x}) \end{cases}$ for $\mathbf{x}$ in $\Omega$, t=0 (5.2d)

where $T_0$, $T_\infty$, $\Gamma$, $q_{n0}$, and $h_c$ are constant temperature, ambient temperature, boundary, constant input heat flux and heat transfer coefficient respectively. Vector $\mathbf{x}$ is the coordinate variables in space $\Omega$. The $\vec{v}$ stands for the velocity vector of the moving mass.

### 5.2.2 Finite Element Formulation of Transient Heat Conduction Equation

Similar to transient eddy current equation (3.5), equation (5.1) is also a parabolic differential equation. The variational formulation to this problem has not been thoroughly solved up to date. There are two remedies to deal with the $\partial T/\partial t$. The first method is to treat it as a constant during variation, then expressed by finite difference method after the variation. The second one is to difference it at first and then carry out the variation after. The first method is used here. For the TLIAs it is extremely difficult to treat the velocity term because of the plunger's uncertain movement pattern and the free convection. To simplify the treatment of free convection, an average heat transfer coefficient will be used. To treat the velocity term, we go for a pessimistic condition that will be the

standstill operation. After these assumptions, we then can solve (5.1) with the setting of $\bar{v}$=0. In this case, the functional of (5.1) will be

$$\Theta = \frac{1}{2}\int_{\Omega}\left[k(\nabla T)^2 + \rho c\frac{dT^2}{dt} - 2qT\right]d\Omega - \oint_{\Gamma_2} q_n T d\Gamma - \oint_{\Gamma_3} h_c T(\frac{T^2}{2} - TT_\infty)d \tag{5.3}$$

From the variational theory we know that the solution of $T$ of (5.1) can be obtained alternatively by solving $\delta\Theta=0$. Substituting (5.3b) and (5.3c) into (5.3), one obtains:

$$\begin{aligned}\delta\Theta &= \int_{\Omega}\{(\delta T)kT - (\delta T)(q - c\rho\frac{\partial T}{\partial t})\}d\Omega \\ &\quad - \int_{\Gamma_2}(\delta T)q_n d\Gamma_2 - \int_{\Gamma_3}(\delta T)h_c(T - T_\infty)d\Gamma_3 \\ &= 0\end{aligned} \tag{5.4}$$

Carrying out the analysis for a typical element and the assembling of the global equation in the standard FEM procedure, we obtain the following system equation for (5.4):

$$\mathbf{KT} + \mathbf{C}\dot{\mathbf{T}} - \mathbf{HT} = \mathbf{Q} - \mathbf{H}T_\infty \tag{5.5}$$

The time derivative term $\dot{\mathbf{T}}$ is then discretized by the BED method as described in chapter 3. The final algebraic matrix equation takes the form of

$$(\mathbf{K} + \Delta t_n^{-1}\mathbf{C} - \mathbf{H})\mathbf{T}_n = \mathbf{Q} - \mathbf{H}T_\infty + \Delta t_n^{-1}\mathbf{C}\mathbf{T}_{n-1} \tag{5.6}$$

Details of elemental analysis of (5.6) are given in appendix B. Solution to (5.6) is straightforward. As we did in solving (3.20), the ICCG method is used here again to solve (5.6).

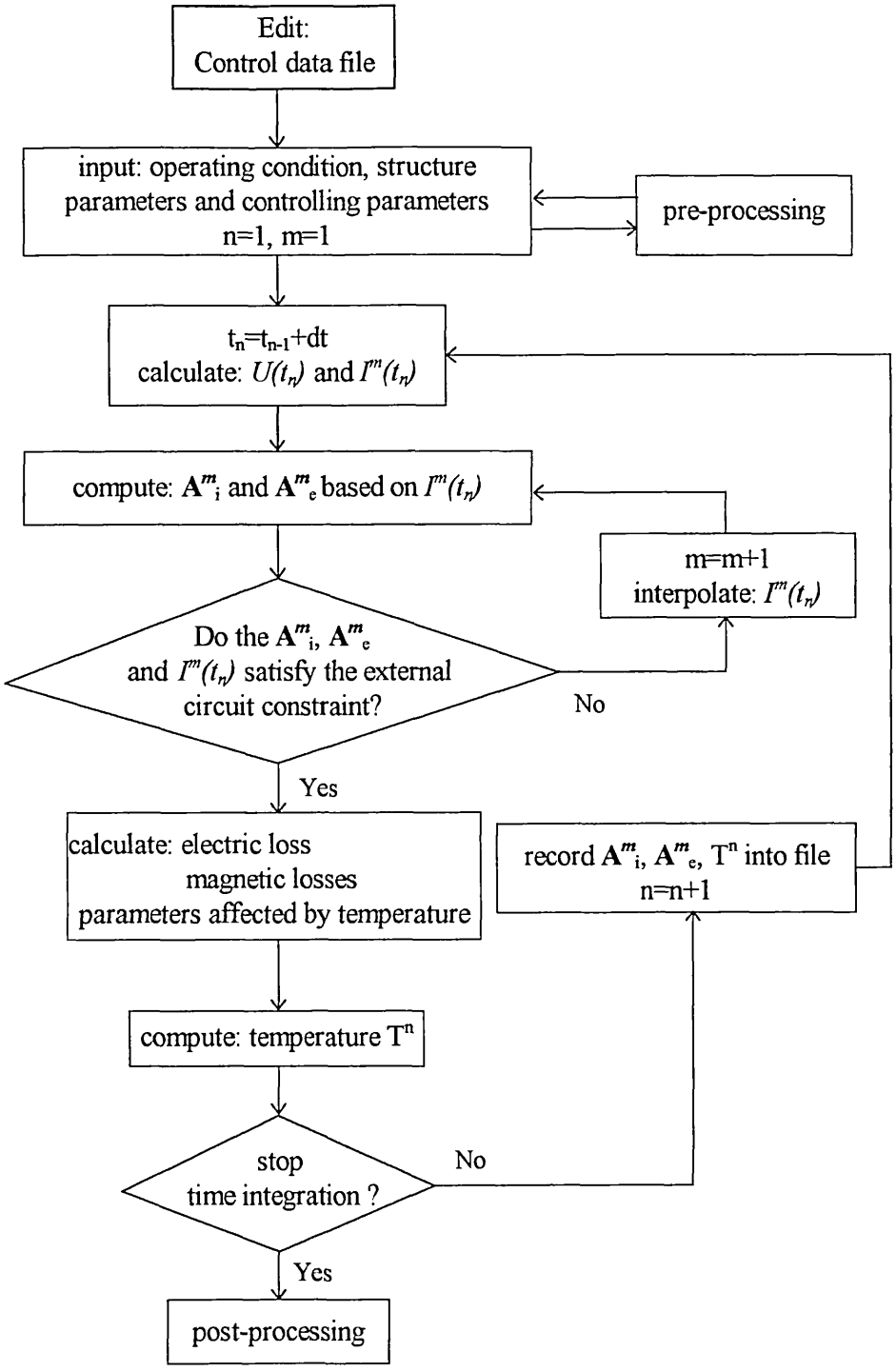


Fig. 5.1 The flow chart of the computation of transient temperature field

From the programming point of view, the FEM software developed in chapter 3 for the computation of electromagnetic field can be easily expanded to incorporate the function

of FE temperature computation, because many program futures and code can be shared between them, such as

- Program structure
- ICCG solver for positive-definite symmetric matrix equation
- Part of elemental computation for **K**, **C**, and **Q**
- Treatment of the Dirichlet boundary condition and the Neumann boundary condition
- Pre-processor and Post-processor

The flow chart of the computation of the transient temperature field is shown in Fig. 5.1 where the computation of electromagnetic field is included to form a complete loop so that transient electromagnetic losses can be computed at the same time.

### 5.2.3 Treatment of Convection Boundary Conditions

The most difficult problem in the heat transfer computation probably comes from the convection process. Because convection involves with mass transfer of energy, fluid dynamics should usually be studied to obtain more accurate solution.

The actuators work under certain fluid environmental condition. The cooling effects from the environment are difficult to be determined exactly without the computation of fluid dynamic equations. This is outside the scope of the research. To simplify the treatment of convection problem, we will take an engineering approach. That is to treat the convection as a boundary condition described by (5.2d). Empirical formulas and coefficients are employed to calculate the heat exchange/convection coefficient.

The heat convection coefficient $h_c$ depends on the geometric arrangement, orientation and surface condition (smooth or rough), as well as the properties and velocity of the fluid. In engineering applications the heat transfer for the entire surface under consideration is of more interest than local values. So an average heat transfer coefficient is used instead of distributed ones. The calculation of the average heat transfer coefficient $\underline{h_c}$ can be calculated by a normalised empirical formula [60,61]:

$$\underline{h}_c = \frac{N_u L}{k_c} \tag{5.7}$$

where the $k_c$ is thermal conductivity, $L$ is nominal length and $N_u$ is the Nusselt number. $N_u$ should be determined by experiment or empirical formula that could be expressed as

$$N_u = c \cdot R_e^m \cdot P_r^n \quad \text{for forced convection} \tag{5.7a}$$

$$N_u = c \cdot N_{Ra}^m \quad \text{for free convection} \tag{5.7b}$$

where $R_e$, $P_r$ and $N_{Ra}$ are the Reynolds number, the Prandtl number and the Rayleigh number respectively. Constants of $c$, $m$ and $n$ can be determined by experiment. The positioning TLIAs are usually placed horizontal. For horizontal cylinders in free convection, the following empirical equations can be adopted,

$$N_u = 1.08 N_{Ra}^{0.10} \qquad 10^{-4} < N_{Ra} < 1 \tag{5.8a}$$

$$N_u = 1.08 N_{Ra}^{0.155} \qquad 1 < N_{Ra} < 10^3 \tag{5.8b}$$

$$N_u = 0.537 N_{Ra}^{0.25} \qquad 10^3 < N_{Ra} < 10^9 \tag{5.8c}$$

When the environment has good ventilation or forced cooling measure is used, different formula and coefficients should be used for the calculation of $N_u$.

### 5.2.4 Treatment of Heat Sources

The heat source $q$ considered here consists of two parts: electric losses and magnetic hysteresis losses. The electric losses include the loss in the winding and the loss in the massive conducting material in which induced current flows. The electric losses are calculated by

$$q_{ele}(t) = \gamma_{eq} |J_s(t)|^2 + \sigma \left| \frac{\partial \vec{A}}{\partial t} \right|^2 \tag{5.9}$$

where $\gamma_{eq}$ is the equivalent resistance of the winding area with the terminal resistance of

$R$. $J_s$ is the excitation current density. The introduction of $\gamma_{eq}$ lets the resistive loss in the winding to be calculated in an easy and unified way as the calculation of eddy current loss expressed by the second term of (5.9).

The temperature influence on the conductivity could be considered in the computation as well. When the temperature range does not extend over Curie transition, the relation of conductivity versus temperature can be approximated by

$$\sigma = \frac{\sigma_0}{1+\alpha(T-T_0)} \tag{5.10}$$

where $\alpha$ is the conductivity temperature coefficient. For our actuators the temperature rise is too low to affect the material property. So all the material properties could be assumed as temperature invariant.

Because the magnetic hysteresis model has not been modelled in the computation of electromagnetic field, we can not get the instant magnetic hysteresis losses. In this case, we can only turn to use traditional empirical formula to calculate the losses. One of the formulae widely used in the industry takes the following form

$$q_{hys} = k_{hys} B_m^{\xi} f^{\zeta} \tag{5.11}$$

where $B_m$ is the amplitude of magnetic field density. Coefficients $k_{hys}$, $\xi$ and $\zeta$ are determined by experiments or given as manufacturer's data. Equation (5.11) usually gives the average hysteresis loss at steady state condition. To accommodate transient property, the $B_m$ can be chosen as the most recent one with the passage of time.

## 5.3 Numerical Computation and Experimental Verification

### 5.3.1 Computation of Transient Temperature Field

The computation and experiments have been carried out on the TLIA-1. The computational area and boundary conditions are shown in Fig. 5.2. The actual external

surface of the actuator is formed by b-c'-d'-d-e-a. We just expand the plunger-end area to include some air-area in the computation to get the temperature distribution in that area. The boundary a-b is the axis of the actuator. We assume that there is no heat flux flowing across this boundary. The boundary a-e-d is the iron-air contacting surface. The free convection boundary condition is applied to it. Most part of the boundary d-c-c'-b is in the air, and is very difficult to be given exact boundary conditions. (Even if we do not consider the area included by d-d'-c'-c-d, the boundary condition is still difficult to determine because of the lack of formula/coefficients to calculate the heat exchange coefficient for such a shape) From the average energy dissipation point of view, we consider the heat exchange rate the same as that for the surface a-e-d. Therefore the same heat exchange coefficient formula of (5.8a) will be used for boundaries a-e-d and d-c-c'-b.

The actuator was simulated as working at a fixed displacement and continuously energised from a triac PSU with the firing delay angle set at $75^0$. The whole solution region was discretised into 3927 triangular finite elements with 7594 nodes. Magnetic hysteresis losses have not been included into the computation for this case. The pattern of temperature distribution is demonstrated by its contour plots shown in Fig. 5.3. The simulation of temperature field has revealed the following phenomena:

- The hottest part of the actuator is the working end of the plunger. This coincides with the electromagnetic analysis and the operation principle.
- The coil's temperature is higher than the temperature of stator/mandrel structure, but lower than plunger's temperature.
- The highest temperature gradient happens between the plunger and the other part of the structure.

Since the coil is the only part susceptible to thermal damage by overheating, its thermal design eventually determines the safe operating region. Forced internal ventilation could be one solution. From the above observation, we can also conclude that a proper thermal insulation and screening to prevent plunger's heat flow from entering the coil could be an effective measure.

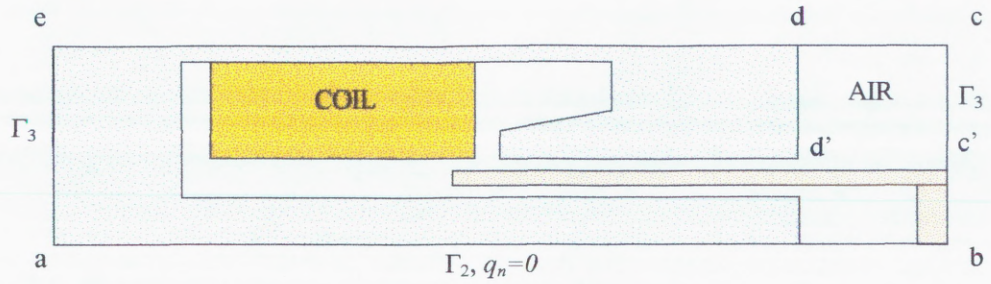


Fig. 5.2 Illustration of computational area and boundary condition

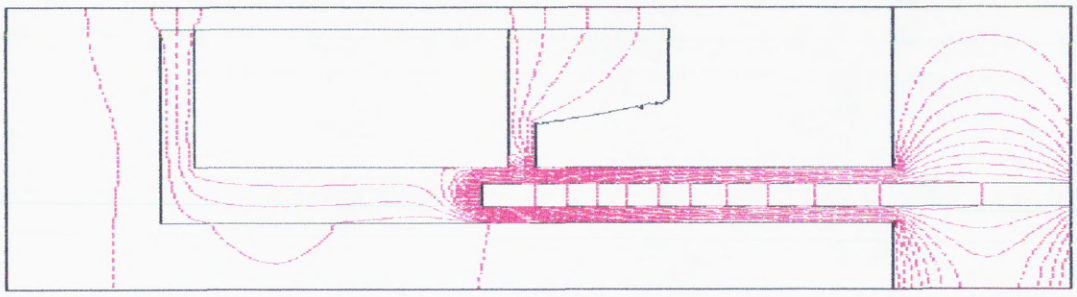

Fig. 5.3(a) Contour plot of TLIA-1's temperature at time=12.5 s

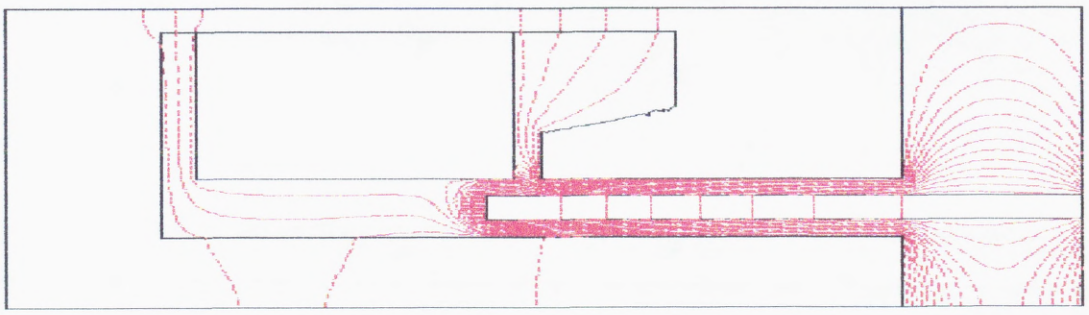

Fig. 5.3(b) Contour plot of TLIA-1's temperature at time=25 s

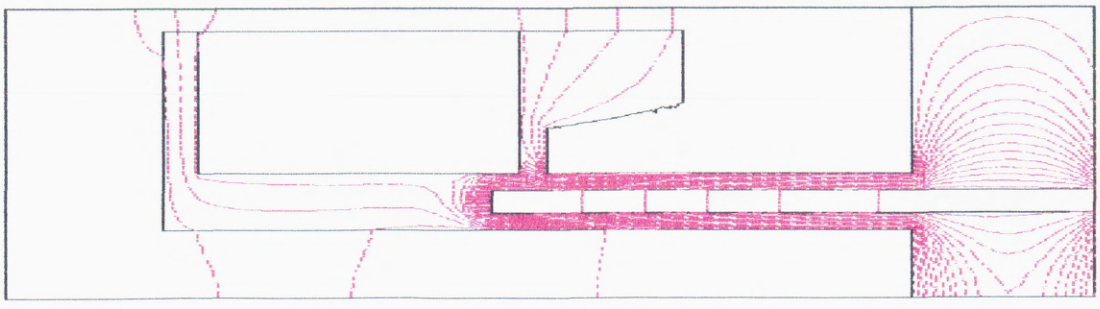

Fig. 5.3(c) Contour plot of TLIA-1's temperature at time=37.5 s

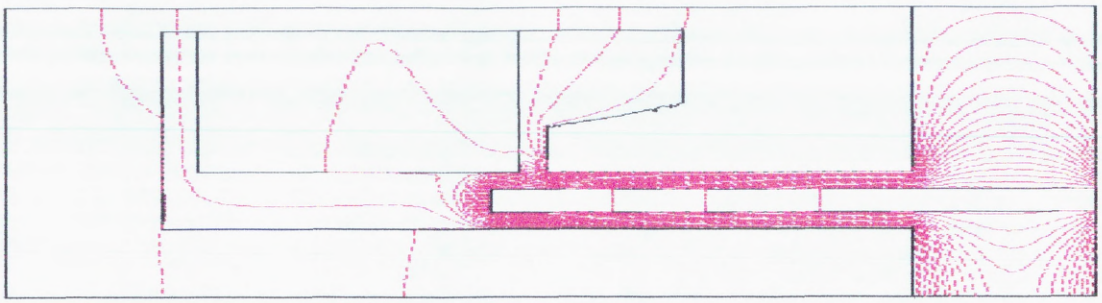

Fig. 5.3(d) Contour plot of TLIA-1's temperature at time=65 s

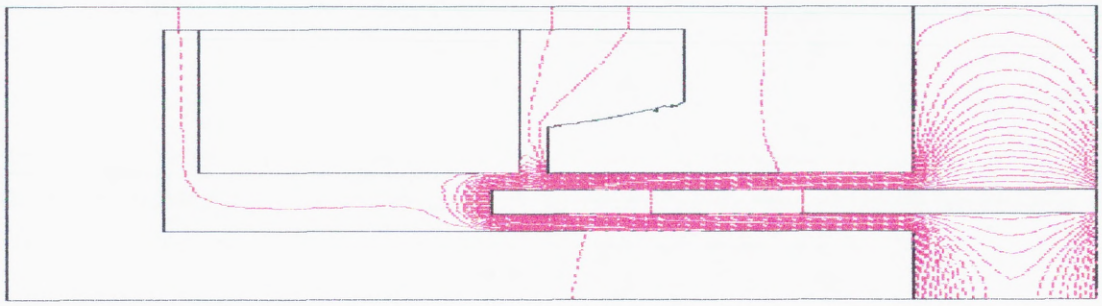

Fig. 5.3(e) Contour plot of TLIA-1's temperature at time=100 s

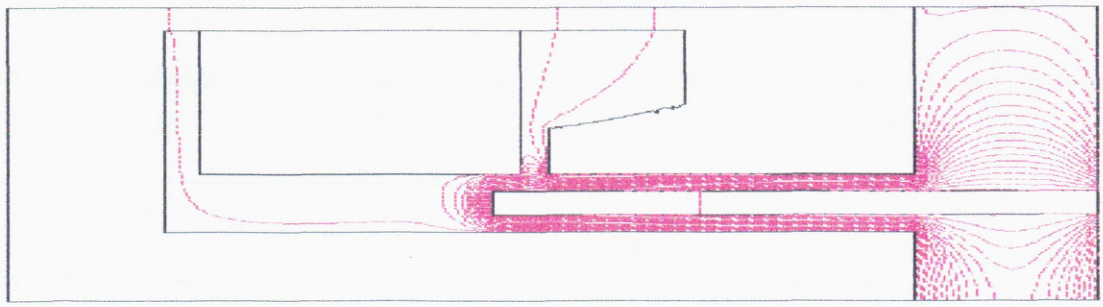

Fig. 5.3(f) Contour plot of TLIA-1's temperature at time=150 s

5.3.2 Experimental Test and Comparison

An experiment was designed to obtain the transient rise of the temperature at some particular spots in the actuator. The experimental configuration, shown in Fig. 5.4, is in a closed loop control. A displacement command is input to the TMS320 DSP controller, which receives the displacement feedback signal from the linear potentiometer and generates a controlling signal to the PSU. In our temperature test, only one displacement was given and the '*S*' is switched at the triac position. The triac was fired at about $75^0$ phase delay angle corresponding to the simulated condition. A copper/copper-nickel thermocouple was used to measure the temperatures at the two positions shown in Fig. 5.5. The temperature was recorded by an X-Y plotter. The tested results and the simulated results are illustrated by Fig. 5.6.

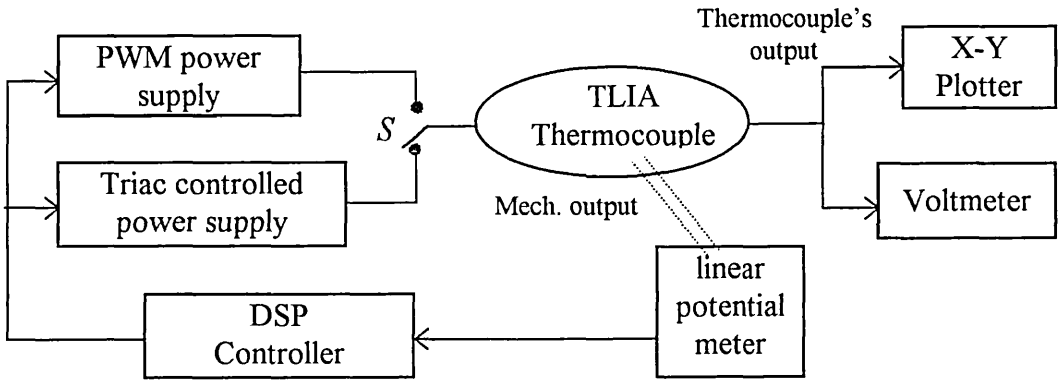


Fig. 5.4 Configuration of the experimental measurement

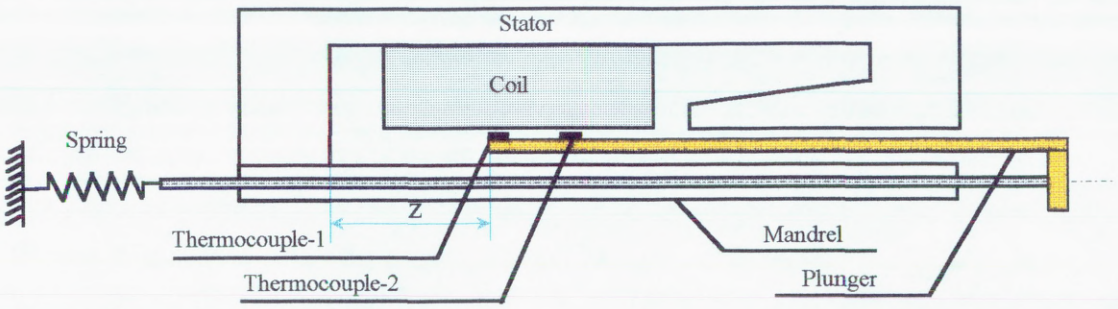


Fig. 5.5 The structure of the TLIA with restraining spring showing the locations of thermocouples

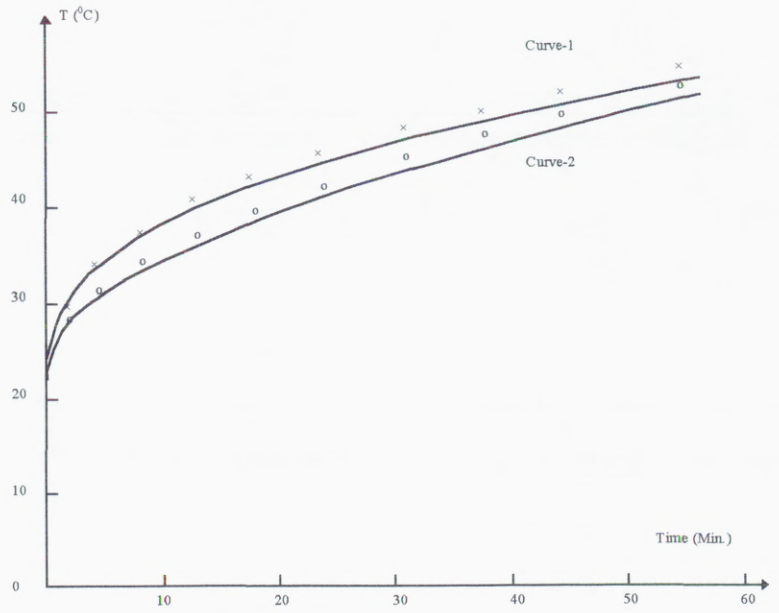


Fig. 5.6 Comparison of the measured and computed temperature rise curves at the location of thermalcoupl-1

Curve-1 : Computed results with $U$=32.5 V(r.m.s.) and z=20mm

Curve-2 : Computed results with $U$=43.5 V(r.m.s.) and z=30mm

× × : Measured results with $U$=32.5 V(r.m.s.) and z=20mm

o o : Measured results with $U$=43.5 V(r.m.s.) and z=30mm

It shows that the measured results generally agree well with the simulated results despite the fact that the simulated temperature is slightly lower than the measured one. This can be explained by

(i) The actual stator is made of the solid steel with magnetic hysteresis losses that was not taken into account in the simulation of electromagnetic field and temperature field

(ii) The Backward Euler's Difference method usually approaches the solution from the low side.

Figure 5.6 also shows the temperature continuously rising even after one hour of continuous operation. This is a predictable but undesirable result, due to the absence of forced ventilation. During testing, on one occasion the coil former was deformed after about 50 minutes of operation with about 2 amperes of current. The temperature at thermocoupl-2 is very close to that of thermocouple-1 with a margin of 5°C lower. Through the simulation we will be able to predict how long the actuator can work safely under a certain environment and know where the bottleneck is in improving the design for thermal protection.

## 5.4 Conclusions

The electromagnetic-thermal coupling problems that characterise the tubular linear induction actuators have been simulated by the time-stepping finite element method. The coupling of the electromagnetic field equations, the external circuit equations and the thermal equation is achieved in a weak form in which the convection effect was treated by empirical formula using average heat transfer coefficient. Good agreements between the computed results and the test results have validated the method and the program. With the coupling to external circuit equations through the simulation of transient electromagnetic field, it is now possible to study the actuator's transient thermal behaviour under various forms of PSUs. This provides a tool to improve the thermal design and to predict the safe operation region.

Although only the temperature in the working end of the plunger has been measured, all the results obtained from the simulation seem to be very realistic. The computation has shown that the highest temperature was located at the working end of the plunger. The hot spot in the plunger will heat the coil quickly when the plunger is placed inside the coil former. Both experiment and simulation indicate the need for extra cooling measures if the actuator is expected to under take moderate current for a long period of time.

# 6 DESIGN OF AN A.C. LINE VOLTAGE CONTROLLER

## 6.1 Introduction

Varying the position of an TLIA requires an a.c. power supply with variable voltage and/or variable frequency. This can be obtained by the use of controlled power supply such as an a.c. line voltage controller or an inverter [62]. Here a.c. line voltage controllers stand for those devices which convert a.c. to a.c. of the same fundamental frequency by using phase control technique, and inverters stand for those devices which convert d.c. to a.c..

A converter can be viewed as a switch-mode power amplifier with high gain because of its low signal power requirement. The low power loss in the switching devices makes the converter efficiency high, typically in the vicinity of 98%. It is rarely practical to use devices under conditions where a significant portion of the circuit voltage occurs across the power semiconductors while current is flowing in them because of the very high internal power dissipation which would result. The performance and, in particular, the low fabrication cost of power semiconductors has enabled power electronics to be used to convert electrical energy from one form to another, to suit specific requirements. The basic element of a converter is an electronic switch having the property of a controllable rectifier. There is a very wide range and variety of semiconductor switching devices that can be considered for use in power converter, such as thyristors, triacs, GTOs, MOSFETs, IGBTs, etc. The requirement on a converter driving our TLIAs is that the converter should be a single phase variable a.c. voltage supply with a control interface to accept the controlling signal from a DSP controller. In general, there are three types of

converters that are suitable for this purpose [63]. These are

- phase-controlled converter
- voltage-fed inverter
- current-fed inverter

The phase-controlled converter can convert a.c. from one input frequency/voltage to an output of another frequency/voltage. Because the TLIAs are designed to use mains power supply as the direct energy source, the first attempt to control voltage is by intuition to vary the r.m.s. value of the alternating input voltage applied to the TLIA without changing the fundamental frequency. This is called as the a.c. line control method. The phase-control technique provides the simplest regulating system for an a.c. line controller. There are several methods by which thyristor control of a.c. lines is possible, namely zero voltage switching, a.c. chopper control and synchronous tapping change. The a.c. chopper control method, which uses thyristors or triacs as the switching devices, was employed in our design, due to the following reasons:

- The zero voltage switching has longer response time, usually in the order of a second for a large variation of a.c. output voltage range. It is too long to be used in a closed loop controller in which the time constant of the plant, here the TLIA, is in the order of microsecond
- The synchronous tapping change method can only provide small variation of a.c. output voltage
- The a.c. chopper control method can provide wider variation of output voltage and has the same response speed that matches the line frequency

Although phase control techniques using thyistors and triacs have wider applications ranging from general motor speed control, industrial process control to domestic electric appliances, etc., they work at low frequency and provide an average level of control [62,64]. It is very difficult to use phase control techniques in the areas where high accuracy and fast response are required, due to their limitation of control. The methods used for motor speed control can be adopted in the positioning control for TLIAs. The requirement on the circuits for the latter is more demanding than the former since TLIAs have a relatively smaller mechanical time constant and higher positioning accuracy. In

this chapter we will discuss the design and analysis of an a.c. line voltage controller as the TLIAs' power supply unit (PSU) by using the triacs chopper control technique.

## 6.2 Full-Wave a.c. Phase Controller

The basic forms of full-wave a.c. phase control circuits are given in Fig. 6.1. The utilisation of back-to-back SCRs, as shown in Fig. 6.1(a), allows a symmetrical control of an a.c. voltage during both halves of an a.c. wave: the SCR-1 controls the positive half cycle and the SCR-2 controls the negative half cycle. In this configuration, two firing controllers are required for each of the thyristors.

In applications where the power required is not very high, a simple, efficient and reliable method is by using triacs instead of SCRs, as illustrated in Fig. 6.1(b). The operational principle of a triac is the same as two back-to-back SCRs connected in parallel. For simplicity, we will use the terminology of SCR to represent a triac that works in a half wave in the analysis and discussion of triacs.

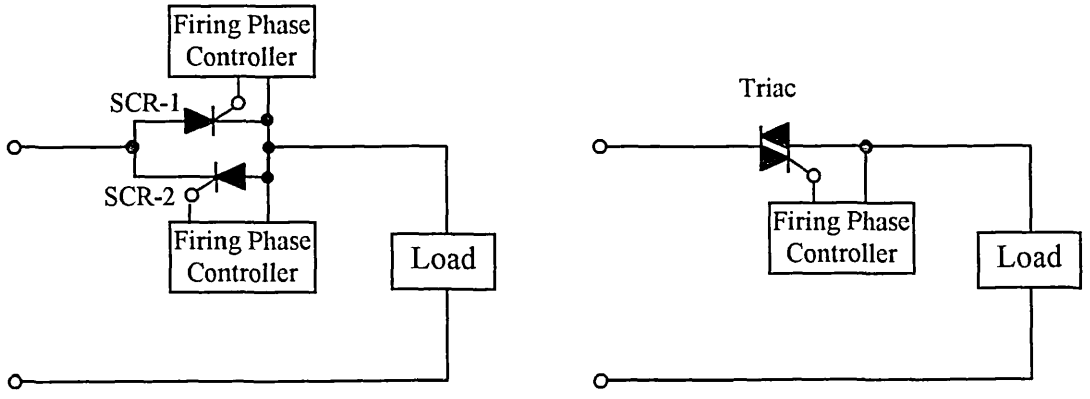


(a) Full-wave controller: two SCRs (b) Full-wave controller: one triac

Fig. 6.1 The principle circuit of an a.c. line controller

In addition to some standard parameters, such as maximum reverse voltage, maximum average current, power dissipation rate, etc., that limit the power-handling capacity of triacs, there are three important issues that relate with their applications in the area of accurate control. They are the inductive load problem, the latching problem and the misconduction problem caused by rapid voltage change ratio.

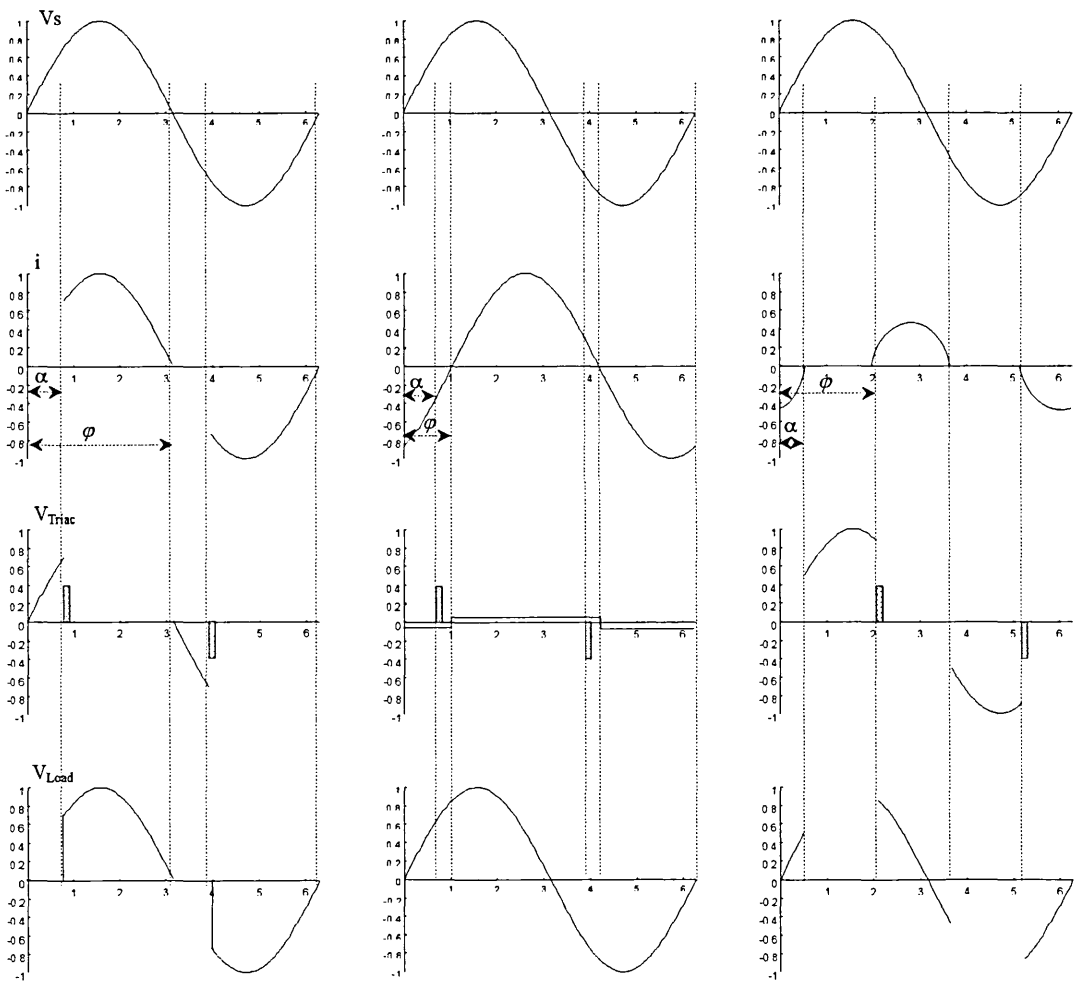


(a) pure resistive load (b) inductive load with $\alpha \leq \varphi$ (c) inductive load with $\alpha > \varphi$

Fig. 6.2 Current and voltage waveforms for three types of load conditions

Figure 6.2 illustrates three typical waveforms for resistive load and inductive load. For a resistive load, Fig. 6.2(a) shows that the voltage waveform applied on the load is just a chopped portion of the input voltage waveform, and thus a very wide range of voltage variation can be obtained. This is very desirable. However a TLIA is equivalent to a network with resistors and inductors. Due to the existence of inductance, the patterns of current waveforms applied on an inductive load are different from those for pure resistive loads. They are influenced by the impedance angle $\varphi$ of the load and the firing phase angle $\alpha$.

When the $\alpha$ is less than or equal to the $\varphi$ for an inductive load, the load current will appear to be continuous, as shown in Fig. 6.2(b). In this case, the actual voltage applied on the load is the same as the input voltage. That is, no part of the input voltage waveform is chopped off. It also means that the load voltage does not vary with the $\alpha$ for any $\alpha \leq \varphi$. Therefore the a.c. line controller is unable to control the voltage applied on the load. When the firing phase angle $\alpha$ is larger than the $\varphi$ of an inductive load, the load current will be discontinuous, as shown in Fig. 6.2(c).

Because the phase of the load current always lags its voltage, a turn-on problem sometimes might occur with an inductive load. This is the so-called latching problem that happens when the SCR anode current has not reached the level of the specified latching current or holding current. The latching current is the current value that must be reached during a turn-on process so that a SCR can remain in conduction state when its gate current is removed. The latching current problem may happen if the duration of firing pulse is too short. This is the first latching problem. The holding current is the anode current needed to maintain SCR conduction after the SCR is fully turned on. With the firing angle increases the load voltage decreases. At some degree the load voltage may be too small and/or its duration may be too short to generate an anode current above holding current level. This causes the second latching problem. The latching problem becomes more severe for positioning TLIA because of its inductive effect and the requirement of a wide voltage range. The circuit design must take into account this problem as well.

SCRs have another characteristic that they can be turned on without any gate current if the rate of change of terminal voltage exceeds a limit. In the case of an inductive load, the terminal voltage may increase rapidly at the turnoff point and may cause undesirable conduction. The limitation to the rate of change of voltage on the load terminal should be taken into consideration in the design as well.

### 6.3 Triggering and Protection Circuit

To simplify the design, a triac is used instead of SRCs. As discussed above, the circuit should provide the following functions

- Variable firing phase angle controlled by a TTL-level voltage that is generated by the D/A converter on the DSP board
- Appropriate synchronising, latching and protection functions

A phase control IC TDA2086 has been chosen to generate the firing pulse. The TDA2086 is a bipolar IC designed for use in a closed or open loop a.c. phase control circuit with resistive or inductive loads. It incorporates a shunt stabiliser that enables it to be powered from the mains or d.c. supply. A basic open loop system is shown in Fig. 6.3.

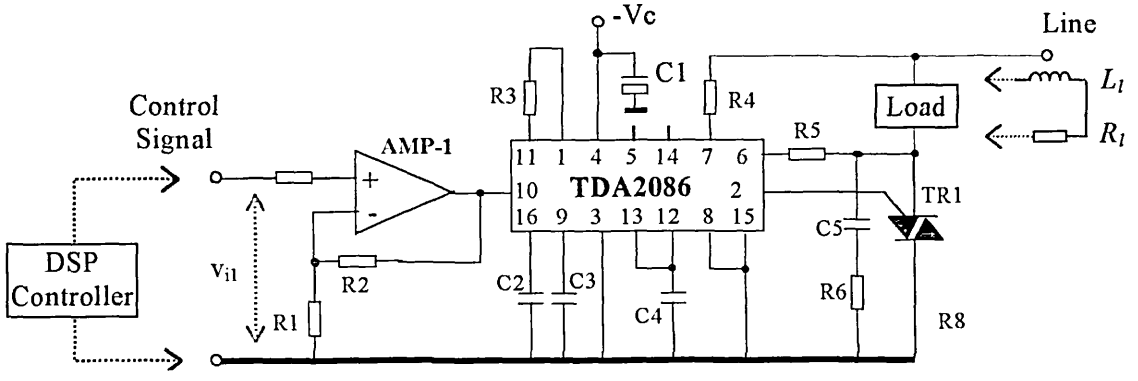


Fig. 6.3 An open loop application of a triac firing control circuit with TDA2086

In the above configuration, the firing phase angle is controlled by a ramp generator, with a capacitor on pin 9, to a maximum determined by the control voltage on pin 10. An operational amplifier AMP-1 provides an interface to the control signal coming from the DSP board. The triac firing pulse is synchronised by delaying the pulse with reference to the zero voltage cross points of the mains cycle, which is determined by the zero voltage detection circuit connected to the line input through resistor R4. With an inductive load, the load current will lag the voltage in phase. So, the triac firing pulse must be delayed until the load current from previous half cycle has ceased. This is achieved by a current synchronisation circuit via R5 to detect the voltage drop on the triac instead of detecting the current directly. The firing pulse is delayed until the absolute current value reflected by the voltage on R5 declines below a certain low level. Firing pulse will be supplied repeatedly for an extended period if the triac fails to latch. The firing pulse width and the spacing of repeated pulse are controlled by a single capacitor on pin 13. To help with latching and to prevent misconduction due to the rapid voltage change, a snubber RC network (C5 and R6) was designed and placed in parallel with the triac.

## 6.4 Control of the TLIA with Two Separate Coils

The TLIA-2 consists of two separate coils that work together to move the plunger and keep the plunger in a balanced position. From the study of its characteristics in Chapter 2, we will find that it can be controlled by two methods: an independent method and a dependent method. Independently controlling the two coils requires two independent phase control circuits plus two analogue output channels from the DSP board. This demands more hardware components and increases the complexity of control code, particularly in the treatment of timing and interrupt between the two control channels. The requirement on the CPU speed will be higher than the case with one output control channel. This becomes more important if complex control algorithm and data processing are involved.

To alleviate the problem of requiring two independent control channels, certain relationship between the two coils can be exploited. We are going to make use of the relationship brought by the back-to-back structure of the actuator, which implies that, for

positioning applications, the direction of change of the absolute current value in one coil can be set opposite to that in another coil. In this case, one of the two phase control circuits uses the direct control signal from the D/A converter which is connected to the DSP, and the other circuit uses the signal derived from the first signal according to the relationship mentioned before. A simple fixed gain differential amplifier has been used in the design to achieve this purpose, which removes the extra strain imposed on the DSP controller. Figure 6.4 shows the principle of the circuit.

The amplifier AMP-1 has two functions. One serves for the same purpose as that used in Fig. 6.3. The other is to assist the generation of the second control voltage through a fixed gain differential amplifier AMP-2. The other input of AMP-2 is a fixed d.c. voltage set at the level at which maximum load voltage will be obtained when AMP-1 is zero. When the output of AMP-1 increases the output of AMP-2 decreases and vice versa, which provides the control function as we need.

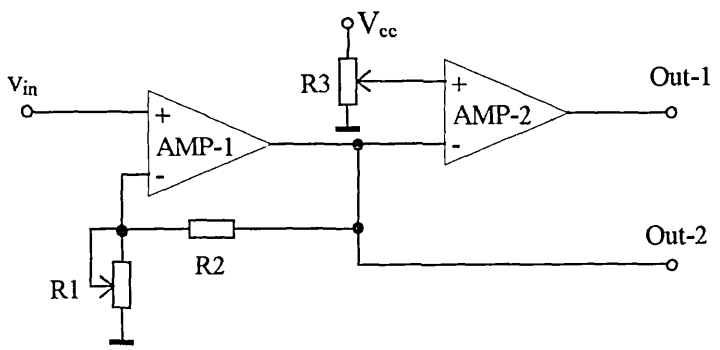


Fig. 6.4 Generating two control signals from one

When the dependent control method is used, the directly controlled signal is reduced to one from two and the final output of the control action is also one - the displacement. This forms a single input single output (SISO) system that brings more advantages in the design of digital controller. This will be seen in chapter 8.

## 6.5 Practical Design of the a.c. Line Phase Controller

We have several TLIAs to be controlled. The main difference between them in the control point of view is that TLIA-1 has just one coil to be controlled and the others, such as TLIA-2, have two. It is obvious that an a.c. line phase controller for TLIA-2 can be used for controlling TLIA-1 as well if they have similar power rating. At the first stage, an a.c. line phase controller for TLIA-1 based on circuit shown in Fig. 6.3 has been design and fabricated. With the development of TLIA-2, that circuit has been further upgraded to incorporate the circuit shown in Fig. 6.4 and some auxiliary functions, to form a two-channel controller. The circuit of the a.c. line controller suitable for both actuators is given in Fig. 6.5.

The majority of the design calculations are carried out around the TDA2086. Details are as follows:

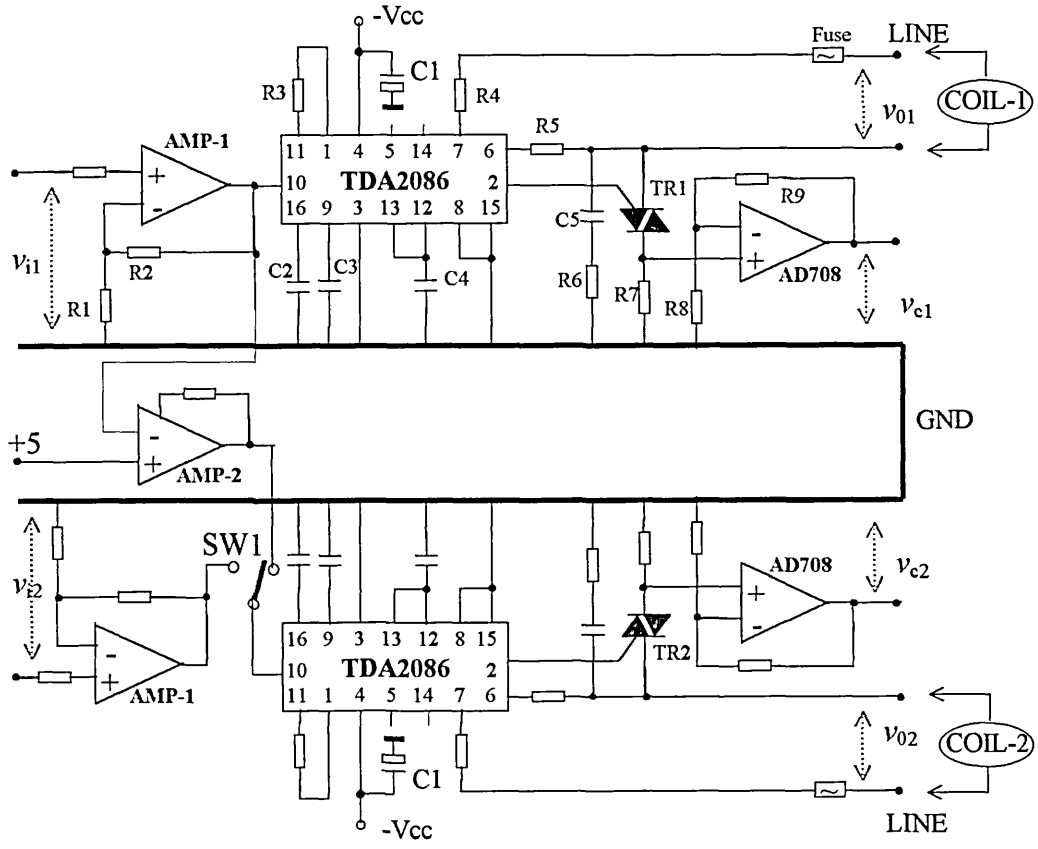


Fig. 6.5 Circuit of an a.c. line phase controller with two output channels

- The amplifier AMP-1

  The reference voltage range of the TDA2086 is from -5V to 0V. The controllable output voltage range of the on-board D/A converter is from about -3V to +3V of which we use -3~0V for the whole range of control. So, one of the requirements on the AMP-1 is to amplify the DSP control signal from -3~0V to -5~0V. The other is to provide high input impedance.

- Acceleration ramp generator

  The acceleration ramp generator limits the rate of change of reference voltage applied to the control amplifier and therefore the rate of change of output voltage. Because the DSP will control the change rate of output voltage, it just needs to be set to react fast enough to follow the change of controlling voltage. The rate can be calculated as

$$V_{ramp} = \frac{I_r}{C_{Pin9}} \quad (volts / \sec ond) \tag{6.1}$$

  where $I_r$ is set internally with a constant of $30\mu A$. If $C_{Pin9}$=$0.01\mu F$, the $V_{ramp}$ will be $3000v/s$. For a control voltage from zero to -5.0V the acceleration time will be 1.67 microsecond which is fast enough for the control of 240V/50Hz mains.

- Zero voltage detector

  The zero voltage detector resets the pulse timing circuit ramp generator near the zero points of each mains' cycle. When the input current on pin-7 is between $\pm 50\mu A$ a reset pulse is generated. However the current limiting resistor $R_{pin7}$ should be chosen to limit the peak current on pin-7 to be less than $\pm 1mA$. The current on pin-7 can be calculated by

$$I_{Pin7} = \frac{V_{Mains}}{R_{Pin7}} \tag{6.2}$$

- Current synchronisation circuit

  It generates an enable signal to the pulse timing circuit if the voltage across the triac is sufficient to produce an input current greater than $\pm 50\mu A$ to pin-6. The peak current should be limited to below $\pm 1mA$ as well. The current on pin-6 can be calculated by

$$I_{Pin6} = \frac{V_{Triac}}{R_{Pin6}} \tag{6.3}$$

- Pulse timing circuit

  A ramp waveform is generated by rapidly charging $C_{pin16}$ on pin-16 to a $V_{be}$ ($\approx 0.7V$) more negative than $V_{Pin11}$ ($\approx -5V$) at the mains zero voltage crossing. After the zero voltage point, $C_{pin16}$ is discharged in a linear fashion by a current $I_d$ defined by

$$I_d = \frac{V_{Pin11} - V_{be}}{R_{Pin1}} \tag{6.4}$$

  When the voltage on $C_{pin16}$ reaches a value determined by output on pin 12, a triac gate pulse is initiated. The triac pulse duration is determined by recharging $C_{pin16}$ to nominally $50mV$ above the original trip voltage. The dynamic working range of the ramp generator is

$$V_{drp} = \frac{I_d}{2 f_{mains} C_{Pin16}} \quad (V) \tag{6.5}$$

  For full phase control the calculated $V_{drp}$ must be less than $V_{Pin11}$.

- Triac gate drive

  When a series resistor is used, the approximate gate drive current could be calculated from

$$I_{Tg} = \frac{V_{Pin4} - V_{Tg} - 1}{R_{Pin2}} \tag{6.6}$$

  There is an internal current limiting so that the capability of providing $I_{Tg}$ is largely independent of the triac gate voltage $V_{Tg}$ and the series resistor $R_{pin2}$. But the use of $R_{pin2}$ will reduce overall power consumption.

- The snubber circuit

  A snubber circuit is designed for two purposes: to help latch and to limit the voltage change rate at the triac terminal. Because the triac is a bi-directional element, the snubber circuit also must be bi-directional and thus only a capacitor and resistor are used. To make sure the total anode current will always be greater than the latching

current even though the triac gate pulse is in short duration, the following empirical calculation is employed to determine the values of the snubber network R5 and C6:

(a). Select R5 so that the initial capacitor discharge current is 1.5 times as large as the latching current:

$$R_5 = \frac{V_c}{1.5 I_{latch}} \tag{6.7}$$

where $V_c$ is the initial value of capacitor voltage which can be chosen as the line voltage and $I_{latch}$ is the latching current value

(b). Select C6 by making the snubber time constant equal to $0.5t_l$

$$C_6 = \frac{t_l}{2R_5} \approx \frac{I_{latch} L}{2V_c R_5} \tag{6.8}$$

where the $t_l$ is time at which the latching current equals the latching value after triac turn on. $L$ is the load inductance.

For the second purpose to limit the voltage change rate, the following formula is used to calculate the maximum voltage change rate across the triac:

$$\left.\frac{dv}{dt}\right|_{\max} = \frac{V_c}{\sqrt{L_l C_5}} \tag{6.9}$$

An effective design of the snubber circuit can satisfy Equations (6.7) to (6.9) and make the circuit suitable for both purposes.

## 6.6 Analysis of the Controller

The instantaneous load circuit equation can be written as

$$V_l = R_l i_l + L_l \frac{di_l}{dt} + E_l \tag{6.10}$$

where $R_l$, $L_l$ and $E_l$ are the resistance, inductance and back emf of the load. It is also assumed that the voltage drop across a conducting triac is negligible and the line voltage is a pure sinusoidal wave with the following expression:

$$V = V_m Sin(2\pi ft) \tag{6.11}$$

where $f$ is the main's frequency. For a full-wave phase controller as used in Fig. 6.3 and 6.5, we can have the following analysis.

### 6.6.1 Pure Resistive Load

The voltage applied on the load can be expressed as

$$V_l = V_m \cdot Sin(2\pi ft) \cdot u_u(k\pi ft - \alpha - k\pi - \pi) \qquad k = 1,2,3,\ldots \tag{6.12}$$

where $u_u(*)$ is a unit delay function. Its r.m.s value can be calculated by

$$\begin{aligned} V_{l.rms} &= \left[\frac{2}{\pi f}\int_0^{\pi} V_m^2 Sin^2(2\pi ft) u_u(\pi ft - \alpha)dt\right]^{0.5} \\ &= \frac{V_m}{\sqrt{2}}\left[1 - \frac{\alpha}{\pi} - \frac{Sin(2\alpha)}{2\pi}\right]^{0.5} \end{aligned} \tag{6.13}$$

$$I_{l.rms} = \frac{V_{l.rms}}{R_l} \tag{6.14}$$

Fig. 6.6 gives the graphic view of the relationship between the r.m.s. value and the $\alpha$.

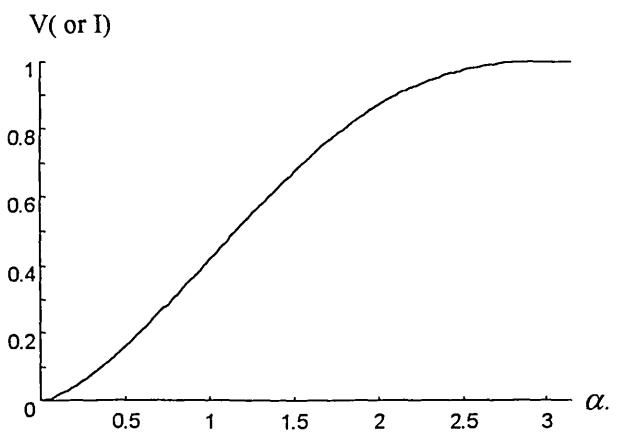


Fig. 6.6 Relationship between the r.m.s. value and the firing delay angle $\alpha$ under a pure resistive load

### 6.6.2 Inductive load

1. Discontinuous Current Cases

Because the current is discontinuous, the governing equation during conduction can be expressed as:

$$\begin{cases} L_l \dfrac{di_l}{dt} + R_l i_l = V_m Sin(\omega t) - E_l \\ \\ i_l(\beta) = i_l(\vartheta) = 0 \end{cases} \qquad \beta \le \omega t \le \vartheta, \vartheta - \beta < \pi \tag{6.15}$$

where $\beta$ and $\vartheta$ are the phase angles to start conducting and stop conducting respectively. Solving the above differential equation with the initial condition of $i_l(\beta)=0$ and the assumption that $E_l$ is a constant , we can obtain the current response as

$$i_l = \frac{V_m}{R_l}\left\{\frac{R_l}{|Z|}Sin(\omega t - \varphi) - \frac{E_l}{V_m} + \left[\frac{E_l}{V_m} - \frac{R_l}{|Z|}Sin(\beta - \varphi)\right]e^{-(\omega t-\beta)/T}\right\} \tag{6.16}$$

where $\omega = 2\pi f$ , $|Z| = \sqrt{R_l^2 + \omega^2 L_l^2}$ , $T = \dfrac{\omega L_l}{R_l}$ and $\varphi = Tan^{-1}\dfrac{\omega L_l}{R_l}$. If $\alpha$ is unknown, then it can be calculated by substituting another condition of $i_l(\vartheta)=0$ into Equation (6.13), which gives:

$$\frac{Cos\varphi Sin(\vartheta - \varphi) - E_l / V_m}{Cos\varphi Sin(\beta - \varphi) - E_l / V_m} = e^{T(\beta-\vartheta)} \tag{6.17}$$

2. Continuous Current Cases

The continuous conducting cases can be solved by Equation (6.15) with the constraint of $\vartheta = \pi + \beta$ instead of zero initial current condition, which yields

$$i_l = \frac{V_m}{R_l}\left\{Cos\varphi Sin(\omega t - \varphi) - \frac{E_l}{V_m} - \frac{2Cos\varphi Sin(\beta - \varphi)}{1 - e^{-\pi/T}} e^{-(\omega t - \beta)/T}\right\} \quad (6.18)$$

In a.c. electromagnetic devices the back emf is usually not a constant. Accurate analysis of such devices should couple the circuit equation with Maxwell's electromagnetic equation, like what we have studied in Chapter 3

## 6.7 Test Results

The circuit was actually fabricated and tested on the TLIAs successfully. Figure 6.7 shows the actual circuit board. The testing of the circuit itself has been carried out for two load conditions. The first one is with a resistive load. The r.m.s value of the output voltage is plotted in Fig. 6.8 against the reference voltage that is the output of the AMP-1. The reason to use reference voltage instead of firing delay angle is that the actual control quantity is the voltage from a D/A converter. Comparing Fig. 6.8 with Fig. 6.6 we can observe that the these two curves are very close except that the actual circuit can not reach 100% phase control, due to several practical limitations on the circuit and triac. The latching problem has been studied by changing the load resistance. With larger resistance the circuit starts to work at higher reference voltage and the doted line will become shorter, which means a narrower variable voltage range. With small resistance the circuit starts to work at lower reference voltage and the doted line stretches longer towards the origin, which means a wider variable voltage range. This can be easily explained that small resistance is easier to reach latching & holding current than large resistance.

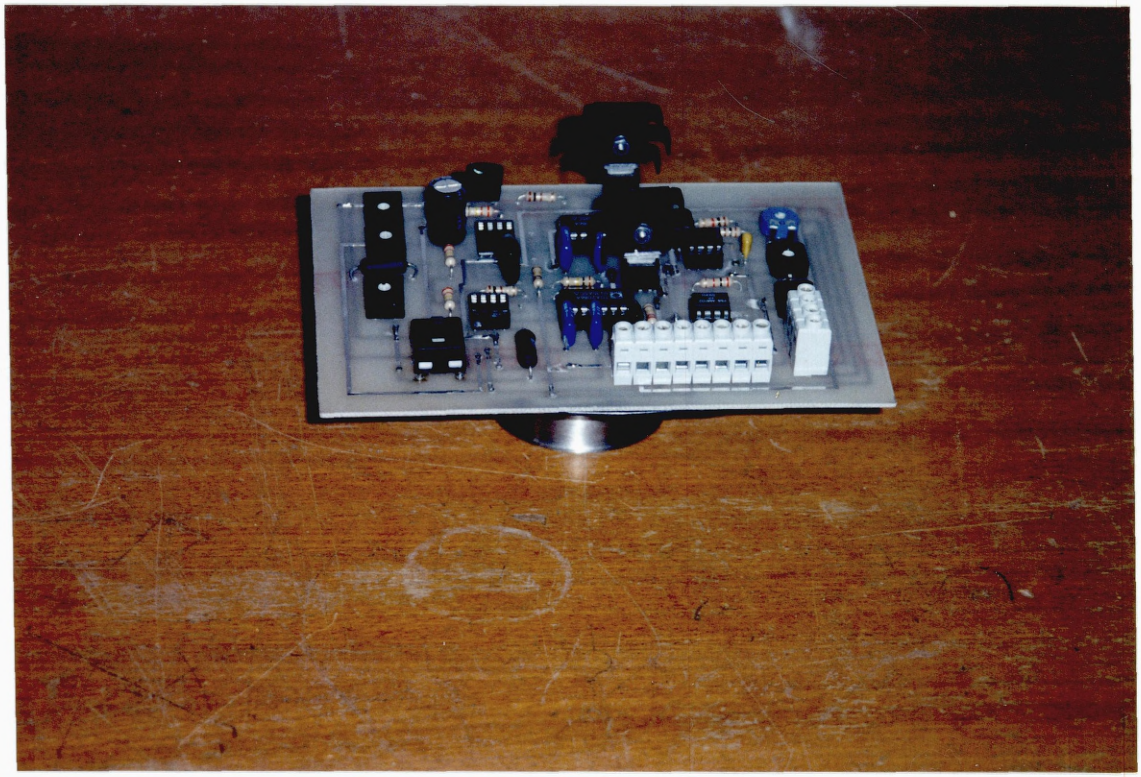

Fig. 6.7 Photograph of the circuit board

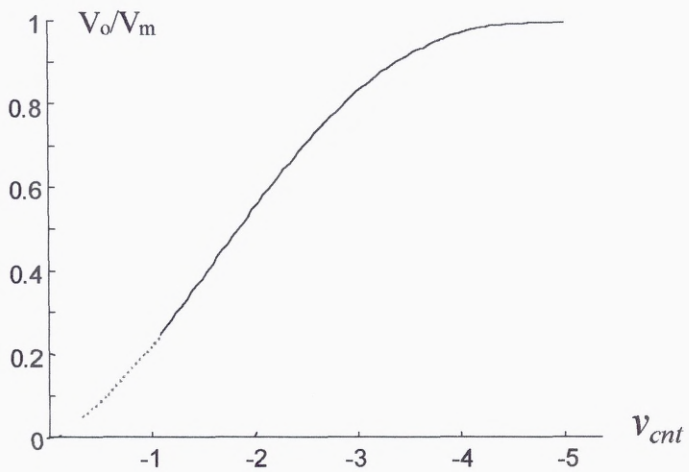


Fig. 6.8 Test result for resistive loads

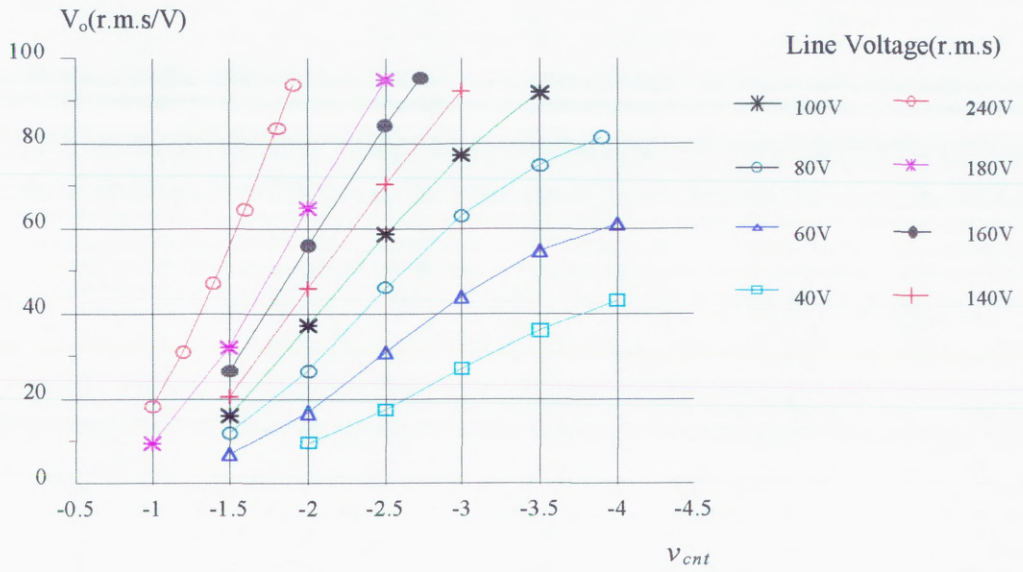


Fig. 6.9 Test results for TLIA-1

The second test was carried out on the TLIA-1 at a fixed position without any displacement. From the test result given in Fig. 6.9 we can observe that the minimum $v_{cnt}$ from which forward the circuit can generate voltage is higher than that under resistive load. The useful range of controlling voltage $v_{cnt}$ or controllable phase angle is limited by the current limitation of the circuit and the line voltage. The maximum control voltage or firing phase angle must be controlled below the point at with a voltage is generated to produce maximum load current in order to avoid damage to electrical insulation of coils. If the mains voltage is lower than a certain value, part of the controlling voltage at the high-end level will be useless due to the inductance of the TLIA causing continuous conduction. In a summery, the useful range of controlling voltage will be narrowed by the inductance of the load.

## 6.8 Discussions

The a.c. line phase-controller has a very simple circuit and has been widely used in application such as lighting, heating, general motor speed control, etc., where the accuracy and response speed are not a vital problem. We have also successfully used it to

achieve multi-step positioning control of the TLIA. With the increasing demand of the positioning accuracy, problems will rise in vibration, overshooting and long settling time. They could be caused by the whole system components: actuator itself, DSP controller and/or the a.c. line controller. Here some effects arising from the a.c. line controller circuit are discussed.

The analysed and the tested results reveal that the control characteristics of the output voltage versus reference voltage are inherently non-linear. The nonlinearity will also be affected by the controllable range of firing phase angle and the actuator's status (for example, displacement, temperature, etc.). It will put an extra burden on the DSP control algorithm which can not totally eliminate/compensate the non-linear effects because the relationship is too complex.

Latching will still be a problem when the circuit is used in a closed loop control. The DSP board generates a transient controlling signal that changes its level according to the control algorithm. There will be instances when the controlling signal asks the controller to fire at a large phase delay angle to produce a small voltage output. In these cases, the circuit may be out of latching due to the two reasons:

- the control signal changes too fast toward zero
- firing delay angle is too large

Once the circuit loses latching, it will fire again but after half cycle of delay. Therefore the control action may be discontinuous.

The discontinuous control characteristics also appear as that the output voltage is determined by the phase angle of the firing pulse. In spite of burst firing pulse, the firing pulse occurs once per half cycle for full-wave controller. Once the triac is in conduction, the DSP controlling signal loses its control over the output voltage applied on the load until next firing pulse comes. This causes the second type of discontinuity in control. This discontinuity will limit the DSP's sampling speed. Otherwise the DSP may cause oscillations that we have experienced. All of these effects are reflected in the form of significant low frequency force fluctuation, which causes the mechanical vibration of the plunger. The vibration becomes more apparent with the increase of firing delay angle.

For the design of control algorithm, it is very difficult to take into account the effect of this latching problem. However, this vibration can be reduced by the filtering effects of the load inductance and the inertia of the plunger if higher frequency power supply is used.

## 6.9 Conclusions

A triac a.c. line phase controller was designed and fabricated to provide variable voltage power supply. It is very cost effective and has been successfully used in the DSP-based closed loop control for the multi-step positioning of TLIAs. For high precision positioning, the phase controller has its limitation and disadvantages in terms of linearity and continuity of control. These disadvantages may be reduced in some degree if dedicated designs in both the actuator and the phase controller is carried out in addition to adopting an appropriate combination of line frequency and voltage.

# 7 DEVELOPMENT OF A VOLTAGE-FED SINGLE PHASE VARIABLE FREQUENCY VARIABLE VOLTAGE CONVERTER

## 7.1 Introduction

The a.c. line phase controller has its inherent limitation in closed loop positioning applications, as discussed in Chapter 6. This motivates us to develop a better PSU. A single-phase a.c. to a.c. variable frequency variable voltage (VFVV) converter has been developed for the control of TLIAs. The reason of adding the function of variable frequency in the converter is for further research.

Generally VFVV converters can be classified into three categories according to their operational principle, namely cycloconverters, voltage-fed converters and current-fed converters [65].

The principle of a cycloconverter is to synthesise the output waveform by selecting an appropriate part of the sinusoidal supply waveform. This method is intrinsically suitable for a low frequency (relative to the supply frequency) converter, and has the advantages of high power limit, relatively low cost and losses.

A current-fed converter uses a large inductor to provide a constant current source rather than a variable voltage source. It is sometimes attractive in motor speed control where the torque developed by a motor depends on the product of flux and current. Speed variation can be achieved by controlling either or both parameters of voltage and current.

Due to the existence of a large inductor, power semiconductors have to withstand high reverse voltage. Therefore devices such as GTOs, power BJTs/MOSFETs/IGBTs are hardly suitable. Using thyristors or triacs will face the similar problems as encountered in the a.c. line phase controller.

Voltage-fed converters can work at high frequency and thus provide fast response to control signal that is very desirable in a closed loop control. Considering another factor that TLIAs prefer voltage control, we have therefore chosen the voltage-fed form of VFVV converter to be developed as the next PSU.

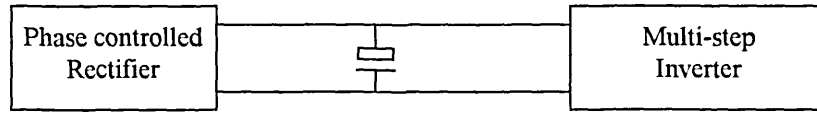


(a) Multistep configuration

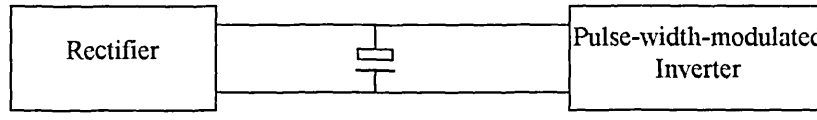


(b) PWM configuration

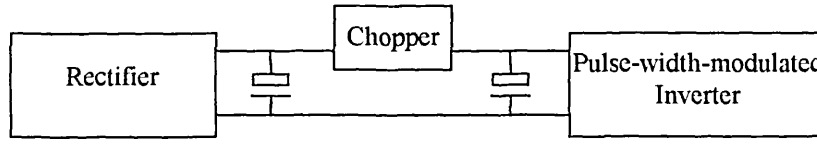


(c) Chopper/PWM configuration

Fig. 7.1 Different configurations of a voltage-fed VFVV converter system with d.c. link

Started in 1960 from the multistep arrangement, as shown in Fig. 7.1(a) which synthesises the output from a variable d.c link voltage by switching at the required frequency, the voltage-fed VFVV converter has evolved to the currently preferred solution of PWM as shown in Fig. 7.1(b) which uses a fixed d.c link voltage to synthesise the output. There are a number of possible solutions derived from these two basic arrangements, which determines the limit of frequency. Generally speaking, relatively high switching frequency is employed at the order of 1kHz. When further higher switching frequency, e.g., 2k-100kHz, is required, a chopper/PWM solution as shown in Fig. 7.1(c) can be used to extend the output frequency to this level as an alternative to the configuration Fig. 7.1(b) which will put higher specification of switch devices on the inverter side. The other advantage of configuration Fig. 7.1(c) is that it can be incorporated with regulator function to provide a d.c. link with lower voltage fluctuation than Fig. 7.1(a) and (b). This is the configuration we have used in our VFVV converter. The d.c. to d.c. chopper regulator and the inverter are treated separately in the design because they work in a relatively independent way.

As we know the PWM technique has the most wide-spread applications. It offers both high efficiency and high power density. This technique was adopted in the designs of the chopper regulator and the inverter.

The development of a power drive for the TLIAs forms an integral part of the whole research project. The reasons of why we develop an inverter PSU by ourselves instead of trying to buy one are,

- First of all, there is a special requirement to use a DSP to control the variable voltage converter and thus the positioning. This requires a proper interface between the converter and the DSP microprocessor
- Secondly the TLIAs are at the development stage, and their characteristics are still under investigation. More flexible power converter with such functions as variable frequency and variable voltage is required
- Thirdly it is required that the power drive and the TLIA must form an integral part of a system
- And finally we have not be able to find a ready-made commercial product that is

suitable for the purposes mentioned above.

Instead of pure theoretical study of different converters and devices, in this chapter we concentrate our efforts on the engineering aspects of the design plus some analysis, based on their application to the TLIAs [66].

## 7.2 Overview of the Topology of the Converter

Figure 7.2 shows the block diagram of the single phase voltage-fed VFVV a.c. to a.c. converter that is to be used together with a DSP board in a closed loop to control the positioning of the TLIA. The system consists of five principal parts:

- Power Supply Unit: it provides two types of d.c. voltages from the mains supply. The high voltage d.c. is to power the TLIA through the chopper and inverter, and the low voltage d.c. is to power all the rest of low-voltage circuits for signal processing and gate driving.
- Chopper Circuit: it functions as a static switch, controlled by PWM pulse, to step down the d.c. voltage which is rectified directly from mains supply to a lower regulated level which is used as a d.c. link voltage for the inverter that follows.
- PWM Chopper Drive: it generates a PWM pulse according to the panel control setting and the feedback of the chopper output, and provides soft start, voltage shift, gate drive with under-voltage protection. So the output voltage of the chopper can be manually controlled and automatically regulated.
- Inverter: a full-bridge topology is used for the inverter to convert d.c. link voltage to an VFVV a.c. output voltage which is also controlled by using PWM technology. Two identical inverters are connected in parallel to the d.c. link to drive two coils of the TLIA when needed.
- Inverter Drive: It provides PWM pulse, logic function, voltage shift and TTL interface to DSP board, gate drive and under-voltage protection function for the inverters.

Details about the design, calculation and analysis of those subsystems will be discussed in the following sections.

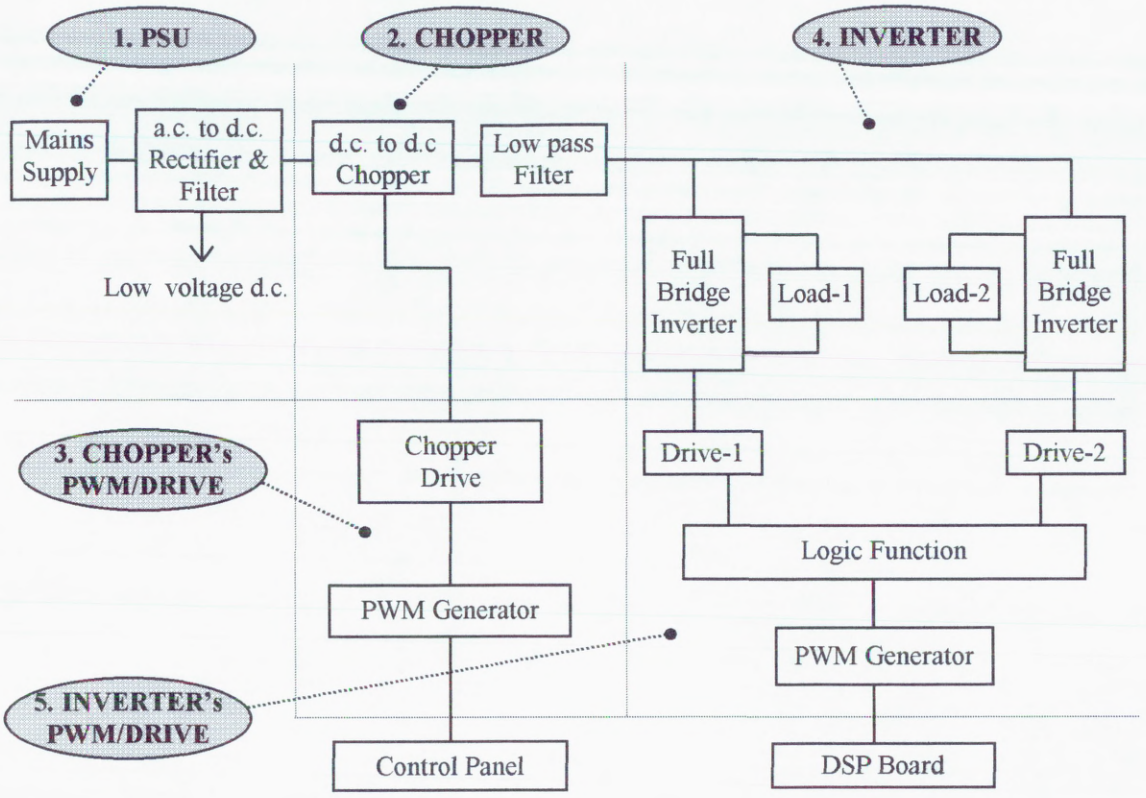


Fig. 7.2 Block diagram of the single phase voltage-fed VFVV a.c. to a.c. converter for TLIAs' position control

## 7.3 The Power Supply Unit

The circuit of power supply unit is given in Fig. 7.3. There are four d.c. outputs. The $V_{s1}$ is a high voltage d.c. used by the chopper circuit and the inverter circuit to power a TLIA. The $V_{s2}$ and $V_{s3}$ are 5V and 15V d.c. voltages for the signal processing circuit and gate drive circuit, except that the chopper's gate drive circuit is powered by another independent 15V voltage source $V_{s4}$. The reason for using an independent $V_{s4}$ is due to that a relatively low gate-drive voltage are required to trigger the power switch device that involves high voltage level and high voltage change. If $V_{s3}$ is used for this purpose, a high frequency pump circuit is required because high frequency is used in the chopper

circuit. It is also possible to derive $V_{s4}$ from $V_{s1}$ by using switching techniques or Zener diode. If $V_{s4}$ is derived from $V_{s1}$ by using switching techniques, it will inevitably involve more complicated circuitry. If $V_{s4}$ is derived from $V_{s1}$ by using Zener diode, larger losses on the associated current-limiting resistor will be incurred. Obtaining an independent $V_{s4}$ from a transformer with two outputs provides a simple solution. For the low voltage sources, there are many voltage regulator ICs available. Therefore there are no particular difficulties in the design of the PSU except to retain enough power reservoir. The selection of $C_1$ may need a little more attention. If $C_1$ is too large, the surge current at switch-on point may be large enough to destroy the bridge rectifier diodes. If $C_1$ is too small, it may not hold enough energy to ensure the chopper circuit can provide good regulation to its output voltage. The calculation of a minimum $C_1$ is discussed in the next section in connection with the chopper design. A resistor $R_{in}$ is used to limit current surge in the rectifier diodes. It should be as small as possible, but must ensure the maximum surge current at worst condition will not exceed the rated value of the diodes. Further more, to reduce losses in $R_{in}$ and provide better surge current protection, an inductor can be used to replace or connected in series with $R_{in}$.

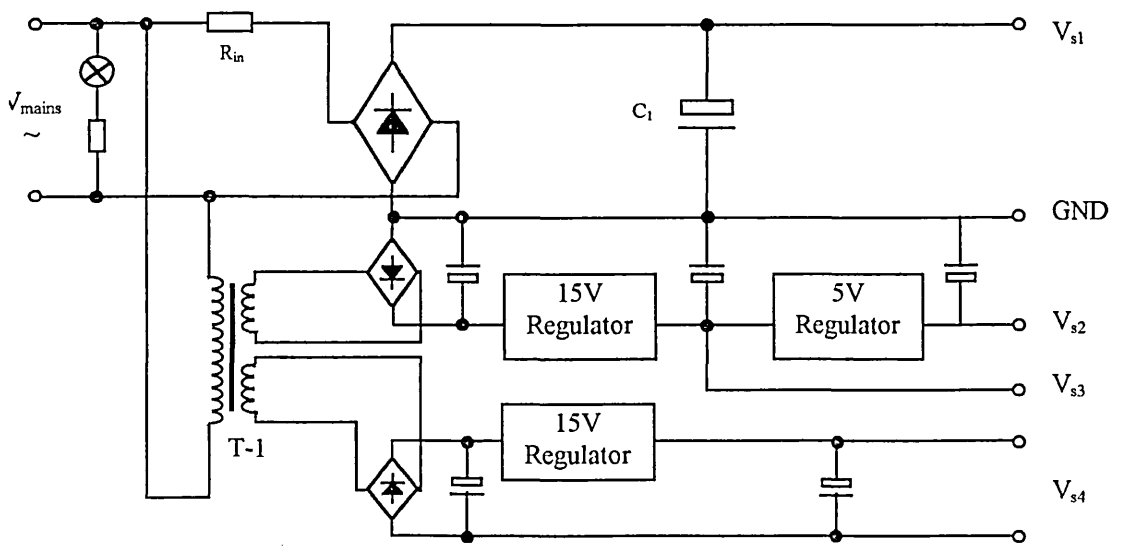


Fig. 7.3 The PSU circuit

## 7.4 The Switch Mode d.c. Chopper

The purpose of the d.c. chopper is to converter one level of d.c. voltage to another d.c. level. A chopper could be designed to work in linear or switch mode. The most significant differences between a linear and a switch mode chopper involve their efficiency, size, weight, material requirement, response time and noise characteristics, etc. The concept of switch mode power conversion is not new, but the technology was not quite ready until the last two decades or so. The availability of fast-switching high-voltage semiconductors, low-cost ferrite and metallic glass materials makes the complete implementation of switch mode power converter more reliable and practicable. We will use PWM technology in the design of our chopper circuit.

In the implementation of PWM d.c chopper, three basic configurations are usually employed. They are the buck converter, the boost converter and the buck-boost converter. Other circuit topologies are usually derived from one or more of these configurations. Figure 7.4 illustrates the basic circuit configurations and gives a brief comparison of these.

The three basic configurations have a common problem that they do not provide isolation between input and output. However, using a transformer for the isolation will degrade the transient performance, and using capacitor for the isolation may impose extra burden on the power switch device.

For our chopper, the output voltage will be lower than the input voltage. To obtain a simple but sufficient solution to the chopper, we have chosen the buck chopper configuration. Its merit of being easy to stabilise regulator loop is favourable, because the equivalent load of a TLIA is a function of displacement and changes over a wide range. The stability is an important issue under this type of application. As for the isolation problem, it is left to be solved on the side of low voltage circuit if needed. Sometimes isolation may not be necessary, determined by the applications of the TLIAs and the configuration of the parent system in which the positioning system is just a subsystem.

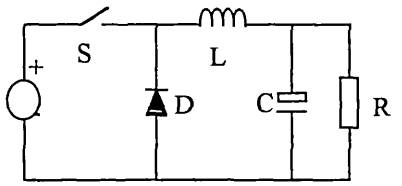


(a) Buck

Advantages:

- high efficiency
- high frequency
- no transformer
- easy to stabilise regulator loop

Disadvantages:

- high current ripple in capacitor
- current limit difficult
- crowbar diode required if S shorts

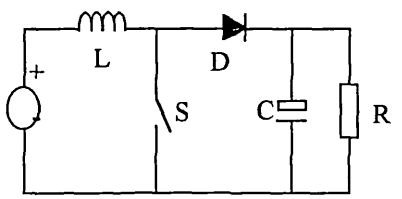


(b) Boost

- high efficiency
- high frequency
- no transformer

- high peak current in S
- poor transient response
- difficult to stabilise regulator loop

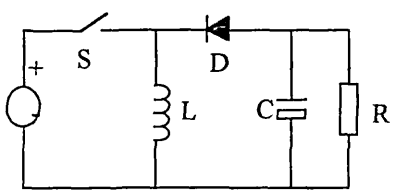


(c) Buck and boost

- high frequency
- no transformer

- high peak current in S
- poor transient response

Fig. 7.4 Three basic chopper configuration and their comparison

### 7.4.1 Design of the Buck Chopper

The actual chopper circuit is shown in Fig. 7.5. A MOSFET is employed as the power switch device, and a damping resistor is used in the output filter. High switching frequency PWM technology is employed to reduce the size of both transformer/inductor and capacitors, which therefore brings the direct benefit of low cost and lightweight of the circuit. However, high switching frequency will increase the switching losses of MOSFETs in addition to the conduction loss. From the power consumption point of view, the switching losses limit the high end of switching frequency. The current

industrial practice usually uses switching frequency ranging between 50kHz and 500kHz in converters. Balancing the cost of semiconductors and our requirements, we have chosen 100kHz for the chopper circuit.

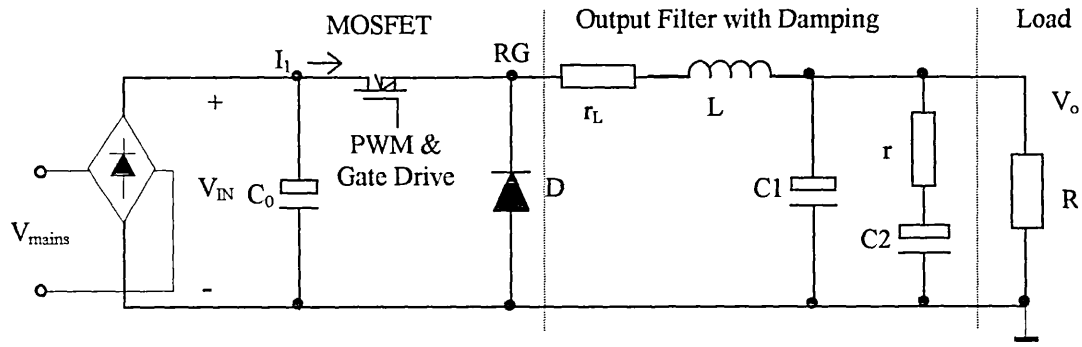


Fig. 7.5 The actual chopper circuit

Design of the chopper circuit involves steady state analysis and transient analysis. For the steady state design, the resistances of $r_L$ and $r$ have very little effect and is neglected therefore. Other assumptions are

- The MOSFET and freewheel diode have zero voltage drop and infinite resistance across them corresponding to conducting state and non-conducting state respectively
- The turn-on and turn-off time is short compared to the switching period
- The impedance of the d.c. link voltage source is negligible
- Output voltage $V_o$ is constant during a cycle of operation

With these assumptions, the time differentiation on the inductor's current and capacitor's voltage can be linearised. So we can have the following analysis:

1. The input d.c. voltage and the filter

The input d.c. is rectified from the mains supply. Because the maximum output voltage required for chopper will not exceed beyond 150V, we propose to use a small input capacitor $C_0$ to reduce the switching losses on the MOSFET. The voltage waveform on

the $C_0$ is shown in Fig. 7.6. It can be seen that the $V_{in}$ will be charged to the line voltage when the line voltage is higher than $V_{in}$, and will discharge itself to $V_{in\cdot min}$. If the $V_{in\cdot min}$ is a moderate value, the discharging happens nearly after the peak voltage of each half cycle. In this case, the relationship for a half cycle can be expressed as:

$$V_{in} = \begin{cases} \sqrt{2}V_{main}Sin(\omega t) & t_1 \le t \le t_2 \quad (7.1a) \\ \sqrt{2}V_{main} - C_0^{-1}I_{1.avg}(t - t_2) & t_2 \le t \le t_3 \quad (7.1b) \end{cases}$$

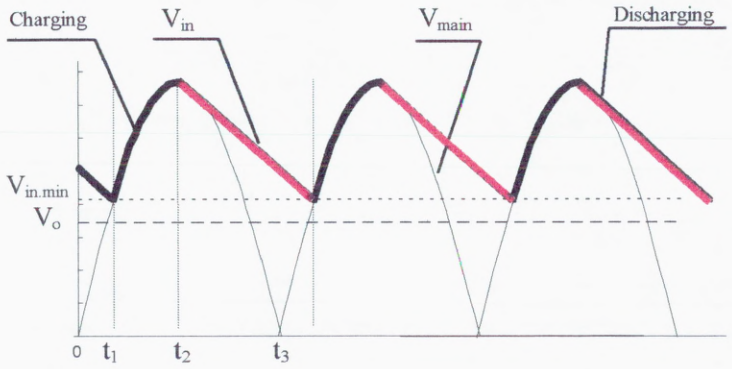


Fig. 7.6 The voltage waveform on the capacitor $C_0$

The filter capacitor $C_0$ should be chosen properly. If $C_0$ is too small, $V_{in}$ will discharge too rapidly to cause a very small drain-to-source voltage drop $V_{ds}$ on the MOSFET. This will cause the chopper out of function. To maintain enough $V_{ds}$ bias for whole range $V_o$ and $V_{in}$, the minimum $C_0$ can be calculated by

$$\begin{cases} C_{0.\min} = \dfrac{I_{1.avg}(t_3 - t_2)(\pi/4 + \omega^{-1}Sin^{-1}(2^{-0.5}V_{0.\max}/V_{main}))}{\sqrt{2}V_{main} - V_{0.\max}} & (7.2a) \\ \dfrac{P_{o.\max}}{I_{1.avg}} = \dfrac{1}{\pi}(\sqrt{2}V_{main} - \sqrt{1 - 0.5V_{0.\max}^2/V_{main}^2}) + \dfrac{\sqrt{2}V_{main} + V_{0.\max}}{2}(t_3 - t_2)\omega & (7.2b) \\ t_3 - t_2 = \pi/4 + \omega^{-1}Sin^{-1}(2^{-0.5}V_{0.\max}/V_{main}) & (7.2c) \end{cases}$$

where the subscripts '$_o$' stands for the chopper's output, $P_{o.max}$ stands for maximum output power, and so on. The MOSFET's current $I_1$ is treated as a constant at the average value because it works at high switching frequency compared with the mains' frequency. Equation (7.2a) and (7.2c) are obtained by solving (7.1) with the setting of $V_{in.min}=V_{o.max}$ and $t_2=\pi/2$. Equation (7.2b) is obtained according to the energy conservation principle that states that during each cycle the energy comes out of $C_0$ should be equal to that of the chopper's output under the assumption that energy loss in the components is negligible.

2. The voltage and current of the output filter

The output of the chopper is to drive an inverter that works at about 1kHz switching frequency. Since the chopper's switching frequency is much higher than the mains' frequency and the inverter's frequency, we can consider the input voltage $V_{in}$ and the output voltage $V_0$ are constant when studying the chopper's output filter in the steady state. The output filter could work at two conditions: continuous current condition and discontinuous current condition, depending on the switching frequency, PWM duty cycle, the inductance and the load current. Both conditions should be considered, due to the wide range of duty cycle that will be involved in the positioning control.

(1). Continuous current condition

At this condition, the current in the inductor will be continuous. The associated voltage and current waveforms can be illustrated by Fig. 7.7.

With the assumptions mentioned before, we can write the circuit equations as

$$\begin{cases} V_{in} = L\dfrac{di_L}{dt} + V_0 \\ i_L(0) = I_{\min} \end{cases} \qquad 0 \le t \le DT \qquad (7.3)$$

for the 'ON' state, and

$$\begin{cases} L\dfrac{di_L}{dt} = -V_0 \\ i_L(0) = I_{\max} \end{cases} \qquad \text{DT} \le t \le \text{T} \tag{7.4}$$

for the 'OFF' state. Solving (7.3) and (7.4), we obtain:

$$V_o = DV_{in} \tag{7.5}$$

$$I_{\max} - I_{\min} = (V_{in} - V_o)DTL^{-1} \tag{7.6}$$

Combined with average current relationship $I_{o.avg}=0.5(I_{max}+I_{min})$, (7.6) can be further expressed as

$$I_{max} = I_{o.avg}+0.5(D+D^2)TV_{in}L^{-1} \tag{7.7}$$

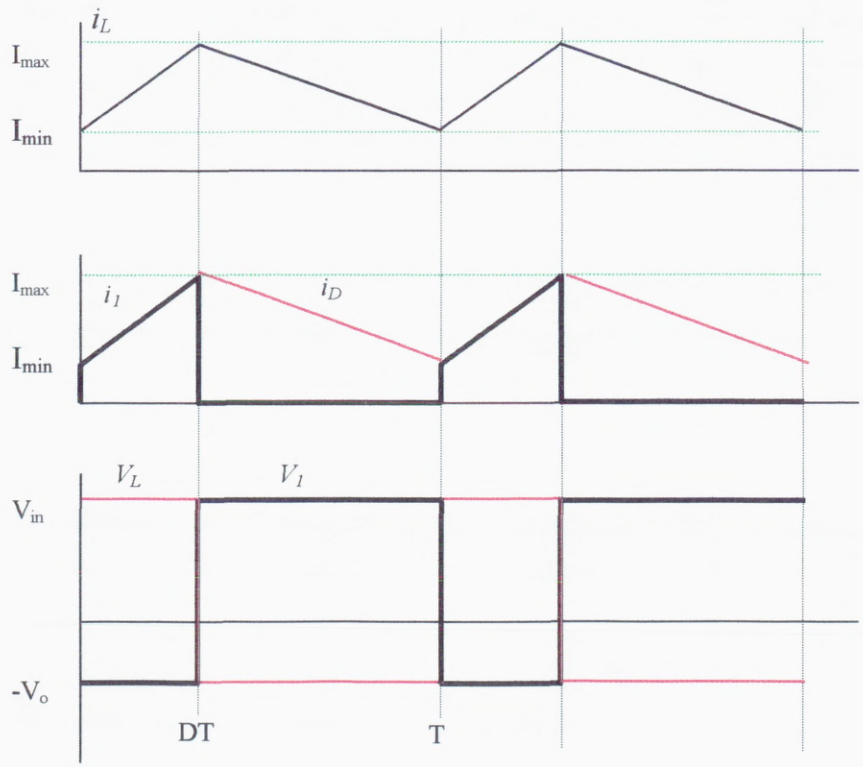


Fig. 7.7 Voltage and Current Waveform at Continuous Current Condition

$$I_{min}= I_{o.avg}-0.5(D+D^2)TV_{in}L^{-1} \tag{7.8}$$

Equation (7.5) means that the chopper's output depends solely on the fraction of time that the switch is closed, provided that the inductor current is continuous. Solving (7.8) for a zero value of $I_{min}$ at $t=T$ yields a relation for the minimum value of the inductance that will maintain continuous inductor current. The minimum value of the inductance is calculated by

$$L_{\min} = (D - D^2)TV_{in}I_{o.avg}^{-1} \tag{7.9}$$

(2). Discontinuous current condition

If the $I_{min}$ reaches zero before the MOSFET switches on, there will be a period in which no current flows in the inductor, i.e., the inductor works in discontinuous current condition. The current waveform in discontinuous condition could be illustrated in Fig. 7.8. The circuit equations for both 'ON' and 'OFF' states are the same as (7.3) and (7.4) except that the equation for 'OFF' state is valid only in the period from DT to $D_1T$. Using equivalent load resistance $R$ instead of average current $I_{o.avg}$, we can obtain the following relationship by solving (7.6) and (7.7)

$$I_{max}=(V_{in}-V_o)DTL^{-1} \tag{7.10}$$

$$I_{max}=V_o(D_1-D)TL^{-1} \tag{7.11}$$

Combining with average energy equilibrium equation $I_{max}V_{in}D=0.5V_oR^{-1}$, we can also obtain:

$$V_o = KV_{in}(\sqrt{1+2K^{-1}} - 1) \tag{7.12}$$

$$D_2 = 0.5D(1+\sqrt{1+2K^{-1}}) \tag{7.13}$$

$$I_{\max} = 4KV_{in}(RD)^{-1}(1+K-K\sqrt{1+2K^{-1}}) \tag{7.14}$$

where

$K=RTD^2L^{-1}/4$

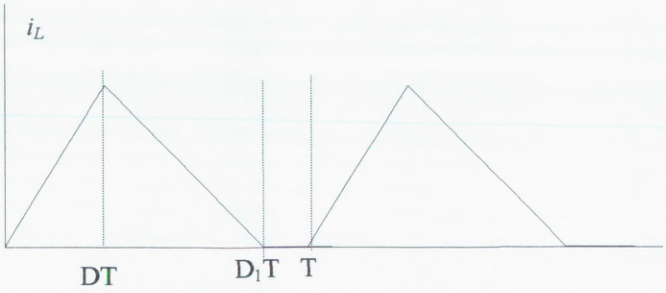


Fig. 7.8 The inductor's current waveform at discontinuous conduction condition

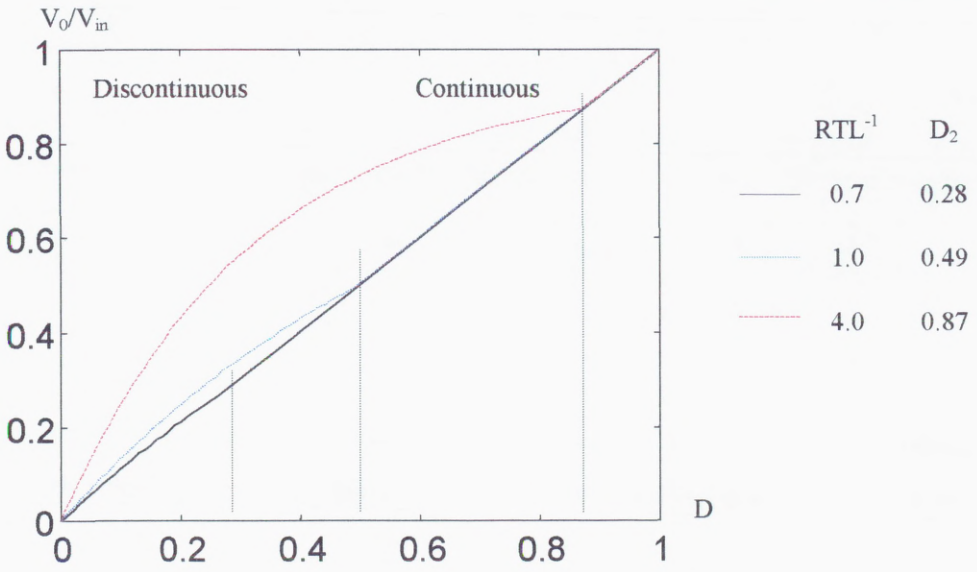


Fig. 7.9 Relationship with duty cycle under discontinuous current condition

Figure 7.9 gives the graphic illustration of the relations of the output voltage and current mode versus duty cycle. From Fig. 7.9 we can see that, for a certain load, the inductor works in a discontinuous mode for a smaller D and works in continuous mode for a larger D. In addition to the output voltage/current changes between the discontinuous

and continuous mode, the dynamic behaviour of the system changes as well. Both conditions should be considered in the design of a closed-loop regulator to avoid system oscillation.

### 7.4.2 The Calculation for the MOSFET

The MOSFET must work in a safe operating region that is limited by three variables:

- Maximum pulsed drain current
- Maximum drain to source voltage
- Maximum junction temperature

The maximum pulsed drain current can be calculated by (7.6) with the setting of $V_o$=0 and D=$D_{max}$ for the extreme cases such as the switch-on moment of mains supply. The Maximum drain to source voltage is the maximum input d.c. voltage. The maximum junction temperate is directly linked with the power losses and cooling.

In spite of the cooling method, power losses are vital factor in selecting power switch devices. The switching losses at turn-on and turn-off will play a major role in the assessment.

During continuous conduction at constant drain current, the MOSFET loss can be calculated by

$$P_c = I_{1.avg}^2 R_{DSS} \tag{7.15}$$

During turn-on and turn-off, power loss's variation with time has the relationship as shown in Fig. 7.10. The areas under the curves are the energy supplied to the MOSFET during turn-on and turn-off respectively in a cycle, which can be calculated by

$$p_{t.on} = 0.5 I_1 V_{DS} (t_2 - t_1) \tag{7.16}$$

$$p_{t.off} = 0.5 I_1 V_{DS} (t_4 - t_3) \tag{7.17}$$

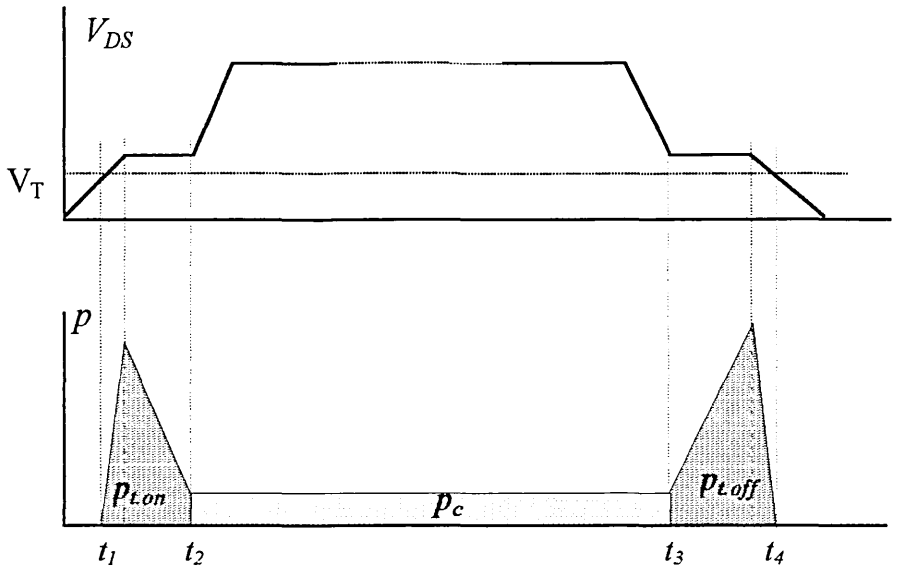


Fig. 7.10 Energy loss per pulse cycle

The total loss can be calculated by the product of frequency and the sum of the above two equations plus the conduction loss

$$P = P_c + f(p_{t.on} + p_{t.off}) \tag{7.18}$$

At low switching frequency, the MOSFET will usually have a relatively high conduction loss compared with BJTs. As the switching frequency increases, the BJTs' switching losses increase faster than the MOSFETs. After some frequency, MOSFETs will have lower total losses than BJTs. This becomes particularly significant in applications for which a high switching frequency is desirable to allow smaller inductors, capacitors and thus lower circuit cost.

In (7.16) and (7.17), the time interval is the only factor that can be controlled to reduce the losses. To reduce the time of turn-on and turn-off, a careful design of the gate drive circuit is required to provide sufficient gate-driving current (both source and sink currents) for rapid switching in addition to matching the switching time of the MOSFET. Usually the total switching time $(t_2-t_1+t_4-t_3)$ of the power switching device should be less than one per cent of the period of the base switching frequency to avoid problems caused by switching losses.

### 7.4.3 The Design of the Inductor

Unlike inductors in other applications, the power inductors operate under loss and/or saturation limited condition that requires special power ferrite with high saturation levels and low losses. The output inductor of a switched mode d.c. chopper has to operate with a d.c. current that causes a d.c. bias magnetic field. Due to these special requirements, the inductor can not be easily found from electronic component suppliers and should be fabricated specially.

There are two remedies to meet the requirement of the output inductor:

- Use gapped low-loss ferrite core
- Use a material with a low permeability and high saturation level

The effect of an air gap in the magnetic circuit is such that much higher field strength is needed to saturate a core. Besides the maximum output current, the inductance must be known before selecting a core and calculating the turns. There are some ready-made ferrite cores for the purpose of building a power inductor. The calculation of turns of the inductor is hugely simplified by using a ready-made core with a data sheet for calculation. We have chosen the RM-series from Philips products with 3C85 ferrite grade. The normalised inductance factor $AL$ and geometrical size are given in the data sheet. With an $AL$ value, the turn or the inductance can be calculated from

$$L=AL*N^2 \tag{7.19}$$

### 7.4.4 PWM Regulator and Drive

It is desired that the output voltage of the chopper be regulated, due to the following two main reasons:

- The input filtering capacitor is a relative small one, as discussed before. It has a large voltage ripple that will change with the load conduction and will be passed onto the output stage if the output voltage is not regulated.
- The effect of the output filter is affected by load and chopper's switching (duty

cycle). A small output filtering capacitor is desirable in the dynamic point of view. However small output filter capacitor has small capability to hold its voltage.

The regulation is achieved by modulating the pulse width at a fixed frequency. Although switching regulators are commercially available as integrated circuits, we will design a particular one to suit the inverters, because we wish to obtain a wide range of output voltage and linearity of control characteristics.

The pulse width modulator used in the chopper is a linear-comparator type. Its operation principle is to compare a linear ramp voltage $V_r$ with a control voltage $V_c$, as shown in Fig. 7.11.

The control voltage $V_c$ is the feedback from the chopper's output voltage. If $V_c$ increases, the comparator will trigger at a higher potential point on the ramp, produce a narrow output pulse which in turn causes the delivery of a lower output voltage, and vice versa. This circuit has a problem that it will generate very high duty cycle (close to an unity) for the first several pulses after the mains power is switched on (during this period the output voltage remains nearly zero). This will cause a large current surge for the power switching devices and may damage the device. To prevent this the pulse width should be limited, which is achieved by introducing a d.c. bias voltage $V_b$ on $V_c$ in the actual circuit, as shown in Fig. 7.12

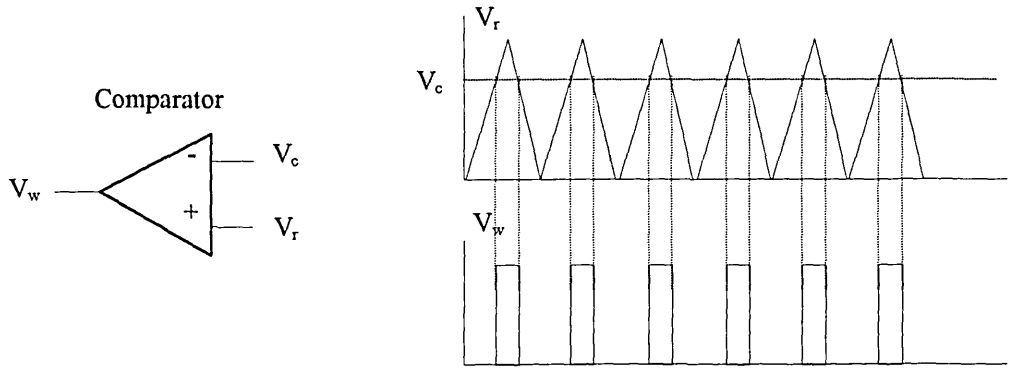


Fig. 7.11 Linear-comparator type of PWM

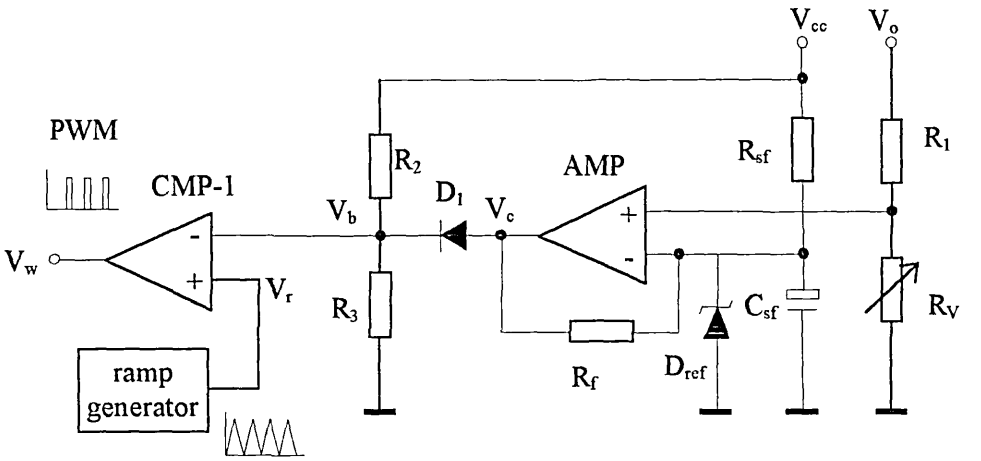


Fig. 7.12 The PWM regulator circuit

The PWM drive circuit is to amplify the PWM signal $V_w$ in order to drive the power switching MOSFET. For the buck chopper circuit we used, the MOSFET's source pin RG has a much higher voltage level (close to the $V_{in}$) than the maximum gate-source voltage (of about 20V usually). To drive the gate, the reference voltage level of the gate driving PWM signal must be shifted to the voltage level of the source pin $V_{RG}$. We have employed the technique that optocouples the PWM signal with the gate-driving circuit powered by an independent voltage supply. This solves the problem that requires floating reference voltage. The optocoupler should be capable of small rise time and fall time, high voltage isolation and noise immunity. The total rise and fall time should be smaller than the time of minimum non-zero duty cycle. We have employed a high-speed Schmidt trigger optocoupler H11N that can satisfactorily work at 100kHz. Power MOSFETs have relatively large gate charging capacitance, which requires the gate drive to be able to provide both source current and sink current with a certain capacity and switching speed. Otherwise the transition period of turn-on and/or turn-off will be prolonged by insufficient driving, and will cause larger switching losses that may incur the thermal damage of the device. Along with the drive's switching speed and output capability that can be easily satisfied even by signal BJTs or MOSFETs, an undervoltage protection is a

very important issue to prevent the power-switching device from working in amplification area. This leads us to use an IC drive integrated with the undervoltage lockout instead of using discrete BJTs or MOSFETs. The PWR-INT200 drive provides these functions and has a typical total switching delay time of about $1.2\mu s$ that just meets our requirement marginally. The gate drive circuit is shown in Fig. 7.13.

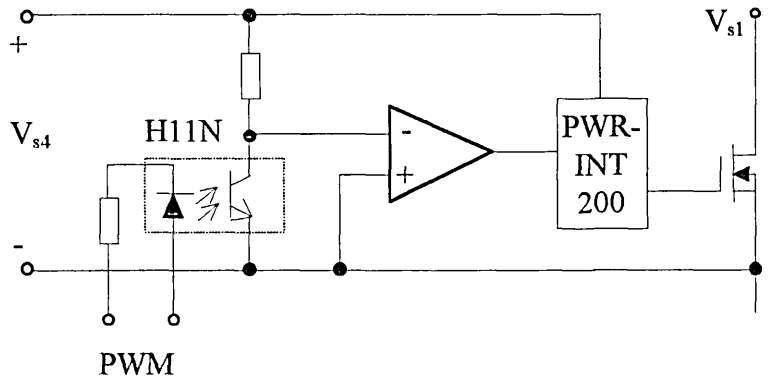


Fig. 7.13 The gate drive circuit for the MOSFET of the chopper

Other protection measures such as those for over-current, over-voltage, over-temperature, etc., have not been considered in the current design. They could be taken into consideration in further design, depending on the actual applications.

### 7.4.5 Stability of the System

To improve the response of the system, a feedback is introduced in the regulator. In principle a system with a negative feedback will be stable and a system with a positive feedback will be unstable. Because of the usage of frequency-dependant components, such as inductors and/or capacitors, and the parasitic effect in the circuit, a negative feedback in a certain frequency range will turn out to be a positive feedback in another frequency range.

Looking back at the configuration of our converter, we can find that it has a very wide range of frequency harmonics based on four fundamental frequencies:

- The mains supply frequency
- The chopper's switching frequency
- The inverter's output frequency
- The inverter's switching frequency

The regulated chopper should be unconditionally stable in such environment. The most effective method to study the stability of a system is by studying the transfer function with state-space method. Switch mode circuits have two states during each switching cycle. This raises difficulties in the use of the state-space method. To solve this problem, an averaging state-space (ASS) method is employed with a certain degree of compromise in accuracy. The ASS method weighs the two state-space equations (corresponding to 'ON' and 'OFF' states) according to the fraction of time each state remains in a switching cycle. To effectively use this method in the chopper circuit, it is assumed that the corner frequency of the output low-pass filter is at least a decade or two below the frequency corresponding to the switching frequency. In the analysis, we will firstly look for the transfer function of the chopper circuit without regulator by the ASS method. Then the transform function in a closed loop is derived according to feedback control theory, which is used directly in assessing the stability of the system.

1. Transfer function of the chopper circuit without regulator

The circuit shown in Fig. 7.5 will be used here again. The $r_L$ and $r$ should not be neglected here, since their small values may play significant role in dynamic analysis. Choosing the inductor's current and capacitors' voltage as the state variables, we can write the state-space equation as

$$\dot{x} = A_1 X + b_1 V_i \qquad \text{for 'ON' state} \tag{7.20}$$

$$\dot{x} = A_2 X + b_2 V_i \qquad \text{for 'OFF' state} \tag{7.21}$$

$$V_o = C^T X \qquad \text{for both states} \tag{7.22}$$

where

$x=[i_L \quad V_{c1} \quad V_{c2}]^T$

$$A_1 = A_2 = \begin{bmatrix} -r_L L^{-1} & L^{-1} & 0 \\ C_1^{-1} & -C_1^{-1}(R^{-1}+r^{-1}) & C_1^{-1}r^{-1} \\ 0 & C_2^{-1}r^{-1} & -C_2^{-1}r^{-1} \end{bmatrix}$$

$b_1=[L^{-1} \quad 0 \quad 0]^T$

$b_2=[0 \quad 0 \quad 0]^T$

$C^T=[0 \quad 1 \quad 0]$

Averaging the state-space Equations (7.20) and (7.21) by multiplying them with the duty cycle factor $d$ and off-duty cycle $d_1$ $(d+d_1=1)$ respectively, we obtain the averaged sate-space equation from the sum of the two multiplications:

$$\dot{x} = A\,X + b\,V_i \tag{7.23}$$

where

$A=A_1$

$b=db_1+d_1b_2=[dL^{-1} \quad 0 \quad 0]^T$

A system can be conditionally stable, unconditionally stable or unstable. Because of this, the relative stability of a system must be assessed at first. The relative stability is the investigation of the system's stability relative to a certain quantity under small signal perturbation. Carrying out small signal perturbation as

$y = \overline{Y} + \hat{y} \qquad y=\{x, d, V_i, V_o\}$

$d_1 = (1-\overline{D}) - \hat{d}$

with the capping of '—' and '^' represent steady-state value and small signal perturbation respectively. Averaging (7.20) and (7.21) with the above perturbation again, we obtain

$$\dot{\hat{x}} = A(\overline{X} + \hat{x}) + b_1(\overline{D} + \hat{d})(\overline{V}_i + \hat{v}_i) \tag{7.24}$$

$$\hat{v}_o = C^T \hat{x} \tag{7.25}$$

Taking the Laplace transformation to (7.24) and (7.25), and setting all initial conditions to zero, we have

$$s\hat{x}(s) = A\hat{x}(s) + b_1\hat{d}(s)(\overline{V}_i + \hat{v}_i(s)) \tag{7.26}$$

$$\hat{v}_o(s) = C^T \hat{x}(s) \tag{7.27}$$

The most useful information from the above equation is the response to variations of $\hat{d}$. With the setting of $\hat{v}_i = 0$, the small signal transfer function of output to duty cycle is:

$$\begin{aligned} \frac{\hat{V}_o(s)}{\hat{d}(s)} &= \frac{C^T b_1 \overline{V}_i}{(sI - A)} \\ &= \overline{V}_i H_e(s) \end{aligned} \tag{7.28}$$

2. The closed loop transfer function

The control diagram of the chopper with a feedback PWM regulator can be simplified as Fig. 7.14(a). The error in the comparator of the PWM is

$$v_e = v_c - v_f = v_c - Av_o \tag{7.29}$$

where the $v_c$ and $v_f$ are the control input signal and the feedback signal respectively, $A$ is the amplification of feedback network. For a linear pule width modulator, the change of the duty cycle is proportional to the $v_e$, i.e.

$$\Delta d = \beta (v_c - v_f) \tag{7.30}$$

where the $\beta$ is called as the modulation factor. Applying Laplace transformation to the above equation under small signal condition, we can have

$$\hat{d} = s^{-1}\beta(v_c - Av_o) \tag{7.31}$$

Then Fig. 7.14(a) can be represented in s-space by the equivalent block diagram of Fig.

7.14(b). The closed loop transfer function corresponding to Fig. 7.14 is

$$\frac{v_o(s)}{v_c(s)} = \frac{\beta \bar{V}_i H_e(s)/s}{1 + A\beta \bar{V}_i H_e(s)/s} \tag{7.32}$$

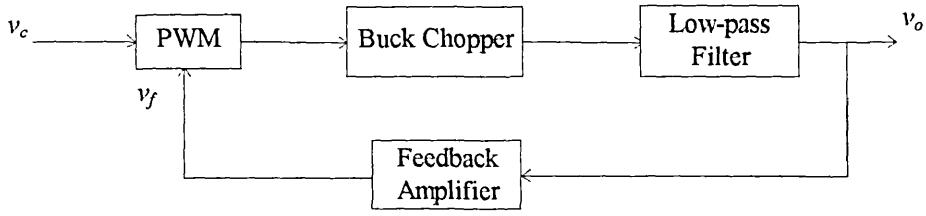


(a) Diagram in function

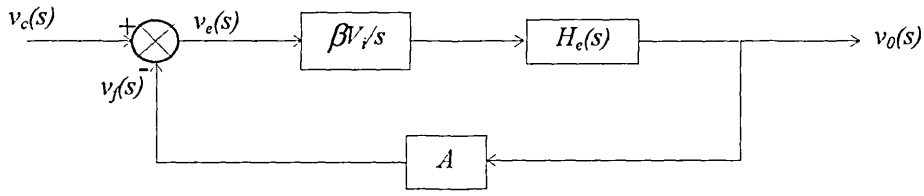


(b) Diagram in s-space

Fig. 7.14 Block diagram of the regulated chopper

3. The stability

From control theory we know that the requirement for a linear time-invariant system to be stable is that all the poles in the closed loop transfer function must lie in the left half of the s-plane. Setting the denominator of (7.32) to zero, we can obtain the poles and make the judgement of whether the regulated chopper system is stable or not, relative to the control signal $v_c$. For an unconditional stability, the accepted norm is to have a gain

margin/change of 6dB and a phase margin/change of 45° in the working frequency range. Figure 7.15 illustrates the gain response and phase response for some combinations of $L$, $C$ and $r$ of the chopper circuit.

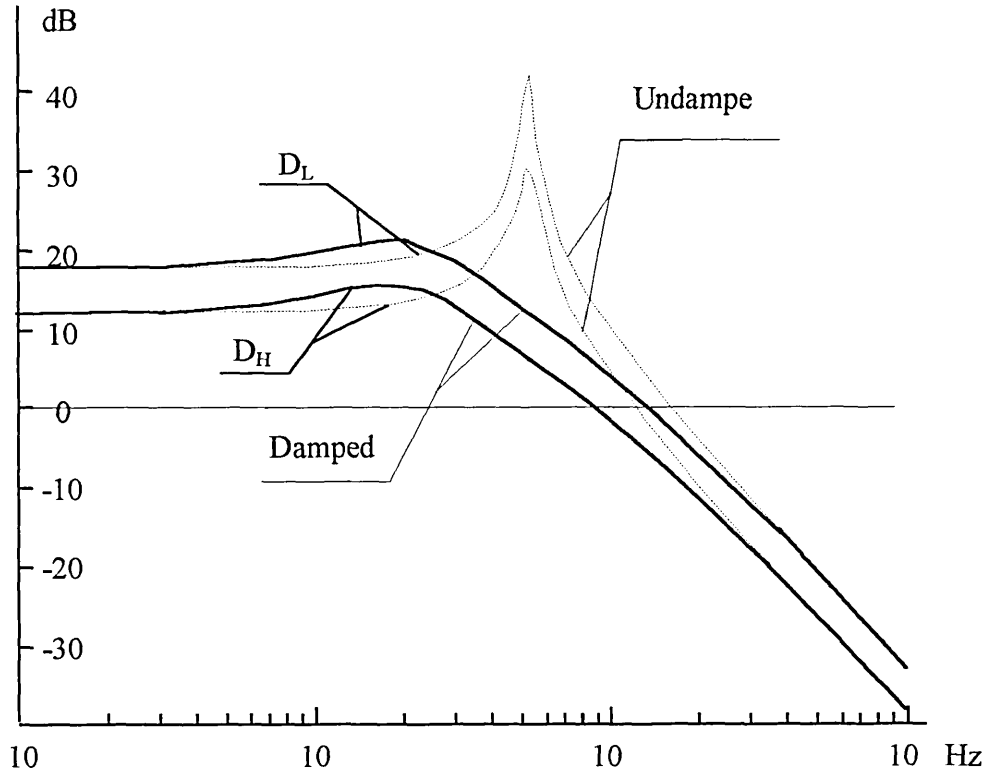


Fig. 7.15(a) Gain response of the chopper circuit

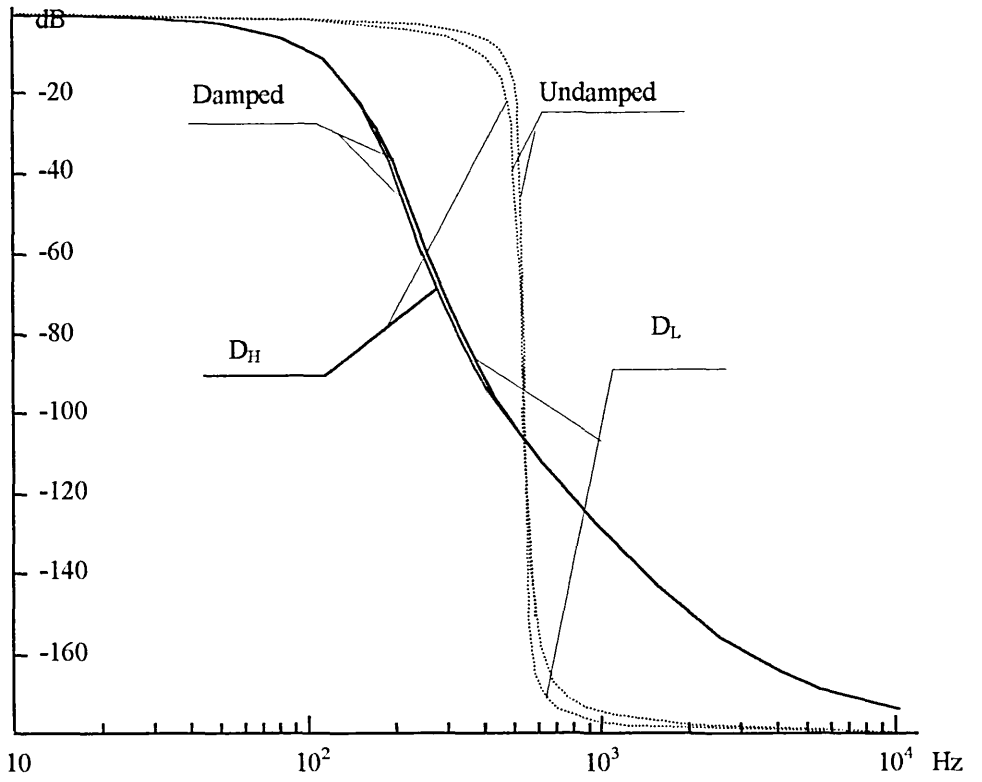


Fig. 7.15(b) Phase response of the chopper circuit

The general implication of the responses is that

- A large L is desirable, but for the bandwidth requirement a small product LC is desirable
- The higher the switching frequency, the wider the frequency band available for manipulating the loop response, but the switching frequency is limited by the power switching devices
- Resistor *r* provides a damping to reduce peaking at resonant frequency and, in turn, reduces the steepness of the slope of the magnitude response. With the damping resistor, the sensitivity of the component tolerance is reduced as well.

An effective damping requires a large damping capacitor $C_2$ that is usually several times

of the output filter capacitor $C_1$. The damping resistor is a high-current low-value one. Due to the difficulty in controlling the accuracy of low-value resistance, L/C ratio should be at least 1 to avoid very low *r*. But the *r* should not be too high because extra power losses will consumed by *r*.

## 7.5 Design of the Single Phase Voltage-Fed Inverter

An inverter is a d.c. to a.c. converter. There are three types of inverters, depending on the type of commutations:

- PWM inverter
- Resonant inverter
- Forced-commutated thyristor inverter

The resonant inverters are very efficient in high-frequency applications requiring fixed output voltage. The forced-commutated thyristor inverters have only advantages in high power applications. The PWM inverters have very wide applications due to the development of fast switching power devices. We will employ PWM technology in the design of the inverter

The voltage-fed inverter uses stiff d.c. voltage source instead of d.c. current source. The chopper circuit developed in previous section provides the d.c. voltage link required by the voltage-fed inverter to be developed here. A variable output voltage is obtained by varying the gain of the inverter, which is accomplished by PWM control within the inverter.

### 7.5.1 Full Bridge Inverter

For PWM bridge inverters, there are two basic topologies: half-bridge and full bridge, as shown in Fig. 7.16.

The half-bridge configuration requires two d.c. sources of equal voltage, which makes it less desirable in most cases. The full-bridge configuration, used in our inverter, uses one

d.c. voltage source and produces the same amplitude of a.c. voltage as half-bridge configuration. During inverter operation, $S_1$ and $S_4$ are simultaneously turned on and off according to the PWM pulse while the $S_2$ and $S_3$ remain open. After the end of each half-cycle, all the four switches reverse their state. Because the inverter is going to drive an inductive load of a TLIA, freewheel diodes should be in parallel connection with each of the power switching devices to provide paths for the flow of bi-directional load current. When the load current flow direction is against the load voltage polarity, energy is returned from the load to the source. So the d.c. voltage source must be capable of absorbing this energy. This usually requires the d.c. voltage source has a capacitor to store the energy. To prevent short circuit and unnecessary power loss from d.c. voltage, a proper timing should be provided to prevent $S_1$ and $S_2$ or $S_3$ and $S_4$ in conduction at the same time.

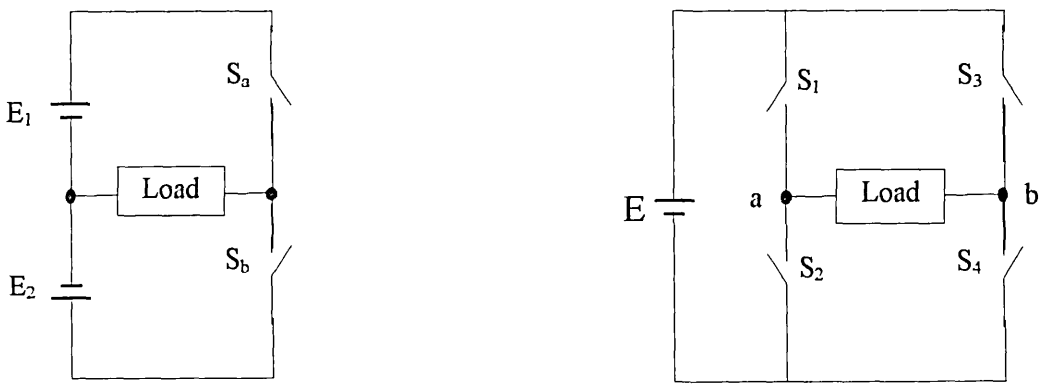


(a) Half bridge (a) Full bridge

Fig. 7.16 Single-phase half-bridge and full-bridge inverter

At present, the TLIAs are designed to work at low frequency of about 50Hz. The switching frequency could be several times of the fundamental output frequency. At this switching frequency range, IGBTs can deliver much lower conduction loss than

MOSFETs, without suffering much switching losses. We have employed IGBTs as the power switching devices in the inverter. Two identical inverters are connected, in parallel, to the d.c. link to drive TLIAs with two control coils.

### 7.5.2 PWM and Logic Circuit

#### 1. Which PWM?

There are various techniques to vary the inverter gain, and thus control the output voltage. The most efficient and widely used method of controlling the gain is to incorporate PWM in the inverter. Even if the topology of inverters could remain the same, PWM method could be in many forms [65, 67-69], such as

- Single PWM
- Multiple PWM
- Sinusoidal PWM
- Modified sinusoidal PWM based on harmonic elimination principle or minimum ripple current principle
- Adaptive current control PWM
- Phase-shift PWM

Since our inverter is to be used in a feedback closed loop, the linearity between the input control voltage and the output voltage is the major concern here. The inverter with linear control characteristics will bring huge advantage in the design of closed loop controller of positioning, which will be discussed in the chapter 8. It is very easy for the single PWM and the multiple PWM methods to obtain this linearity from a simple circuit. However the multiple PWM method has a better distortion factor than the single PWM method. So we come to use a linear modulation of uniform pulse width for the multiple PWM method. The linear modulation of uniform pulse width technique is the same as that used in the chopper's PWM chopper except that the control voltage $V_c$ is from the D/A converter on the DSP board.

2. The Logic Function

For the multiple PWM inverter there are two types of signal involved: the PWM switching pulse and the signal to control the inverter's output frequency. In order to make use of logic IC chips we treat these two signals as a logic signal in our circuit. The desired timing sequence of the gate-driving pulse for the four switching devices is illustrated in Fig. 7.17. Their logical functions are

$$S_1 = S_4 = C \cap W \tag{7.33}$$

$$S_2 = S_3 = \overline{C} \cap W \tag{7.34}$$

where the $W$ and $C$ represent the PWM logic signal and output frequency control logic signal respectively, $S_{1\sim4}$ stands for the logic gate drive signal.

When the number of pulse in per cycle is small, C should be synchronised with W to keep balance between the two halve cycle of output. For simplicity we derive C from W by using a binary counter. In this way, the inverter's output frequency can be controlled by changing the fundamental frequency of the PWM or the base number of the counter. The base number of the counter is the number of pulses during one output cycle interval. When it is set to one, the circuit is degraded into a single PWM. However the counter should not work directly on the W signal because W may have zero or unit duty cycle that will cause errors in counting. To prevent this problem a triggering signal synchronised with the ramp signal of the PWM generator is used for the counter. We have employed a waveform generator chip RS8038 that can generate ramp signal and synchronised square wave signal. The ramp signal is used for pulse width modulation and the square wave signal is used by the counter.

Figure 7.18 describes the circuit that generates the logic function for two inverters. As mentioned in Chapter 6, the second coil could be controlled dependently or independently. For independent control, a second PWM signal will be generated according to external control signal $V_{c2}$. The dependent control with linear relationship can be achieved very easily in this circuit by inverting the first PWM signal as the second

PWM signal. The manual switch $S_m$ used in the circuit is for the selection of control mode of the second inverter.

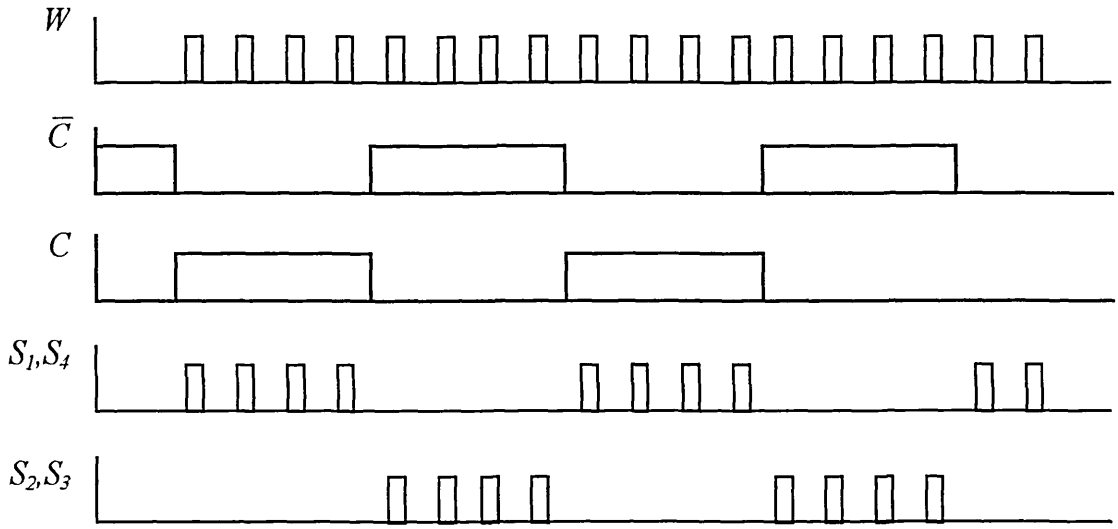


Fig. 7.17 Timing sequence of gate driving logic function with base number of eight per cycle of output frequency

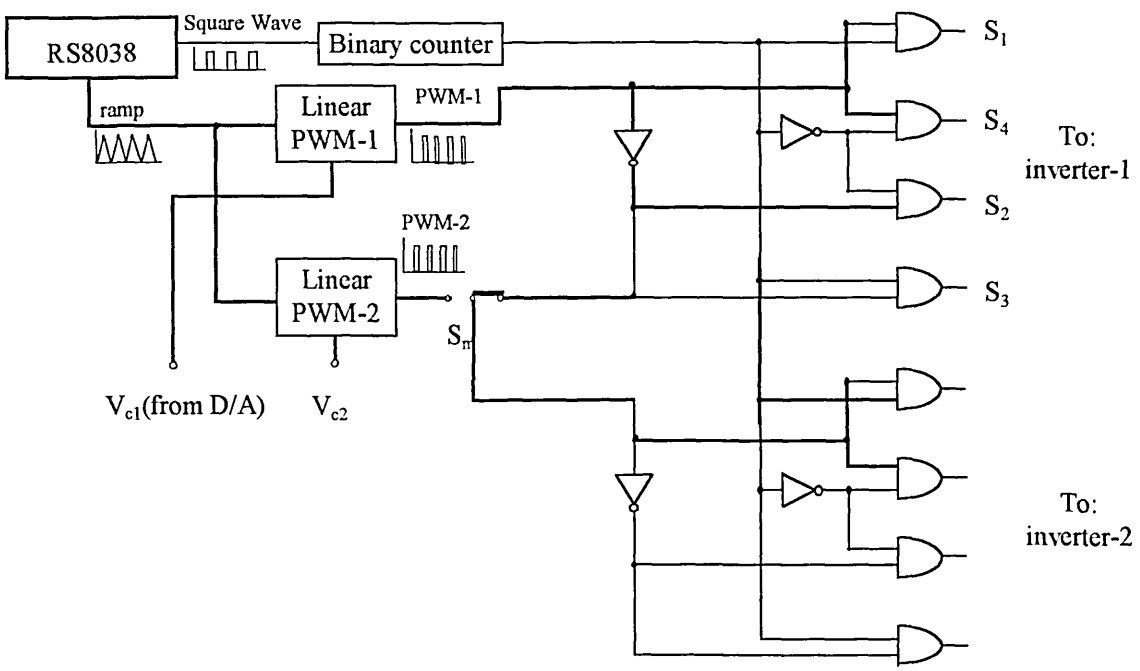


Fig. 7.18 The circuit for generating two PWM logic signals

### 7.5.3 The Gate Drive

For the full-bridge inverter configuration, the upper half of the power switching devices $S_1$ and $S_3$ should have floating reference voltages at point 'a' and 'b' that are shown in Fig. 7.16. The voltages at points 'a' and 'b' will change between zero and $+V_{in}$. This requires their gate driving voltages must be pumped to and float with the voltage at reference points 'a' and 'b'. To achieve this purpose floating voltage sources are designed for $S_1$ and $S_3$.

Similar to the requirement of the MOSFET gate drive of the chopper, major considerations in the design of gate drive should be paid to the switching speed, driving current, under-voltage protection, and noise rejection. Enough switching speed and driving current (sink and source current) are essential factors to quickly turn on/off the IGBTs and thus to reduce switching losses. Undervoltage protection (lockout) is also a vital factor to prevent IGBTs from working at amplification area that may cause thermal defect of the devices. Noise rejection provides a protection of fault switching action caused by the EMI of high frequency sources from the chopper circuit.

Pairs of high-side and low-side drive ICs PWR-INT200/201 are used in the design. The inverter circuit with its gate drive is shown in Fig. 7.19. The *LS* signals directly control low-side MOSFETs. The $\overline{HS}$ signals cause the PWR-INT200 to command the PWR-INT201 to turn high-side IGBTs on or off as required. Unlike the solution to use an independent voltage source in the chopper's drive, floating voltage sources for the high-side drivers are derived from $V_{DD}$ through $D_n$ and $C_n$ (n=1,3) in the inverter's drive. There are four floating voltage sources required for two full-bridge inverters. When the low-side IGBT is turned onto saturation, $C_n$ is quickly charged to $V_{DD}$ through $D_n$. When the low-side IGBT is turned off, the high-side PWR-INT201 is turned on and powered by $C_n$ whose voltage floats with the voltage at point 'a' or 'b'. The *LS* and $\overline{HS}$ voltage levels are compatible with 5V CMOS logical level, which lets the driver can to be driven directly from logic ICs. A logic inverter is used in front of $\overline{HS}$ to convert active-high logic $S_1$ and $S_4$ into active-low logic signals required by $\overline{HS}$s.

Protection is achieved by the functions incorporated in the PWR-INT200/201. An RS-latch in the PWR-INT200 prevents the low-side driver and high-side driver from being on at the same time, regardless of the input signal. To match the propagation delay of both sides, the PWR-INT200 provides switching delay to further prevent both sides from being turned on at the same time during switching transitions. Both *LS* and $\overline{HS}$ inputs are Schmidt-triggered, which provides a certain degree of immunity to high frequency noise.

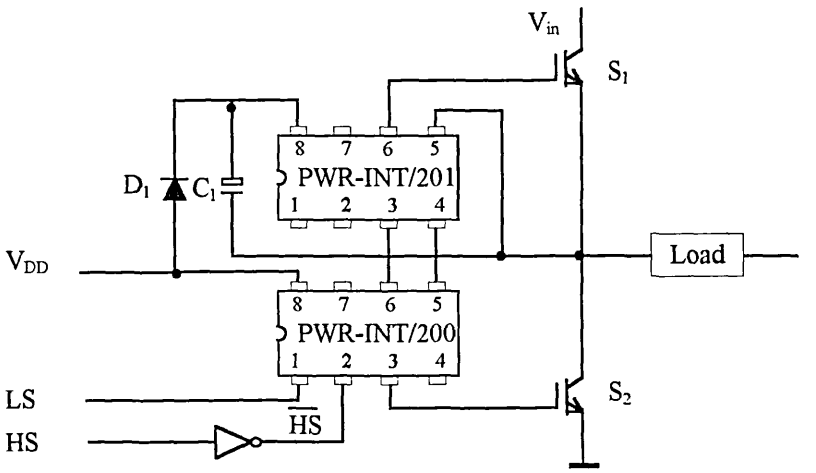


Fig. 7.19 Half the inverter with its gate-driving circuit

## 7.6 EMI Problems

Switch-mode power electronic circuits, by switching large amount of current at high voltage, can generate electrical signals that could affect other electronic systems. This is particularly apparent in the d.c. to d.c. chopper in our system. This unwanted signal causes the so-called electromagnetic interference (EMI). It can be transmitted by radiation through space or by conduction along cables. Hence it is particularly difficult to eliminate EMI.

Apart from emitting EMI, the control circuit could also be affected by EMI generated by its own power circuitry. This is what in considered here. We have experienced that the EMI emitted from the chopper circuitry caused malfunction of some logic ICs in the inverter circuit.

Although the chopper and the inverter both work in PWM switching mode and generate EMI, the chopper has much higher current and voltage change rate than the inverter, and thus become the major cause of EMI in our system. The logic ICs are all low voltage semiconductors, compared with the chopper's operating voltage. This makes the logic ICs more susceptible to EMI from the chopper. With the output current increase, we have observed two apparent phenomena caused by chopper's EMI, which are

- The frequencies of the ramp generators in both the chopper and the inverter, particularly in inverter, were disturbed with the switching action. This can be explained as EMI interfering with the reference voltage and the integrated voltage on the ramp capacitor are interfered by the EMI. So, the comparator will compare two signals contaminated with EMI noise, which will inevitably cause inaccuracy in the timing and thus the frequency.
- The counter IC may malfunction when the output current exceeds a certain level. As we know, all logic ICs have a certain noise immunity that ensures a proper function of all the other logic chips. The reason why only the counter IC is more susceptible to noise than other logic chips is due to the fact that it is an unsynchronised ripple counter. Solution to this problem is to use a synchronised counter or to reduce the EMI level. However, using a synchronised counter will change the whole circuit configuration a lot. The best way is to reduce self-induced EMI with slight modification of the circuit.

We are not going to study the whole EMI and EMC theory here, but will concentrate on solving the EMI problems encountered in the fabrication of the circuit.

By studying the configuration of the whole system we can see that a dual output transformer is used to provide power for all signal/drive circuits of both the chopper and the inverter. The transformer used in the design is a general purpose one without

electrostatic shielding. So significant parasitic capacitance exists among its three windings. The parasitic capacitance provides a connection path for high frequency noise emitted from the chopper. We estimate this is to be one of the major sources of our EMI problem. Instead of buying another transformer with electrostatic shielding, we alter the design of the chopper to reduce the EMI. The revised chopper circuit is shown in Fig. 7.20. The chopper's drive circuit has the reference voltage at point RG at the source pin of the MOSFET. For the old circuit as shown in Fig. 7.5, $V_{RG}$ may jump between 0 and $V_{in}$ at turn-on or turn-off transition process under continuous current condition, or between $V_o$ and $V_{in}$ under discontinuous condition. The voltage change rate $d(V_{RG})/dt$ will be very large since the switching transition period is very short. It is the high $d(V_{RG})/dt$ that causes EMI mainly through the transformer's parasitic capacitance. For the revised circuit, the $d(V_{RG})/dt$ equals $d(V_{in}-V_o)/dt$. Since $V_{in}$ and $V_o$ are voltages on relative large filtering capacitors with small voltage change rate, the $d(V_{RG})/dt$ will be much smaller than that of the old circuit. The $d(I)/dt$ will not cause much EMI through space transmission for the current rating, for the two reasons:

- The current in the inductor can not change rapidly.
- The high current switching in the circuit tracks will not produce much electromagnetic field due to the fact that not many high-current carrying tracks are involved in the tracks.

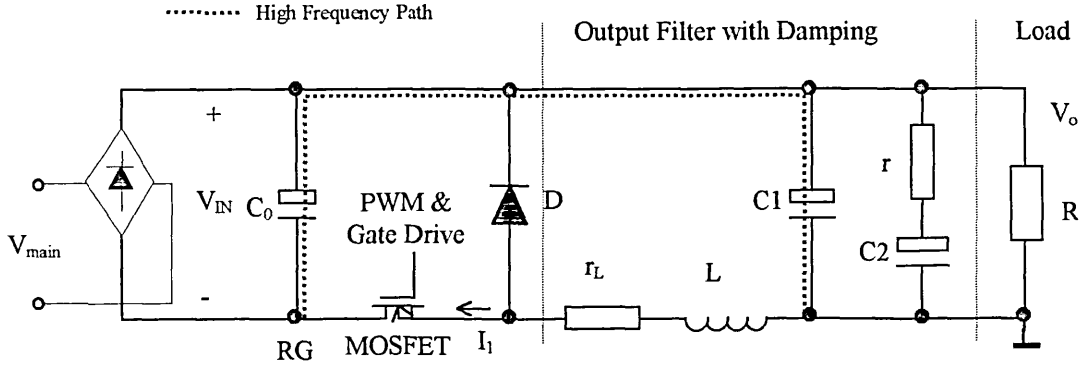


Fig. 7.20 The revised chopper circuit

In addition to alternative the design of the chopper circuit and to use high-frequency decoupling capacitors for ICs, other efforts have been made to reduce the self-induced EMI, which are:

- Increasing the cross section of the power supply track to reduce their impedance, which can reduce common impedance coupling
- Partitioning the system into subsystems according to the frequency and power levels to reduce interference between subsystems
- Having a proper grounding arrangement. A modified single point grounding system is employed, which allows subsystems grounded at local so as to eliminate common impedance grounding coupling and low frequency ground loops.

With the above measures, we have effectively solved the self-induced EMI problems for the circuit. We did not consider the EMI for other systems and has not carried out much theoretical study of this topic, as it is outside the scope of the current research.

The following picture is the physical inverter we designed. It can provide the functions as specified before, i.e.

- Manual control of output frequency
- External and/or manual control of output voltage
- Two control modes: independent control by using two control signals and dependent control by using one control signal
- A low-pass amplifier for processing external signal which could be the sensor's feed back in the actuator positioning system
- One channel input/output interface to the A/D and D/A converter

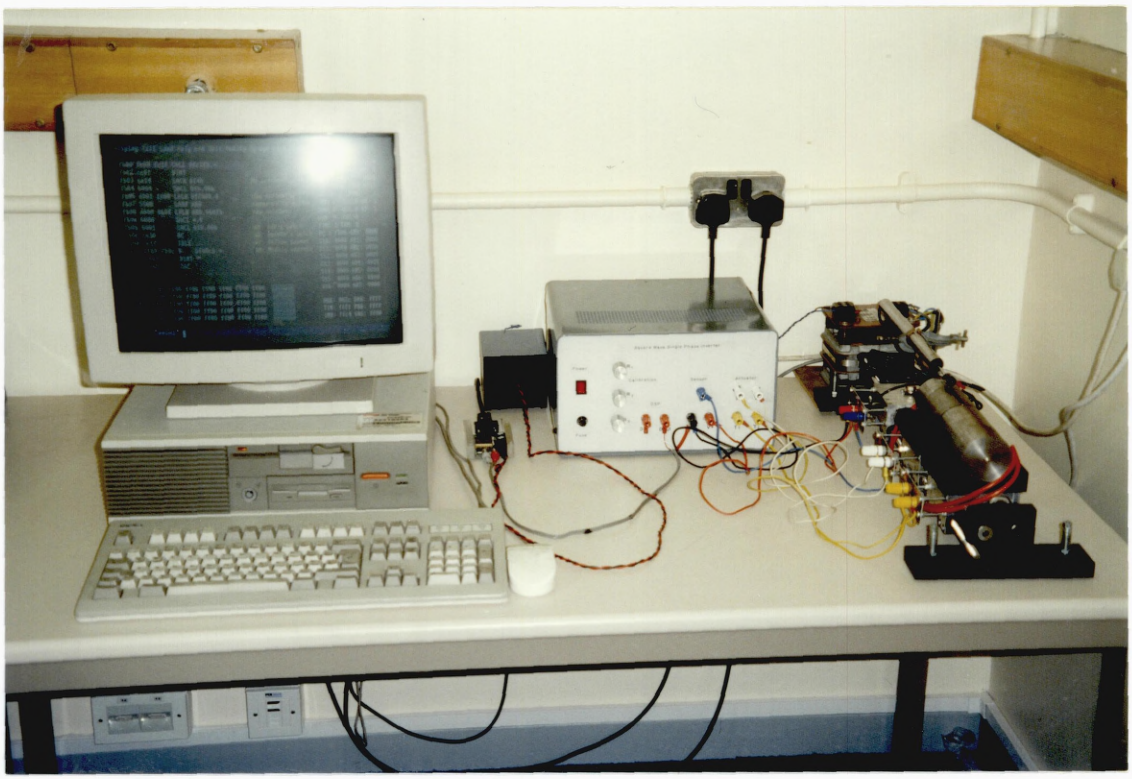

Fig. 7.21 The photograph of the single phase VFVV converter

## 7.7 Conclusions

A single-phase voltage-fed VFVV converter with linear control characteristics has been developed for the control and further study of TLIAs. The converter consists of a d.c. to d.c. buck type chopper and two parallel-connected full-bridge d.c. to a.c. inverter. Switch mode PWM technology has been used in the design of both the chopper and the inverter to achieve high efficiency, high power density and light weight. Cost and efficiency has been taken into account in choosing the topology and configuration of the

converter. In addition to explanation of the operation principle and design of the circuit, a steady-state analysis method is used for most of the design's calculation, and an averaging state-space method is used to study the dynamics of the system. Particular attention is paid to reducing the switching losses of the power switch devices and reducing the self-induced EMI, which were encountered in the fabrication engineering. This circuit has been successfully used to drive the TLIAs.

# 8 POSITION CONTROL BY USING DSP TECHNIQUES

## 8.1 Introduction

With the ever increasing requirement in terms of high positioning accuracy and response speed, much effort was spent to improve the performance of the actuator by modifying the structural design. However while most of these attempts were rather successful, the characteristic limitations of the mechanical system are still present. Internal physical features such as friction force, non-linear characteristics and process parameters variation are always present and hinder the performance of actuating system [70]. Analogue controllers are not flexible enough to deal with these major restrictions. Digital control systems offer many advantages over their analogue counterparts. Among these advantages are the following:

- Low susceptibility to environmental conditions
- Interference rejection associated with digital signal transmission
- Zero 'drift' of parameters
- Perform highly complex tasks at low cost
- Flexibility of easily making changes in software

A simple combination of conventional closed loop control with microprocessor based controller and a sophisticated digital control algorithm could considerably improve the dynamic as well as the static characteristics of an actuator system. However, digital control techniques have limitations such as:

- The introduction of errors or noise due to the finite precision of digital computation and the abrupt changes due to the discrete-time nature of digital control
- The need for more sophisticated engineering in order to take advantages of high-

performance control algorithms

- Greater limitation on speed of operation
- Greater potential for catastrophic failure

These should be properly considered at the stage of preliminary evaluation of the technique to be used. Here we will just concentrate on the digital control technique in the realisation of TLIA's positioning control.

Designs of digital controllers usually are divided into two categories: the transform method and the state-space method, which are also referred to as classic method and modern method respectively [71,72]. The difference in the two approaches is entirely in the design method. The end result, a set of difference equations providing control, is identical. The main advantage of the state-space approach to control is its ability to handle Multi-Input Multi-Output (MIMO) systems. For a Single-Input and Single-Output (SISO) system, the classical method has the merits of simplicity and clarity. Therefore, we have chosen the classical transform in the design of the controller for the TLIA system that is configured as a SISO system as discussed in the previous two chapters.

One of the straightforward design methods for the digital controller is to emulate a continuous controller by digital implementation. Because the design and analysis of analogue controllers have been better understood, it is highly practicable to design a digital controller by digitising an analogue controller. The major property required by the digitised controller is the fidelity of the impulse and frequency response of the original analogue controller. The fidelity depends on the sampling rate and on the particular method of discretization. The common properties are that by lowering the sampling rate, the fidelity and accuracy of the digitised controller are decreased.

Another design method is to discretize the system model at the outset, then to implement the design entirely using the discrete representation. This method is referred to as z-plane design, discrete design or direct digital design. Theoretically the behaviour of a closed

loop system with discrete design controller is not dependent on the initial choice of the sampling rate because none of discretization of analogue controller is considered. Due to saturation of the controller in practical systems and inter-sampling behaviour not detected by the z-transform analysis, the effectiveness of the method will be quickly destroyed if a reasonable sampling rate is not chosen. Obviously the effectiveness of the method is limited in the linear domain and at the sampling points.

All numerical design procedures are based on an inexact model of the physical system, and the starting point of most control is with a linear time-invariant model of the plant to be controlled. Hence numerical design simply gets us to the point where we can experiment with the physical system, or with an accurate simulation that includes the system non-linearity, time-variation components, and so on. Design is generally too complex if the accurate simulation model, sometimes called a truth model in optimal filter designs, is used. Thus, in one sense, any type of numerical design procedure is by trial and error, with the final form and coefficients of the controller determined by several iterations of the first numerical design and then experimentation with either the physical system or an accurate simulation. So it is usually expedient to approximate the plant with a linear model. To obtain a linear plant model to which linear control system design methods apply, a linear approximation about the nominal non-linear plant operating conditions should be made. The non-linearity may be corrected from a linearized model. In this sense, it is difficult to obtain a unanimous conclusion in comparing emulation method with the discrete design method. In many cases, use of both methods gives the best result.

All of these limitations caused by inaccurate modelling which obviously exists for the current design of TLIAs have led to the following strategy. The design theory of digital controllers was used to get the initial design and the final determination of parameters is tuned through experiments. Our main objective in this chapter is concentrated on the digital control of TLIA position. The emphasis is on the design of a digital control system and its physical realisation.

## 8.2 Basic Function of a Digital Control System

The general structure of a controlled system has the following four hierarchical levels:

- Process level
- Information acquisition
- Signal processing
- Supervision level and external devices

Each level is designed for a particular task. Depending on the complexity of the controlled process and the overall system, a usage is optional. For a continuous plant with mechanical system to be controlled electrically, the whole control system can be shown as the Fig. 8.1, where A/D and D/A converters are employed to perform conversion between continuous signal and digital signal. At the process level, the Energy Transducer transforms and amplifies the controlling signal to drive the Electromechanical System. The sensor transforms the mechanical movement into an analogue electric signal that is converted into digital signal by the A/D converter. The plant to be controlled in the design of the controller should be the whole subsystem consisting of the Energy Transducer, the Electromechanical System and the Sensor.

The process identification is of primary interest at the information acquisition level. The configuration of Fig. 8.1 shows an on-line process identification. Measured signals are used to determine the actuator's behaviour within a class of mathematical model. If the process behaviour remains invariant the identification is done only once. The process identification can also be carried out off-line if the transfer function can be easily obtained with some simplification.

Depending on the estimated process parameters, a controller calculation is called afterwards. The calculated results are converted into an analogue signal that is used to control the Energy Transducer by a D/A converter.

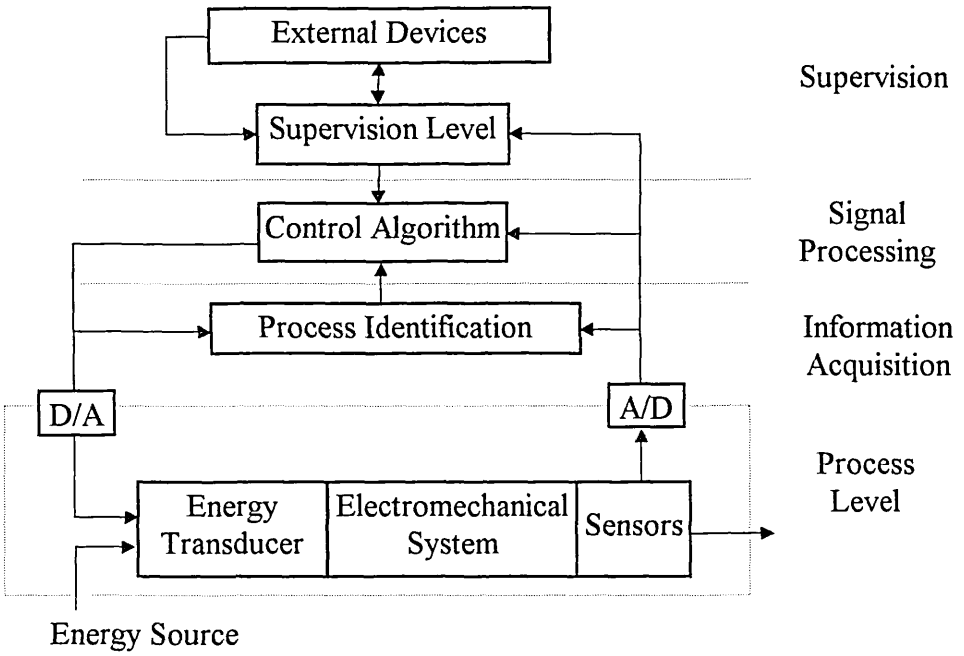


Fig. 8.1 General structure of digital controlled process

For our TLIA positioning system, the Energy Transducer, the Electromechanical System and the Sensor correspond to the PWM drive, the actuator and the linearly variable differential transformer (LVDT) respectively. The plant process is considered as time-invariant system. The process identification was carried out by off-line calculation.

## 8.3 Plant Model of the TLIA Positioning System

In order to design the controller for a dynamic system, it is necessary to have a model that will adequately describe the system's motion. A model may be obtained by examining the internal structure of the system. However, it is often the case that, because of extremely complex physical phenomena, the law of science is not adequate to give a satisfactory description of the dynamic plant that we wish to control. In these circumstances, experiments are carried out to construct models and estimate unknown plant parameter. This is the so-called system identification or process identification.

For a time-variant system, the system identification should be carried out with the development of the plant process. This requires the system identification to be incorporated into the control loop. Obviously this on-line system identification will take extra time, and thus require faster hardware to compensate it. Strictly speaking, our actuator control system is a time-variant system, because of the temperature rise. We will make a simplification to neglect the temperature-dependent effect and assume the system is time-invariant. This is a reasonable assumption, due to the fact that the range of temperature change and the maximum temperature are not very high. Under this assumption, we can take the system identification out of the control loop, i.e., off-line system identification.

The TLIA positioning system has the control configuration as shown in Fig. 8.2. To carry out system identification, we will first establish an appropriate mathematical model, and then estimate the parameters of the model by a set of carefully designed dedicated experiments.

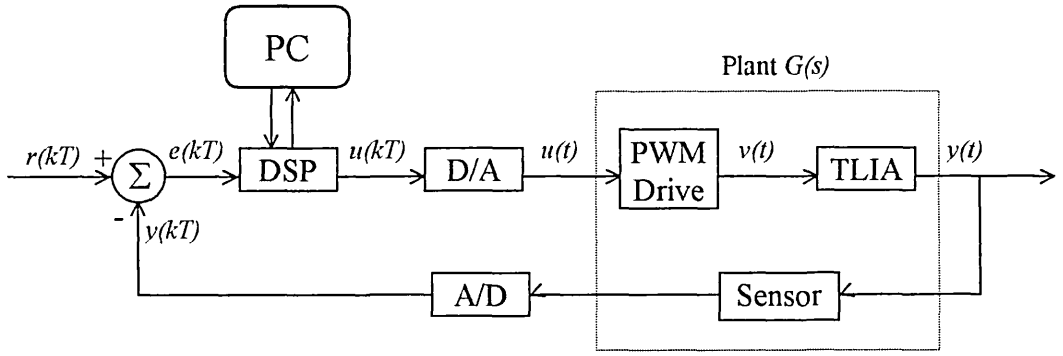


Fig. 8.2 Block diagram of the TLIA positioning control system

### 8.3.1 The Mathematical Model

The plant has two types of quantities involved in the control process: electrical signal and

mechanical movement. The mathematical model we are looking for is a transfer function between the mechanical output $y(t)$ and the control signal $u(t)$.

As discussed in chapters 6 and 7, the triac controlled PSU has non-linear control characteristics and the PWM PSU has a linear one. Due to the switch mode operation of both power drives there will be inevitably a time delay in the response. Assuming that the time delay is an integral multiple $n$ of the sampling period $T$, and neglecting the high order harmonic components, we can express the relationship between the output voltage v(t) and the input voltage u(t) as:

$$v(t)=A_p\aleph_p(t-nT)u(t-nT) \qquad n=\{1,2,3,\ldots\} \tag{8.1a}$$

where $\aleph_p$ is unity for PWM drive and a non-linear function for the triac drive. Generally speaking, $\aleph_p$ should involve load conditions [73,74]. For simplicity we use the time-delayed r.m.s. value to expressed it. This gives the following relationship:

$$\aleph_p(t)=\begin{cases} 1 & \text{For PWM PSU} \\ [1-\dfrac{u}{u_m}-\dfrac{1}{\pi}\sin(\dfrac{2\pi u}{u_m})]^{0.5} & \text{For Triac PSU with pure resistive load} \end{cases} \tag{8.1b}$$

The LVDT sensor can be considered as a linear device for which the electromagnetic force and the response delay are negligible. However its friction force is not small enough to be neglected, which will be discussed later. From the mechanical point of view, the TLIA and the linear potentiometer can be considered as an integrated part. Their continuous time model of the dynamics results in a second-order ordinary differential equation in a simple mass-spring configuration as

$$M\frac{\partial y^2}{\partial t^2}+C_d\frac{\partial y}{\partial t}+C_s y=F_e-F_f-F_g \tag{8.2}$$

where $M$ and $C_d$ are the total mass and damping coefficient of the TLIA-sensor structure. The $C_s$ is the spring constant. For TLIA-2, $C_s$ equals zero because a spring does not exist in the structure. $F_f$ is the dry friction force. It is a stochastic-dependent non-linear factor

that can not be given an exact value. We will not consider it at the stage of mathematical model. $F_g$ is the gravity force from the mass of the plunger. When the plunger of the actuator is placed level, the $F_g$ is zero. Otherwise there will be a constant force of $F_g$ that can be balanced by giving a bias voltage $u_b$ or $v_b$. So $F_g$ could not be included in the transfer function for the easy of mathematical derivation. $F_e$ is the electromagnetic force generated on the plunger and is a function of displacement $y$ and voltage $v$. The relationship among $F_e$, $y$ and $v$ is a non-linear function that can not be obtained explicitly at the moment. For simplicity, we just give a notation to describe their relation between $F_e(t)$ and $v(t)$ as

$$F_e(t) = \aleph_m(y, v)v(t) \tag{8.3}$$

Combining (8.1) and (8.3) into (8.2) and then carrying out a Laplace transform of (8.2) with zero initial setting, we can obtain the transfer function for the plant as,

$$\frac{y(s)}{u(s)} = \aleph(y(s), u(s), s)G(s) \tag{8.4}$$

with

$$G(s) = \frac{A_p e^{-nT}}{s^2 M + sC_d + C_s}$$

$$\aleph(s) = \mathcal{L}[\aleph_p(t)\,\aleph_m(t)]$$

We here put all the non-linear contribution into the function $\aleph$. This makes the transfer function above looks like a common second order system that we are familiar with. If $\aleph$ can be linearized under certain condition or with certain correction scheme, the designed of the controller can then be much simplified. This is the method that we are using in our design.

### 8.3.2 Calculation and Estimation of Parameters

In the transfer function $G(s)$ of (8.4), the parameters of $A_p$, $M$ and $C_s$ can be measured directly. The difficulties are the determinations of $C_d$ and $F_f$ and $\aleph$. To determine these

parameters experiments are resorted to. The experiments should be designed to uncouple these factors as much as possible. One of the set of experiments could be

- The first test is to measure the dry friction force $F_f$. The $F_f$ is a speed-dependent and maybe position dependent factor. Here we only consider the static force and neglect dynamic and stochastic effects. The static $F_f(y)$ is measured at different positions throughout the whole stroke length. An average value $\underline{F_f}$ can then be calculated to replace $F_f(y)$.
- The second test is to estimate $C_d$ by applying a constant force, such as a fixed weight, to the plunger, and measuring the response of the system. The test configuration is shown in Fig. 8.3. The $C_d$ can be calculated by matching the data from the experiment to (8.2). When a data acquisition technique is used, a central difference form of (8.2) can be used straight forward for the calculation of $C_d$ as,

$$M(y_{k+1}+y_{k-1}-2y_k)+0.5C_dT(y_{k+1}-y_{k-1})+C_sT^2y_k=T^2(F_w-\underline{F_f}) \qquad F_w>\underline{F_f} \tag{8.5}$$

where the $T$ is the sampling interval, $F_w$ is the fixed weight and $\underline{F_f}$ is the average dry friction force including those from the pulley and the LVDT. So, with every three sampling points, a $C_d$ can be calculated from the above equation. Due to the fact that measurement will been interfered by noise and may suffer inaccuracy from instruments and the limit of sampling rate, the $C_d$ calculated from the above equation may differ with different sets of sampling. To improve the accuracy, the averaged value $\underline{C_d}$ is used instead of $C_d$.

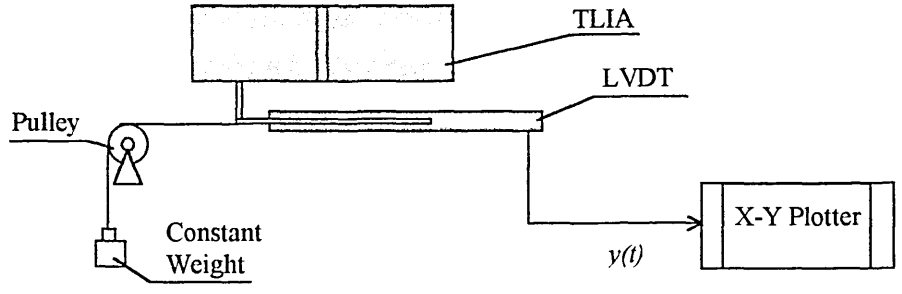


Fig. 8.3 Configuration for measuring $C_d$

- The final task is to identify the non-linear function $\aleph_m$. Because of magnetic saturation involved, it is not possible to obtain an exact expression of $\aleph_m$ in a mathematical expression with limited number of lumped parameters. We will match experimental relations with a simpler mathematical expression. From Fig. 2.8 we can observe that, under constant voltage, the electromagnetic force will be close to a linear relationship with displacement in the majority of the whole stroke length. From Fig. 2.6 and Fig. 2.7 we can derive that the relationship between the electromagnetic force and the voltage is close to a parabolic curve. Based on these observation, we can construct a general mathematical model for the force as,

$$F_e = \sum_{i=n1}^{n2} A_i v^i(t) \sum_{j=m1}^{m2} B_j y^j(t) \qquad y_{min} \le y \le y_{max} \tag{8.6}$$

It is too complex to use the above expression with many coefficients to be determined. We will use the most significant terms to simply the model. The simplified model will take the form of

$$F_e=[K_a v^2(t)+K_b v(t)][Q_0-Q_y y(t)] \qquad y_{min} \le y \le y_{max} \tag{8.7a}$$

or

$$F_e=\aleph_m(y,v)v(t) \qquad y_{min} \le y \le y_{max} \tag{8.7b}$$

with the non-linear function of

$$\aleph_m(y,u)= K_1 v(t)y(t)+K_2 y(t)+K_3 v(t)+K_4 \tag{8.7c}$$

In the above equation there are four parameters to be estimated. The usual way to estimate these parameters is by using the least square error estimation method. Here an extended version of the least square estimation method is used for Equation (8.7b), due to the two variables $v(t)$ and $y(t)$ involved. Assuming N measurements were made on $y$, $v$ and $F_e$, and expressing (8.7b) in vector form

$$F_e=Xk \tag{8.8}$$

with

$F_e=[F_1 \quad F_2 \quad \ldots \quad F_n]^T$

$X=[x_1 \quad x_2 \quad \ldots \quad x_n]^T$

$x_i=[v^2y \quad vy \quad v^2 \quad v \ ]$

$k=[k_1 \quad k_2 \quad k_3 \quad k_4]^T$

then the square error function in Hilbert space will be

$$e=(F_e-Xk)^T(F_e-Xk) \tag{8.9}$$

By differentiating $e$ with respect to $k$ and setting the result equal to zero for a minimum, one obtains the least-square estimated value of $K$ as

$$K=(X^TX)^{-1}(X^TF_e) \tag{8.10}$$

on the condition that $X^TX$ is invertable or non-singular in order to find a unique solution.

The uniqueness of (8.10) is dependent on how the model is selected and what input signal $X$ is used. Because the model described by (8.7) is backed by the experiments, the uniqueness problem is left on the $X$. Theoretical study tells us that the signal $X$ should fluctuate enough to avoid linear combinations among sampled data sets. Since (8.7) does not form a complete expression of the physical system, the $K$ may show non-linearity or deviation between different sampling sets of test results. This problem was also solved by averaging them again to avoid being trapped in the ring with non-linearity.

## 8.4 Design of Linear Digital Controller

Equation (8.4) indicates that the plant transfer function is the product of the non-linear transfer function and a second order linear transfer function. This is equivalent to a cascade connection of two plants with these two transfer functions respectively, as shown in Fig. 8.4. To treat the non-linearity, an inverse function of $\aleph^{-1}$ will be

introduced for correction of linear controller, which will be discussed in the next section. Therefore, after the non-linear correction, the plant can be considered as a common second order system. For general purpose with the consideration of a time delay $\vartheta$, the following linear transfer function is considered

$$G(s) = \frac{Ae^{-\vartheta s}}{(1+\tau_1 s)(1+\tau_2 s)} \tag{8.11}$$

where $A=A_p/C_s$, $\tau_1+\tau_2=C_d/C_s$, $\tau_1\tau_2=M/C_s$ if $Cs\neq 0$ or $A=A_p/C_d$, $\tau_1=M/C_d$, $\tau_2\Rightarrow\infty$ if $Cs\neq 0$.

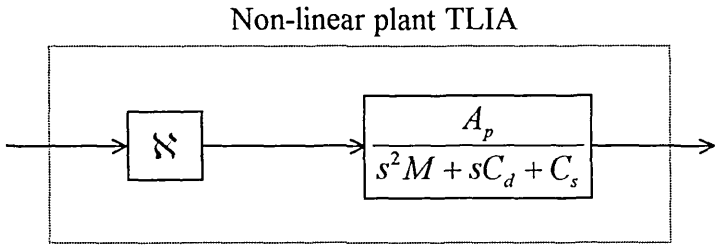


Fig. 8.4 Equivalent plant in cascade connection

To aid the design and analysis in digital domain, z-transform is adopted here for the similar purpose as the Laplace transform in continuous domain. This requires all the continuous process should be transformed into discrete expression (z-transform), which is carried out in the next section.

### 8.4.1 Discretisation of a Continuous System

The TLIA positioning control configuration involves three components that deal with continuous signals. They are the A/D converter, D/A converter and the TLIA. Three fundamental problems are associated with the discretization, which are sampling, data reconstruction and z transfer function.

1. Sampling

Sampling rate is a key factor in a successful digital control design. The selection of the best sampling rate is a compromise, depending on the properties of the signal, the reconstruction method and the characteristics of the system. Generally, the performance of a digital controller improves with increasing sampling rates, but cost may also increase with faster sampling. A low sampling rate means more time is available for the control calculation, hence more control capability is available for a given microprocessor, The low end of sampling rate is limited by Shannon's sampling theorem which states that in order to reconstruct an unknown band-limited continuous signal from samples of that signal, one must use a sampling rate at least twice as fast as the highest frequency contained in the unknown signal. So, the selection of sampling rate can then based on bandwidth as well. It is important to pre-filter the signal being sampled in accordance with Shannon's sampling theorem so as to remove all unwanted high frequencies, and thus prevent the possibility of aliasing.

2. Reconstruction

Reconstruction of analogue signal from discrete data happens in D/A converter, and is usually done by using a polynomial extrapolation or other related method. The most common reconstruction polynomial extrapolator is the zero-order-hold (ZOH) in which the signal is held constant during two consecutive sampling intervals. The D/A converter we used in the design is of the ZOH type. ZOH function can be expressed by the expression

$$u_{ZOH}(t)=u_u(t-kT)-u_u(t-kT-T) \qquad kT\le t\le(k+1)T \tag{8.12}$$

where $u_u(*)$ is a unit delay function. It has the following Laplace transfer function

$$H_{ZOH}(s)=(1-e^{-sT})/s \tag{8.13}$$

3. *Z*-transfer function

With the reconstruction function $H_{ZOH}$ and the plant transfer function $G$ in s-plane, the closed loop digital control can be further illustrated in Fig. 8.5. Because we use discrete design method to design digital controller *D(z)*, transfer functions expressed in s-plane should be transformed to z-plane. There are many methods available, such as Impulse invariant transformation (z-transform), Mapping of differentials, Bilinear transformation, Matched z-transform, etc.. The z-transform method is used here because other methods are more susceptible to the selection of the sampling rates. The z-transfer function of the second order *G(s)* and $H_{ZOH}$ is

$$G(z) = Z[\frac{1-e^{-\varpi}}{s}\frac{Ae^{-nTs}}{(1+\tau_1 s)(1+\tau_2 s)}] \tag{8.14}$$

The above transformation will lead to the following result

$$G(z) = \frac{Az^{-n}(b_1 + b_2 z^{-1})z^{-1}}{(1-e^{-T/\tau_1}z^{-1})(1-e^{-T/\tau_2}z^{-1})} \tag{8.15}$$

where

$$b_1 = 1 + (\tau_1 e^{-T/\tau_1} - \tau_2 e^{-T/\tau_2})(\tau_2 - \tau_1)^{-1}$$

$$b_2 = e^{-T/\tau_1 - T/\tau_2} + (\tau_1 e^{-T/\tau_2} - \tau_2 e^{-T/\tau_1})(\tau_2 - \tau_1)^{-1}$$

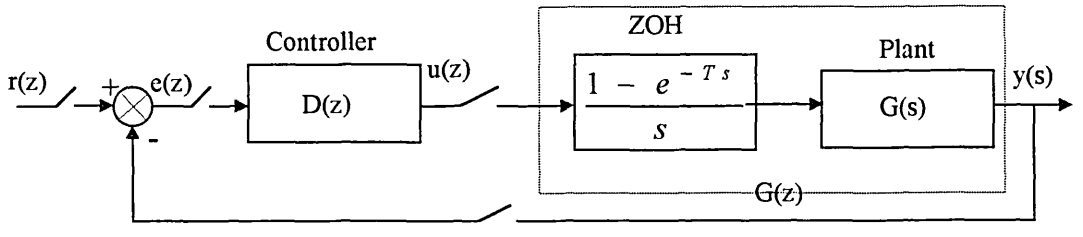


Fig. 8.5 Diagram of general closed loop digital control

### 8.4.2 Digital Controller Design by Direct Synthesis Method

The closed loop z-transfer function for the control configuration of Fig. 8.5 is

$$H(z) = \frac{y(z)}{r(z)} = \frac{D(z)G(z)}{1 + D(z)G(z)} \tag{8.16}$$

The direct synthesis method consists of determining the controller transfer function *D(z)* that is required to produce a specific closed loop response *S(z)*. If *G(z)* is known and *S(z)* is specified, implementation of direct synthesis method is just to replace *H(z)* by *S(z)* in (8.16), which gives the required *D(z)* as

$$D(z) = \frac{1}{G(z)} \frac{S(z)}{1 - S(z)} \tag{8.17}$$

From (8.17) we can see that this design will cancel the plant effects and add whatever is necessary to give the desired *S(z)*. Because of limitation in the realisation of a physical controller, specification on *S(z)* should be constrained to avoid trying to achieve the impossible. Variations in constraints lead to different methods. But two constraints are common in the category of direct synthesis method. They are the constraint of causality and constraint of stability.

1. Constraint on Causality

From z-transform theory we know that if *D(z)* is causal, then as $z \to \infty$, its transfer function is well behaved, i.e., it does not have a pole at infinity. According to (8.17), the constraint for *D(z)* to be causal could be stated as: *S(z)* must at least have the same order of zero at infinity as the zero of *G(z)* at infinity. The causality requirement on *S(z)* requires that the closed loop system must have at least as long a delay as the plant has. This is particularly important in our design because there is a significant delay involved in the switch mode PSU.

2. Constraint on Stability

The stability constraint can be obtained from the analysis of poles of the closed loop system. The poles of the closed loop system are the roots of the equation

$$1+D(z)G(z)=0 \tag{8.18}$$

From z-transform theory we know that the requirement of a stable system is that its poles in the z-plane are within a unit circle. If there is a common factor in D(z) and $G(z)$ as would occur if $D(z)$ were called upon to cancel a pole or zero of G(z), this factor will remain as a factor of (8.18). So, if the factor is outside the unit circle, the system is unstable. This means that D(z) should not contain poles and zeros on or outside the unit circle. By studying (8.17), we can conclude the stability criteria as

- $1-S(z)$ must contain zeros which locate at the same positions in z-plane as all of those poles of $G(z)$ that locate on and outside the unit circle
- $S(z)$ must contain zeros which locate at the same positions in z-plane as all of those zeros of $G(z)$ that locate on and outside the unit circle

When the TLIA positioning system is working within a stable region as we assumed, all the poles of transfer function (8.7) fall within the unit cycle. In this case, the stability constraints mentioned above do not take any effects in selecting $S(z)$, and the causal constraint on selecting $S(z)$ requires only that the delay time of $S(z)$ is not less than that of $G(z)$. In this case, a particular selection of $S(z)$ is to assume the desired closed-loop transfer function as a first order lag of the form:

$$S(z)=\lambda e^{-\theta s}/(s+\lambda) \qquad \lambda>0 \tag{8.19}$$

This is also referred to as Hahline method. Its z-transform with ZOH and integral time delay of $\theta=mT$ is

$$S(z)=\frac{(1-e^{-\lambda T})z^{-m-1}}{1-e^{-\lambda T}z^{-1}} \qquad m=1,2,3,\ldots \tag{8.20}$$

Using the direct synthesis relationship of (8.17), we obtain the controller's z-transform

expression:

$$D(z)=\frac{1}{G(z)}\frac{(1-e^{-\lambda T})z^{-m-1}}{1-e^{-\lambda T}z^{-1}-(1-e^{-\lambda T})z^{-m-1}} \tag{8.21}$$

Substituting (8.15) into (8.21) gives

$$D(z)=\frac{1-e^{-\lambda T}}{A}\frac{(1-e^{-T/\tau_1}z^{-1})(1-e^{-T/\tau_2}z^{-1})z^{-(m-n)}}{[1-e^{-\lambda T}z^{-1}-(1-e^{-\lambda T})z^{-m-1}](b_1+b_2z^{-1})} \qquad m\geq n \tag{8.22}$$

The Dahlin method does not apply any constraint on the controlling signal *u(z)* and time constant λ which affects the response of *u(t)* in addition to *y(z)*. That means firstly that λ may be beyond the system's capability if it is too small, and secondly the u(t) could be out of the saturation level which is limited by the physical D/A converter and system hardware configuration. For the TLIA system the saturation caused by the hardware appears as

- The PWM drive requires only a positive single-ended control signal of *u(t)* with a maximum controllable voltage of +3(Volts/dc)
- The D/A converter has a limited output signal level converting a 14-bits binary data

The positive saturation can be easily controlled by lowering the coefficient *A* with a sacrifice of resolution rate, which is usually not a problem. The negative voltage problem can be overcome by clamping the *u(t)* to zero when negative, but this results in a response with overshoot.

Besides the problems caused by physical limitation, the controlling signal may suffer oscillation that causes inter-sampling ripple in the output response. The reason for the oscillation lies in the fact that the controlling signal's z-transfer function has poles in the vicinity of the unit circle. Different from the plant transfer function of (8.7), the closed loop controller's transfer function is

$$C(z)=\frac{u(z)}{r(z)}=\frac{D(z)}{1+D(z)G(z)}=\frac{S(z)}{G(z)} \tag{8.23}$$

All the zeros in *G(z)* will be canceled in *D(z)* by *1-S(z)*, but will become poles in the *C(z)*. So, if any of these zeros is close to the unit circle, the controller's response will have oscillation.

One of the effective methods to improve the performance is to remove all the *D(z)*'s poles that lie in or around the unit circle. This is realized by substituting $z=1$ in all the factors of *D(z)*'s denominator with the exception of the integrator term $(1-z^{-1})$. This treatment will bring some degradation of system response, however the degradation is usually very small compared to the improvement to the actuation signal. For the secondary order system of (8.7), this treatment will lead to a controller of D(z) with a similar representation of common PID controller that can be written as

$$D(z) = K\frac{[(1+T/T_i+T_d/T)-(1+2T_d/T)z^{-1}+T_dz^{-2}/T]}{1-z^{-1}} \tag{8.24}$$

## 8.5 Non-linear Correction

From the dynamic point of view, non-linearity can be further classified as static and dynamic. Although there is no general technique available to handle all non-linear problems, we will develop a particular method for the TLIA positioning system. Here only static non-linearity is considered, i.e., the time-independent factor is neglected in the treatment of non-linearity. The actual TLIA positioning system has mainly two non-linear sources in force as

- $\aleph$ in the transfer function of *y(s)/u(s)*
- Dry friction force $F_f$ in both the actuator and the LVDT sensor

According to the definition of $\aleph$, the total net force $F$ acting on the moving mechanical parts can be expressed as

$$F(y,u)=\aleph(y,u)u(t)-\underline{F_f} \tag{8.25}$$

The strategy to correct the non-linearity is to find another control signal $u^*(t)$ with the

correction carried out in the microprocessor so that the linear transfer function $G(s)$ can be used for the control of $u^*(t)$. With the correction the normal control action $u(t)$ for linear plant is then replaced by the corrected value $u^*(t)$. An inverse correction method is used in our design. It can be expressed as

$$u(t) = u^*(t) / \Re(y,u) \tag{8.26}$$

with the inverse non-linear function $\Re^{-1}$

$$\Re^{-1}(y,u) = [\aleph(y,u) - \underline{F_f} / u]^{-1} \tag{8.27}$$

Figure 8.6 shows the principle of the non-linear correction by using inverse function.

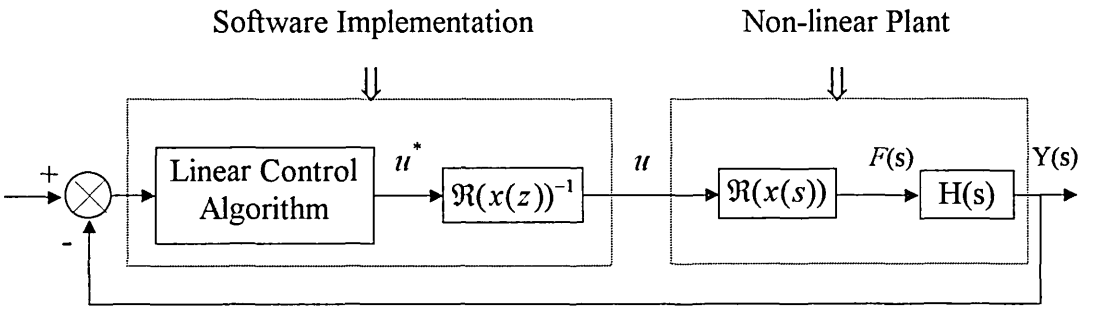


Figure. 8.6 Correction of non-linear characteristics

8.5.1 Non-linear Correction for TLIA-2

Equation (8.27) is just suitable for one control signal needed for the TLIA-1. However, the TLIA-2 needs two control signals $u_1$ and $u_2$ to control its two coils. Here we only consider the case that $u_1$ and $u_2$ are dependently controlled by one control signal $u$, as discussed in the previous Chapter. With PWM PSU ($\aleph_p=1$), the following relationship should be put into (8.3) to calculate the electromagnetic force

$u_1(t)=u(t)$

$y_1(t)=y(t)$

$u_2(t)=u_m(t)-u(t)$ (8.28)

$y_2(t)=y_m(t)-y(t)$

$v(t)=A_p u(t)$

where the subscript '$_m$' denotes the maximum value. Then the total force and reverse function are

$$F(y,u)=[\aleph_m(y,u)u-\aleph_m(y_{max}-y,u_{max}-u)(u_{max}-u)-\underline{F_f}] \quad (8.29)$$

$$\Re(y,u)=[\aleph_m(y,u)u-\aleph_m(y_{max}-y,u_{max}-u)(u_{max}-u)-\underline{F_f}]^{-1}u \quad (8.30)$$

Substituting (8.7c) into (8.30), we obtain

$$\Re(y,u)=[K_a+K_b u+K_c y+K_d uy+K_e u^2+K_f yu^2-\underline{F_f}]^{-1}u \quad (8.31)$$

with

$K_a=-(A_pK_1y_mu_m+K_2y_m+K_3A_pu_m+K_4)u_m$

$K_b=A_pK_1y_mu_m+A_pK_3u_m+K_4-K_a/u_m$

$K_c=(A_pK_1u_m+K_2)u_m$

$K_d=-2A_pK_1u_m$

$K_e=-A_pK_1y_m$

$K_f=2A_pK_1$

For triac PSU, the $\aleph_p$ will bring extra non-linearity that is a function of line voltage, control voltage and load impedance. It is too difficult to get the exact relationship among variables due to the fact that the TLIA's impedance changes with its position. However, the above correction scheme is still workable with slower sampling rate and smaller amplification to compromise the performance.

### 8.5.2 Compensation for Dry Friction Force

Although friction is also one of source non-linearity, it has a special hysteresis-like, direction dependent, characteristics. The main control problem with friction that occurs when high positioning accuracy is required. If the process stops in hysteresis before set point is reached, only integral part of a linear control algorithm is capable of compensating the influence of friction. The mechanical hysteresis will cause system oscillation and enlarge settling time if it is not treated properly. The following characteristics for processes with dry friction are found:

- The process remains at standstill if $F_{dc-} \leq F_f \leq F_{dc+}$
- Positive movement is obtained if $F_f > F_{dc+}$
- Negative movement is obtained if $F_f < F_{dc-}$

The basic control problem for a process with hysteresis is caused by the first characteristic. In particular, the control strategy becomes difficult, as the hysteresis must be compensated with each overshoot. The common analogue friction compensation is the dynamic linearisation by adding a high frequency periodic signal to the normal control. It will bring the disadvantage of extra mechanical wearing and damped dynamics.

Another way to deal with this non-linearity of dry friction force is based on the idea that the friction can be interpreted as d.c. values. The unknown offset is obtained by using a measured hysteresis or by identifying the dc value using parameter estimation techniques. The friction is then compensated by a so-called explicit feed-forward compensation, which adds an appropriate compensation value to the normal controller. The common Coulomb friction model is used, which can be expressed as

$$F_f = \begin{cases} F_{dc} \cdot sign(\dot{y}) & \text{For } \dot{y} \neq 0 \\ F_{dc} & \text{For } \dot{y} = 0^+ \\ -F_{dc} & \text{For } \dot{y} = 0^- \end{cases} \tag{8.32}$$

The success of the compensation depends mainly on the quality of the estimated compensation value. If the actual friction value is exactly known, compensation in one sampling interval can be performed. In the worst case (overestimation of the hysteresis) the control loop may become unstable. Therefore, a damping coefficient $\alpha(\leq 1)$ is introduced:

$$F_f=(1-\alpha)|F_{dc}|\text{sign}(y_t-y_{t-1}) \tag{8.33}$$

For linear plant, the actual manipulation is carried on the controlling voltage having the same relationship as the above equation. Since the TLIA is a non-linear plant, the compensation of dry friction force was implemented together with other non-linear correction, as described by (8.31), in our design. The diagram of dry friction compensation is shown in Fig. 8.7 with non-linear correction.

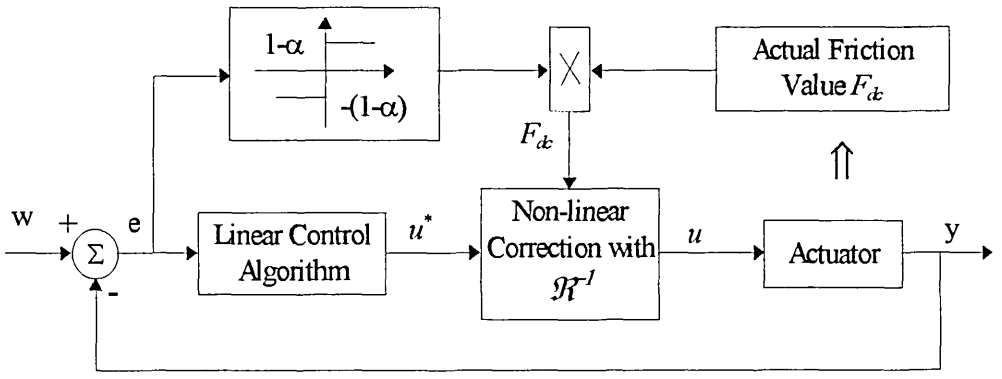


Fig. 8.7 Explicit feed-forward compensation of friction combined with other non-linear correction

## 8.6 TLIA's Positioning Controlled by DSP

Implementation of microprocessor control systems requires more than knowledge of control theory. Knowledge of hardware, including microprocessor, D/A and A/D converter, power amplifier, and measurement devices, is also very important. Another important issue is the method of software implementation of control algorithm. All of

them form an integral system. Although some of the knowledge is specific to the control system, they should be fully understood in the practical design and implementation. The basics of our hardware and software implementation of the digital controller will be discussed at first. Then the application for TLIA-2 driven by the PWM PSU and the Triac PSU will be illustrated.

### 8.6.1 Hardware Implementation

At the hart of the digital controller is a processor that could range from standard microprocessors to special-purpose digital signal processor (DSP). The primary difference is in the instruction sets and execution speed of particular instructions. Because digital control involves much numerical computation, the instruction sets for special-purpose signal processors are rich in math capabilities and are better suited for control applications than the standard microprocessor. For most control applications it is advantageous to select a processor that does not require much supporting hardware. General-purpose processors often require a legion of support functions including clock, bus control, memory control, interrupt control, I/O registers, communications adapters, and memory. Many DSPs integrates most of these support functions in a single chip processor and minimise the component count. Due to the above reason, a DSP kit was employed in our design. The kit comes with a TMS320C26 DSP and a 14-bits analogue interface circuit (AIC) TLC3240 that performs A/D and D/A conversion [75]. The schematic of the DSP kit is given in the appendix D.

The TMS320C26 uses Harvard-type architecture that maximises processing power by maintaining two separate memory bus, data memory and program memory, for full-speed execution. It has a 256 word internal program ROM and 64k-words of total data memory address space with three on-chip RAM blocks, configurable either as separate program and data space or as three contiguous data blocks. System control is supported by the program counter, hardware stack, PC-related hardware, the external reset signal, interrupts, the status registers, the on-chip timer and the repeated counter. An on-chip full-duplex serial port provides direct communication with serial devices such as serial A/D and D/A converters. Among these futures, memory configuration, interrupts, status

registers and serial communication should be fully considered in the hardware-software integration that will be discussed in section 8.4.2.

The AIC unit (TLC3240) is a complete A/D and D/A input/output system. It provides 14-bit resolution of conversion. Data transmission between the AIC and the DSP is through a serial port, which allows direct interface to the TMS320C26. The serial ports can work in synchronous mode or asynchronous mode, communicating in 8-bits bytes or 16-bits words. A flexible control scheme in timing, filtering and analogue voltage mode (differential or single ended) functions can be selected and adjusted coincidentally via software control. There are a switchable bandpass filter and a low-pass filter at the input and output stage respectively. The DSP board has been built with the AIC circuit-configured in 16-bits word communication, single-ended analogue voltage mode. The things left to set are the timer, communication mode and digital scale, which must be properly set and incorporated into the whole control code.

The LVDT sensor has a maximum stroke from *-50mm* to *+50mm*. An electronic circuit has been assembled together with the LVDT so that it can work under d.c. voltage with a sensitivity of 60mv/mm at 10V d.c. However, we have experienced the problem that it emits significant noise at about 5kHz. We will not try to improve the LVDT, instead will reduce the noise interference through hardware and software. A RC low-pass network was used to filter the noise before the A/D converter, and a fourth-order Infinite Impulse Response (IIR) digital filter has been implemented on the digitised signal in the DSP. Because the input filter required is a low-pass type, the AIC's built-in bandpass input filter can not be used and should be switched out of the signal path.

There is another non-linearity problem called saturation on which attention should be paid in both hardware and software implementation. Hardware saturation exists due to finite voltage/current limits for the analogue I/O, and due to the plant limitations. To avoid plant (including the power drive and the actuator) saturation, the following constraints should be applied to the power drive and the displacement sensor:

- The maximum output voltage should not drive the actuator into severe magnetic saturation or cause thermal damage to the actuator. This requires the power handling

capability of the PSU matches well with the actuator.

- The interface voltage to the D/A converter should be in the same range, i.e., the maximum D/A output voltage will just command the maximum output from the power drive. This can be done by calibrating the amplification coefficient of the power drive.
- The sensor's output voltage should be scaled within the saturated voltage of the A/D input.

With these measures, the only saturation problem is left with the D/A converters that are controlled by software. It means that the saturation problem is left to be solved only by software after the above calibration and adjustment. To solve the last saturation problem, the software code should be carefully designed.

### 8.6.2 Software Implementation

In addition to implementing control algorithm, the software should consist of other functions to get the DSP-AIC system work properly. We have employed assembly language to develop the code with the aid of the DSK Debugger (DSKD) which is an window/menu-oriented software interface to refine the code and/or correct errors. The DSKD works in a PC, shows the code, data, and status of the processor, and provides commands to load and execute code in various modes (such as single-step, breakpoint, and run-time halt). When the C26 is reset, the on-chip bootload ROM locates a debugging and communication kernel code into on-chip RAM beginning with memory block B0. The communication is by using XF and BIO through a bi-directional RS232 cable. The following configuration and resources should be reserved for the use of DSKD:

- The C26 must be set in microcomputer mode ($MP / \overline{MC} = 0$), which has been set on the DSP board
- First 256 words of B0 and whole of B2 must be configured as program RAM for the use of debugger communication kernel
- interrupts INT2 and TRAP should not be masked
- All of RAM block B2 should be reserved for the use of TRAP.

The flow chart for the DSP code development is shown in Fig. 8.8.

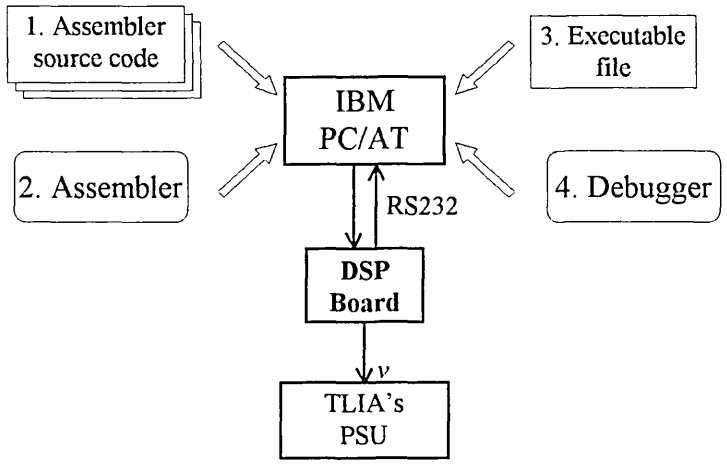


Fig. 8.8 Illustration of DSP code development with DSKD

As we know digital control requires proper control of sampling, therefore timing is an important factor that will determine the overall performance of the control system. Interrupt technique was used to control the execution of the control algorithm [76]. There are two questions here: how to control the transmit and receive between the DSP and the AIC and how to control their timing. Firstly, we decided to use synchronous communication mode that is preferred in control systems. Under this mode, transmit and receive activities take place within the same frame synchronised pulse (FSP). So the control of sampling rate is translated to the control of the FSP timing. There are two ways to control the FSP's timing by using the DSP on-chip time counter or using the AIC's timer. Using the AIC's timer will affect/control its on-chip filter's frequency range. There is no difference here because the on-chip bandpass input filter will not be used and the roll-off frequency of the lowpass output filter will be suitable for the low frequency control purpose for wide range of FSP's frequency. We employed the FSP from the AIC to control the sampling. The configuration and communication protocol for the AIC and the system setting for the DSP, which were used in the coding, are shown in Table 8-1 and Table 8-2.

The transmission protocol of the AIC is the same as the primary receive protocol except that *d15* through *d2* go to A/D converter and *d0-d1* have no meaning.

Figure 8.9 represents the flow chart of the program for the DSP controlled TLIA positioning system. One characteristics of the figure is the larger program code dedicated to things other than calculation of the control algorithm. Actually most of the system management code is provided with the DSKD. Our main concentration is on the control algorithm and its practical realisation under the development environment provided by DSKD [71].

Table 8.1(a) Primary serial receive protocol of the AIC

| d15 .... d0 | Setting | Meaning |
|---|---|---|
| \|d15 ... d2 \|1 1 | d0=1, d1=1 | d15 through d2 go to D/A converter; a secondary transmission will immediately follow to configure the AIC; TA, RA, TB RB go to TXA, RXA, TXB, RXB respectively for the timing |
| \|d15 ... d2 \|0 0 | d0=0, d1=0 | d15 through d2 go to D/A converter; TA, RA, TB RB go to TXA, RXA, TXB, RXB respectively for the timing |

Table 8.1(b) Secondary serial receive protocol of the AIC

| d15 .... .... d0 | Setting | Meaning |
|---|---|---|
| x x x x x x x x 0 0 1 0 0 0 1 1 | d0=1,<br>d1=1<br>d2=0<br>d3=0<br>d4=0<br>d5=1<br>d6=0<br>d7=0 | set control register<br>delete the bandpass input filter<br>disable the loopback function for testing<br>disable the secondary input AUX IN+ & AUX IN- pins<br>set synchronous transmit and receive sections<br>set gain control as ± 3V analogue input with half-scale<br>A/D conversion<br>A/D conversion |
| x x \|←TA→\| x x \|←RA→\|0 0 | d0=0,<br>d1=0 | receive unsigned binary TA and RA (5-bits) |
| x \|← TB →\| x \|← RB →\|1 0 | d0=0,<br>d1=1 | receive unsigned binary TB and RB(6-bits) |

Table 8.2 System setting of the C26:

| Mode | Setting | Meaning |
|---|---|---|
| Memory | CONF=2 | B2 and B3 are data RAM, B0 and B1 are Program RAM |
| Interrupt | IMR=14h | Xint,Tint,Int1,Int0 are masked, Rint and Int2 are unmasked |
| Serial Com. | FSM=1, TSM=0 | Serial communication works in Frame Synchronising Mode Frame Synchronising Signal is an external input |
| Sign Ext. | SXM=1 | Sign extension is enabled |
| Saturation | OVM=1 | Saturation mode is set, which set the ALU to largest positive 7FFFFFFFh or negative 8000000h according to the direction of overflow |

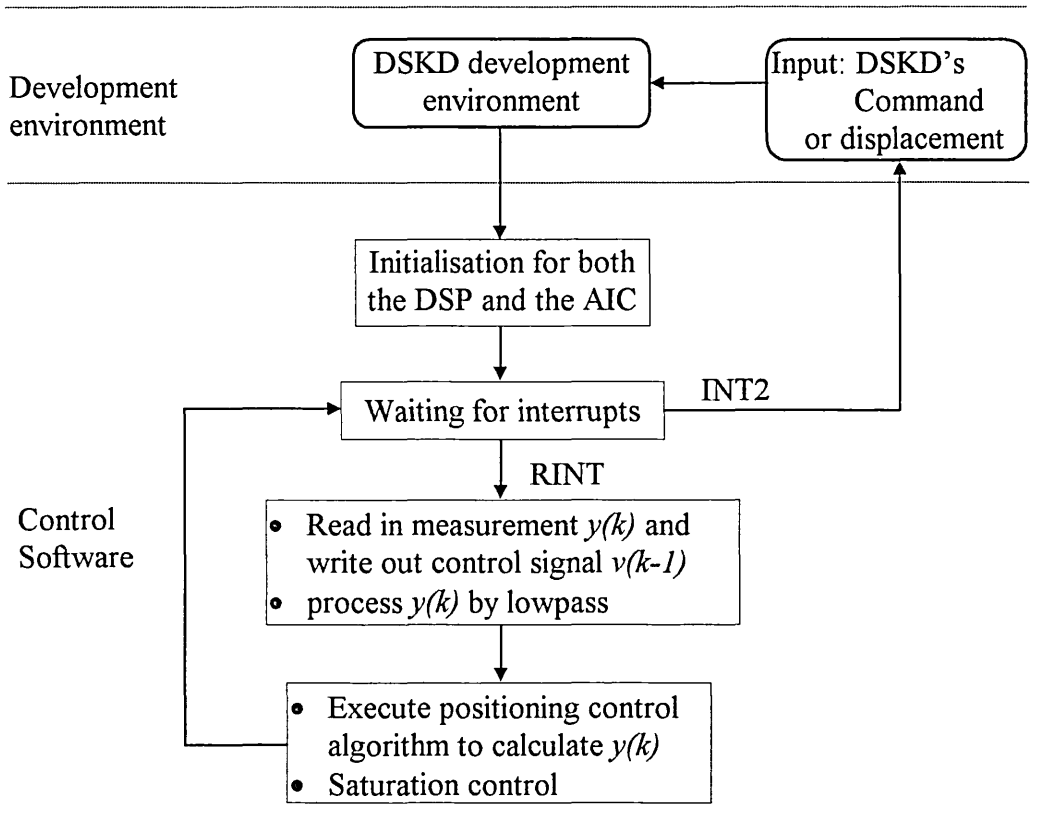


Fig. 8.9 Program Structure for the Control of the TLIA Position

The C26 has a 32-bits fixed point ALC dealing with 16-bits data. Although it is capable of carrying out floating-point operations, extra floating-point math algorithms are required. This will significantly reduce the CPU percentage available to process the control algorithm. (It could be tens to hundreds times slower than fixed-point operation, up to the math operation.) So a fixed-point number system was used in the coding of control algorithm [77]. To avoid early saturation, a variable scaling scheme was employed with the fixed-point operation. A software saturation control was implemented at the last stage so as to prevent unachievable signals that may occur in extreme cases.

## 8.7 Integration of the Different Aspects of the Research

It is deemed useful to digress a little at this stage and discuss how the various aspects of the research described in the previous chapters fall into place. This is necessary before the performance of the final integrated system in the form of a computer controlled positioning mechanism is introduced in section 8.8. The various stages of the research leading to the results presented in section 8.8 can be summarised as follows:

- A preliminary study of the different forms of linear induction machines was undertaken and their force versus displacement characteristics studied. The desirable shape of the characteristic needed for positioning application was identified in Fig. 1.4(b)

- The next stage of the research was to identify the basic topology of the single-phase actuator that would have the desired characteristic of Fig. 1.4(b) either in full or in part. The topology identified is shown in Fig. 2.3 and its characteristic in Fig. 2.4. In order to change the characteristic of Fig. 2.4, changes to the basic topology were investigated using finite element modelling. The final geometry arrived at, referred to as design CD-4 in the thesis, is shown in Fig. 2.17

- In order to predict the electromechanical and thermal performance of CD-4 under real operating condition, the finite element software developed is described in chapters 3, 4 and 5. In the course of this phase of the research, new and useful

techniques in circuit-field coupling (chapter 3) and force calculation by Maxwell stress summation were found (chapter 4). If the actuator is used in a closed poorly ventilated environment such as the interior of an automatic teller machine, then temperature rise becomes an important consideration. Therefore the electromagnetic field solution software was extended to include coupling the thermal field as well in chapter 5.

- The power supply unit (PSU) with a computer interface needed for the actuator could not be purchased as an off-the-shelf product. Therefore two types of the PSU, the triac controlled design and the variable frequency variable voltage inverter design were constructed. Their theory and design are discussed in chapters 6 and 7. The CAD software described in chapters 3, 4 and 5 can readily model the actuator excited by either of these PSUs as can be seen in Fig. 3.7 and Fig. 3.10.

To operate the actuator in a closed loop and control it in real time, digital control techniques were adopted. This chapter has addressed the theoretical background of such a control strategy with an off-the-shelf DSP control kit. The development of the necessary software has been presented and we are now ready to look the performance of the full integrated system in the next section.

## 8.8 Application to TLIA-2's Positioning

The first task in the design of the controller is to carry out system identification through experiment. Due to the fact that TLIA2 uses sliding mechanism, its dry friction force is much larger than that of TLIA1 that uses linear bearing. The hysteresis loop caused by dry friction force is shown in Fig. 8.10 from which a d.c. voltage can be obtained for dry friction force compensation using (8.33). To use (8.31), an averaged friction force was measured directly, which is given in Table 8.3. Figure 8.11 shows the displacement response of the TLIA2's under constant force. It was used for the calculation of $\underline{C}_d$. The TLIA2's parameters are listed in Table 8.3.

Table 8.3 parameters for TLIA-2 system

| | *M(kg)* | *Cd(N.s/m)* | *Cs(N/m)* | $F_f$ |
|---|---|---|---|---|
| TLIA-2 plus LVDT | 0.078 | 0.0884 | 0.0 | 0.216 |

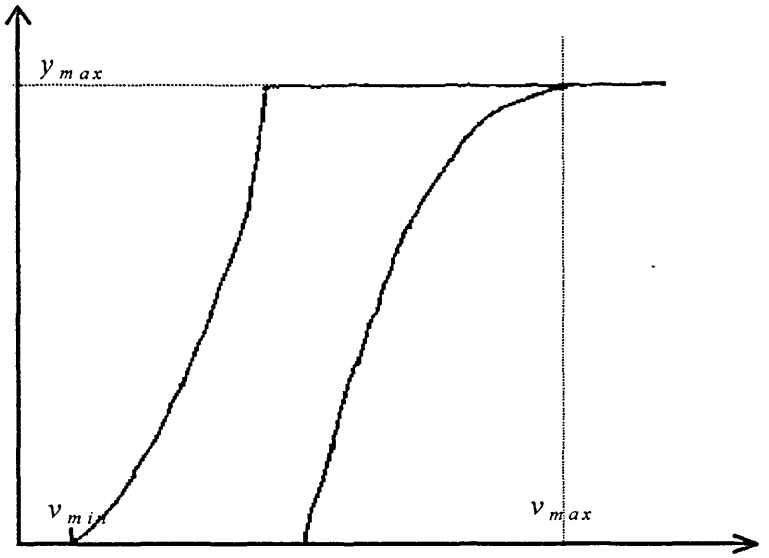


Fig. 8.10 The static friction hysteresis loop for TLIA-2

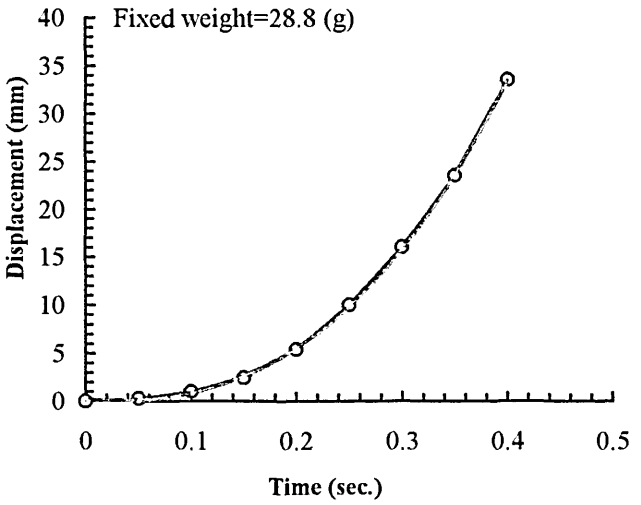


Fig. 8.11 The response for testing $C_d$ under constant force excitation

1. Application of Positioning control with the PWM PSU

First we consider the case with the PWM PSU. The main frequency and PWM pulse frequency are set at 50Hz and 900Hz respectively. The maximum possible time delay is 1/900 second. Therefore, we have chosen the sampling interval of 1/868.1 second which should be greater than the maximum time delay. Considering the PWM circuit has very fast response in relative to the sampling speed, the possible time delay incurred in the PWM driver is one pulse, which corresponds to $n \approx 1$. We assume there is no delay from the PSU to the TLIA response because the TLIA is an analogue device. That means $m$ should be equal to or greater than $n$. We specify a minimum delay time of $m=1$ for a fast response. The open loop time constant of the actuator equals $\tau_1^{-1}=C_d/M=1.337$ and $\tau_2^{-1}=0$. The initial value of the specified closed loop time constant $\lambda$ is chosen at 3 times as fast as the open loop system, which gives $\lambda=0.38$s. With the above setting, the digital controllers of (8.22) can be expressed as

$$D(z)=\frac{3.414\times10^3}{A}\frac{(1-0.9984z^{-1})(1-z^{-1})}{(1+0.9995z^{-1})(1+0.003z^{-1})(1-z^{-1})} \tag{8.33}$$

There is a common factor $(1-z^{-1})$ in the above equation that is left for the purpose to represent a general PID controller. The pole at z=-0.9995 is introduced to cancel the plant zero. Because it is close to the unit circle in z-plane, it may cause the control signal oscillation. The second pole at z=-0.003 is close to zero, resulting little effect on the actuation. Further improvement can be made by removing all the poles which lies in or around z=1 with the exception of the integral term $(1-z^{-1})$, resulting in a controller in the form of a common PID controller.

$$D(z)=\frac{1.709\times10^3}{A}\frac{(1-1.9984z^{-1}+0.9984z^{-2})}{(1-z^{-1})} \tag{8.34}$$

For the non-linear process identification, the following sampling data are used for the least square estimation method.

| $n$ | $v^2y$ | $vy$ | $v^2$ | $v$ | $F_e$ |
|---|---|---|---|---|---|
| 1 | 0 | 0 | 0 | 0 | 0 |
| 2 | 0 | 0 | 100.00 | 10.00 | 0.18 |
| 3 | 0 | 0 | 196.00 | 14.00 | 0.30 |
| 4 | 0 | 0 | 324.00 | 18.00 | 0.51 |
| 5 | 0 | 0 | 484.00 | 22.00 | 0.76 |
| 6 | 0 | 0 | 676.00 | 26.00 | 1.01 |
| 7 | 0 | 0 | 900.00 | 30.00 | 1.33 |
| 8 | 0 | 0 | 1156.00 | 34.00 | 1.67 |
| 9 | 2.00 | 0.20 | 100.00 | 10.00 | 0.08 |
| 10 | 3.92 | 0.28 | 196.00 | 14.00 | 0.14 |
| 11 | 6.48 | 0.36 | 324.00 | 18.00 | 0.23 |
| 12 | 8.68 | 0.44 | 484.00 | 22.00 | 0.34 |
| 13 | 13.52 | 0.52 | 676.00 | 26.00 | 0.45 |
| 14 | 18.00 | 0.60 | 900.00 | 30.00 | 0.61 |
| 15 | 23.12 | 0.68 | 1156.00 | 34.00 | 0.84 |

Applying (8.10), we obtain

$$[K_1 \quad K_2 \quad K_3 \quad K_4]^T=[-28.94 \quad -282.9 \quad 1.308 \quad 4.867]^T \times 10^{-3}$$

The maximum stroke of the actuator is about 0.06m. The maximum D/A output voltage is $u_{max}$=3V at which a 100% duty cycle of PWM pulse will be generated. When the maximum driving voltage is set at 30V amplitude, the PWM drive's amplification is $A_p$=30/3=10. Just substitute all these coefficients into (8.30) we can obtain the final non-linear correction formula as

$$\Re^{-1}=0.0749-0.0329u-3.45y+1.74yu+0.0174u^2-0.579yu^2-0.0126u^{-1}* sign(\dot{y})$$

Figure 8.12 shows the response of the positioning at 7, 22 and 35 mm respectively. It can be seen that the settling time ranges from 0.35 to 0.6 second that fits well with the designed target of 0.38 second, considering the errors in modelling and parameter identification. We also observe that the settling time increases with the increase of displacement to be positioned. This is obviously the direct result of the sloping control

characteristics. Although the sloping control characteristics will prolong the settling time, it enables the actuator to be positioned in open loop control under constant load.

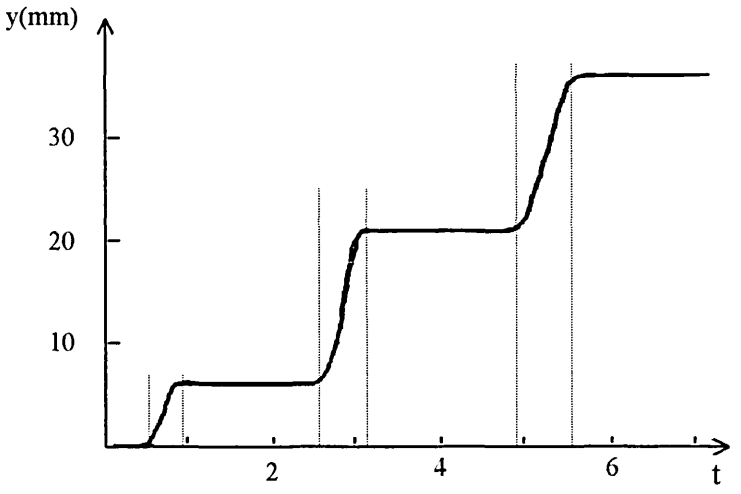


Figure 8.12 The response of positioning with PWM PSU

2. Application of Positioning Control with the a.c. Line Controller

When the triac PSU is used to drive the actuator, only the frequency difference was considered in the design of the controller. Due to the triacs control both the positive and negative cycles of the mains supply, the frequency of triggering pulse is 100Hz. Therefore the maximum possible time delay is 1/100 second. We have chosen the sampling interval of 1/88.5 second, and $n=m=1$. When the specified closed loop time constant $\lambda$ was firstly chosen as the same as the PWM PSU, i.e. $\lambda$=0.38s, the closed loop system could not be controlled at a stable position throughout the whole stroke length. This can be explained as the result of the PSU's non-linearity, which was not considered in the controller. We then increased $\lambda$ until $\lambda$=0.88s, thereafter a good positioning performance could be obtained. The positioning response curve is shown in Fig. 8.13. Comparing with Fig. 8.12, we can observe that the triac PSU has longer settling time, larger overshoot and more vibration around the balanced position. This is reasonable

because of the larger λ, its extra non-linearity and maybe a little bit latching problem. Although the positioning under triac PSU is a little bit slower than under PWM, the triac controlled PSU is more cost effective.

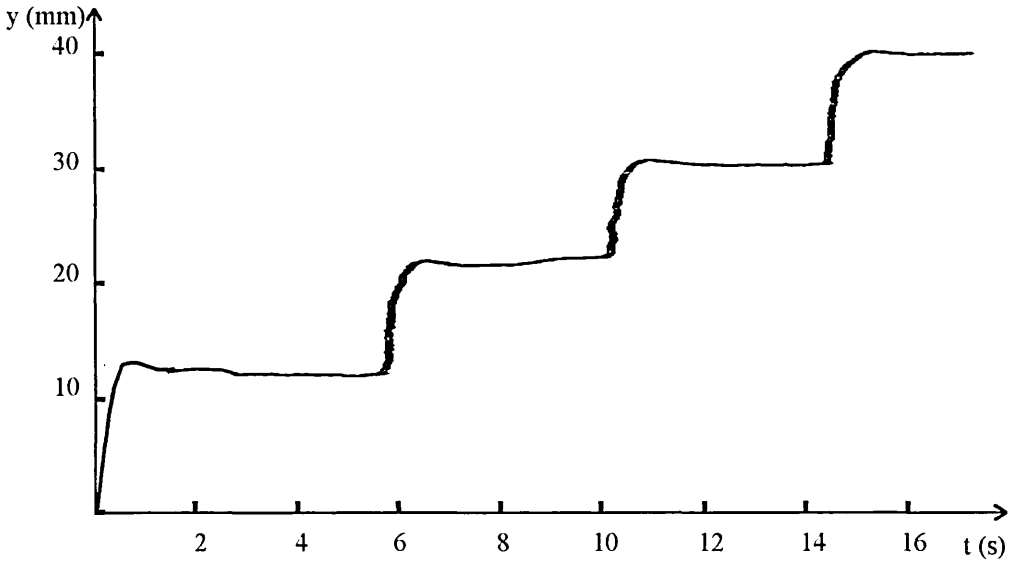


Fig. 8.13 The response of positioning with the a.c. line controller

## 8.8 Conclusions

Digital control technology has been successfully applied to the TLIA's positioning control system. The controller was firstly designed through direct synthetic method based on the linear plant model. Then a non-linear correction and dry force compensation was incorporated into it by using inverse function. The control algorithm was coded in Assembly language and was implemented in the DSP kit under its development environment. In addition to the control algorithm, appropriate setting, configuration and communication protocol for the DSP and AIC was considered in the development of the control code to get the hardware work together with the software controller. The non-linear correction, particularly the dry friction force compensation for the TLIA-2, has

shown its significant role in reducing overshooting and settling time. Because of the error in the modelling of the non-linear plant, the stochastic effect of dry friction force and the noise interference, the positioning response and its repeatability will have a certain range of difference that is more displacement relevant. This is a topic relating to the requirement of positioning accuracy and speed. It did not pose a problem for our design that requires 0.5mm of positioning accuracy in about 40mm stroke length. The whole control system developed has achieved the initial objective to provide a fast response with a high accuracy. Successful demonstration has been given to the project founder AT&T.

# 9 CONCLUSIONS

## 9.1 General

The research has covered areas of knowledge and technology in finite element CAD, power electronics and digital control. The achievement can be split into four areas of work

(i) Actuator: A new single-phase TLIA suitable for positioning application has been developed, which had been patented through AT&T Scotland. The new actuator has a monotonously decreasing control characteristic, which enables the actuator to be used in applications with both open-loop positioning control and closed-loop positioning control. The back-to-back structure employed in the current design provides an electric spring whose stiffness is controllable by adjusting the terminal voltage. These provide lot of versatility to use different control methods.

(ii) Design and Analysis Tools: There are several subtopics involved in this issue, which are

- New eddy current model: The DMVP method has been developed to model the eddy current field coupled with external circuits under voltage excitation. This method can significantly accelerate computation speed.
- New scheme to calculate electromagnetic force. It has been discovered that most of elements have common-mode errors on the vertex potentials. Therefore a new scheme based on MSTBM has been proposed. It can eliminate path-dependency and improve force accuracy from fundamental treatment of the field quantities (B,H).
- Improvement to the original pre-processor, solver and post-processor to achieve a faster analysis by a more convenient and reliable design tools.

- Development of transient simulation software which can analysis transient current response, transient electromagnetic field and transient temperature field of the single-phase TLIAs.

(iii) Power Supply and Driving Unit (PSDU): Two PSDUs, the triac one and the PWM one, have been successfully designed, fabricated and applied to control the TLIA. Because they work in switch-mode, power consumption has been reduced considerably. Both PSDUs have an analogue interface compatible with CMOS logical circuit. A d.c. voltage from any source can be utilised to control their output through the analogous interface.

(iv) Digital Positioning Control: A general TMS320C26 DSP has been used to implement digital positioning control. There are two issues involved here. One is the digital controller. The other is the actual realisation of the control algorithm. For the digital controller, it was designed by using second order model of TLIA with linear and constant parameters. Dry force compensation and non-linear correction were carried out after the linear controller in a cascade connection. For the actual realisation, the control algorithm was coded in Assembly language on the DSP by using fixed-point operation. Sampling control was realised by programmable hardware-generated interrupt. The DSP-based controller has also successfully driven the PSDU to positioning the actuator. The resolution achieved is less than 0.5mm that is the target set at the beginning of the project.

Although much theoretical studies and practical work have been carried out with great satisfaction, there is much room for further development of the system because of expanding and technology. It is worthy looking into potential research that may possibly bring direct benefit in the near future. These consist of the rest of the chapter.

## 9.2 Discussion on Future Work

### 9.2.1 Improvement of TLIA's Design

We can look into the improvement of TLIA from three aspects: material, ventilation and structure.

(i) Material: For the current actuator, the yoke/mandrel is made of solid mild steal, and the plunger is made of copper or aluminium, because they are in the research stage at the moment. For the final product, it is hardly to accept to use solid mild steal due to the large eddy current loss that will be incurred in these parts. Although we have tried to use ferrite instead of mild steal, it has not been successful. It is still worthy to investigate ferrite yoke/mandrel. In addition to ferrite, composite plastic/steel powder and traditional steel lamination can be also considered to reduce eddy current loss and increase thrust. The plunger can be also improved by using different materials and/or structures. Three possible structure/material arrangements are suggested for further investigation. They are sleeve composite plunger, annuli composite plunger and mesh composite plunger, as shown in Fig. 9.1.

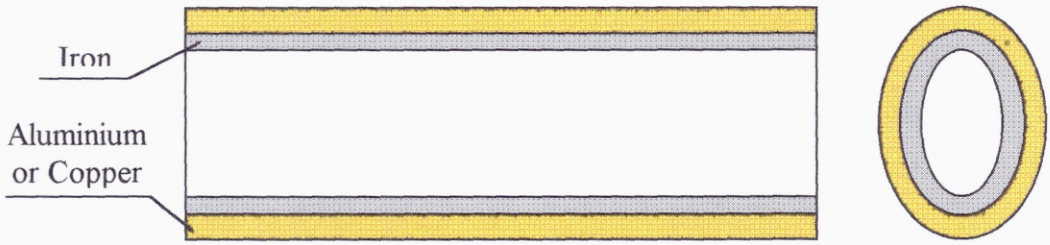


Fig. 9.1(a) Sleeve composite plunger

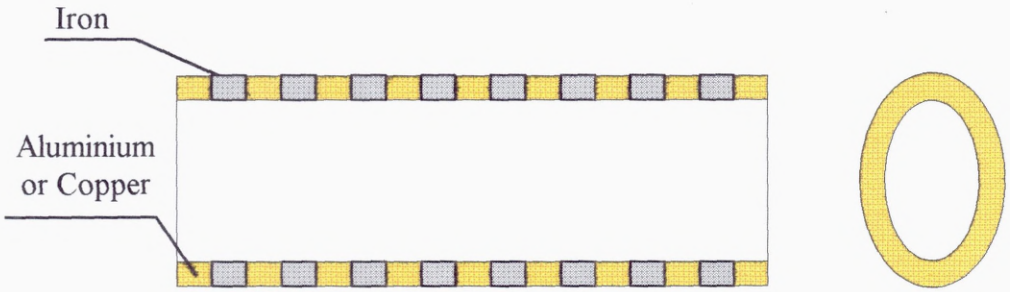


Fig. 9.1(b) Annuli composite plunger

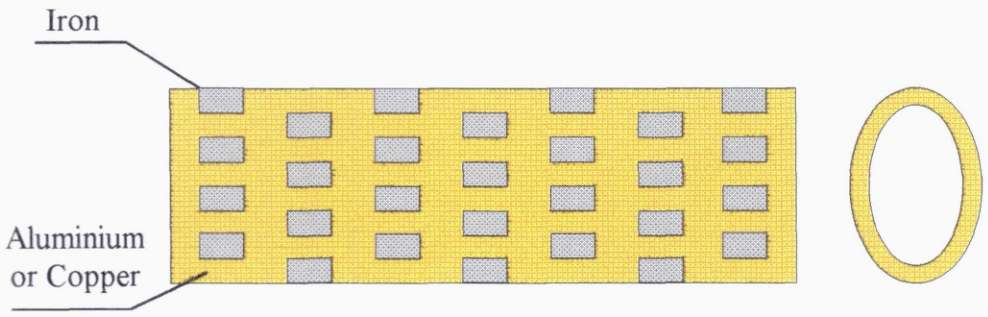


Fig. 9.1(c) Mesh composite plunger

(ii) Ventilation: Even if the eddy current losses in yoke/mandrel can be reduced to a very low level, the eddy current in plunger is useful and inevitable in order to produce thrust. The eddy current loss in plunger is similar to that in the rotor of an induction motor. However the resultant temperature rise in TLIA will be quicker and higher than in induction motors for the same rate of loss, due to poor ventilation that exists in TLIAs in comparison with induction motors. If the positioning application is under continuous operation or has large duty cycle with high load, the temperature rise would pose a problem. In these cases proper forced ventilation should be considered in the TLIAs' design. It could be an external forced ventilation or integrated internal forced ventilation by using non-conductive fluid as heat-removing media. Any of those considerations will need to change the TLIA design.

(iii) Structure:

There are many other configurations of the single-phase TLIAs that can be derived from the current structure and/or from the concepts developed in rotary machines. Those new structures for plunger mentioned in (i) and the U-shape yoke/mandrel mentioned in chapter 2 are some of the direct modifications that can be applied to the current design. Also other force restraining schemes, such as d.c. devices using voice coil and permanent magnet, would be an alternative to the current design.

### 9.2.2 Design Analysis Tools

The current design analysis method should be adequate to the engineering application of the current TLIAs' structures. However there is increasing demand to simulate magnetic hysteresis and mechanical movement. Coupling mechanical movement can be easily incorporated into current analysis software. Simulation of magnetic hysteresis could pose some problems according to our literature survey. There are two problems in the treatment of magnetic hysteresis. One is the mathematical modelling of hysteresis characteristics. The other is the steep rise of CPU time required when hysteresis property is simulated. With the development of the DMVP method, it can be expected to find favourable application areas such as

- Simulation of switch-mode operation
- Modelling hysteresis
- Parallel computation

Although only application to switch-mode operation has been carried out in this research, the other two prospective application areas are directly derived from the intrinsic characteristics of the DMVP method and the particular requirements. Its actual value to the other two areas would depend on the future development and application of the method.

### 9.2.3 Control Hardware

At present the PSDU was designed and fabricated by ourselves and the DSP board was purchased. First of all the PSDU could be improved in terms of cutting cost and providing more protection. Secondly it is suggested to integrate the DSP chip with the PSDU. This integration will mainly involve moving the DSP and the AIC chips on to the PSDU. As for the circuit protection, three types of protection should be considered. They are,

- Power semiconductor's protection. This will involve over-current protection to the chopper circuit and the full-bridge inverter circuit.

- Grounding/earthing: Proper arrangement of grounding would reduce electromagnetic interference between different parts of the circuits. Proper earthing would provide a good reference potential for digital circuits, which are more susceptible to the damage caused by voltage surge and static voltage, in addition to enhancing safety of users.
- Isolation: If the PSDU is energised directly from the mains, high voltage may be passed onto external circuit once it is broken. This could damage some expensive external circuit that is connected to monitor or control the circuit. For instance, if we wish the DSP board to be immunised from any high voltage from the PSDU, we may need an optocoupler interface between the two circuits. Isolation may need to be applied on the drives of power semiconductors to prevent damage of drive circuit when power semiconductors are broken.

### 9.2.4 Control Software

In this research, we have only been able to apply traditional digital control method adopting a second-order model with fixed parameter plant. It has been observed that many new control methods have been developed in digital control, such as adaptive control, optimal control, vector control, fuzzy control, neural network control, etc.. Because of the nature of a TLIA with its non-linearities, temperature-dependent parameters and parameter deviations from one actuator to another, those modern digital control methods would provide a solution to those problems. With the increase of computing power of single DSP, it is also possible to combine part of the PSDU's function into the control software to reduce the cost. For instance the DSP can be used to generate firing pulse for the triac circuit or logical switching signal for the PWM circuit.

# References


[1] A. Kanai, H. Sano, J.Yoshioka and M. Miyashita, 'Positioining of a 200kg Carriage on Plain Bearing Guideways to Nanometer Accuracy with a Force-operated Linear Actuator', *Nanotechnology*, 1991, pp43-51

[2] G.Hu and C.B. Rajanathan, 'Dynamic Analysis of Voltage Excited Tubular Linear Induction Actuators', *IEE Proc. of International Conference on Computation in Electromagnetics*, November 1991, London, pp319-322

[3] R. Akmese and J.F.Eastham, 'Design of Permanent Magnet Flat Linear Motors for Standstill Applications', *IEEE Trans. on Magn.*, Vol.28, No.5, September 1992, pp3042-44

[4] S. Osawa, M. Wada, M. Karita, D. Ebihara and T. Yokoi, 'Light-weight Type Linear Induction Motor and Its Characteristics', *IEEE Trans. on Magn.*, Vol.28, No.5, September 1992, pp3003-5

[5] T. Maeda and H. Fujita, 'Characteristics of Linear Actuator with Semiclosed Magnetic Circuit Excited by Discharge Current of Capacitor', *Electrical Engineering in Japan*, Vol.113, No.8, 1993, pp136-41 (Translated from Denki Gakkai Ronbunshi, Vol.112-D, No.10, October 1992, pp972-76)

[6] J.F. Gieras and D. Carter, 'Computation of Temperature Distribution in the Longitudinal Section of a Single-sided Linear Induction Motor', *ICEMA*, Vol.1, September 1993, pp180-5

[7] C.B. Rajanathan and G. Hu, 'A Novel Tubular Linear Induction Actuator', *Proc. of ICEM'92*, Manchester, UK, September, 1992, pp137-40

[8] G.W. Mclean, 'Review of Recent Progress in Linear Motors', *IEE Proc.-Pt.B*, Vol.135, No.6, November 1988, pp380-416.

[9] E.R. Laithwaite, 'Induction Machines for Special Purposes', *George Newnes Ltd.*, 1966

[10] E.R. Laithwaite, 'Linear Electric Motors', *Mills & Boon Ltd, London*, 1971

[11] M. Poloujadoff, 'The Theory of Linear Induction Machinery', *Oxford University Press*, 1980

[12] G. Hu, 'Computer Aided Analysis and Design of a Single Phase Tubular Linear Actuator', *Ph.D Thesis, University of Abertay Dundee*, 1993

[13] B.V. Jayawant, 'Induction Machines', *Mcgraw-Hill Publishing Company Limited*, 1968

[14] S. Ratnajeevan H. Hoole, 'Computer-Aided Analysis and Design of Electromagnetic Devices', *Elsevier Science Publishing Co., Inc.*, 1988

[15] P.P. Silvester, 'Software Applications in Electrical Engineering', *Computational Mechanics Publications* 1993

[16] Vlado Ostovic, 'Computer-aided Analysis of Electric Machines', *Prentice Hall International (UK) Limited*, 1994

[17] B. Ancelle, J.L. Coulomb and B. Morel, 'Implementation of a Computer Aided Design System for Electromagnets in an Industrial Environment', *IEEE Trans on Magn.*, Vol. 16, 1980, pp806-8

[18] J. Simkin and C.W. Trowbridge, 'Optimizing Electromagnetic Devices Combining Direct Search Method with Simulated Annealing', *IEEE Trans on Magn*,Vol.28, No.2, March 1992, pp1545-48

[19] D.N. Dyck and D.A. Lowther, 'Automated Design of Magnetic Devices by Optimizing Material Distribution', *Proc. of the 10th-COMPUMAG*, Berlin, July, 1995, pp256-7

[20] C.R.I. Emson and J. Simkin, 'An Optimal Method for 3-D Eddy Currents', *IEEE Trans. on Magn.*, Vol.19, 1983, pp2450-52

[21] C.R.I Emson, J. Simkin and C.W. Trowbridge, 'Further Developments in Three Dimensional Eddy Current Analysis', *IEEE Trans. on Magn.*,Vol.21, 1985, pp2231-3

[22] D. Rodger and J.F. Eastham, 'A Formulation for Low Frequency Eddy Current Solutions', *IEEE Trans. on Magn.*, Vol.19, November 1983, pp2443-6

[23] D. Rodger, 'A Finite Element Method for Calculating Power Frequency Three Dimensional Electromagnetic Field Distributions', *Proc. IEE, Vol.130*, Pt.A, No.5, 1983, pp233-8

[24] D.Rodger and J.F. Eastham, 'Finite Element Solution of 3D Eddy Currents in Magnetically Linear Conductors at Power Frequency', *IEEE Trans. on Magn.* Vol.18, No.2, 1982, pp481-5

[25] P.P. Silvester and M.V.K. Chari, 'Finite-Element Solution of Saturable Magnetic Field Problems', *ibid*, 1970, Vol.89, p1642

[26] R.L. Stoll, 'The Analysis of Eddy Currents', *Clarendon Press*, 1974

[27] L. Komzsik and P. Poschmann, 'Iterative Solution Techniques for Finite Element Applications', Finite Elements in Analysis and Design, *Elsevier Science Publishers B.V.*, 1993, pp373-79

[28] C.B. Rajanathan and G. Hu, 'Electromechanical Transient Characteristics of an Induction Actuator by Finite Element Analysis', Proc. of *the 5th IEEE Biennial Conference on Electromagnetic Field Computation*, Claremont, California, USA, August, 1992

[29] D. Rodge, T. Karagular and P.J. Leonard, 'A Formulation for 3D Moving Conductor Eddy Current Problems with Smooth Rotors', *IEEE Trans. on Magn.*, Vol.26, 1990, pp2359-63

[30] E. Cardelli, M. Gimignani and M. Raugi, 'Numerical Modelling of 3-D Coupled Electromagnetic and Heating Diffusion Problems', *IEEE Trans. on Magn.*, Vol.30, No.5, Sep. 1994, pp3331-4

[31] I.A. Tsukerman, A. Konrad, G. Meunier and J.C. Sabonnadière, 'Coupled Field-Circuit Problems: Trends and Accomplishments', *IEEE Trans. on Magn.*, Vol.29, No.2, March 1993, pp1701-05

[32] I.A.Tsukerman et al., 'A Survey of Numerical Method for Transient Eddy Current Problems', *IEEE Trans. on Magn.*, Vol.29, No.2, March 1993, pp1171-15

[33] K.Preis, O.Biro, R.Dyczij-Edlinger and K.R. Richter, 'Application of FEM to Coupled Electric,Thermal and Mechanical Problems', *IEEE Trans. on Magn.*, Vol.30, No.5, September 1994

[34] K. Yuan and K. Chen, 'A New Algorithm for Coupled Solution of Electric, Magnetic and Mechanical Systems in Dynamic Simulation of Solenoid Actuator', *ibid*, Vol.26, No.3, May, 1990, pp1189-97

[35] F. Delincé, A.Nicolet, F.Henrotte, A.Genon and W. Legros, 'Influence of Hysteresis on the Behaviour of Coupled Finite Element - Electric Circuit Models', *IEEE Trans. on Magn.*, Vol. 30, No. 5, September 1994, pp3383-86

[36] P. Alotto, 'A 2D Finite Element Procedure for Magnetic Analysis Involving Non-linear and Hysteretic Materials', *IEEE Trans. on Magn.*, Vol.30, No.5, September 1994, pp3379-82

[37] A. Nicolet, F. Delincé, N. Bamps, A. Grenon and W. Legros, 'A Coupling Between Electric Circuits and 2D Magnetic Field Modeling', *IEEE Trans. on Magn.*, Vol.29, No.2, March 1993, pp1697-99

[38] E.G. Strangas, 'Coupling the Circuit Equations to the Non-linear Time Dependent Field Solution in Inverter Driven Induction Motors', *IEEE Trans. on Magn.*, Vol.21, No.6, November 1985, pp2408-11

[39] Fràncis Piriou and Adel Razek, 'Coupling of Saturated Electromagnetic Systems to Non-linear Power Electronic Devices', *IEEE Trans. on Magn.*, Vol. 25, No. 1, January 1988, pp275-77

[40] Q.Z. Shi and D. Chen, 'Analysis of Transient Magnetic Fields Coupled to Mechanical Motion in Solenoidal Electromagnet Excited by Voltage Source', *IEEE*

*Trans. on Magn.*, Vol.. 28, No. 2, March 1992, pp1315-17

[41] T. Dreher, R. Perrin-Bit, G. Meunier and J.L. Coulomb, 'A Three Dimensional Finite Element Modelling of Rotating Machine Involving Movement and External Circuit', *Proc. of the 10th-COMPUMAG*, Berlin, July, 1995, pp398-9

[42] P. Hammond, 'Use of Potentials in Calculation of Electromagnetic Fields', *Proc. IEE, Pt. A*, Vol.129, 1982, p106

[43] T.W. Preston and A.B.J. Reece,'Solution of 3-Dimensional Eddy Current Problem; the T-Ω Method', *ibid*, 1982, MAG., Vol.18, p486

[44] C.F. Bryant, C.R.I. Emson, J.Simkin and C.W. Trowbridge, 'Lorentz Gauge-the Search for Maximum Efficiency of Solution', *Proc. of the 10th COMPUMAG*, Berlin, July, 1995, pp428-9

[45] O.C. Zienkiewicz and R.l. Taylor, 'The Finite Element Method', *McGraw-Hill Book Company Ltd., UK*, 1989

[46] T. Nakata, edited, '3-D Electromagntic Field Analysis', *James & James*, 1990

[47] K. Komeza, A. Pelikant, J. Tegopoulos and S. Wiak, 'Comparative Computation of Forces and Torques of Electromagnetic Devices by Means of Different Formula', *IEEE Trans. on Magn.*, Vol.30, No.5, 1994, pp3475-78

[48] T.W. Nehl, and D.A. Field, 'Accuracy of Force Calculations Using First Order Tetrahedra for Electromagnetic Devices with Small Air Gaps', *IEEE Trans. on Magn.*, Vol.27, No.5, 1991, pp4250-53

[49] W. Müller, 'Comparison of Different Methods of Force Calculation', *IEEE Trans. on Magn.*, Vol. 26, NO. 2, 1990, pp1058-61

[50] E.S. Hamdi, A.F. Licariao-Nogueira and P.P. Silvester, 'Torque Computation by Mean and Difference Potentials', *Proc. IEE, Pt.A*,Vol.140, No.2, 1993, pp151-54

[51] G. Henneberger, P.K. Sattler and D. Shen, 'Force Calculation with Analytical Accuracy in the Finite Element Based Computational Magnetostatics', *IEEE Trans. on Magn.*, Vol.27, No.5, 1991, pp4254-57

[52] T. Tärnhuvud and K. Reichert, 'Accuracy Problems of Forces and Torque Calculation in FE-Systems', *IEEE Trans. on Magn.*, Vol.24, No.1, 1988

[53] A.N. Wignall, A.J. Gilbert and S.J. Yang,'Calculation of Forces and Magnetised Ferrous Cores Using Maxwell Stress Method', *IEEE Trans. on Magn.*, Vol.24, No.1, 1988, pp.459-62

[54] I. Tsukerman, J.D. Lavers and A. Konrad,'Using Complementary Formulations for Accurate Computations of Magnetostatic Fields and Forces in a Synchronous Motor', *IEEE Trans. on Magn.*, Vol.30, No.5, 1994, pp3479-82

[55] J.L. Coulomb, 'A Methodology for the Determination of Global Electromechanical Quantities from a Finite Element Analysis and Its Application to the Evaluation of Magnetic Forces, Torques and Stiffness', *IEEE Trans. on Magn.*, Vol.19, No.6, Vovember 1983, pp2514-19

[56] P. Hammond and J. Penman, 'Calculation of Inductance and Capacitance by Means of Dual Energy Principles', *Proc. IEE*, Vol.123, No.6, 1976, pp554-559

[57] A. Bejan, 'Heat Transfer', John Wiley & Sons, Inc., 1993

[58] José Américo Dias Pinto, Carlos F. Lemos Antunes and A. Paulo Bre Coimbra, 'Transient Heating and Cooling Analysis in an Electromagnetic Device', *IEEE Trans. on Magn.*, Vol.30, No.5, September 1994, pp3339-42

[59] M. Jarnieux, G.Reyne and G.Meunier. 'FEM Modelling of the Magnetic Thermal, Electrical and Mechanical Transient Phenomena in Linear Induction Lunchers', *IEEE Trans. on Magn.*, Vol.30, No.5, Sep. 1994, pp3312-5

[60] R. W. Lewis, K. Morgan, H.R. Thomas and K.N. Seetharamu, 'The Finite Element Method in Heat Transfer Analysis', *John Wiley & Sons, Inc.*, 1996

[61] H. Wolf, 'Heat Transfer', *Happer & Row Publishers, New York*, 1983.

[62] J. F. Gieras, 'Linear Induction Drives', *Oxford University Press Inc., New York*, 1994

[63] Takashi Kenjo, 'Power Electronics for the Microprocessor Age', *Oxford Science Publications* 1990

[64] A. Mansouri, M. Abignoli, B. Laporte and D. Nassr, 'Modelisation, Commande Optimisee en Vitesse Variable D✣n Moteur Asynchrone Monophase', *European Power Electronics, Chapter Symposium: Electric Drive Design and Applications*, 1994, pp463-8

[65] N. Mohan, et al., 'Power Electronics, Converters, Applications and Design', *Wiley*,1995

[66] A.I. Pressman, 'Switching Power Supply Design', *McGraw-Hill*, 1991

[67] B. Maurice, 'Simplified Digital Control for Three Phase Induction Motor Drive', *EPE Journal*, Vol.2, No.3, October 1992, pp181-90

[68] H. Miyazaki and M. Ono, 'A Speed Control System for AC Induction Motor Application to Home Appliances', *Proc. of Intelligent Motion*, June 1993, pp230-6

[69] J. Nicolai and T. Castagnet, 'Controlling a DC Motor with a Low-end Miro-Controller', *Proc. of Intelligent Motion*, June 1993, pp422-31

[70] D.K. Miu, ' Mechatronics', *Spring-verlag New York, Inc.*, 1993

[71] C.L. Philips and H.T. Nagle, 'Digital Control System Analysis and Design', *Prentice-Hall, Inc.*, 1995

[72] H.H. Hostetter, 'Digital Control System Design', *Holt, Rinehart and Winston, Inc.*, 1988

[73] A. Kawamura and T. Yokoyama, 'Comparison of Five Different Approaches for Real Time Digital Feedback Control of PWM Inverters', *Conference record of the '1990 IEEE Industrial Application Society Annual Meeting'*, Vol.2, 1990, pp1005-11

[74] S.L. Tung, L.H. Ho, H.C. Yeh and Y.Y. Tzou, 'DSP-based Digital Control of a PWM Inverter for Sine Wave Tracking by Optimal State Feedback Technique', IEEE, (?)

[75] Texas Instruments, 'TMS320C2x DSP Starter Kit User's Guide', *Texas Instruments Incorporated*, March 1993

[76] Texas Instruments, 'TMS320C2x User's Guide', *Texas Instruments Incorporated*, January 1993

[77] Kun-Shan Lin, edited. 'Digital Signal Processing Applications', *Prentice-Hall, Inc.*, 1987

[1]

# Appendix A. Finite Element Formulation for Axi-symmetric Transient Eddy Current Problems

In axi-symmetric form, the governing equation for transient eddy current problems will be:

$$\frac{\partial}{\partial z}(\nu\frac{\partial A_\vartheta}{\partial z})+\frac{\partial}{\partial r}(\frac{\nu}{r}\frac{\partial rA_\vartheta}{\partial r})-\sigma\frac{\partial A_\vartheta}{\partial t}=-J_\vartheta \tag{A.1}$$

Its FE solution requires both boundary conditions and initial conditions. Three types of boundary conditions are usually encounter in electrical engineering. They are:

(i) $A_\vartheta = A_{\vartheta 0}$ on $\Gamma^1$ (A.2a)

(ii) $\frac{\nu}{r}\frac{\partial rA_\vartheta}{\partial n}=-H_t$ on $\Gamma^2$ (A.2b)

(iii) $A_\theta|_{\Gamma a}= A_\theta|_{\Gamma b}$ on $\Gamma_a$ or $\Gamma_b$ (A.2c)

Due to its first order differentiation against time, it has only one initial condition which is

(iv) $A_\theta|_{t=0}= A_\theta(0)$ (A.2d)

In order to obtain the familiar form expressed in Cartesian coordinate, we can make the following substitutions:

$x=z;$ $y=r;$ $J=J_\theta;$ $q=-H_t;$

$\mu^r=y\mu;$ $\nu^r=\nu/y;$ $\sigma^r=\sigma/y;$ $A^r=yA_\theta$

then, (A.1) can be rewritten as

$$\begin{cases} \dfrac{\partial}{\partial x}(v^r \dfrac{\partial A^r}{xz}) + \dfrac{\partial}{\partial y}(v^r \dfrac{\partial A^r}{\partial y}) - \sigma^r \dfrac{\partial A^r \vartheta}{\partial t} = -J & (A.3a) \\ A^r = A_0^r & (A.3b) \\ v^r \dfrac{\partial A^r}{\partial n} = q_n & (A.3c) \end{cases}$$

The functional corresponding to (A.3) is

$$\Theta = \iint_\Omega \left\{ \frac{v}{2y}\left[\left(\frac{\partial A^r}{\partial x}\right)^2 + \left(\frac{\partial A^r}{\partial x}\right)^2\right] + \frac{\sigma}{2y}\left(\frac{\partial A^r}{\partial t}\right)^2 - JA^r \right\} dxdy - \int_{\Gamma^2} qA^r d\Gamma \qquad (A.4)$$

If the whole region $\Omega$ is divided into many small sun-regions $\Omega^e\{e=1,2,\ldots E\}$, and in each $\Omega^e$ the following interpolations are introduced

$$A_e^r = \sum_{i=1}^{p} N_{e,i} A_{e,i}^r \qquad (A.5a)$$

$$x = \sum_{i=1}^{p} N_{e,i} x_i \qquad (A.5b)$$

$$y = \sum_{i=1}^{p} N_{e,i} y_i \qquad (A.5c)$$

Carrying out variation to (A.4), one can obtain

$$\frac{\partial \Theta}{\partial A_{e,j}^r} = 0 \qquad j=1,2,\ldots\ldots p \qquad (A.6)$$

$$\iint_{\Omega_e} \frac{v}{y}\left[\frac{\partial A_e^r}{\partial x}\frac{\partial}{\partial A_{e,j}^r}\left(\frac{\partial A_e^r}{\partial x}\right) + \frac{\partial A^r}{\partial y}\frac{\partial}{\partial A_{e,j}^r}\left(\frac{\partial A_e^r}{\partial y}\right)\right] dxdy + \qquad j=1,2,\ldots\ldots p \qquad (A.7)$$

$$\iint_{\Omega_e}\left[\frac{\sigma}{y}\frac{\partial}{\partial t}\left(A_e^r \frac{\partial A_e^r}{\partial A_{e,j}}\right) - J\frac{\partial A_e^r}{\partial A_{e,j}}\right] dxdy - \int_{\Gamma_e^2} q_n \frac{\partial A_e^r}{\partial A_{e,j}} = 0$$

Substituting (A.5) into (A.6) gives the elemental analysis as

$$\iint_{\Omega_e} \frac{\nu}{y}\left[\frac{\partial N_{e,j}}{\partial x}\sum_{i=1}^{p}\left(A_{e,i}^{r}\frac{\partial N_{e,i}}{\partial x}\right)+\frac{\partial N_{e,j}}{\partial y}\sum_{i=1}^{p}\left(A_{e,i}^{r}\frac{\partial N_{e,i}}{\partial y}\right)\right]dxdy+$$

$$j=1,2,\ldots\ldots p \qquad \text{(A.8)}$$

$$\iint_{\Omega_e}\left[\frac{\sigma}{y}N_{e,j}\sum_{i=1}^{p}(N_{e,i}\frac{\partial A_{e,i}^{r}}{\partial t})-JN_{e,j}\right]dxdy-\int_{\Gamma_e^2}q_n N_{e,j}d\Gamma=0$$

If we use matrix notation to describe (A.8), we can assume the elemental analysis has the matrix equation as

$$S^e A_e^r + T^e \dot{A}_e^r = b_e \qquad \text{(A.9)}$$

where

$$A_e^r=[A^r_{e,1} \quad A^r_{e,2} \quad \ldots\ldots \quad A^r_{e,p}]^T \qquad \text{(A.10a)}$$

$$\dot{A}_e^r = \frac{\partial A_e^r}{\partial t} \qquad \text{(A.10b)}$$

$$b_e=[b_{e1} \quad b_{e2} \quad \ldots\ldots \quad b_{ep}]^T \qquad \text{(A.10c)}$$

$$\zeta=[\zeta_{i,j}] \qquad \zeta=S^e,\ T^e; \qquad i=1,2,\ldots\ldots p; \qquad j=1,2,\ldots\ldots p \qquad \text{(A.10d)}$$

$$S_{i,j}^e = \iint_{\Omega_e}\frac{\nu}{y}\left(\frac{\partial N_{e,i}}{\partial x}\frac{\partial N_{e,j}}{\partial x}+\frac{\partial N_{e,i}}{\partial y}\frac{\partial N_{e,j}}{\partial y}\right)dxdy \qquad \text{(A.10e)}$$

$$T_{i,j}^e = \iint_{\Omega_e}\frac{\sigma}{y}N_{e,i}N_{e,j}dxdy \qquad \text{(A.10f)}$$

$$b_{e,j} = -\iint_{\Omega_e} J^e N_{e,j}dxdy-\int_{\Gamma_e^2}q_n^e N_{e,j}d\Gamma \qquad \text{(A.10g)}$$

Appropriate interpolation functions $N^e_i$ must be used to ensure the consistency of elemental interpolation. For triangular element, the interpolation function can be chosen as

$$N_{e,l} = \frac{\Delta_l}{\Delta} \qquad \text{(A.11a)}$$

$$N_{e,m} = \frac{\Delta_m}{\Delta} \tag{A.11b}$$

$$N_{e,n} = \frac{\Delta_m}{\Delta} \tag{A.11c}$$

with the following relationships

$$\Delta = \frac{1}{2}\begin{vmatrix} 1 & x_l & y_l \\ 1 & x_m & y_m \\ 1 & x_n & y_n \end{vmatrix}$$

$$\Delta_l = \frac{1}{2}\begin{vmatrix} 1 & x & y \\ 1 & x_m & y_m \\ 1 & x_n & y_n \end{vmatrix}$$

$$\Delta_m = \frac{1}{2}\begin{vmatrix} 1 & x_l & y_l \\ 1 & x & y \\ 1 & x_n & y_n \end{vmatrix}$$

$$\Delta_n = \frac{1}{2}\begin{vmatrix} 1 & x_l & y_l \\ 1 & x_m & y_m \\ 1 & x & y \end{vmatrix}$$

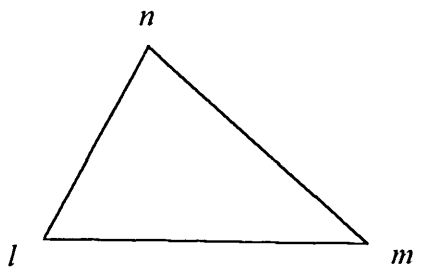


Fig. A.1 Vertex notation for triangular element

Substituting (A.11) into (A.10), we can obtain the elemental analysis straight forward.

# Appendix B. Finite Element Formulation for Axi-symmetric Transient Temperature Problems

When velocity effect is not directly treated in the heat transfer equation, the heat transfer equation becomes:

$$\nabla \cdot (k\nabla T) - \rho c \frac{\partial T}{\partial t} = -q \tag{B.1}$$

Its axi-symmetric form is

$$\frac{\partial}{\partial z}(k\frac{\partial T}{\partial z}) + \frac{\partial}{\partial r}(\frac{k}{r}\frac{\partial r T}{\partial r}) - \rho c \frac{\partial A_\vartheta}{\partial t} = -q \tag{B.2}$$

Equation (B.2) has identical form of (A.1) with the corresponding relationship:

$T=A_\vartheta$; $k=\nu$; $\rho c=\sigma$; $q=J_\vartheta$

Therefore all the analysis and formulations to $A_\vartheta$ in appendix A can be used directly here. The only special treatment required in the temperature computation is the heat convection boundary condition that is not treated in Appendix A. For the heat convection boundary:

$$\left.\frac{\partial T^r}{\partial n}\right|_{\Gamma_3} = h_c(\mathbf{x},t)(T^r - T^r_\infty) \qquad \text{for } \mathbf{x} \text{ on } \Gamma_3,\ t>0 \tag{B.3}$$

an additional term will appear in the functional, which is

$$\Theta_{add} = \int_{\Gamma_3}(h_c T^r_\infty T^r)d\Gamma - \frac{1}{2}\int_{\Gamma_3}(h_c T^r T^r)d\Gamma \tag{B.4}$$

The first of (B.4) is the same as the Neumann boundary condition of (A.3c), which has been treated as well. The only thing left is to treat the second term in (B.4). Carrying out variation to the second term of (B.4) gives

$$\frac{\partial \Theta_{add}\big|_{2nd}}{\partial T^r_{e,j}} = -h_c \int_{\Gamma_3} \frac{\partial T^r_e}{\partial T^r_{e,j}} d\Gamma$$

$$= -h_c \int_{\Gamma_3} N_{e,j} \sum_{i=1}^{p} N_{e,i} T^r_{e,i} d\Gamma \qquad j=1,2,\ldots\ldots p \qquad \text{(B.5)}$$

The change needs to be made in the temperature computation can be summered as

- Adding the contribution of (A.10e) to $S^e_{i,j}$
- Adding the contribution of the first term of (B.4) to $b_{e,j}$ of (A.10g) by changing $q^e_n$ to $q^e_n$ -$h_c$

# Appendix C. Analytical Solution for a Slot Containing Rectangular Conductors

Assuming there are '$p$' conductors with rectangular cross-section, as shown in Fig. C.1, the current density in each conductor is expressed by

$$J = \begin{cases} \sum_{p=1}^{q} J_p & b_{1b} > x_p > b_p, \quad and \quad b_{1b} > x_p > b_p \\ 0 & Otherwise \end{cases} \tag{C.1}$$

and the MVP is governed by

$$\frac{\partial^2 A_z}{\partial x^2} + \frac{\partial^2 A_z}{\partial y^2} = -\mu_0 J(x,y) \tag{C.2}$$

with the boundary conditions

$$\left.\frac{\partial A_z}{\partial y}\right|_{y=0} = \left.\frac{\partial A_z}{\partial y}\right|_{y=h} = \left.\frac{\partial A_z}{\partial y}\right|_{x=b} = \left.\frac{\partial A_z}{\partial x}\right|_{x=0} = 0 \tag{C.3}$$

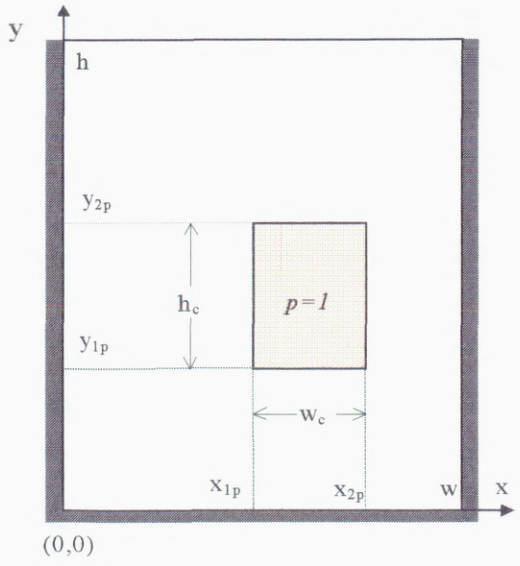


Fig. C.1 A slot containing a conductor

The expression of (C.1) can be expended in into a Fourier series with the following form:

$$J = \sum_{p=1}^{q}\sum_{j=1}^{\infty}\sum_{k=1}^{\infty} J_{j,k}\cos m_j x \cos n_k y \tag{C.4}$$

with

$$J_{1,1} = 0$$

$$J_{j,1} = \frac{2}{hw}\sum_{p=1}^{q} J_p(y_{2p} - y_{1p})\left(\frac{\sin m_j x_{2p} - \sin m_j x_{1p}}{m_j}\right)$$

$$J_{1,k} = \frac{2}{hw}\sum_{p=1}^{q} J_p(x_{2p} - x_{1p})\left(\frac{\sin n_k y_{2p} - \sin n_k y_{1p}}{n_k}\right)$$

$$J_{j,k}\Big|_{j,k\neq 1} = \frac{4}{hw}\sum_{p=1}^{q} J_p\left(\frac{\sin m_j x_{2p} - \sin m_j x_{1p}}{m_j} \times \frac{\sin n_k y_{2p} - \sin n_k y_{1p}}{n_k}\right)$$

For (C.4), (C.2) will have the following general form of solution

$$A_z = \sum_{p=1}^{q}\sum_{j=1}^{\infty}\sum_{k=1}^{\infty}(C_{aj}\cos m_j x + C_{bj}\sin m_j x)(B_{aj}\cos n_k y + B_{bj}\sin n_k y) \tag{C.5}$$

Applying (C.3) to (C.5), we can obtain

$$m_j = (j-1)\frac{\pi}{w} \qquad j=1,2,\ldots\ldots\infty \tag{C.6a}$$

$$n_k = (2k-1)\frac{\pi}{2h} \qquad k=1,2,\ldots\ldots\infty \tag{C.6b}$$

Therefore (C.5) becomes

$$A_z = \sum_{p=1}^{q}\sum_{j=1}^{\infty}\sum_{k=1}^{\infty} A_{j,k}\cos m_j x \cos n_k y \tag{C.7}$$

Substituting (C.7) and (C.4) into (C.2) gives the following formula to calculate $A_{j,k}$:

$$A_{j,k} = \frac{\mu_0 J_{j,k}}{m_j^2 + n_k^2} \tag{C.8}$$

So we have obtained the final analytical expression of $A_z$ as

$$A_z = \frac{2\mu_0 h^2 b^2}{\pi^2} \sum_{p=1}^{q} \sum_{j=1}^{\infty} \sum_{k=1}^{\infty} \frac{J_{j,k}}{(2k-1)^2 b^2 + 4(j-1)^2 h^2} \cos\frac{(j-1)\pi x}{b} \cos\frac{(2k-1)\pi y}{2h} \qquad \text{(C.9)}$$

# Appendix D: Schematics of the DSP kit

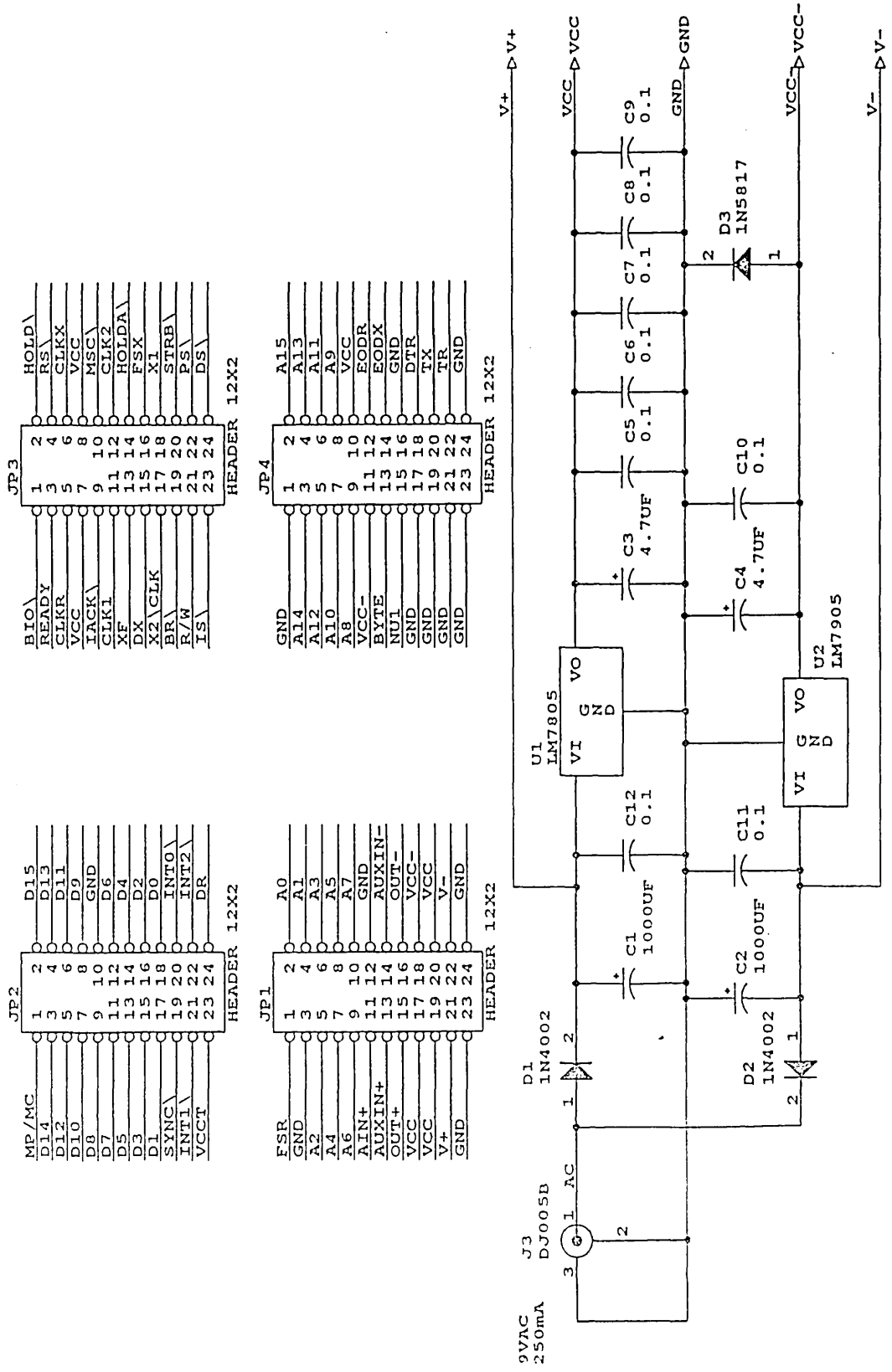

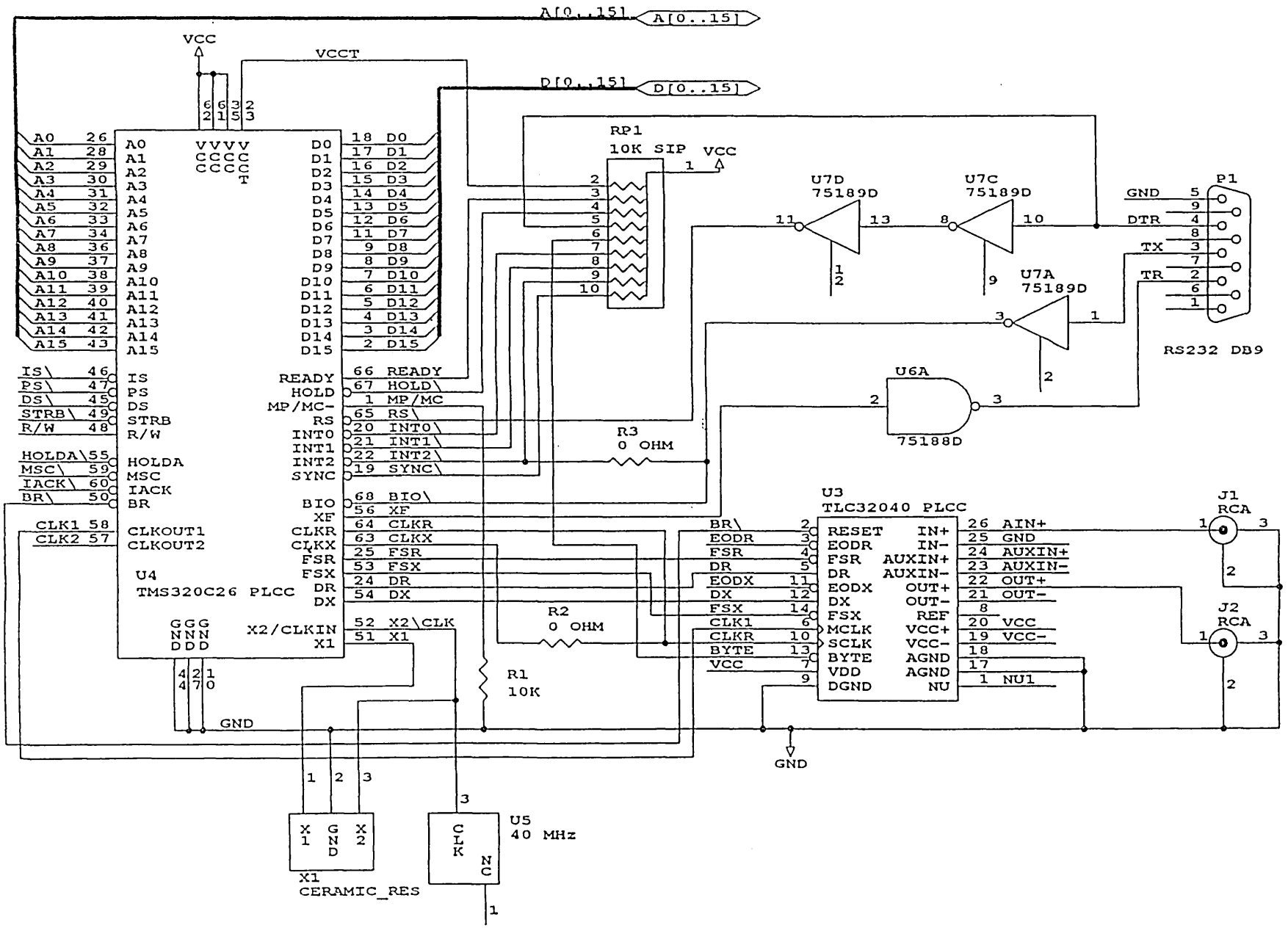
A[0..15]
A[0..15]
VCC
VCCT
D[0..15]
D[0..15]
RP1
10K SIP
VCC
U7D
75189D
U7C
75189D
U7A
75189D
P1
RS232 DB9
GND
DTR
TX
TR
U6A
75188D
R3
0 OHM
R2
0 OHM
R1
10K
U4
TMS320C26 PLCC
U3
TLC32040 PLCC
J1
RCA
J2
RCA
U5
40 MHz
X1
CERAMIC_RES
GND
A0
A1
A2
A3
A4
A5
A6
A7
A8
A9
A10
A11
A12
A13
A14
A15
IS\
PS\
DS\
STRB\
R/W
HOLDA\
MSC\
IACK\
BR\
CLK1
CLK2
CLKOUT1
CLKOUT2
D0
D1
D2
D3
D4
D5
D6
D7
D8
D9
D10
D11
D12
D13
D14
D15
READY
HOLD\
MP/MC
RS\
INT0\
INT1\
INT2\
SYNC\
BIO\
XF
CLKR
CLKX
FSR
FSX
DR
DX
X2/CLKIN
X1
X2\CLK
RESET
EODR
FSR
DR
EODX
DX
FSX
CLK1
CLKR
BYTE
VCC
MCLK
SCLK
BYTE
VDD
DGND
IN+
IN-
AUXIN+
AUXIN-
OUT+
OUT-
REF
VCC+
VCC-
AGND
AGND
NU
AIN+
GND
AUXIN+
AUXIN-
OUT+
OUT-
VCC
VCC-
NU1

# Appendix E

## Referred Publications Arising from the Research

**The full text of the published papers cited below has been removed from the e-thesis due to copyright restrictions:**

**Z. W. Shi and C. B. Rajanathan, "A new method to improve the accuracy of Maxwell stress based force calculation in computational electromagnetic fields," 1996 Third International Conference on Computation in Electromagnetics (Conf. Publ. No. 420), Bath, UK, 1996, pp. 241-246. doi: 10.1049/cp:19960192**

# Simulation of a New Type of Actuator Under Different Forms of Excitations

Z.W. Shi and C.B. Rajanathan
The University of Abertay Dundee
Bell street, DUNDEE DD1 1HG, UK

ABSTRACT

A method of simulating the dynamic performance of a tubular linear induction actuator (TLIA) operating under different forms of excitations is described. This method is based on coupling the circuit equations with the electromagnetic field equations that are solved by finite element method. Comparisons between experiments and simulations are included to show the effectiveness of the simulation method.

## 1. INTRODUCTION

The geometry of the single phase TLIA that has been designed and constructed is shown in Figure 1. Its simple structure and characteristics are inherently suitable for positioning in a stepless/continuous manner under open-loop or closed-loop control.

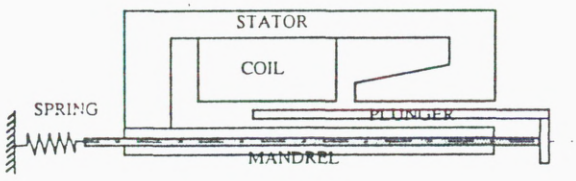


Fig. 1 The structure of the TLIA with restraining spring.

The operating principle of the actuator is based on the Lorentz electromagnetic force that is generated by the interaction between the main magnetic field and the induced eddy currents in the plunger. The total electromagnetic force in the form of axial thrust will vary with the position of the plunger under constant voltage or constant current excitation. Therefore control of the TLIA can be achieved by real-time control of the applied voltage or current. In this work the terminal voltage control method was adopted.

The waveforms of the excitation voltages considered include continuous sinusoidal wave, phase controlled sinusoidal wave and square wave. The transient characteristics caused by the nature of the electric supply with these three voltage waveforms can be categorised into two classes: the effects of point-on-switching and the effects of the waveform of the excitation voltage. These two aspects are examined in this paper.

The distributed nature of the induced currents precludes the use of equivalent circuit methods with equivalent lumped parameters. Therefore the governing equations are formulated in terms of field variables. The electrical circuit equations describing the external supply are coupled with the Maxwell's electromagnetic field equations, which are solved by finite element, with voltage sources as excitations.

As is well known Maxwell's equations for electromagnetic fields are usually formulated with current excitation. To introduce voltage excitation in the equations, two approaches are available : direct coupling and indirect coupling. We have adopted the indirect coupling method with a new model to deal with the transient eddy current problems. It is shown that a very fast simulation can be achieved with this method when the material properties are assumed to be linear. This enables the simulation of the linear system, with moderate numbers of electromagnetic components, by solving electromagnetic field equations along with electrical circuit equations. Even in non-linear cases, this method is faster than directly coupling method in most transient analysis, if modified Newton's iteration method is used, due to the fewer non-zero elements in the total stiffness matrix.

To treat the time derivative term in the solution of parabolic problems there exist many algorithms. The Backward Euler's algorithm is adopted in this work and provides sufficient accuracy, as shown in later sections of the paper, for continuous voltage excitation. For excitation with waveforms involving step changes, this method limits the accuracy of the solution and special treatment is needed.

## 2. METHOD OF SIMULATION

The governing equations for transient eddy current problems expressed in terms of the vector potentials are:

$$\nabla \times \nu \nabla \times \mathbf{A} = \frac{N}{S} i(t) - \sigma \frac{\partial \mathbf{A}}{\partial t} \qquad (1)$$

$$\mathbf{B} = \nabla \times \mathbf{A}$$

$$\mathbf{H} = \nu \mathbf{B}$$

where $\mathbf{A}$, $\nu$, $\sigma$, $i$, $S$ and $N$ are the magnetic vector potential, the magnetic reluctivity, the electrical conductivity, the excitation current, the area of cross section of the exciting coil and the number of turns of the winding respectively. Since the electromagnetic device is inductive the circuit equation can be written

$$u(t) = R \cdot i(t) + \frac{\partial \Psi}{\partial t} = R \cdot i(t) + \frac{\partial}{\partial t}\int_S (\nabla \times A) \cdot ds \quad (2)$$

where $u$, $R$ and $\Psi$ are the terminal voltage, the resistance of the coil and the flux linkage of the coil respectively.

Application of the finite element method to Eqn.(1) with appropriate gauge and boundary conditions, leads to the following linear matrix equation

$$[K][A] + [E]\frac{\partial A}{\partial t} = [C]i \quad (3)$$

By separating the magnetic vector potential into two components, as $A=A_j+A_e$, and using the Backward Euler's algorithm, the final matrix equations corresponding to Eqn.(1) can be expressed as:

$$[K'][A_j^n] = [K + \frac{E}{t^n - t^{n-1}}][A_j^n] = [C]i(t^n) \quad (4)$$

$$[K'][A_e^n] = [K + \frac{E}{t^n - t^{n-1}}][A_e^n] = \frac{1}{t^n - t^{n-1}}[E][A^{n-1}] \quad (5)$$

Eqn.(4) and (5) are solved by the Incomplete Choleski Conjugate Gradient method (ICCG) on account of its fast convergence. The separation of A into $A_j$ and $A_e$ proves very efficient for linear cases. Firstly, Eqn.(4) and (5) have the same stiffness matrix of [K']. The incomplete factorisation to [K'] needs to be done only once. Secondly, Eqn.(4) is also solved once at each time step while iteratively searching for $i(t^n)$ that satisfies Eqn.(2). And finally, Eqn.(3) is solved once as well in the whole time span for unit excitation current to get $A_j^0$ , from which we find $A_j^n$ as $A_j^n = A_j^0 \cdot i(t^n)$. For non-linear cases, the modified Newton's iteration method can be applied to Eqn.(3).

Direct coupling method puts Eqn.(2) into Eqn.(3) and solves the resultant single matrix equation. Instead we solve Eqn.(4) and (5) for linear cases or Eqn.(3) for non-linear cases. This leads to fewer non-zero elements than the direct method, with the constraint of Eqn.(2) by current search method. Many interpolation methods and searching methods are available and details could be found in the reference [6].

## 3. APPLICATION

The method was applied to a TLIA shown in Fig.1. The geometry is such that axi-symmetric form of the finite element formulation needs to be used. The finite elements. A time step of $0.2\times10^{-3}$ s. was chosen in the Backward Euler's Integration. The typical flux distribution at $t=0.2\times10^{-3}$ and $t=0.202\times10^{-2}$ s are shown in Fig.2 and Fig.3.

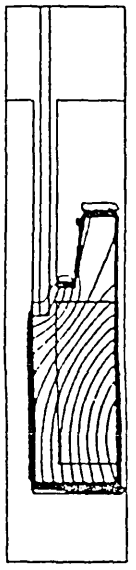

Fig.1 Flux distribution at time=$0.2\times10^{-3}$ s

Fig.2 Flux distribution at time=$0.202\times10^{-2}$ s

The dynamic responses of the TLIA under three forms of excitation voltages were investigated. The first case is sinusoidal excitation condition. The second is triac-controlled sinusoidal excitation and the third case is triac-controlled excitation with square wave. The waveforms of current, excitation voltage and back emf ( the second term on the right hand side of Eqn(2) ) is shown in Fig.(4)-(6) respectively.

In these simulations, an indirect coupling method was used with linear material properties assumed. Under these conditions, very fast simulations have been achieved by the method of separating the magnetic vector potential into two components .

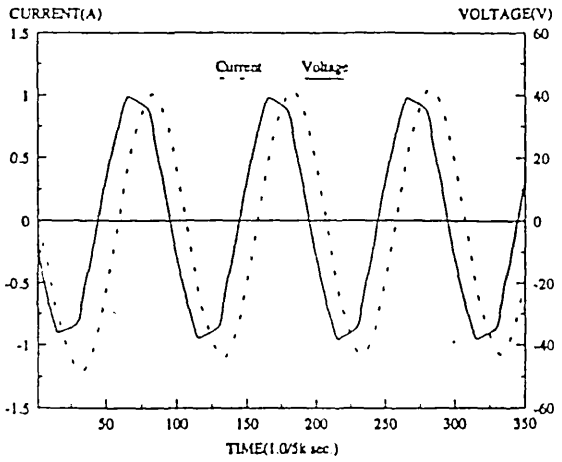


Fig. 4 The simulated current wave form with experimental voltage excitation(no triac control) at switching-on angle=$314^0$

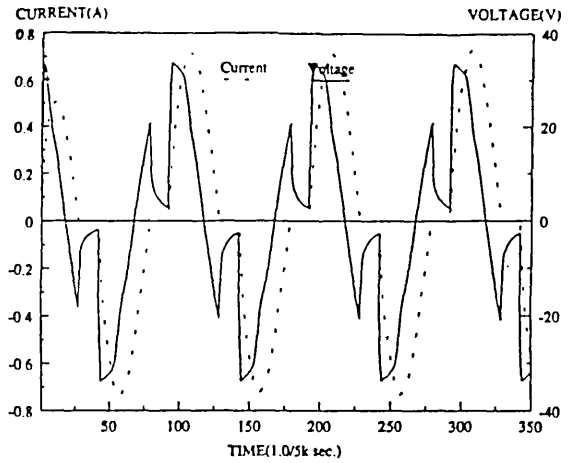


Fig.5 The simulated current and voltage(when triac is gated off) wave forms with triac controlled sinusoidal excitation at firing phase =$90^0$ and switching-on angle=$115.2^0$, same voltage waveform as experiment when triac is conducting

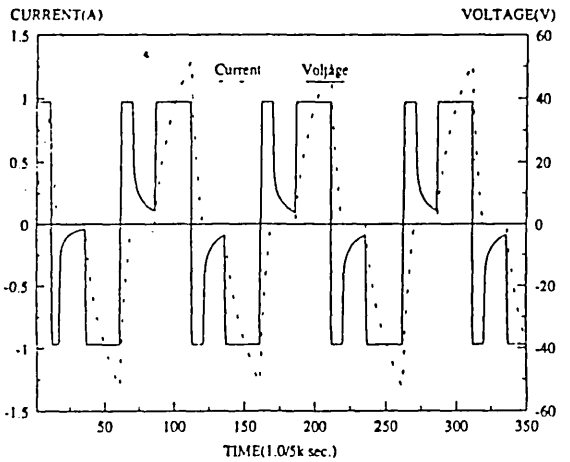


Fig.6 The simulated current wave form with ideal square wave excitation at firing phase =$90^0$ and switching-on angle=$135^0$

## 4. EXPERIMENTAL INVESTIGATION

Experimental work was carried out on the TLIA supplied with 50Hz ac power controlled by a triac. The control circuit designed and constructed uses a 0-5 V dc to control the firing phase of the triac. A precision linear potential meter was used to detect the position of the moving member and to generate a feedback voltage reflecting the position. A TMS320C26 DSP processor served as the central real time controller. The responses of the system were monitored with a digital data acquisition hardware board mounted on a PC. The configuration is illustrated in Fig.7.

The experimental work was carried out under standstill conditions as in the simulation. Two types of voltage waveforms, the sinusoidal and phase delayed under triac control, were investigated with different points-on-wave switching and firing phase angles. The transient voltages and currents recorded by digital data acquisition technique, are shown in Fig.8 and Fig.9.

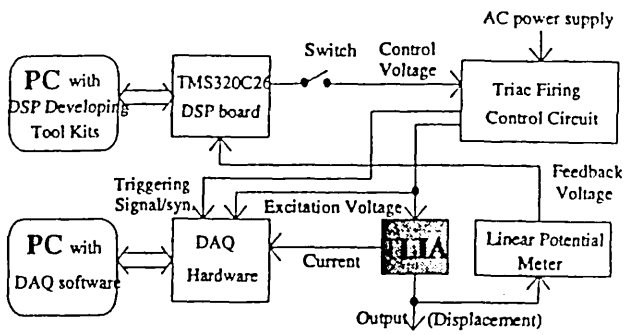


Fig.7 Diagram of configuration for experiments

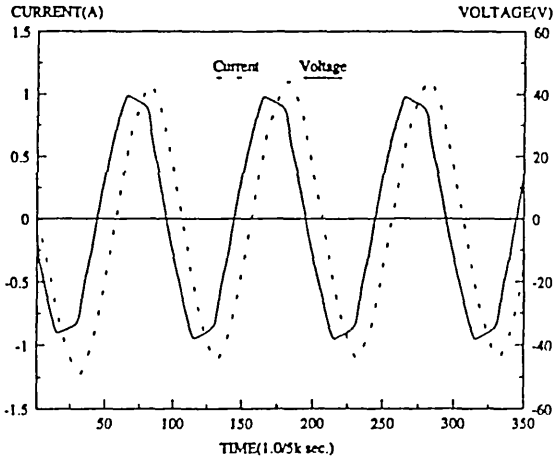


Fig.8 The tested wavesforms of current and terminal voltage at switching-on angle=$314^0$ without triac control

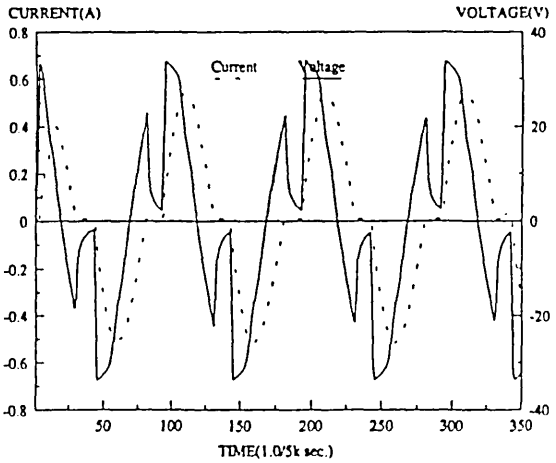


Fig.9 The tested wave forms of current and terminal voltage under triac controlled sinusoidal excitation at firing phase =$90^0$ and switching-on angle=$115.2^0$

## 5. DISCUSSION

In the experiment, the ac power supply to the control effects within the transformer, the output voltage from circuit was obtained from the 240 V mains through a transformer. It was observed that due to the saturation the controlled power supply was a distorted sinusoid. In the simulation software developed, the excitation voltage can be generated inside the software or can be input through an external file that stores voltage waveform . Both of the method to generate voltages were used in the study.

The simulation results using external file containing the actual voltage values are seen in Fig.4 and Fig.5. A pure sinusoidal wave with the same voltage amplitude generated by software produces the results seen in Fig.10. Comparing Fig.4 with Fig.10, it is apparent that Fig.4 is much closer to the experiment shown in Fig.8.

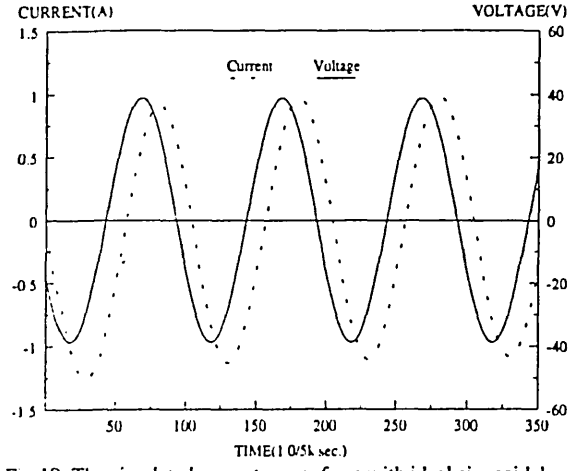


Fig.10 The simulated current wave form with ideal sinusoidal voltage excitation at switching-on angle=$314^0$

Due to the solid iron construction of the TLIA the magnetic permeability will change according to the current even if magnetic hysteresis is neglected. The magnetic permeability is lower than the average linear permeability when magnetic field density is very small. And lower magnetic permeability will cause larger excitation current if other conditions are the same. This is also reflected in the computations. It is believed that accuracy can be improved by using non-linear magnetic permeability.

The simulation has revealed that the errors in the predicted current waveform become larger when the excitation voltage has step changes such as in triac control. This can be seen by comparing Fig.(5) and (9). The reason is that the high frequency components will generate significant skin effects on all conducting materials. This results in a reduction in equivalent conductivity and penetration depth of eddy current, and reduces the excitation current. Although the transient involving of high frequencies dies away quickly, it will change the initial conditions for the time integration.

## 6. CONCLUSION

The experimental results have confirmed that the proposed method can simulate the TLIA under a variety of supply conditions. This method can be extended to incorporate mechanical movement without modification in the formulation if the electrical time constant is negligible compared to the mechanical time constant. That the coupled equations can be quickly solved under linear cases enables the simulation of large systems, which might consist of many electromagnetic devices linked together, by directly solving electromagnetic field equations described in differential form and the coupled circuit equations containing integral of field quantities.

## 7. REFERENCES


[1] G.W.Mclean, 1988, IEE Proc., *Review of Recent Progress in Linear Motors*, Pt.B, Vol.135, No.6, Nov., pp380-416.

[2] G.Hu and C.B. Rajanathan, 'Dynamic Analysis of Voltage Excited Tubular Linear Induction Actuators', IEE Proc. of ICCE'91 London, pp319-322

[3] I.A.Tsukerman et al., 'A Survey of Numerical Method for Transient Eddy Current Problems', IEEE Tran. on MAG, Vol.29, No.2, pp1171-15, March 1993

[4] Q.Z. Shi and D. Chen, 'Analysis of Transient Magnetic Fields Coupled to Mechanical Motion in Solenoidal Electromagnet Excited by Voltage Source', IEEE Tran. on MAG, Vol.20, No.2, March 1992, pp1315-17

[5] K.Preis, O.Biro, R.Dyczij-Edlinger and K.R. Richter, 'Application of FEM to Coupled Electric,Thermal and Mechanical Problems', IEEE Trans. on MAG., Vol.30, No.5, Spetember 1994

[6] Z.W. Shi and C.B. Rajanathan, 'A Method of Approach to Transient Eddy Current Problems Coupled with Voltage Sources', Paper No.51 , 10th COMPUMAG Conference, Berlin, July,1995

# A Method of Approach to Transient Eddy Current Problems Coupled with Voltage Sources

Z.W. Shi and C.B. Rajanathan
Department of Electronic and Electrical Engineering
University of Abertay Dundee
Bell Street, Dundee DD1 1HG, UK

*Abstract*—**This paper presents a new method of approach to transient eddy current problems with voltage excitations coupled by indirect methods. In linear cases, the magnetic vector potential is separated into two components to avoid redundant computation and thus hugely reduce the total CPU time. In nonlinear cases, either an elemental time-domain piecewise linearisation method or a Newton iterative method is adopted. A restarting function and second order interpolations are incorporated into an ICCG solver to accelerate the convergence. The method is applied to the modelling of a prototype tubular linear induction actuator. Results have shown that the method proposed is very efficient.**

## I. Introduction

In recent years, much effort has been directed towards time-dependent eddy current problems, especially those coupled with external voltage sources and/or mechanical movement to simulate the operation of real systems. Coupling mechanical movement involves redistribution of the meshes and leads to asymmetry in the stiffness matrix when the contribution due to the velocity term is not negligible. However the external voltage may be coupled while preserving the symmetry of the stiffness matrix and thus permitting the use of fast algorithms to solve large sparse symmetric matrix equation. There are two basic methods, the indirect and the direct, to deal with the field equations coupled with external electrical circuit equations[1]-[3].

The direct method could be implemented in two ways. One is to consider excitation currents as new variables to be solved together with field variables and this results in a higher order of matrix equation[2][4]. The other is to put the constraints of the circuit equations implicitly into the field equations and this results in a same order, but less sparse matrix equation[5][6]. Both approaches require modifying the global stiffness matrix arising from the discretized field equations and increase the non-zero elements and bandwidths. Although the direct coupling method needs only one computation to satisfy both field and circuit equations at each time step or nonlinear iterative step, the total storage demanded and the CPU time incurred are significantly higher compared to the indirect coupling method if the discretized nodes in the winding area are a moderate fraction of the total number of nodes [2][7].

The indirect method is an iterative procedure based on an initial estimated current and a current searching scheme. It preserves the advantage of symmetry and sparseness of the global stiffness matrix by separating circuit equations from field equations. The drawback is the introduction of iterative solutions between field and circuit equations. However, those iterations can be confined to be carried out only on the circuit equations in linear cases by separating magnetic vector potential into two components as described in the next section.

In the indirect method, the standard procedure executes nested iterations, e.g., current searching nests nonlinear search iteration that nests conjugate gradient searching. The total iterations will be Ni·Nn·Nt, where Ni, Nn and Nt stand for iteration numbers in the above three searches respectively. Since the convergence of all searching methods is related to initial conditions, another way to accelerate the convergence is by improving the initial estimations. It is achieved by combining second order interpolations with iterative solution algorithm in a restarting form.

## II. Formulation

At low frequencies where displacement current can be neglected, the governing equation for transient eddy current problems can be expressed in magnetic vector potential A as,

$$\nabla\times\nu\nabla\times\mathbf{A}-\sigma\frac{\partial\mathbf{A}}{\partial t}=\frac{N}{S}i(t) \tag{1}$$

where ν, σ, N and S are magnetic permeability, conductivity, turns and area of cross section of the winding with current $i(t)$ respectively. Equation (1) can be discretized into finite element form and expressed as (2), through weighted residual method or functional minimisation method with suitable gauge for A.

$$[\mathbf{K}][\mathbf{A}]+[\mathbf{E}][\frac{\partial\mathbf{A}}{\partial t}]=[\mathbf{C}]i(t) \tag{2}$$

If the electric device is driven by voltage, the current $i(t)$ in (2) must satisfy the following external electrical circuit equation at the same time,

$$\begin{aligned} u(t) &= R(t)\cdot i(t)+\frac{d\Phi}{dt} \\ &= R(t)\cdot i(t)+\frac{d}{dt}\sum_{e=1}^{w}\int_{l_e}\mathbf{A}\cdot dl \end{aligned} \tag{3}$$

Manuscript received July 10, 1995

where $\Phi$ is the magnetic flux linkage of the winding, $w$ is the total number of discretized elements in the winding area, $l_e$ is the integral path encompassing element $e$ and $R(t)$ is the equivalent resistance in series with the winding. We treat $R$ as variable to emulate various conditions not reflected by $u(t)$, such as time-dependant switching action, current-dependent nonlinearity, etc.. These phenomena are common in drive circuits employing electronic components such as diodes, triacs, and power transistors. Therefore the voltage $u(t)$ can be a time function such as a sinusoidal wave, a square wave, a saw-tooth wave, etc.. For simplicity a stable Backward Euler's Difference method is adopted here to treat the time derivative terms in (2) and (3).

*A. Non-linear cases*

Nonlinearities could be treated in two ways. One is to apply full excitation suddenly in one step with a robust, hence complicated, iterative searching method. Another is to apply the excitation gradually step-by-step with a simple iterative searching method, which is called artificial annealing. Since the solution of transient problems by using discrete time integration technique has the effect of artificial annealing to nonlinear property, a modified Newton-Raphson method will work effectively in these cases. The resultant iterative form of (2) can be expressed as:

$$[\mathbf{J}^n][\mathbf{A}^n_{m+1}-\mathbf{A}^n_m]=[\mathbf{C}]i_{m+1}(t^n)+[\mathbf{E}^n_m][\mathbf{A}^{n-1}]-[\mathbf{K}_m][\mathbf{A}^n_m] \tag{4}$$

where superscript $n$, and subscript $m$ are indices for time step number and nonlinear iteration number respectively.

At certain time step $n$, it is a good approach to calculate the Jaccobi matrix $[\mathbf{J}^n]$ from previous solution $\mathbf{A}^{n'-1}(n'\le n)$, which remains unchanged in the two iterative loops in the search for $i_{m+1}(t^n)$ and $\nu^n_m$ that follow. If the magnetic nonlinearity is considered, we can see that $\mathbf{A}^{n-1}$ just makes a constant contribution to $\mathbf{A}^n$. From the fixed time point of view, $\mathbf{A}^n$ is an implicit function of magnetic nonlinearity reflected in $i_{m+1}(t^n)$ and $\mathbf{A}^{n-1}$, but changes only during the current searching procedure. From the time span point of view, $i(t^n)$ and $\mathbf{A}^n$ are both functions of time. So two initial estimations can be introduced. The first one uses a parabolic curve fitting which just accounts for the time evolution factor. It can be expressed as:

$$\begin{aligned} f^n = & \frac{(t^n-t^{n-2})(t^n-t^{n-1})}{(t^{n-3}-t^{n-2})(t^{n-3}-t^{n-1})}f^{n-3} \\ & + \frac{(t^n-t^{n-3})(t^n-t^{n-1})}{(t^{n-2}-t^{n-3})(t^{n-2}-t^{n-1})}f^{n-2} \\ & + \frac{(t^n-t^{n-2})(t^n-t^{n-3})}{(t^{n-1}-t^{n-2})(t^{n-1}-t^{n-3})}f^{n-1} \end{aligned} \tag{5}$$

where $f$ could be current $i$ or vector potential A. This equation is used for the estimation of initial values of $i_0{}^n$ and $\mathbf{A}_0{}^n$ at each integral time step. The second one is a Newton interpolation that discards the time factor and can be expressed as:

$$f(x_{m+1})=f_m+\frac{f_m-f_{m-1}}{x_m-x_{m-1}}(x_{m+1}-x_m) \tag{6}$$

where $f$ could be potential A when $x$ is current $i$ or current $i$ when $x$ is voltage $u$. This equation is used for the iterative search for the excitation current.

*B. Linear cases*

In linear cases, a different treatment is preferable. We introduce two new components $\mathbf{A}_i$ and $\mathbf{A}_e$, defined as:

$$\mathbf{A}=\mathbf{A}_i+\mathbf{A}_e \tag{7}$$

Then (1) can be separated into the following two equations

$$\nabla\times\nu\nabla\times\mathbf{A}^n_i-\sigma\frac{\mathbf{A}^n_i}{\Delta t^n}=\frac{N\cdot i(t^n)}{S} \tag{8}$$

$$\nabla\times\nu\nabla\times\mathbf{A}^n_e-\sigma\frac{\mathbf{A}^n_e}{\Delta t^n}=-\frac{\sigma}{\Delta t^n}\mathbf{A}^{n-1} \tag{9}$$

The physical meaning is that $\mathbf{A}_i{}^n$ is the contribution from current $i(t^n)$ and $\mathbf{A}_e{}^n$ is the contribution from historical $\mathbf{A}^{n-1}$. $\mathbf{A}_i{}^n$ and $\mathbf{A}_e{}^n$ are decoupled within the current integration step, but coupled from one time step to another. Because (8) and (9) have the same differential operator, the same stiffness matrice applies, which can be expresses as:

$$[\mathbf{K}(\Delta t^n)][\mathbf{A}^n_i]=[\mathbf{C}]i(t^n) \tag{10}$$

$$[\mathbf{K}(\Delta t^n)][\mathbf{A}^n_e]=[\mathbf{E}][\mathbf{A}^{n-1}_i+\mathbf{A}^{n-1}_e] \tag{11}$$

The major advantage of separating A into $\mathbf{A}_i$ and $\mathbf{A}_e$ is that, if a constant time step is used, (10) needs being solved only $k$ times in all of time steps($k$ is the number of independent exciting currents) and (11) needs being solved only once during the current searching at each time step. Then an iterative current searching is only carried out on $i(t^n)$ using (6). Besides, equation(5) can still be used for the initial estimation for $i$ and $\mathbf{A}_e$.

This method works also with nonlinear materials if an elemental time-domain piecewise linearisation method is used, i.e., the material properties such as magnetic permeability and/or conductivity, are updated element by element according to the elemental field density computed in the previous time step and remains unchanged within the current time step. For many engineering applications, this

type of nonlinear approximation can provide enough accuracy with appropriate time steps.

*C. The ICCG solver*

The resultant linear algebraic equations are solved by the Incomplete Choleski Conjugate Gradient(ICCG) algorithm in standard form, that is, all the fillings in the Incomplete Choleski(IC) factorisation are discarded. Hence the resultant preconditioning matrix has the same pattern of the matrix to be conditioned. A restarting function is incorporated into the algorithm to accelerate the convergence. When the estimated potential $A_0^n$ is obtained from (5) or (6), it can be used as the initial value for the Conjugate Gradient(CG) iteration, starting from,

$$[p_0^n] = -[g_0^n] = ([L]^{-1}[M][L]^{-T})([L]^T[A_0^n]) - [L]^{-1}[r] \quad (12)$$

where [M] is the stiffness matrix or Jaccobi matrix, [L] is the lower triangle matrix from IC factorisation for preconditioning [M], [r] is the right hand side of the linear matrix equation, $[p_0^n]$ is the initial searching direction for the CG iteration and $[g_0^n]$ is the initial gradient direction. The block diagram of the ICCG with restarting function is shown in Figure 1.

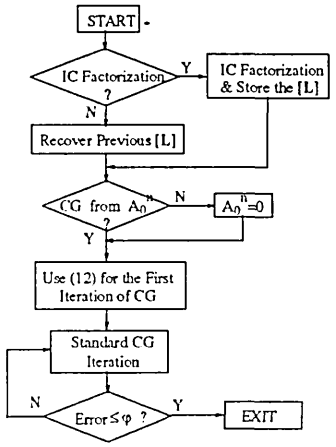


Fig. 1. Block diagram of ICCG with restarting function

## III. AN EXAMPLE OF APPLICATION

To verify the efficiency of this method, it is applied to a tubular linear induction actuator(TLIA) shown in Fig.2. The exciting coil is connected to an external voltage source of $50\sin(100\pi t+\phi_0)$. It is assumed that all ferromaterials are nonlinear with equivalent conductivity of 0.15E+7 (s/m) and the plunger has conductivity of 0.509E+8(s/m) with a relative magnetic permeability of unity.

Due to the structure of the TLIA, an axi-symmetric finite element form is adopted. The resultant matrix equation is solved by ICCG method. Two cases have been investigated. The first one is excited by pure sinusoidal voltage with two initial phase angles of $\phi_0=0^0$ and $\phi_0=90^0$. The second one is a

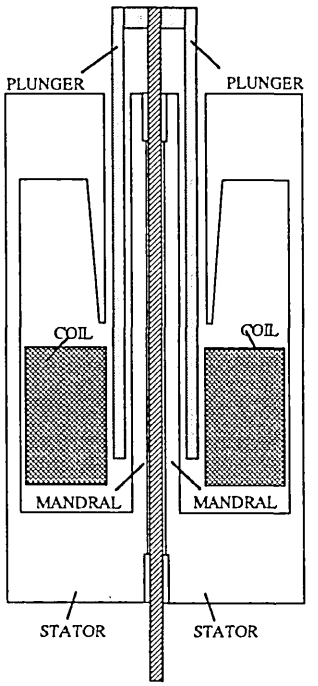


Fig. 2. The TLIA structure

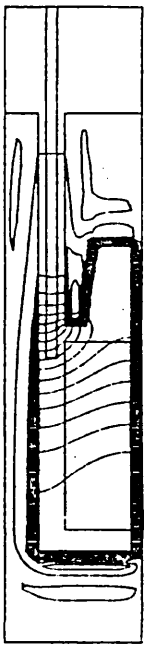

Fig. 3. Typical flux distribution

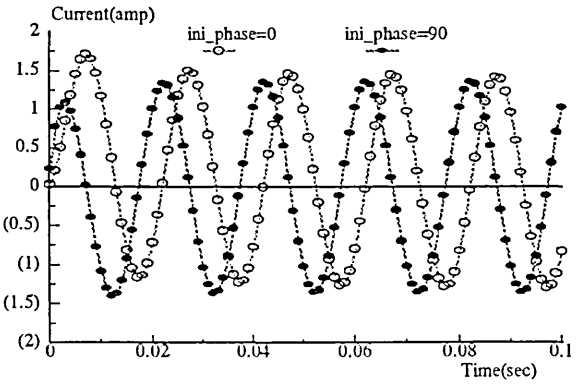


Fig. 4. Current waveforms at $\phi_0=0^0$ and $\phi_0=90^0$

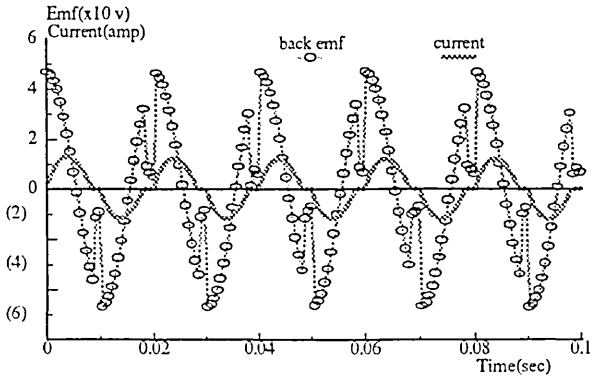


Fig. 5. Waveforms of current and back-emf under triac control

triac current-controlled one at 75° firing delay angle with the same voltage supply. The typical flux distribution is shown in Fig.3. The waveforms of excitation currents for both cases

TABLE I
DETAILS OF DISCRETISATION

| | Total Elements | Total Nodes(Nt) | Nodes in Winding Area (Nw) | Nw/Nt |
|---|---|---|---|---|
| Scheme A | 7594 | 3927 | 523 | 0.133 |
| Scheme B | 3128 | 1654 | 192 | 0.116 |

TABLE II
COMPARISON BETWEEN DIRECT AND INDIRECT COUPLING METHODS

| | Scheme A & Indirect Coupling | Scheme B & Indirect Coupling | Scheme A & Direct Coupling | Scheme B & Direct Coupling |
|---|---|---|---|---|
| Storage | 15447 | 6417 | 148918 | 23683 |
| Iterations | 80 | 46 | 56 | 40 |
| Time-1(s) | 2.29 | 0.78 | 12.22 | 2.52 |
| Time-2(s) | 0.27 | 0.09 | 76.99 | 3.56 |
| Time-3(s) | 9.37 | 2.36 | 46.29 | 5.56 |

Storage: Number of total non-zero elements in the matrix [L].
Time-1: CPU time in the assembling
Time-2: CPU time in the Incomplete Choleski factorisation
Time-3: CPU time in the Conjugate Gradient iterations from zero initial condition of $A0^n$.
The computation was carried out on a DEC Alpha 3000/400 workstation.

are shown in Fig.4 and Fig.5. The computation experiments show the convergence can be quickly reached within few iterations for current searching.

To make comparison between direct coupling method and indirect coupling method, two discretisation schemes for the same problem are studied. The details of discretisations are listed in Table I. For the direct coupling method the voltage is treated as the direct excitation source while the circuit equation is merged into the filed equations instead of treating the excitation current as an independent variable. The storage requirement and CPU time for both cases are presented in Table II based on one solution of linear matrix equation.

From Table II we can observe that the storage requirement of indirect coupling method is much less than that of direct coupling method, as is the the CPU time. The ratio of Nw/Nt can be used as the indicator to measure storage and CPU time. It is apparent the bigger the Nw/Nt, the larger the storage and CPU time for the same discretized node number. When Nw/Nt is very small, there is no significant difference between these two methods.

The total transient process will usually last several excitation cycles, and requires several hundred integral time steps. For linear cases the total CPU time is about the number of integral time steps multiplied by the figure listed in Table II. The saving in the CPU time with our proposed method can be calculated in the same straight forward manner for both linear cases and nonlinear cases with the elemental time-domain piecewise linearisation technique. As for precise nonlinear computation using iteration method in the form of (4), there is no clear conclusion as to which coupling method is superior because of factors such as level of nonlinearity or saturation, length of time steps, balancing strategy between CPU time and storage, etc.

## IV. CONCLUSION

It has been shown that the CPU time can be considerably reduced by separating the conventional magnetic vector potential A into two components $A_i$ and $A_e$ accompanied by iterative solutions with a restarting function. Although it is based on linear conditions, it can be adapted to treat nonlinearities effectively by the elemental time-domain piecewise linearisation technique with appropriate time step values. This method can also be implemented on other eddy current models such as A-Φ, A-Ψ, A-Ψ-Φ, with variable time steps.

## REFERENCES


[1] G.Hu and C.B. Rajanathan, 'Dynamic Analysis of Voltage Excited Tubular Linear Induction Actuators', *IEE Proc. of International Conference on Computation in Electromagnetics*, November. 1991, London, pp319-322

[2] Francis Piriou and Adel Razek, 'Coupling of Saturated Electromagnetic Systems to Non-linear Power Electronic Devices', *IEEE Trans. Magn.*, Vol. 25, No. 1, January 1988, pp275-77

[3] I.A. Tsukerman, A. Konrad, G. Meunier and J.C. Sabonnadière, 'Coupled Field-Circuit Problems: Trends and Accomplishments', *IEEE Trans. on Magn.*, Vol.29, No.2, March 1993, pp1701-05

[4] A. Nicolet, F. Delincé, N. Bamps, A. Grenon and W. Legros, 'A Coupling Between Electric Circuits and 2D Magnetic Field Modeling', *IEEE Trans. on Magn.*, Vol.29, No.2, March 1993, pp1697-99

[5] Q.Z. Shi and D. Chen, 'Analysis of Transient Magnetic Fields Coupled to Mechanical Motion in Solenoidal Electromagnet Excited by Voltage Source', *IEEE Trans. Magn.*, Vol.. 28, No. 2, March 1992, pp1315-17

[6] F.Delincé, A.Nicolet, F.Henrotte, A.Genon and W. Legros, 'Influence of Hysteresis on the Behaviour of Coupled Finite Element - Electric Circuit Models', *IEEE Trans. Magn.*, Vol. 30, No. 5, September 1994, pp 3383-86

[7] B. Ancelle, J.L. Coulomb and B. Morel, 'Implementation of a computer aided design system for electromagnets in an industrial environment', *IEEE Trans, Magn.*, Vol. 16, 1980, pp806-8

# Computation of Non-linear Transient Eddy Current Electromagnetic Fields in Devices Driven by Power Electronic Circuits

Z.W. Shi and C.B. Rajanathan
University of Abertay Dundee, Bell Street, Dundee DD1 1HG, UK

*Abstract*—A method of computing non-linear, transient electromagnetic fields with eddy currents, in which the magnetic vector potential is decomposed into two components is presented. The transient electromagnetic field is coupled with equations describing the external driving circuits with power electronic components. The non-linearity of magnetic materials is treated through a modified Newton's non-linear iterative scheme combined with a time-domain, piecewise elemental linearisation that enables the implementation of the decomposed magnetic vector potential method. A practical application of the method to a study of the transient characteristics of a tubular linear actuator is presented to show the effectiveness of the proposed method.

## I. Introduction

In current engineering practice there is an ever increasing use of power conditioning semiconductor devices such as MOSFETs, IGBTs, GTOs, etc., in the control of both conventional and new forms of electromagnetic devices. Traditionally, such electromagnetic devices and their controlling circuits have been studied separately at first, and then coupled together in a weak form in which parts of their static or dynamic parameters are used. This kind of analysis where the electromagnetic equations and circuit equations are solved separately, will lead to a significant errors when the combined system is non-linear [1]. Consequently, it is necessary to use a strong coupling method, which solves the electromagnetic field equation and external circuit equation simultaneously.

In the simultaneous solution of these coupled equations, two strategies can be adopted. These are categorised as the direct coupling methods and the indirect coupling methods [2]-[4]. Since the switch mode operation is widely favoured in power electronic driving circuits owing to the lesser power consumption and losses incurred in the power semiconductors working under this mode, our study will be focused on this mode of operation. It means that the high frequency components in both voltage and current will be rich, especially in pulse width modulated (PWM) mode, and therefore the number of discrete time steps should be much more than under continuous mode. For example, a typical PWM ac driving circuit will work at a switching frequency of above ten times higher than the base frequency, and a PWM dc driving circuit could work at about 100kHz.

Manuscript received March 19, 1996
Z.W. Shi, e-mail:EERZW@TAY.AC.UK, fax (+44) 01382-308261
C.B. Rajanathan, e-mail:EETCBR@TAY.AC.UK

There are many techniques described in the literature on the coupling of field and circuit equations [2]-[6]. However few of them relate to practical power electronic circuits working in the switch mode. In this paper, the decomposed magnetic vector potential (DMVP) method that the authors proposed in [2], is being extended to compute the non-linear transient electromagnetic fields with eddy currents, coupling a practical external circuit which has thyristors or IGBTs. The balance between the requirements of the speed of computation and the accuracy of the simulation is achieved by the judicious choice of either the time domain elemental piecewise linearisation method, or the modified Newon's non-linear iterative method, according to the instantaneous saturation level which is reflected by the average magnetic reluctivity or the excitation current.

## II. Method Of Modelling

In terms of the conventional magnetic vector potential **A** the governing equations for transient eddy current problems can be expressed as:

$$\nabla\times\nu\nabla\times\mathbf{A}-\sigma\frac{\partial\mathbf{A}}{\partial t}=\frac{N}{S}i(t) \tag{1}$$

where N and S are the turns and area of cross section of the excitation winding respectively with a current $i(t)$ flowing in it. Since most of the electromagnetic devices are voltage fed, an external circuit equation should be solved together with (1), which can be generally expressed as:

$$u(t)=R\cdot i(t)+\frac{d}{dt}\int_l \mathbf{A}\cdot dl \tag{2}$$

Different combination of voltage $u(t)$ and equivalent resistance function $R$ are used to simulate the behaviour of power semiconductors under different operating conditions. This will be discussed in the next section.

In the present study we assume that (1) has non-linear material properties and (2) has two-state linear properties corresponding to the 'on' and 'off' states in switch mode.

Coupling (1) and (2) is usually achieved by resorting to either the so-called direct method or the indirect method. In the work presented here, the indirect coupling method is used because of its advantages in terms of storage and CPU time when the number of nodes in the discretised winding area is not very small compared with the total nodes. In this approach the above two equations are solved separately in conjunction with a certain algorithm to search for the proper excitation current satisfying both equations.

Using the backward Euler's integration scheme, the time differential terms are treated in difference form as

$$dx/dt\big|_{t=t^n} = (x^n - x^{n-1})/(t^n - t^{n-1}) \quad (3)$$

where the super script $n$ denotes the time steps. Assuming linear properties are maintained from $t^{n-1}$ to $t^n$ and substituting (3) into (1) and (2), we can decompose the conventional magnetic vector potential A into two new vector potentials of $A_i^n$ and $A_e^n$. Then (1) can be alternatively expressed by the following equations :

$$\mathbf{A}^n = \mathbf{A}_i^n + \mathbf{A}_e^n \quad (4)$$

$$\Delta t^n \cdot \nabla \times \nu \nabla \times \mathbf{A}_i^n - \sigma \mathbf{A}_i^n = i\left(t^n\right)\Delta t^n N / S \quad (5)$$

$$\Delta t^n \nabla \times \nu \nabla \times \mathbf{A}_e^n - \sigma \mathbf{A}_e^n = -\sigma \mathbf{A}^{n-1} \quad (6)$$

Since (5) and(6) have the same differential operator, they will yield the same stiffness matrix as,

$$[K(\nu^n)][\mathbf{A}_i^n] = [C]i^n \quad (7)$$

$$[K(\nu^n)][\mathbf{A}_e^n] = [B][\mathbf{A}^n] \quad (8)$$

Bearing in mind that the treatment of material non-linearity can be also approached by an artificial annealing method, and if the time steps are small enough, as is the case to couple switch mode power electronic circuit where very fine time steps are required to accommodate the rapid switch action, we can treat the non-linear term of $[K]$ as,

$$[K(\nu^n)] \approx [K(\nu^{n-1})] \quad (9)$$

where $[K(\nu^{n-1})]$ is calculated from $[\mathbf{A}^{n-1}]$. Because $[K(\nu^{n-1})]$ is constant at the time step n, a preconditioned factorisation method as ICCG is effectively used to factorize $[K(\nu^{n-1})]$, and (7) and (8) are solved with only two separate conjugate gradient iterations. Once $\mathbf{A}_i^n$ and $\mathbf{A}_e^n$ are obtained, the search for the excitation current can be carried out with simple interpolation methods.

This scheme forms the basis of the time-domain elemental piecewise linearisation (TEPL) for the DMVP method. It merges non-linear iteration into time integration and confines the current searching to the circuit equation only. It is very fast, but it will result in larger error when magnetic reluctivity changes rapidly between the consecutive two integral steps. To reduce this error, a more strictly non-linear iteration, the modified Newton's non-linear iterative (MNNI) method described by (10) and (11) is used.

$$[J(\nu^{n-1})][\Delta \mathbf{A}_i^n]^k = [C]i^n - [K(\nu^{k-1})][\mathbf{A}_i^n]^{k-1} \quad (10)$$

$$[J(\nu^{n-1})][\Delta \mathbf{A}_e^n]^k = [B][\mathbf{A}^{n-1}] - [K(\nu^{k-1})][\mathbf{A}_e^n]^{k-1} \quad (11)$$

In (10) and (11) the superscript $k$ denotes the non-linear iterative steps. The current searching should be co-operated into the iterative procedure of the solution of (10) and (11) to accelerate the convergence.

Switching between the TEPL method and the MNNI method should be determined by the time differential of average magnetic reluctivity $d\tilde{\nu}/dt$, which can be further expressed as

$$\frac{d\tilde{\nu}}{dt} = \frac{\partial \tilde{\nu}}{\partial B}\frac{\partial B}{\partial t} \approx \lambda \frac{\partial \tilde{\nu}}{\partial B} \quad (12)$$

When $d\tilde{\nu}/dB$ is very small, equivalently $d\tilde{\nu}/dt$ is also very small, and the TEPL method could be used effectively. Otherwise the MNNI method should be used instead. Figure 1 shows the $d\nu_r/dB$ curve of a typical grain oriented lamination. For a given critical value of $d\nu/dB$, the border between the two methods, distinguished by P1 and P2 in Figure 2, can be easily determined by the average reluctivity. Alternatively P1 and P2 can also be determined by giving critical excitation currents .

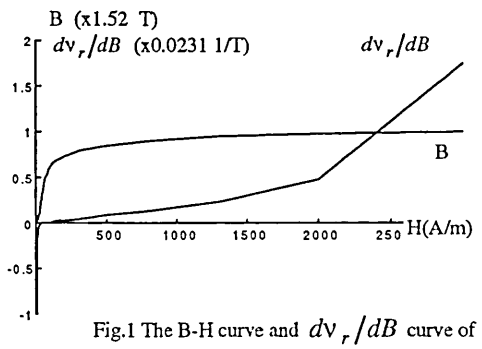


Fig.1 The B-H curve and $d\nu_r/dB$ curve of a typical limination

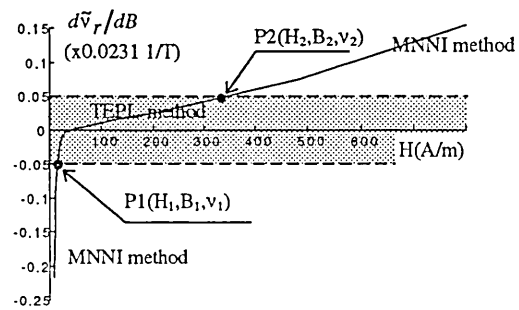


Fig.2 The areas for TEPL method and MNNI method with the setting of $|d\tilde{\nu}_r/dB|$=0.05

## III. Application And Analysis

### A. *The Electromagnetic Device*

The method is applied to a single phase tubular linear induction actuator (TLIA). The principal structure of the TLIA is shown in Figure 3. There are eddy currents induced in the plunger, which interact with the main flux to produce a thrust force. If the stator and mandrel are made of solid iron, the eddy currents in them should be taken into account as well. The electromagnetic field of the TLIA is axisymmetric. The simulation of transient response has been

carried out under the condition that the plunger is at a fixed position, i.e., no mechanical movement involved.

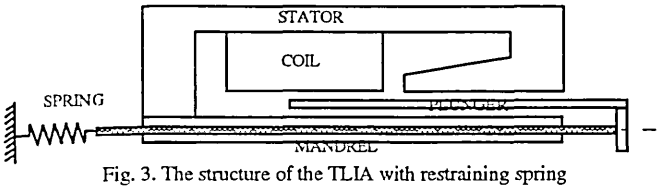


Fig. 3. The structure of the TLIA with restraining spring

*B. The External Circuit*

The actuator has been developed for a controllable positioning application, the control being achieved by the drive circuitry. In the present work, the actuator is energised by two methods:

*1) Triac controller:* A part of sinusoidal voltage supply, controlled by the triac, is fed to the actuator, as shown in Figure 4.

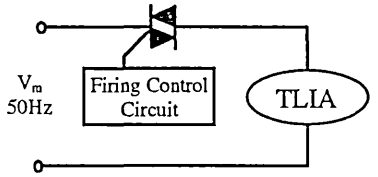


Fig. 4. TLIA under the triac control

We use the following relation for the use in (2)

*i.* $u(t)=V_m\mathrm{Sin}(2\pi ft+\phi_0)-V_{th}$

*ii.* R(t)=r when the triac is in conducting mode, or
R(t)=$10^7 r$ when the triac is in inhibiting mode

where $V_m$ is the voltage amplitude, $\phi_0$ is the firing phase angle, $V_{th}$ is the voltage drop on the triac and $r$ is the winding resistance.

When a load is inductive as most electromagnetic devices are, special attention should be paid to R(t), as the triac will be inhibited from conducting only after the current crosses the zero level and before the next triggering pulse arrives. A large resistance of $10^7 r$ is used to express the triac in the inhibiting mode. As for the voltage drop $V_{th}$, although it is current dependent, its magnitude relative to $V_m$ is small. A constant value of 1.0 volt for $V_{th}$ is used in our computations.

*2) PWM controlled DC to AC converter*: A dc supply is converted into a PWM ac through a driving circuit employing a fully controlled bridge with IGBTs and flywheel diodes, as shown in Figure 5.

It is assumed that the inductance and the PWM frequency are properly chosen to maintain a continuous current flow between two consecutive PWM pulses. The following two relations are used in (2).

i. u(t)= sign(sin($2\pi ft+\phi_0$))($V_{dc}$-2$V_{sat}$), when the IGBTs are switched on. Otherwise, u(t)= -sign(Sin($2\pi ft+\phi_0$))2$V_{cl}$.

ii. R(t)=r

where $V_{sat}$ is the saturated voltage drop on a IGBT, $V_{cl}$ is the voltage clamped by the flywheel diodes.

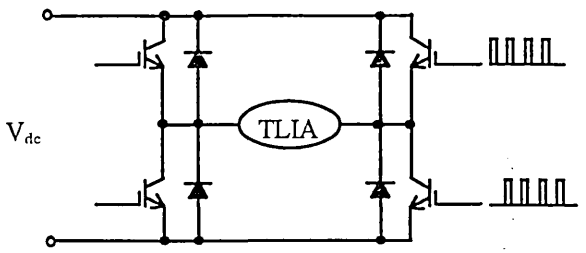


Fig. 5. Full bridge PWM controlled TLIA

For more exact representations of the characteristics of power semiconductors, classical expressions under exponential form can be used. However this will lead to complexities in dealing with the non-linearities of the external circuit. In this paper, we treat this non linearity as a two-state switch with a fixed voltage drop.

*C. Simulated Results*

In order to examine the effectiveness of the scheme, the step response of the TLIA is studied first. An equal length of integral time step is used with the setting of $\Delta t=2.5\times10^{-5}$ second. Four methods, the linear method with $u_r$=6000, the full MNNI method, the full TEPL method and the proposed method, have been investigated. The current responses and relative errors are given in Fig.6.

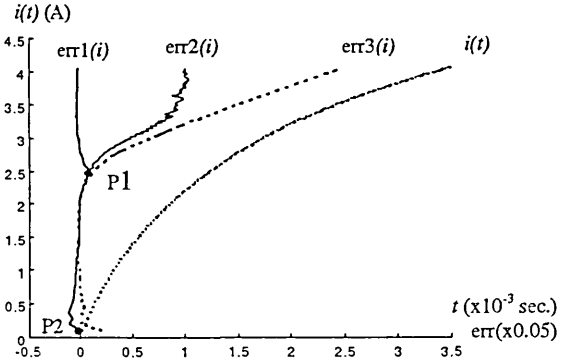


Fig.6 The step response of the TLIA

*i(i):* excitation current computed by the full MNNI method
err1*(i):* the error from the proposed method, relative to *i(t)*, with border setting at *i(P1)=0.1 (A)* and *i(P2)=2.5 (A)*
eer2*(i):* the error from the full TEPL method, relative to *i(t)*
eer3*(i):* the error from the full linear method, relative to *i(t)*

In addition to the small error evident in our proposed scheme as shown in Figure 6, the CPU time is significantly saved, compared with those by the standard MNNI method. It can also be seen that there is very small difference between err1*(i)* and *err2(i)* when *i* is small. This is caused by the air gap and non-ferromagnetic material in the path of the main flux, which reduces the non linearity at a small current. So, the P1 point can be set at *i*=0 without loss of accuracy for such a structure in which an air gap and/or non-ferromagnetic materials exist in the path of main magnetic flux.

The next example is the triac controlled sinusoidal voltage supply. With a setting of $f$=50Hz, $\phi_0$=0 and firing phase angle $\phi_{tr}=120^0$, the transient response was simulated. The back electromotive force (BEF) and the current obtained by this simulation are shown in Figure 7. For a fixed time integral step, it is difficult to predict the exact time when the current reaches zero. An interpolation or a variable step length is required to calculated the BEF at the time the triac switches from conducting to inhibiting state. We treat this problem by the use of a delayed switch technique which sets the triac to inhibiting state after the current crosses the zero level. When the time step is small, the delayed switching works very well because of the very small time delay of switching of practical components.

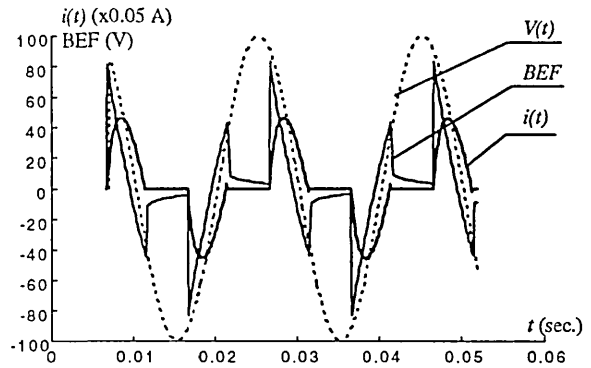


Fig.7 the responses of BEF and current of the TLIA under triac controlled sinusoidal voltage supply

Finally the transient response of TLIA driven by the PWM circuitry shown in Figure 5 was simulated. The base frequency and the PWM switch frequency were set at 100Hz and 1.5kHz respectively. The duty cycle of the PWM pulse was 0.3 and the switching on phase angle was $74^0$. A $0.3\text{x}10^{-4}$ fixed time step was used, which gives 8 integral steps within the duty period and 19 integral steps in the off-duty period. The responses of the BEF and the current are given in Figure 8.

In the above two simulations, the proposed method is used with the border setting at $i(P1)$=0 and $i(P2)$=2.5 A. This setting is based on the study of step response. Actually only TEPL method based on the DMVP method has taken effect, due to the current has not gone beyond the P2 point.

## IV. Conclusion

The transient non-linear behaviour of electromagnetic devices driven by switch mode power electronic circuits can be effectively simulated with the proposed method. The border points P1 and P2 are dependent on the structure. An appropriate choice of the border points will produce both high accuracy and fast solution. The power of the method could be exploited in transient simulations taking into account of hysterysis property of ferromagnetic materials as well.

## Acknowledgment

The authors thank Professor R W Johnson, Head of the School of Engineering at the University of Abertay Dundee for his support and encouragement. The financial support provided by AT&T (GIS) Scotland for this research is gratefully acknowledged.

## References

[1] Francis Piriou and Adel Razek, 'Coupling of Saturated Electromagnetic Systems to Non-linear Power Electronic Devices', *IEEE Trans. on Magn.*, Vol.24, pp274-77, 1988

[2] Z.W. Shi and C.B. Rajanathan, 'A Method of Approach to Transient Eddy Current Problems Coupled with Voltage Sources', , *Conference Record of 10th COMPUMAG Conference*, Paper PI1-8, pp650-651, 1995

[3] A. Nicolet, F. Delincé, N.Bamps, A.Grnon and W.Legros, 'A Coupling Between Electric Circuits and 2D Magnetic Field Modeling', *IEEE, Trans. on Magn.*, Vol.29, pp1697-700, 1993

[4] S.Q. Zheng and D. Chen, 'Analysis of Transient Magnetic Fields Coupled to Mechanical Motion in Solenoidal Electromagnet Excited by Voltage Source', *IEEE Trans. on Magn.* , Vol.28, pp 1315-17,1992

[5] I.A. Tsukerman, A.Konrad, G.Meunier and J.C. Sabonnadiére, 'Coupled Field-Circuit Problems: Trends and Accomplishments', *IEEE Trans. on Magn.*, Vol.29, pp1701-04, 1993

[6] P.S. Sangha and D. Rodger, 'Design and Analysis of Voltage Fed Axisymmetric Actuators', *IEEE Trans. on Magn.*, Vol.30, pp3241-43 1994

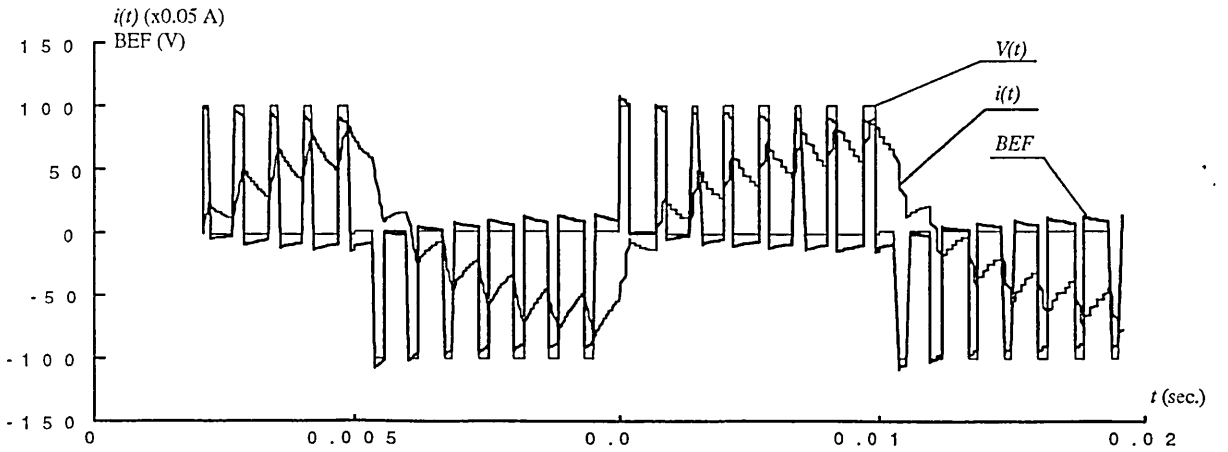


Fig.8 the responses of BEF and current of the TLIA under PWM driving

# Computation of Transient Temperature Field in a Linear Induction Actuator Driven by Power Electronic Circuits

Z.W. Shi and C.B. Rajanathan
School of Engineering, University of Abertay Dundee
Bell street, DUNDEE DD1 1HG, UK

## ABSTRACT

The transient temperature field of a tubular linear induction actuator is simulated by time stepping finite element method (FEM). The coupling of the electromagnetic field equations, the external circuit equations and the thermal equation is achieved in a weak form. Good agreement between the computed results and the experimentally determined test results confirms the effectiveness of the method.

## INTRODUCTION

The rise of temperature in many electromagnetic devices, due to various losses which are of electromagetic origin, plays a vital role in their safe operation[1]. This problem becomes more important in linear induction actuators for positioning application, due to the three main factors:

- the large eddy current losses induced from main magnetic field
- the poorer ventilation facilities
- temperature dependence of properties of materials

The thermal influence of these factors will not only cause the break down electrical insulation by the overheating of windings, but also bring extra complications in positioning control. When forced ventilation becomes unavoidable, the whole system becomes more complex than their rotary counterpart and some of the inherent advantages, such as robustness and simplicity, of linear induction actuators suddenly disappear. Therefore a precise temperature calculation plays a vital role in such designs where temperature rise is the main factor limiting its operating duration under continuous excitation.

The traditional non-numerical analytical methods can only predict the average temperature in particular components of electromagnetic devices with simple structures. Practical devices usually have complex geometric shape and lack the empirical parameters required by analytical method at the development stage of a product. Modern developments in the finite element method overcomes these problems ans enables the accurate pred-determination of the entrire temperature distribution within electromagnetic devices of any shape.

The computation of the temperature field by FEM requires the coupling of the electromagnetic field described by Maxwell's equations, with the equations discribing the state of the external driving circuits. The thermal and electromagnetic equations can be coupled by either a direct coupling method or an indirect coupling method [2]-[3]. Generally speaking, the physical properties of materials such as the electric conductivity, the magnetic permeability, etc., are temperature dependent. Therefore ideally the thermal equation and the electromagnetic equation should be solved together as simultaneous equations. This is the so called direct electromagnetic-thermal coupling method.

For electromagnetic devices working in the low frequency range and used as driving/positioning mechanisms, their electric transient time constant is one or two orders smaller than thermal time constant. The maximum temperature will not exceed beyond their Curie point after which material properties change dramatically. In these cases, the thermal equation and the electromagnetic equation can be solved separately without loss of accuracy. This is the so called indirect electromagnetic-thermal coupling method. It is this indirect coupling that is used in this paper.

The simpler time-harmonic form of Maxwell's equations should provide adequate accuracy for the purpose of temperature computation for those electromagnetic devices with constant loads. In positioning applications, however, the time-harmonic form is not good enough, due to the fact that the position may change in unpredictable patterns and the total settling time required will be different from position to position. So, a time-dependent form of the Maxwell's equation will be more appropriate in these cases. A dual magnetic vector potential method proposed by the authors in [4] and [5] is used here, extending it further to couple the thermal equation and simulate the transient temperature distribution in a tubular linear induction actuator being developed for positioning applications. The standard backward Euler's difference method is used to treat all the time derivatives in the equations.

## NUMERICAL MODELLING

### A. The Electromagnetic Field Equations

The time dependent Maxwell's equation and the constitutive relationships can be expressed as

$$\nabla \times \bar{H} = \bar{J}_s + \bar{J}_e \tag{1}$$

$$\bar{J}_e = -\sigma \frac{\partial \bar{B}}{\partial t} \tag{2}$$

$$\bar{H} = \nu \bar{B} \tag{3}$$

$$\bar{J}_s = \frac{N \cdot I(t)}{S} \tag{4}$$

where $\bar{J}_s$ is the excitation current density of the winding with number turns $N$, cross section area $S$ and current $I(t)$, $\bar{J}_e$ is the induced current density in the massive conductive material with conductivity of $\sigma$, and $\nu$ is the magnetic reluctivity.

Dual magnetic vector potentials $\bar{A}_s$ and $\bar{A}_e$ are introduced to assist the computation and these are defined in a time discretized form as,

$$\bar{B}^n = \nabla \times (\bar{A}_s^n + \bar{A}_e^n) \tag{5}$$

$$\Delta t^n \cdot \nabla \times \nu \nabla \times \bar{A}_s^n - \sigma \bar{A}_s^n = \Delta t^n \cdot \bar{J}_s \tag{6}$$

$$\Delta t^n \cdot \nabla \times \nu \nabla \times \bar{A}_e^n - \sigma \bar{A}_e^n = -\sigma (A_s^{n-1} + A_e^{n-1}) \tag{7}$$

Once $\bar{J}_s$ or $I(t)$ is known, $\bar{A}_s$ can be computed from (6) and then $\bar{A}_e$ can be computed from (7). As is well known, the vast majority of electromagnetic devices are voltage driven. Consequently when they are used in either open loop control or closed loop control, the directly available control variable is the voltage that can be simulated numerically according to the control algorithm. The time variation and magnitude of the current for a given voltage can only be computed by coupling the external circuit equation with (6) and (7).

B. Coupling of the External Circuit Equation

Assuming that the voltage $U(t)$ is obtained through a separate computation/simulation process and that no independent capacitors exist in the loop encompassing $U(t)$ and the electromagnetic device, we can express the external circuit as

$$U(t) = \frac{R \cdot S \cdot |\bar{J}_s|}{N} + \frac{d}{dt} \oint_l (\bar{A}_s + \bar{A}_e) \cdot d\bar{l} \tag{8}$$

where $R$ is the equivalent winding resistance in the form of a lumped parameter. The second term in (8) represents the back electromotive force induced in the winding.

The apparently straightforward procedure to couple (8) with (6) and (7) is to substitute the $\bar{J}_s$ from (8). However,our previous reported studies have shown that this direct coupling will result in more CPU time in the computation when the winding area is not small. In this case (i.e. when the winding area is meshed with a large number of nodes), it is better to separate (8) from (6) and (7). This measure requires the introduction of an iterative search procedure to determine the correct $\bar{J}_s$ that will satisfy both (8) and (6). A second order search algorithm in the form of Newton's interpolation method was adopted by the authors, which can be expressed as,

$$I_{m+1} = I_m + \frac{U_{m+1} - U_m}{U_m - U_{m-1}} (I_m - I_{m-1}) \tag{9}$$

The particular issue raised by the use of power electronic components, such as MOSFETs, IGBTs, Thyristors, Triacs, etc., in the circuit is the simulation of the effect of switching action. In the FEM implementation, the authors have successfully used different combinations of voltage $U(t)$ and equivalent resistance $R(t)$ to simulate the behaviour of power semiconductors under different operating conditions as discussed in detail in [5].

C. Thermal Equation with Electric Losses as Heat Sources

The diffusion equation describing the temperature field associated with the heat conduction in a material is,

$$\rho c (\frac{\partial T}{\partial t} + \bar{v} \cdot \nabla T) - \nabla \cdot (k \nabla T) = q \tag{10}$$

where ρ, $c$, $k$ and $q$ are mass density, specific heat, thermal conductivity and heat source density respectively. The term $\bar{v}$ is the velocity which can be neglected in devices used for positioning applications. For the electromagnetic devices, there are three types of boundary conditions to be deal with:

- Dirichlet boundary condition: $T|_{\Gamma_1} = T_0$
- Neumann boundary condition: $k \left.\frac{\partial T}{\partial n}\right|_{\Gamma_2} = q_{n0}$
- Convection boundary condition: $\left.\frac{\partial T}{\partial n}\right|_{\Gamma_3} = h_c (T - T_\infty)$

where $T_0$, $T_\infty$, $\Gamma$, $q_{n0}$, and $h_c$ are constant temperature, ambient temperature, boundary, constant input heat flux and heat transfer coefficient respectively.

The determination of the heat transfer coefficient could be achieved by solving the boundary layer equations only for the simple flow situation. However a more practical approach frequently involves calculating the average heat transfer coefficient $\bar{h}_c$ from empirical relations such as

$$\bar{h}_c = \frac{N_u \cdot L}{k} \tag{11}$$

where $L$ is the characteristic length, $N_u$ is the Nusselt number that can be calculated from the empirical formula of $N_u = c \cdot R_e^m \cdot P_r^n$ for forced convection or $N_u = c \cdot N_{Ra}^m$ for free convection. $R_e$, $P_r$ and $N_{Ra}$ are the Reynolds number, the Prandtl number and the Rayleigh number respectively. The constants $c$, $m$ and $n$ should be determined by experiments. For horizontal cylinders in free convection these parameters are given by, $N_u = 1.08 N_{Ra}^{0.1}$ for $10^{-4} < N_{Ra} < 1$, $N_u = 1.08 N_{Ra}^{0.155}$ for $1 < N_{Ra} < 10^3$ and $N_u = 0.537 N_{Ra}^{0.25}$ for $10^3 < N_{Ra} < 10^9$ [7].

Since the temperature range will not exceed beyond the Curie point, the temperature influence on material conductivity is approximated by

$$\sigma = \frac{\sigma_0}{1 + a(T - T_0)} \tag{12}$$

where $a$ is the temperature coefficient of conductivity.

The heat source $q$ considered here consists of two parts. These are the losses in the winding and the losses in the massive conductive material in which induced currents flow. It is calculated by

$$q(t) = \gamma_{eq} |J_s(t)|^2 + \sigma \left| \frac{\partial \bar{A}}{\partial t} \right|^2 \tag{13}$$

where $\gamma_{eq}$ is the equivalent conductivity of the winding area with the terminal resistance of $R$. The magnetic hysterisis loss is neglected in the above equation. Considering the fact that the electromagnetic field computation is carried out in the transient form, we can easily take account of the magnetic hysterisis loss provided that an appropriate magnetic hysterisis model is incorporated into the computation of the electromagnetic field.

The introduction of $\gamma_{eq}$ lets the resistive losses in the winding to be calculated in an easy and unified way as the calculation of eddy current losses.

The energy function correspondent to (10) with $\bar{v}=0$ can be expressed as

$$\Im = \frac{1}{2}\int_{\Omega}[k\nabla T\cdot\nabla T - \rho c\left|\frac{dT}{dt}\right|^2 - 2qT]d\Omega - \oint_{\Gamma_1\ldots\Gamma_3} T\nabla T\cdot\bar{n}\cdot d\Gamma \qquad (14)$$

The FEM can be applied directly to the above equation. With a backward Euler's difference method to treat time derivatives, all the stiffness matrix obtained from (6), (7) and (14) are positive definite that enable us to use the Incomplete Choleski Conjugate gradient (ICCG) method to obtained a fast solution.

## APPLICATION TO A TLIA

The geometry of the single phase TLIA that has been designed and constructed and used for experimental verfications is shown in Fig. 1. Its simple structure and characteristics are inherently suitable for positioning in a stepless and continuous manner under open or closed loop control.

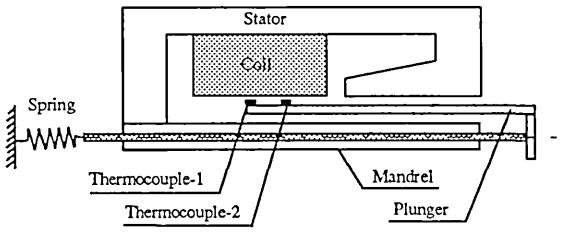


Fig. 1 The structure of the TLIA with restraining spring and the locations of thermocouples

The operating principle of the actuator is based on the Lorentz electromagnetic force that is generated by the interaction between the main magnetic field and the induced eddy currents in the plunger. The total electromagnetic force in the form of axial thrust will vary with the position of the plunger under constant voltage or constant current excitation. Therefore control of the TLIA can be achieved by real-time control of the applied voltage or current. In this work the terminal voltage control method was adopted. The waveforms of the excitation voltages could be continuous sinusoidal wave or a pulse width modulated square wave.

Due to the axial symmetry of the structure, an axi-symmetric FEM formulation is applied to the TLIA. Fig.2 shows the flow chart of the computation of the transient electromagnetic field and the temperature field.

A triac controlled sinusoidal voltage supply with the firing delay angle set at $75^0$ was simulated for the case when the plunger is at a fixed position. To model in the *r-z* plane, the cross section was descretized into 3927 triangular finite elements with 7594 nodes. Due to the fact that the actuator is operated in a horizontal position in open air without forced ventilation, the formula $N_u = 1.08N_{Ra}^{0.1}$ was used to calculate the average heat transfer coefficient. The typical contours of the transient temperature distribution computed by this method are shown in Fig. 3.

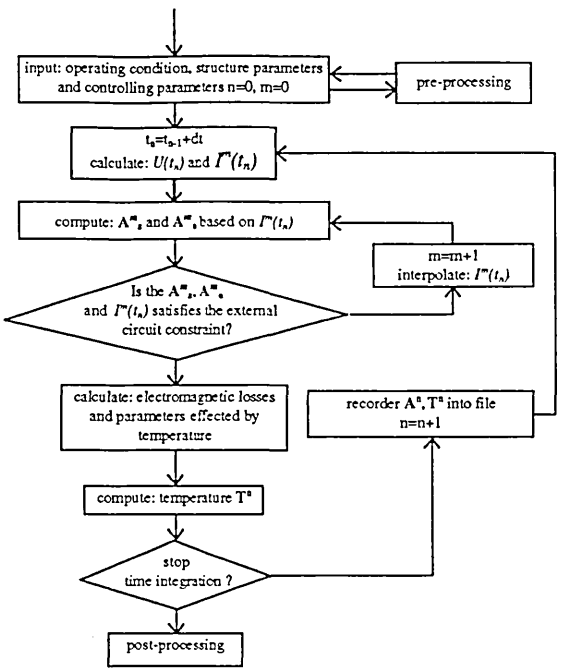


Fig. 2 the flow chart of the computation of transient electromagnetic field and temperature field

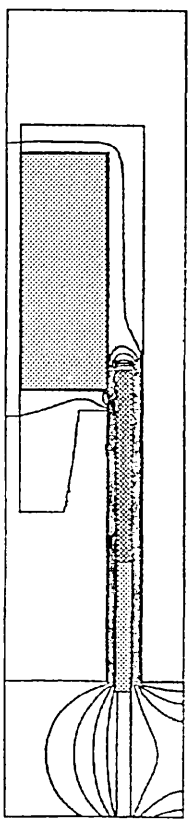

Fig. 3a. The temperature contours of a TLIA at time=25 seconds

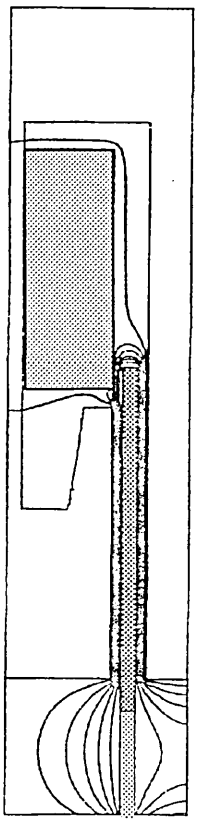

Fig. 3b. The temperature contours of a TLIA at time=50 seconds

The above figures reveal that the plunger contains the hottest parts of the structure concentrated around the working end. The position where thermocouple-1 is placed seen in Fig. 1, is the hot spot in the plunger. Since the stator

coil is the only part susceptible to damage by overheating as it is so close to the hot plunger, its design and that of the coil former eventually determine the safe operating region. We can also conclude that only forced internal ventilation can significantly enlarge the safety operation region.

The experimental configuration shown in Fig. 4 was used to carry out tests to verify the simulation results.

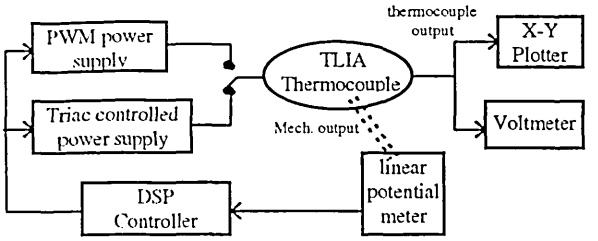


Fig. 4 Configuration of the experimental measurement

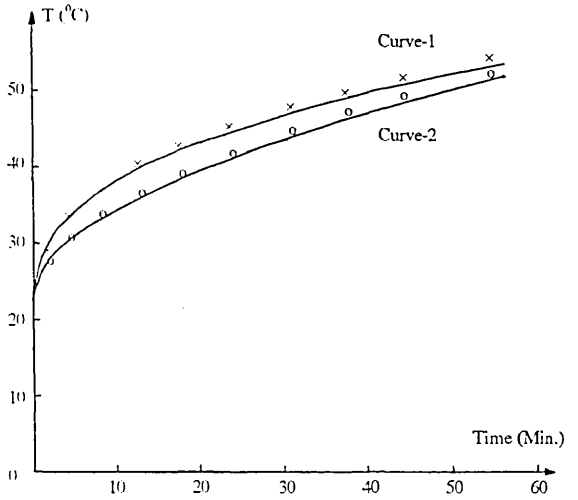


Fig. 5 Comparison of the measured and computed temperature rising curves and test point-1

Curve-1: computed results with $U$=32.5 V(r.m.s.) and z=20mm
Curve-2: computed results with $U$=43.5 V(r.m.s.) and z=30mm
x x : measured results with $U$=32.5 V(r.m.s.) and z=20mm
o o : measured results with $U$=43.5 V(r.m.s.) and z=30mm

In the closed loop control scheme seen in Fig.4, the TMS320 DSP controller receives the displacement feedback signal from the linear potentiometer and generates the controlling signal to the power supply unit that produces the appropriate driving voltage. In our temperature tests, only a constant controlling voltage, i.e. constant driving voltage, is used, which is set to provide a burst of firing pulses with a $75^0$ phase delay angle. The electric transient process was fully taken into account. However, the mechanical transient process was not considered since the method of simulating the electromagnetic field has not incorporate mechanical movement and control algorithm. A copper/copper-nickel thermocouple was used to measure the temperature at the two positions shown in Fig. 1. The transient temperature curves for test point-1 are illustrated in Fig 5. Both measured and simulated results are given. From Fig. 5 we can see that the measured results agree well with the simulated results despite the fact that the simulated temperature is slightly lower than the measured one. It can be explained by the fact that the actual stator is made of the solid steel with magnetic hysterisis losses that is not taken into account in the simulation of electromagnetic field.

Fig. 5 also shows the temperature continuously rising even after one hour of continuous operation. This is an expected result. During testing, on one occasion the coil former was deformed after about 50 minutes of operation with about 2 amperes of current.

## CONCLUSION

The electromagnetic-thermal coupling problems that characterise the tubular linear induction actuators have been simulated by the time dependent finite element method. Although only the temperature in the working end of the plunger has been measured, all the results obtained from the simulation seem to be very realistic. The computation shows that the highest temperature is located at the working end of the plunger. Both experiment and simulation indicate the need for forced cooling if the actuator is expected to under take moderate current for a long periods of time.

## ACKNOWLEDGEMENT

The authors thank Professor R W Johnson, Head of the School of Engineering at the University of Abertay Dundee, for his support and encouragement. The financial support provided by AT&T(GIS) Scotland for this research is gratefully acknowledged.

## REFERENCE

[1] J.F. Gieras and D. Carter, 'Computation of temperature Distribution in the Longitudinal Section of a Single-sided Linear Induction Motor', ICEMA, Vol.1, Sep. 1993, pp180-5

[2] M. Jarnieux, G.Reyne and G.Meunier. 'FEM Modelling of the Magnetic Thermal, Electrical and Mechanical Transient Phenomena in Linear Induction Lunchers', IEEE Trans. on Magn., Vol.30, No.5, Sep. 1994, pp3312-5

[3] José Américo Dias Pinto, Carlos F. Lemos Antunes and A. Paulo Bre Coimbra, 'Transient Heating and Cooling Analysis in an Electromagnetic Device', IEEE Trans. on Magn., Vol.30, No.5, Sep. 1994, pp 3339-42

[4] Z.W. Shi and C.B. Rajanathan, 'A Method of Approach to Transient Eddy Current Problems Coupled with Voltage Sources', Proc. of COMPUMAG'95, Berlin, July 1995

[5] Z.W. Shi and C.B. Rajanathan, 'Computation of Non-linear Transient Eddy Current Electromagnetic Fields in Devices Driven by Power Electronic Circuits', The Seventh Biennial IEEE Conference on Electromagnetic Field Computation, Okayama, Japan, March 1996

[6] E. Cardelli, M. Gimignani and M. Raugi, 'Numerical Modelling of 3-D Coupled Electromagnetic and Heating Diffusion Problems', IEEE Trans. on Magn., Vol.30, No.5, Sep. 1994, pp3331-4

[7] Helmut Wolf, 'Heat Transfer', Happer & Row Publishers, New York, 1983.